UNIVERSIDADE DE SÃO PAULO
INSTITUTO DE FÍSICA DE SÃO CARLOS

Marcos Paulo Miotti

Technical thermodynamics of an inhomogeneous gas around the Bose-Einstein transition using the global-variable method

São Carlos

2021

Marcos Paulo Miotti

Technical thermodynamics of an inhomogeneous gas around the Bose-Einstein transition using the global-variable method

Dissertation presented to the Graduate Program in Physics at the Instituto de Física de São Carlos da Universidade de São Paulo, to obtain the degree of Master in Science.

Concentration area: Theoretical and Experimental Physics

Advisor: Prof. Dr. Vanderlei Salvador Bagnato

Corrected version

(Original version available on the Program Unit)

São Carlos

2021

Miotti, Marcos Paulo
Technical thermodynamics of an inhomogeneous gas around the Bose-Einstein transition using the global-variable method / Marcos Paulo Miotti; advisor Vanderlei Salvador Bagnato - corrected version -- São Carlos 2021.
165 p.

Dissertation (Master's degree - Graduate Program in Theoretical and Experimental Physics) -- Instituto de Física de São Carlos, Universidade de São Paulo - Brasil , 2021.

1. Bose-Einstein condensation. 2. Quantum gases. 3. Thermodynamics. I. Bagnato, Vanderlei Salvador, advisor. II. Title.

ACKNOWLEDGEMENTS

The author hereby lists the supporters of this master's project:

- the Coordination for the Improvement of Higher Education Personnel (CAPES) and the National Council for Scientific and Technological Development (CNPq);
- the staff of the São Carlos Institute of Physics (IFSC) and the University of São Paulo (USP) at São Carlos;
- the leadership and staff of the Research Center in Optics and Photonics (CePOF) and the Atomic Physics Laboratory.

There is no glory in your sacrifice.
God-King Xerxes to King Leonidas in *300*.

ABSTRACT

MIOTTI, M. P. **Technical thermodynamics of an inhomogeneous gas around the Bose-Einstein transition using the global-variable method**. 2021. 165p. Dissertation (Master in Science) - Instituto de Física de São Carlos, Universidade de São Paulo, São Carlos, 2021.

Thermodynamics of non-uniform systems has always been a challenging topic in the physical sciences. In the field of quantum gases, that subject is mainly studied with ultracold samples trapped in a harmonic potential, the first kind of confinement ever made to atomic fluids.[1] Nascimbène *et al.*[2] have already described a method to measure locally the equation of state and heat capacity of a harmonically trapped quantum gas. Nonetheless, local measurements cannot provide the volume-dependent susceptibilities of an inhomogeneous system, namely the thermal expansion and compressibility, meaning that the thermodynamic description of harmonically trapped gases is still incomplete. To solve that issue, Romero and Bagnato[3,4] proposed canonical variables of work for a gas in a harmonic trap, which work like pressure and volume for a gas in a vessel and allow global measurements on the system. Therefore, we describe here our methodology to measure the thermodynamic susceptibilities of a harmonically trapped gas around the Bose-Einstein transition using the Romero-Bagnato formalism. Our experiments were divided in different phases, each having the harmonic trap with unique frequencies, related to the formalism's extensive variable. In each phase, we prepared individual samples of rubidium-87 gas in the trap and imaged them using the time-of-flight technique. Next, we fitted our images with the bimodal model and found the *in situ* density profiles of the samples with the standard regression procedures. Then, we determined the phase's equation of state as a function of temperature and number of atoms. For the thermodynamic analysis, we used an empirical model that we developed to fit the equation-of-state curves, allowing us to represent our data in terms of mathematical coefficients. In that way, we found the curves of internal energy, heat capacity, thermal expansion and compressibility, thus achieving a full thermodynamic description of a harmonically trapped gas. Our method and its results are unprecedented in the literature and might contribute to the further understanding of non-uniform systems, as well as the future development of quantum thermal engines.

Keywords: Bose-Einstein condensation. Quantum gases. Thermodynamics.

RESUMO

MIOTTI, M. P. **Termodinâmica técnica de um gás inomogênio ao redor da transição de Bose-Einstein usando o método das variáveis globais**. 2021. 165p. Dissertação (Mestrado em Ciências) - Instituto de Física de São Carlos, Universidade de São Paulo, São Carlos, 2021.

A termodinâmica de sistemas não-uniformes sempre foi um tópico desafiador nas ciências físicas. No campo de gases quânticos, esse assunto é principalmente estudado com amostras ultrafrias aprisionadas em um potencial harmônico, o primeiro tipo de confinamento feito para fluidos atômicos.[1] Nascimbène *et al.*[2] já descreveram um método para medir localmente a equação de estado e a capacidade calorífica de um gás quântico aprisionado harmonicamente. Todavia, medidas locais não conseguem prover as susceptibilidades dependentes do volume de um sistema inomogêneo, nomeadamente a expansão térmica e a compressibilidade, significando que a descrição termodinâmica de gases aprisionados harmonicamente está ainda incompleta. Para resolver esse empecilho, Romero e Bagnato[3,4] propuseram variáveis canônicas de trabalho para um gás em uma armadilha harmônica, que funcionam como pressão e volume para um gás em um recipiente e permitem medidas globais sobre o sistema. Portanto, descrevemos aqui nossa metodologia para medir as susceptibilidades termodinâmicas de um gás aprisionado harmonicamente ao redor da transição de Bose-Einstein usando o formalismo de Romero-Bagnato. Nossos experimentos foram divididos em diferentes fases, cada uma tendo uma armadilha harmômica com frequências únicas, relacionadas à variável extensiva do formalismo. Em cada fase, preparamos amostras individuais de gás rubídio-87 na armadilha e capturamos as imagens delas com a técnica de tempo de voo. Depois, ajustamos a função do modelo bimodal às imagens e encontramos os perfis de densidade *in situ* das amostras com os procedimentos normais de regressão. Então, determinamos a equação de estado da fase experimental como função da temperatura e do número atômico. Para a análise termodinâmica, usamos um modelo empírico que desenvolvemos para ajustar as curvas de equação de estado, permitindo-nos representar nossos dados em termos de coeficientes matemáticos. Dessa forma, encontramos as curvas da energia interna, da capacidade calorífica, da expansão térmica e da compressibilidade, assim obtendo uma descrição termodinâmica completa de uma gás aprisionado harmonicamente. Nosso método e seus resultados são imprecedentes na literatura e devem contribuir para o entendimento subsequente de sistemas não-uniformes, assim como para o futuro desenvolvimento de máquinas térmicas quânticas.

Palavras-chave: Condensação de Bose-Einstein. Gases quânticos. Termodinâmica.

CONTENTS

1 INTRODUCTION

We, the author and his co-workers, present in this chapter a brief historical account on studies of quantum gases of bosons, particularly the research on their thermodynamic properties, as well as our motivations for having developed this project.

1.1 The Quest for the Bose-Einstein Condensate

In 1924, Albert Einstein received a paper from Satyendra Nath Bose, in which the Indian physicist derived Planck's radiation law using a statistical distribution he found for radiation quanta (now called *photons*), without any argument relying on classical physics. Einstein was impressed, and on Bose's behalf, he translated the paper to German and submitted it to the now-defunct *Zeitschrift für Physik* (*Z. Phys.*), which published the article in the same year.[5] In the meanwhile, Einstein also worked on an extension of Bose statistics to ideal gases, seeking for an equivalence between radiation and matter (particularly the particles that are now called *bosons*). He succeeded quickly and his findings were also published in the *Z. Phys.* as a two-part article,[6,7] between the end of 1924 and the beginning of 1925.

In his work, Einstein found an astonishing result: according to the statistical distribution to material particles he derived, whose particular case for zero-mass particles is Bose's photon statistics, there would be a certain temperature that a gas would be energetically "saturated", then any new particle added to the system would "fall out" into lowest energy level (a zero-energy ground state in Einstein's paper), in way that the new particles would not contribute to the internal energy. He noticed that this supposed phenomenon was a phase transition in the momentum space, since the particles in the gas would "condensed" into the ground state when the "critical temperature" was reached.

The hypothetical phase transition that Einstein pointed out have not received much attention from the physical community at that time, specially after Uhlenbeck[8] in 1927 have questioned the nature of the transition in his PhD thesis. However, in 1938, Uhlenbeck himself co-working wih Kahn[9] took back his former objection, and months later London[10] argued that the sharp peak of the heat capacity and emergence of the superfluid state in liquid helium around 2.17 K (called the "λ point") was an evidence for Bose-Einstein condensation. For the next five decades, the field of low-temperature physics have grown expressively, and many sophisticated techniques have been developed. Yet, no sign of Bose-Einstein condensation in dilute gases has been spotted until the early 1990s.

In 1995, seventy years after Bose-Einstein statistics being proposed, three research groups in the USA reported the achievement of Bose-Einstein condensation in ultracold,

dilute gases of alkali metals, under highly controlled conditions: Cornell and Wieman's team at Boulder, using rubidium[11]; Ketterle's team at Cambridge, using sodium,[12] and Hulet's team at Houston, using lithium.[13] For this remarkable breakthrough, Cornell, Wieman and Ketterle shared the Nobel Prize in Physics in 2001. After 1995, gases of other elements have also been brought to quantum degeneracy by many research groups around the world: hydrogen[14] in 1998; helium[15] and potassium[16] in 2001; cesium[17] in 2003; chromium[18] in 2005; ytterbium[19] in 2007; dysprosium[20] in 2011, and erbium[21] in 2012.

1.2 Experimental Research on Thermodynamics of Quantum Gases

As early as the quantum degenerancy in harmonically trapped, dilute gases was achieved, the first studies on the thermal properties of those systems began. The first paper reporting measurements of the internal energy and the heat capacity of a rubidium gas in a harmonic trap was published by Ensher *et al.*,[22] back in 1996. In the years that followed, many other publications reporting thermal properties of the same kind of the system were made.

However, the most complete study on the thermodynamics of a gas in a harmonic potential was presented in 2004 by Gerbier and his co-workers,[23,24] in which the researchers made very precise experiments that could be compared with self-consistent Hartree-Fock calculations, ensuring the validity of that theoretical model.

From 2004 to the present days, many cold-atom laboratories around the world have built experiment apparatuses with box-potential traps, which were report in 2005.[25] As the mathematical formulation of classical thermodynamics was developed under the assumption of homogeneous systems, it is easier to make any experimental investigation when the density of the samples is constant. Notwithstading, there are many experimental setups still working with harmonic traps, such as the laboratories at São Carlos, and there many things can be explored with those systems, as we will show shortly.

1.3 Studies of Bose-Einstein Condensation in São Carlos

Brazil was the first country in Latin America to start experimental research on quantum gases. The first laboratory have been built in the 1990s at the São Carlos Institute of Physics, an unit of the University of São Paulo at São Carlos, where this master's project was developed. The production of Bose-Einstein condensates in that laboratory was firstly reported in Farias's PhD thesis,[26] back in 2004. From that time to the present days, São Carlos has became a wordwide reference in the research on quantum gases, specially in fields of quantum turbulence and thermodynamics of harmonically confined gases.

On the studies on thermodynamics, the São Carlos group is particularly notori-

ous for proposing an alternative method to analyze the thermal properties of a quantum gas confined in harmonic-potential traps, which induces non-uniform density profiles on the trapped samples. This method was developed together with the Ciudad de México quantum-gas research group, based at Universidad Nacional Autónoma de México (UNAM), and the core idea behind it is to find *global conjugated variables* in a nonhomogeneous gas that can *replace* conjugated variables that are not very defined in the system, which are volume and pressure in this case. For this reason, this approach is called the *Global-Variable Method* (GVM), and it was be the key analysis tool for the development of this study.

To show how useful the GVM can be, here is a list of the main experimental findings that our group have obtained from experiments with harmonically trapped atomic gases:

- equation of state around the Bose-Einstein transition[27];
- heat capacity around the Bose-transition[28];
- equation of state at the absolute zero[29];
- compressibility coefficient[30];
- thermal expansion coefficient[31];
- speed of sound in Bose-condensed gases.[32]

1.4 About this Dissertation

From the atmospheric density to the global distribution of household wealth, nonuniform systems are widely common in nature, and understading their behavior is certainly one of many challenges of contemporary science. In the last thirty years, that issue has also being investigated in the emerging field of ultracold quantum gases, particularly with samples confined in harmonic potentials. The reason is twofold: on the experimental side, techniques using harmonic potentials to trap and manipulate atomic gases at submicrokelvin temperatures are already well understood and generally feasible to implement[1]; on the theoretical side, the features of an ideal gas in a harmonic potential are well known, as one of the few cases of analitically solvable, nonhomogeneous systems.[33] Hence, harmonically trapped, ultracold gases are great toy models to study the behavior of inhomogeneous systems.

As mentioned before in this chapter, in the particular case of weakly interacting, Bose-Einstein-condensed gases in harmonic traps, the earliest measurements of their thermodynamic properties have been published by Ensher *et al.*[22] in 1996. Later, Gerbier *et al.*[23,24] have reported in 2004 precise measurements of the critical temperature and internal energy, showing that mean-field calculations agree with their findings. Finally in 2010, Nascimbène *et al.*[2] have described a sophisticated technique to map the pressure distribution in a harmonically trapped sample, thus measuring the equation of state locally. Despite all those advances, the inhomogeneous density added to the inexistence of

a confining volume prevent local measurements of the volume-dependent susceptibilities, namely the thermal expansion and compressibility coefficients, which are essential to a full thermodynamic description of the system. Therefore, the thermodynamics of a gas in a harmonic trap is problem still open to solve.

Aware of the limitations of local measurements, Romero and Bagnato[3,4] have proposed in 2005 a different formalism to tackle the problem stated above. As the gas in a harmonic potential is a mathematically solvable system, it should have macroscopic quantities equivalent to canonical variables of work, which function like pressure and volume for a gas confined in a vessel. Using statistical mechanical arguments, Romero and Bagnato found those quantities, which were called *global variables*, as they allowed global measurements on the system. From that time to the present, independent measurements of equation of state,[27] heat capacity,[34] compressibility[30] and thermal expansion[31] using the global-variable formalism have been done, but none of them presented a universal procedure to measure all those quantities as a single experiment, due specially to limited data. On that account, we will present here our own methodology to obtain the equation of state and all the thermodynamic susceptibilities of a harmonically trapped gas, providing for the first time the complete thermodynamics of that kind of system.

As we shown in Sec. 1.3, the past publications have presented different properties of the gas samples individually, but none of those studies have shown a full thermodynamic description of the system, especially due to the limited amount of experiment data. To fill this gap, we started this master's project intending to carry on a long-term set of experiments to acquire a large set of experiment data, with which the full thermodynamic description could be obtained. However, our main goal here is to show that it is possible to provide that description by using a simplified mathematical model to represent the empirical equation of state of the gas, which was the approach we chose during the development of this project. The seminal details are all presented here.

For the sake of guiding the readers, here is a summary of this thesis:

- in Chap. 2, we review the statistical mechanics of quantum gases and other key concepts necessary to this study;
- in Chap. 3, we introduce and discuss the theoretical framework of the GVM;
- in Chap. 4, we explain how the experimental apparatus that we used works;
- in Chap. 5, we discuss our analytical methods for treating the acquired data;
- in Chap. 6, we present the set of thermodynamic quantities we obtained from the experimental data, which provide a complete thermodynamic description of a gas sample in a harmonic potential;
- in Chap. 7, we summarize the main achievements of this project.

2 PHYSICS OF QUANTUM GASES

In this chapter, we will see the fundamental concepts behind the behavior of gases at low densities. The statistical distributions of quantum gases will be described in Section 2.1. The author refered to Huang's[35] and Pethick and Smith's[36] textbooks to write this chapter. More specific references will be cited in the text.

2.1 Quantum Statistics

As far as it is known, elementary particles can be divided into two classes: the half-integer spin *fermions* and the integer spin *bosons*. The former obey Pauli exclusion principle, which means that two identical fermions cannot occupy the same quantum state, while the latter have no restrition on the number of identical bosons that can populate the same state. For that reason, systems of many fermions and bosons follow different statistical distributions, which mean their physical properties are utterly different. On the account, let us consider a gas of identical fermions or identical bosons in thermal equilibrium, whose ground-state energy level is zero. The average number of particles that occupy a certain quantum state s of energy ε_s in that system is

$$\bar{N}_s^{\pm} = \frac{g_s}{e^{(\varepsilon_s - \mu)/(kT)} \pm 1}, \tag{2.1}$$

in which g_s is called the degeneracy of the s-th state (the number of individual states that share the same energy level), T is the temperature, μ is the chemical potential and k is the Boltzmann constant. Eq. (2.1) is called *Fermi-Dirac distribution* for fermions $(+)$ and *Bose-Einstein distribution* for bosons $(-)$. As we can readily see, in the limits of very low numbers of particles ($\bar{N}_s^{\pm} \ll 1$) and very high temperatures ($T \to \infty$), both Fermi-Dirac and Bose-Einstein distributions reduce to Maxwell-Boltzmann distribution.

As Eq. (2.1) describes physical systems, it is usually solved by setting constraints on the total number of particles N and the internal energy E, according to the expressions

$$N = \sum_s \bar{N}_s^{\pm} \qquad \text{and} \qquad E = \sum_s \bar{N}_s^{\pm} \varepsilon_s. \tag{2.2}$$

Nonetheless, it is still very difficult to compute the sums in Eq. (2.2) in general. For that reason, we will use the *continuous spectrum approximation*, in which the set of energy levels is taken as a continuum, therefore turning the summations in Eq. (2.2) into integrals. That approach is valid when the thermal energy is much greater than the energy level spacing,

i. e.,

$$kT >> \varepsilon_{s+1} - \varepsilon_s. \tag{2.3}$$

Formally, we take every g_s as a partition, then the summations in Eq. (2.2) become Riemann's sums. Hence, we obtain

$$N = \lim_{\max(g_s)\to 0} \sum_s \frac{g_s}{e^{(\varepsilon_s-\mu)/(kT)} \pm 1} = \int_{G_\varepsilon} \frac{1}{e^{(\varepsilon-\mu)/(kT)} \pm 1}\, \mathrm{d}g \tag{2.4}$$

and

$$E = \lim_{\max(g_s)\to 0} \sum_s \frac{\varepsilon_s g_s}{e^{(\varepsilon_s-\mu)/(kT)} \pm 1} = \int_{G_\varepsilon} \frac{\varepsilon}{e^{(\varepsilon-\mu)/(kT)} \pm 1}\, \mathrm{d}g, \tag{2.5}$$

whose integrals run over the phase-space domain G_ε.

We need now to determine how the phase-space differential $\mathrm{d}g$ is connected to the continuous energy ε. Let us consider for this purpose that the system is subjected to a position-dependent potential $U = U(\boldsymbol{r})$. For a set of particles in the energy range $\varepsilon \to \varepsilon + \mathrm{d}\varepsilon$, the total energy is

$$\varepsilon = \frac{p^2}{2m} + U(\boldsymbol{r}), \tag{2.6}$$

in which $p = \|\boldsymbol{p}\|$ is the norm of the momentum vector of the particles. Moreover, it is no mystery that

$$\mathrm{d}g = \frac{1}{(2\pi\hbar)^3}\, \mathrm{d}^3p\, \mathrm{d}^3r \tag{2.7}$$

As the kinectic energy depends only on p, it is easier to write the momentum-space differential in spherical coordinates, i. e.,

$$\mathrm{d}^3p = 4\pi p^2 \mathrm{d}p \tag{2.8}$$

Hence, by isolating p in Eq. (2.6) and substituting it into Eq. 2.8, we get

$$\mathrm{d}^3p = 2\pi(2m)^{3/2}\sqrt{\varepsilon - U(\boldsymbol{r})}\, \mathrm{d}\varepsilon, \tag{2.9}$$

thus Eq. (2.7) can be written as

$$\mathrm{d}g = \frac{2\pi(2m)^{3/2}\sqrt{\varepsilon - U(\boldsymbol{r})}}{(2\pi\hbar)^3}\, \mathrm{d}^3r\, \mathrm{d}\varepsilon. \tag{2.10}$$

Now we can finally rewrite Eqs. (2.4) and (2.5) as

$$N = \int_0^\infty \frac{\varrho(\varepsilon)}{e^{(\varepsilon_s-\mu)/(kT)} \pm 1}\, \mathrm{d}\varepsilon \quad \text{and} \quad E = \int_0^\infty \frac{\varepsilon\varrho(\varepsilon)}{e^{(\varepsilon_s-\mu)/(kT)} \pm 1}\, \mathrm{d}\varepsilon, \tag{2.11}$$

in which we defined the *density of states*

$$\varrho(\varepsilon) \equiv \frac{2\pi(2m)^{3/2}}{(2\pi\hbar)^3} \iiint_{R_\varepsilon} \sqrt{\varepsilon - U(\boldsymbol{r})}\, \mathrm{d}^3 r, \tag{2.12}$$

whose space domain of integration R_ε depends on the condition $\varepsilon \geq U$. The results in Eqs. (2.11) are remarkable, since we have simple expressions to calculate the thermodynamic properties of a gas subjected to generic potential $U = U(\boldsymbol{r})$, whether the integrals have analytical solutions or not. It is worthy to remind that Eq. (2.11) hold only if the conditions in Eq. (2.3) are satisfied. As a consequence, the continuous-spectrum approximation cannot be used at very low temperatures and for few-body systems.

Henceforth, we will the thermal properties of two notorious cases: the box potential, which is the standard option used in the usual thermodynamic studies, and the harmonic potential, which was the first potential able to trap gas samples that could be Bose-condensed and is the potential that was used in experiments described in Chaps. 5 and 6. For the brevity, the calculation of the density-of-states functions of those cases will be described in Appx. A, as we presented in the previous lines the whole formalism to determine the thermodynamic properties of a gas subjected to a general potential.

On the one hand, for a gas subjected to a box potential of volume V, the Hamiltonian is

$$H(\{\boldsymbol{r_i}\},\{\boldsymbol{p_i}\}) = \begin{cases} \displaystyle\sum_{i=1}^{N} \frac{\|\boldsymbol{p_i}\|^2}{2m} & \text{inside the box of volume } V. \\ 0 & \text{outside the box of volume } V. \end{cases} \tag{2.13}$$

Within the box, the potential energy is zero, thus the internal energy of the system purely kinetic, as we see in the first line of Eq. (2.13). Moreover, the potential isolates thermally the gas from its surroundings, which explains why the Hamiltonian goes to zero outside the box. On that account, we use the density of states presented in Eq. (A.9) and the constraint equations (2.11) to find the total number of particles,

$$N(T,V,\mu) = \frac{V}{\lambda_{\mathrm{th}}^3(T)} g_{3/2}(e^{\mu/(kT)}), \tag{2.14}$$

and its internal energy,

$$E(T,V,\mu) = \frac{3}{2}kT\ \frac{V}{\lambda_{\mathrm{th}}^3(T)} g_{5/2}(e^{\mu/(kT)}), \tag{2.15}$$

in which we see the *polylogarithm* or *Bose's function*, whose definition is

$$g_\nu(\xi) \equiv \sum_{i=1}^{\infty} \frac{\xi^i}{i^\nu}, \tag{2.16}$$

and the *thermal de Broglie wavelength*, set as

$$\lambda_{\mathrm{th}}(T) \equiv \frac{2\pi\hbar}{\sqrt{2\pi mkT}}. \tag{2.17}$$

On the other hand, in the case of a gas in a harmonic potential, whose Cartesian natural frequencies are ω_x, ω_y and ω_z, the Hamiltonian is

$$H(\{\boldsymbol{r_i}\},\{\boldsymbol{p_i}\}) = \sum_{i=1}^{N} \frac{\|\boldsymbol{p_i}\|^2}{2m} + \sum_{i=1}^{N} \sum_{u=x,y,z} \frac{m\omega_u^2 u^2}{2}, \tag{2.18}$$

in which the first term on the right-hand side is again the total kinetic energy of the particles and the term term on tha same side is the external harmonic potential the particles are subjected to. Hence, we solve Eqs. (2.11) substituting Eq. (A.10) into them and find the total number of particles,

$$N(T,\bar{\omega},\mu) = \left(\frac{kT}{\hbar\bar{\omega}}\right)^3 g_3(e^{\mu/(kT)}), \tag{2.19}$$

and the internal energy,

$$E(T,\bar{\omega},\mu) = 3kT\left(\frac{kT}{\hbar\bar{\omega}}\right)^3 g_4(e^{\mu/(kT)}), \tag{2.20}$$

in which we see the geometric mean of the harmonic-potential frequencies,

$$\bar{\omega} \equiv (\omega_x\omega_y\omega_z)^{1/3}. \tag{2.21}$$

Now we have recalled a few properties of a Bose gas confined box and harmonic potentials, let us see how Bose-Einstein condensation takes place in either cases.

2.2 Bose-Einstein Condensation

We know from classical thermodynamics that the chemical potential μ of an ideal gas is always negative and it increases as the temperature T descreases. Therefore, there

must be a temperature in which $\mu = 0$, in which the total number of atoms in Eq. (2.14) and (2.19) will be equaled to a constant (once V and $\bar{\omega}$ are kept constant). As Einstein well noticed, any new particle that is add to the gas at this point will be out of the equality, and they will not contribute to the internal energy as well, as the Eqs. (2.15) and (2.20) are also equaled to a constant. The only explanation to this weird phenomenon is that the new particles are also falling out to the zero-energy ground state, in which they cannot contribute to the total energy. That punctual, abrupt change of behavior is the phase transition in the momentum space, which we call the *Bose-Einstein condensation*.

The temperature in which $\mu = 0$ is called *critical temperature* and the point in the mathematical space of thermodynamic functions where that temperature is reached is called the *critical point*. In the case of the ideal gas in a box potential, we set $\mu = 0$ into Eq. (2.14) and find the critical temperature

$$T_c = \frac{\hbar^2}{2\pi m k}\left(\frac{1}{g_{3/2}(1)}\frac{N}{V}\right)^{2/3}. \tag{2.22}$$

For $T < T_c$, Eq. (2.14) with $\mu = 0$ describes the non-Bose-condensed particles N_{T}, which are collectively called the *thermal cloud* of the gas. Hence, the fraction of Bose-condensed particles, collectively called the Bose-Einstein condensate, is given as

$$\frac{N_0}{N} = 1 - \frac{1}{N}\frac{V}{\lambda_{\mathrm{th}}^3(T)}g_{3/2}(1). \tag{2.23}$$

We use the same procedure again to find the critical temperature of the ideal gas in a harmonic potential using Eq. (2.19),

$$T_c = \frac{\hbar\bar{\omega}}{k}\left(\frac{N}{g_3(1)}\right)^{1/3}, \tag{2.24}$$

and its Bose-condensed fraction,

$$\frac{N_0}{N} = 1 - \frac{1}{N}\left(\frac{kT}{\hbar\bar{\omega}}\right)^3 g_3(1), \tag{2.25}$$

In either case, the sum of particles of the thermal cloud and of the Bose-Einstein condensate gives the total number of atoms of the gas

$$N = N_0 + N_{\mathrm{T}}. \tag{2.26}$$

Obviously, $N_0 = 0$ for $T \geq T_c$.

Ideal cases give us insight on the properties of behavior of a physical system, but particles of a gas in the real world do interact, therefore we need a more sophisticated

theory to analyze our experiments. For this reason, let us understand the Gross-Pitaevskii theory in Sec. 2.3 and see how it can help us in our investigation.

2.3 Gross-Pitaevskii Theory

In the real gases, atomic interations are always present and, in fact, they play a seminal role in achieving the Bose-Einstein condensation in the experiments, as a gas can only cool down and reach thermal equilibrium at lower temperatures if its particles exchange energy by interacting. For that reason, let us look now at a very useful approach to understand the quantum-mechanical behavior of a gas with weak, short-ranged, repulsive interactions, a model that describe accurately the experimental results presented in this thesis. Therefore, let us consider a system of N identical bosons in a stationary state, whose time-independent wavefunction is

$$\Psi(\{\boldsymbol{r_i}\}) = \prod_{i=1}^{N} \phi(\boldsymbol{r_i}); \quad \int_D |\phi(\boldsymbol{r_i})| \mathrm{d}^3 r_i = 1, \tag{2.27}$$

in which ϕ is obviously the time-independent wavefunction of each boson. That system is subjected to an external, position-dependent potential $U(\boldsymbol{r})$ and its interactions will be taken as a boson-boson Fermi pseudopotential.[37] Therefore, the Hamiltonian of the system is

$$H = \sum_{i=1}^{N} \left[\frac{\|\boldsymbol{p_i}\|^2}{2m} + U(\boldsymbol{r_i}) \right] + \frac{4\pi\hbar^2 a_s}{m} \sum_{\substack{i=1 \\ j=1 \\ i \neq j}}^{N} \delta(\boldsymbol{r_i} - \boldsymbol{r_j}), \tag{2.28}$$

in which a_s is called the s-wave scattering length, the effective distance between two particles when they interact. As shown in detail in chapter 6 of Pethick and Smith's book,[36] we can use the variational method to find the ground-state wavefunction of the system at $T = 0$ K, i. e., a totally Bose-condensed gas. The final result is a nonlinear Schrödinger equation known as *Gross-Pitaevskii Equation*, whose form is

$$\left[-\frac{\hbar^2}{2m} \nabla^2 + U(\boldsymbol{r}) + \frac{4\pi\hbar^2 a_s}{m} |\Psi(\boldsymbol{r})|^2 \right] \psi_0(\boldsymbol{r}) = \mu \psi_0(\boldsymbol{r}), \tag{2.29}$$

in which the Bose-Einstein condensate wavefunction ψ_0 is subjected to the normalization condition

$$\iiint_D |\psi(\boldsymbol{r})|^2 \mathrm{d}^3 r = N. \tag{2.30}$$

Therefore, we can interpret $|\psi_0(\boldsymbol{r})|^2$ as the density of the gas.

Eq. (2.29) is a remarkable result, especially for theorists who work on numerical solutions, but it would be better for us if we could find an analytical solution for it. Hence, we could suppose that as temperature is zero, the kinetic energy term in Eq. (2.29) can be neglected, making it algebraic. This approach is called the *Thomas-Fermi Approximation*,[37] firstly employed in nuclear physics. As a result, we find that the density of a Thomas-Fermi condensate is

$$|\psi_0(\boldsymbol{r})|^2 = n_{\text{TF}}(\boldsymbol{r}) = \begin{cases} \dfrac{m[\mu - U(\boldsymbol{r})]}{4\pi\hbar^2 a_s}; & U \leq \mu. \\ 0; & U > \mu. \end{cases} \tag{2.31}$$

What is interesting about this approach is that we can now estimate the volume occupied by a condensate, which according to Eq. (2.31) must be

$$V_{\text{TF}} = 3\sqrt{2}\pi \left(\frac{\mu}{m\bar{\omega}^2}\right)^{3/2}. \tag{2.32}$$

In the experiments that will be described in Chaps. 5 and 6, both Gross-Pitavskii and Thomas-Fermi theories suit very well to describe the experimental data we collected. This is particularly advantageous, because the whole treatment of data becomes much faster and easier.

2.4 Thermal Cloud in a Bose-Condensed Gas

A gas is purely Bose-condensed only at $T = 0$ K. In the laboratory, Bose-Einstein condensates are produced at a finite temperature T and are always surrounded by a cloud of classical gas, conveniently called *thermal cloud*. That cloud is important to the dynamics of the Bose-Einstein condensates, since it influence how the condensate behave, as the atoms of both Bose-condensed and thermal clouds are always (in general weakly) interacting. Interactions are vital to a thermodynamic system, as it ensures that the system can change its temperature and evolve to other thermodynamic states.

As You and Holland[38] have demonstrated, a cloud of purely thermal, non-interacting atoms initially confined in a harmonic potential like

$$U(x, y, z) = \frac{1}{2}m(\omega_x^2 x^2 + \omega_y^2 y^2 + \omega_z^2 z^2), \tag{2.33}$$

that is released into a zero-potential zone has a characteristic ballistic expansion, which for time interval t long enough ($t \gg (\omega_x\omega_y\omega_z)^{-1/3}$) will make the thermal cloud's density

$n = n(x, y, z)$ take a Gaussian shape. In the case that $\omega_y = \omega_z$, the optical density profile (i. e., the three-dimensional density profile integrated in one direction, say z-direction) is

$$\mathrm{OD}(x, y) = \int_{\Gamma_z} n(x, y, z)\mathrm{d}z = \frac{\exp\left(-\frac{x^2}{2\sigma_x^2(t)} - \frac{y^2}{2\sigma_y^2(t)}\right)}{2\pi\sqrt{\sigma_x^2(t)\sigma_y^2(t)}}, \tag{2.34}$$

in which $\{\sigma_i(t)\}_{u=x,y}$ are the u-direction size of the expanded thermal cloud, found by

$$\sigma_u(t) = \sqrt{\sigma_u^{t=0} + \frac{kTt^2}{m}}; \quad u = x, y, \tag{2.35}$$

in which $\{\sigma_u^{t=0}\}_u = x, y$ is called the *in situ* u-direction size of the cloud, its dimension while resting inside the harmonic potential. As we will learn later in Sec. 4.6, knowing how the thermal cloud evolves in free expansion is important in our experiments, since we made our measurements in those conditions.

Now we outlined the main topics on statistical mechanics that are necessary to this thesis, let us continue our literature review seeing the formalism of the Global-Variable Method in Chap. 3.

3 GLOBAL-VARIABLE METHOD

We give here a naïve but complete introduction to the Global-Variable Method, the kernel of this project. We start in Sec. 3.1 presenting the fundamentals of the method in classical statistical mechanics, then we describe in Sec. 3.2 we define the canonical variables of work for a harmonically confined gas.

3.1 A Heuristic Introduction

Let us recall the canonical partition function of a classical gas of N indistinguishable particles at temperature T:

$$Z = \frac{1}{(2\pi\hbar)^{3N} N!} \int_D \mathrm{d}^3 r_1 \mathrm{d}^3 p_1 \cdots \mathrm{d}^3 r_N \mathrm{d}^3 p_N \; e^{-H(\boldsymbol{r_1},\cdots,\boldsymbol{r_N},\boldsymbol{p_1},\cdots,\boldsymbol{p_N})/(kT)}, \tag{3.1}$$

in which H is the system's Hamiltonian and D is the integration domain in the phase space. As the main theme of this project is the thermodynamics of a gas trapped in a harmonic potential. Therefore, let us use Eq. (3.1) to calculate the canonical partitions functions of an ideal gas in a box potential and a gas in a harmonic potential, then find and compare their thermodynamic properties. Both solutions are given in Appendix B and their results will be analyzed in the next lines.

For an ideal classical gas confined in a box of volume V, the canonical partition function is

$$Z_{\text{box}} = \frac{V^N}{N!} \left(\frac{mkT}{2\pi\hbar^2} \right)^{3N/2}, \tag{3.2}$$

while in the case of an ideal classical gas subjected to the harmonic potential, the canonical partition function is

$$Z_{\text{HP}} = \frac{1}{N!} \left(\frac{kT}{\hbar\bar{\omega}} \right)^{3N}; \tag{3.3}$$

As stated by the formalism of statistical mechanics, the Helmholtz potential of a physical system is

$$F = -kT \log(Z) \tag{3.4}$$

Hence, the average hydrostatic pressure of the ideal gas in a box potential is

$$P = -\left.\frac{\partial F_{\text{box}}}{\partial V}\right|_{T,N} = \frac{NkT}{V}, \tag{3.5}$$

which is, as expected, the equation of state of an ideal gas in classical regime.

For a harmonically trapped gas, the pressure distribution is spatially nonhomogeneous, which means that the equation of state cannot be determined with the standard framework of statistical mechanics. However, the Helmholtz potential $F_{\text{HP}} = F_{\text{HP}}(T, N, \bar{\omega})$ of a harmonic system has an interesting partial derivative,

$$-\left.\frac{\partial F_{\text{HP}}}{\partial(\bar{\omega}^{-3})}\right|_{T,N} = \frac{NkT}{\bar{\omega}^{-3}}, \tag{3.6}$$

which is formally identical to Eq. (3.5). That curious result is the starting point to the Romero and Bagnato's global-variable formalism.

3.2 Conjugate Variables of Work for Harmonically Trapped Gases

Having the conclusions of Section 3.1 in mind, let us define the extensive variable of work for a gas in a harmonic potential as

$$\mathcal{V} \equiv \frac{1}{\bar{\omega}^3}; \quad \bar{\omega} \equiv \sqrt[3]{\omega_x \omega_y \omega_z}, \tag{3.7}$$

which we call *volume parameter*, although it is also called *global volume* in the literature.[3] The next step is to prove that $\mathcal{V}$ is extensive. Therefore, let us look at Eqs. (2.19) and (2.20), which are respectively the total number of particles and the internal energy of an ideal gas in harmonic potential. Both quantities are extensive variables, which means that if the left-hand sides of Eqs. (2.19) and (2.20) are extensive, then their right-hand sides must also be extensive. On that account, there must be at least one extensive variable in the right-hand sides, which cannot be the temperature and the chemcial potential, both intensive quantities. The remaining option is the geometric mean of the harmonic-potential frequencies, hence the volume parameter defined in Eq. (3.7) is extensive.

Another proof to the extensiveness of the volume parameter can be seen in Eq. (2.32), which determines the expected volume of a Bose-Einstein condensate at 0 K in the Thomas-Fermi limit. Once again, we observe that left-hand side of the expression is extensive and the only candidate to extensive variable in the right-hand side is $\bar{\omega}$. However, Eq. (2.32) also shows a clear connection between the volume occupied by the gas, which is the standard extensive variable of work in the constant-density (box potential) case, and the natural frenquencies of the confining potential.

As a last point, let us rewrite the formula for the critical temperature of an ideal gas in a harmonic potential in Eq. (2.24) substituting Eq. (3.7) into it:

$$T_c = \frac{\hbar}{k}\left(\frac{1}{g_3(1)}\frac{N}{\mathcal{V}}\right)^{1/3}. \tag{3.8}$$

We notice that new expression in Eq. (6.7) is very similar to Eq. (2.22), which is the critical temperature of an ideal gas in a box. Therefore, let us compare how those formulae behave in the thermodynamic limit: for Eq. (2.22), the result is imediate and we see that T_c is not affected in the thermodynamic limit; for Eq. (6.7),

As the volume parameter is an extensive variable, there must be an intensive variable which forms a thermodynamic conjugated pair. That variable will be called *pressure parameter* and, from the formalism of statistical mechanics, it is defined as

$$\mathcal{P} \equiv -\left.\frac{\partial F}{\partial \mathcal{V}}\right|_{T,N}. \tag{3.9}$$

From the thermal properties of a gas in a harmonic potential seen in Eqs. (2.19) and (2.20), it is easy to show that

$$\mathcal{P}(T,\bar{\omega},\mu) = kT\left(\frac{kT}{\hbar}\right)^3 g_4(e^{\mu/(kT)}), \tag{3.10}$$

which means that the internal energy in (2.20) can be written as

$$E(\mathcal{P},\mathcal{V}) = 3\mathcal{P}\mathcal{V}, \tag{3.11}$$

an expression that holds for both ideal and weakly interacting gases.

Besides, as demonstrated in Appx. C, the pressure parameter is related to the density of the gas and a harmonic potential $U_{\text{H}} = U_{\text{H}}(\boldsymbol{r})$ that confines it by the integral formula

$$\mathcal{P} = \frac{2}{3\mathcal{V}}\iiint_{D_U} n(\boldsymbol{r})U_{\text{H}}(\boldsymbol{r})\mathrm{d}^3r. \tag{3.12}$$

As we will see in Chaps. 4 and 5, we have means to measure the density and the harmonic-potential frequencies, therefore we can determine experimentally the pressure and volume parameters of a gas trapped in harmonic potential, allowing us to perform a full thermodynamic study using the Global-Variable Method.

For a general potential U, the integral formula of the pressure parameter becomes

$$\mathcal{PV} = \frac{1}{3} \iiint_{D_U} n(\boldsymbol{r})\boldsymbol{r} \cdot \boldsymbol{\nabla} U(\boldsymbol{r}) \mathrm{d}^3 r. \tag{3.13}$$

as demonstrated by Sandoval and Romero.[39]

4 BEC1 QUANTUM-GAS MACHINE

In this chapter, the experimental apparatus that has been used in this project will be described. The machine is coloquially called "BEC1", since it was the first experimental setup to study Bose-Einstein condensation in the Atomic Physics Laboratory. The main reference for this chapter was Fritsch's PhD thesis,[40] which shows the lastest version of the setup. More details about the machine's development and assembly can be found in Tavares's master's thesis[41] and Shiozaki's PhD thesis.[28]

4.1 Introduction

Over two decades after achieving Bose-Einstein condensation in dilute, ultracold gases, many techniques have been developed to obtain quantum degeneracy in gaseous samples of different bosonic atoms in highly controlled conditions. However, all techniques have a few common traits: the samples must be handled in a very low pressure enviroment, comparable to the interstellar void, and they also must be cooled below microkelvin temperatures, which can only be done with laser cooling. Hence, a setup to produce Bose-Einstein condensates must necessarily have an ultra-high-vacuum system and a laser system. Besides, the whole process must be automate by an electronic control system.

Our experimental apparatus, the BEC1 machine, is runned with gas of rubidium (chemical symbol: Rb), which is a very common choice among the cold-atoms laboratories around the world. There are several experimental advantages in building a rubidium quantum-gas machine, such as the cost of the equipments, which are generally cheaper than the equipments used in machines runned with gases of other elements. Our configuration allows us to work with both Bose-condensable isotypes of the element, ^{85}Rb and ^{87}Rb, although we only use the ^{87}Rb isotype currently, in the $|F = 2, m_F = 2\rangle$ and $|F = 2, m_F = -1\rangle$ hyperfine states. More information about the spectroscopical properties of rubidium-87 can be found in the comprehensive study made by Steck.[42]

4.2 Vacuum System

A perspective view of the vacuum system of our experimental apparatus in shown in Fig. 1. There are three distinct parts in the system: the magneto-optical-trap (MOT1) chamber, in which the atoms used in the experiments are initially captured; the differential pumping connection, a pipe through which the atoms are transfered from the MOT1 chamber to the science chamber; and the MOT2 or science chamber, in which the atoms are Bose-condensed. That kind of assembly is called *double MOT configuration*, and we will see shortly in Sec. 4.3 how it works. For now, notice the difference of pressure between

the MOT1 chamber and the science chamber. In the former, the background pressure is around 10^{-8} torr, at which the collision losses during the cooling process would be too high, then the achieving of a phase-space density high enough to permit Bose-Einstein condensation would not be possible. For that reason, the atoms captured in the MOT1 chamber are transfered to the science chamber, in which the $\sim 10^{-12}$ background pressure allows an effective cooling and consequently the attaining of quantum degeneracy.

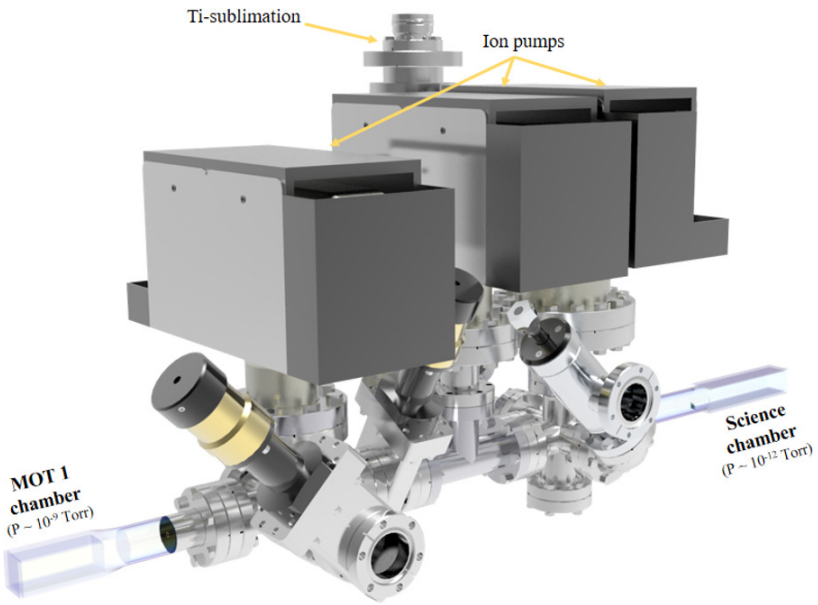

Figure 1 – Computer-assisted drawing of the vacuum system in the BEC1 machine. The double-MOT configuration can be seen in the scheme above, as well as the typical pressures achieved within the vaccum chambers. We can also see three ion pumps and one titanium (Ti) sublimation pump.
Source: FRITSCH.[40]

4.3 Double Magnetico-Optical Trap Configuration

The atoms used in the experiments are dispensered by a heated rubidium-oxide filament and capture in MOT1 chamber in Fig. 1 by a configuration of magnetic and light fields called *magneto-optical trap*, whose physical setup is presented in Fig. 2. The magnetic field is generated by a pair of coils in anti-Helmholtz configuration, and the light consist of three pairs of circularly polarized, retro-reflected, independent laser beams. The frequency of the light is red-detuned with the $5S_{1/2}(F = 2) \rightarrow 5P_{3/2}(F = 3)$ transition in order to cold the atoms, rather than heat them. The confinement is provided by a balance among detuning, light polarization and anti-Helmholtz magnetic field, which creates a position-dependent restoring force over the atomic cloud. At the end, it is possible to trap about 3×10^8 atoms at ~ 320 K in the MOT1 chamber.

Notice that all the light used in the experimental apparatus is provided by three commercial diode lasers made by *TOPTICA Photonics AG*: two *TA Pro* and one *DLX110L*.

The lasers are electronically locked to a hyperfine line of rubidium, whose signal comes from satured-absortion spectrocospy setups. Moreover, in order to match in exact frequencies required in the experiments, acousto-optic modulators are used to manipulate the frequency of the laser beams, and a vast set of optical components are used to prepare the beams before the are sent to the experimental sequence, summarized in Fig. 3.

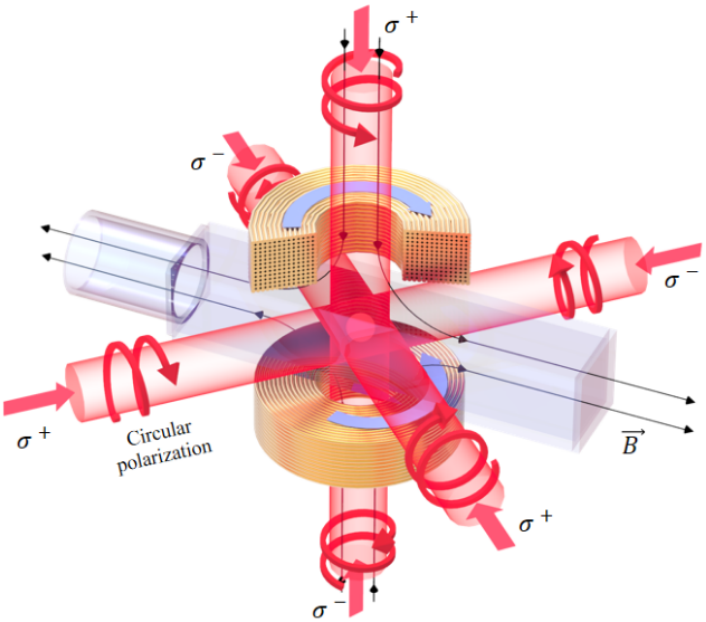

Figure 2 – Scheme of a magneto-optical trap (MOT), composed of three pairs of orthogonal, counterpropagating laser beams, each pair with beams of opposite σ circularization, and a pair of coils in anti-Helmholtz configuration. Each of the two MOTs in our machine is built around a vacuum chamber, which is the glass cell in the image above.
Source: FRITSCH.[40]

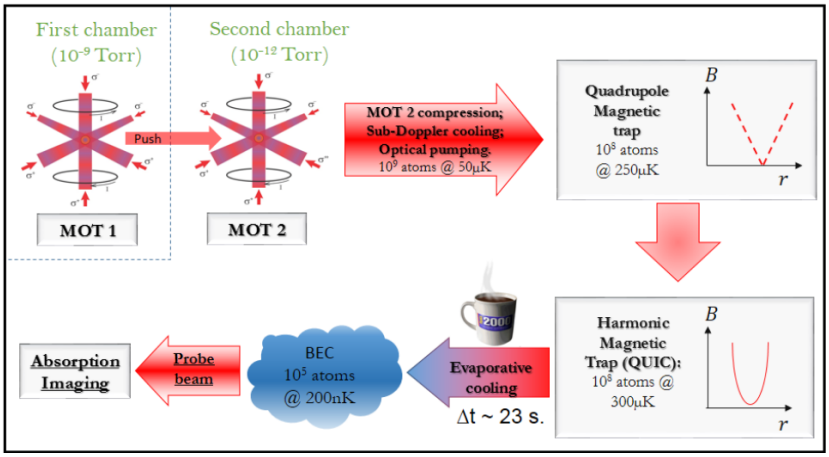

Figure 3 – Block diagram summarizing the Bose-Einstein condensation achieving process in our system.
Source: FRITSCH.[40]

During the experimental sequence, the atoms trapped in the MOT1 are continuously transfered to the MOT2 in the science chamber by a 2-mW, MOT1-transition-resonant pushing laser beam, for a interval of about 30 s. After that, the pushing beam is blocked and the MOT2 is loaded with the atomic cloud for the science experiments, which is usually made up of $\sim 2 \times 10$ atoms initially. That cloud is transfered from the MOT2 field to a purely magnetic field, as shown next in Sec. 4.4, a process that generally tends to increase the system's temperature and has many technical details that we will describe here for the sake of briefness (check Fritsch's thesis,[40] p. 46, Sec. 4.4 for them). To achieve the quantum degenerancy, the cloud in the magnetic trap is cooled by an evaporative process using a radiofrequency signal, as will be explained in Sec. 4.5.

4.4 Magnetic Trap

The laser beams of MOT2 are shut off and the atomic cloud is confined only by the quadrupolar field of the anti-Helmholtz coils, whose field is radidly increased from 20 G/cm to 75 G/cm in a few miliseconds, avoiding in that way the loss of many atoms. The magnetic-field gradient is then increased linearly until 330 G/cm for 400 ms, increasing the effective collision rate within the cloud, which will be important for the system's thermalization during the evaporative cooling.

Although the quadrupolar field is highly efficient in capturing atoms, its zero-field minimum makes atoms susceptible to suffer transitions to non-trappable states, known as Majorana transitions, which makes the anti-Helmholtz configuration not enough to our purpose. The solution is to set up a *Ioffe coil* in the perpendicular direction to the anti-Helmholtz-coils axis, as seen in Fig. 4, creating the so-called quadrupolar-and-Ioffe-coil (QUIC) configuration.

In Fig. 5, we see how the x-direction (Ioffe coil's axis) QUIC field evolves from the initial purely quadrupolar field to a final, non-zero-minimum harmonic field, as the Ioffe coil's current approaches the value of the anti-Helmholtz coils' current. The potential experienced by the trapped atoms is

$$U(x, y, z) = U_0 + \frac{1}{2} m[\omega_x^2 x^2 + \omega_\rho^2 (y^2 + z^2)]; \quad U_0 \neq 0. \tag{4.1}$$

whose the two out of three frequencies of same values (the radial frequency ω_ρ) make the cloud being cillidrically symmetric along the Ioffe coil's axis (of frequency ω_x) or "cigar-shaped".

4.5 Radiofrequency Evaporation

As the atomic cloud is rightly confined in the harmonic potential, its temperature must be lowered, until the phase-space density of the system is high enough to

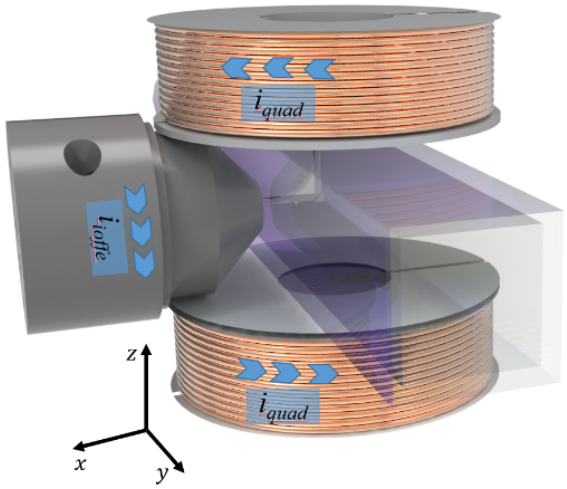

Figure 4 – Scheme of the magnetic trap in the quadrupole-and-Ioffe-coils (QUIC) configuration around the science chamber's glass cell. The quadrupole coils are formed by the MOT2's anti-Helmholtz-configuration coils, whose magnetic field's mininum is zero. The Ioffe coil's transforms the quadrupole potential into a non-zero-minimum harmonic potential, which traps our samples.
Source: FRITSCH.[40]

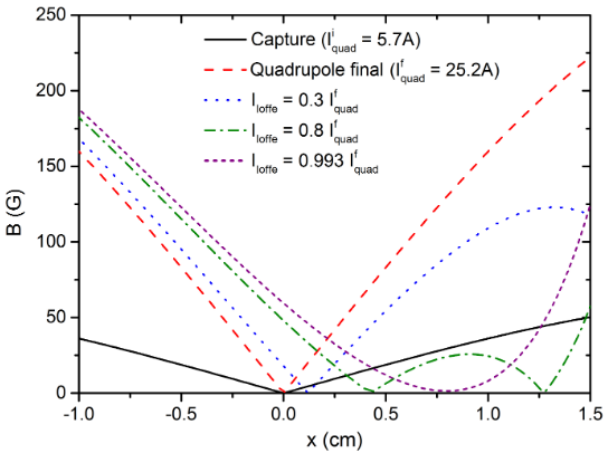

Figure 5 – Evolution of the quadrupole magnetic field (red dashed line) into the wanted harmonic potential (violet dashed line) in the Ioffe coil's axial direction (x-direction in Fig. 4).
Source: FRITSCH.[40]

Bose-Einstein condensation take place. The cooling is made by an application of a radiofrequency signal, which progressively removes the fastest atoms in the cloud. That process is known as evaporative cooling, and it is possible because the energy between two Zeeman levels in the system is proportional to the magnetic field. Therefore, the atoms of higher kinetic energy will feel more the radiofrequency signal than the ones of lower kinetic energy, making this technique very efficient.

The basic idea behind the radiofrequency evaporative cooling is shown in Fig. 6, in which the signal removes the high-kinetic-energy tail of the Boltzmann distribution,

making the system to thermalize at a lower temperature. As the evaporation continues, the frequency of the evaporating signal must be lowered in order to affect the fastest atoms of the system's new Boltzmann distribution, but the lowering must not be too fast, otherwise the system will not have time to thermalize. The optimal frequency ramp is exponential-like and it takes about 23 s, as presented in Fig. 7. After all that, the cloud is finally Bose-condensed and the imaging process detailed in Sec. 4.6 begins.

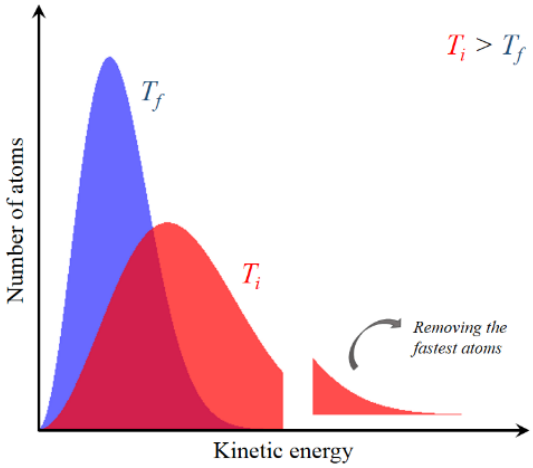

Figure 6 – Radiofrequency (RF) evaporation process. The RF signal removes the fastest atoms of the magnetically trapped cloud at temperature T_i, thus cutting off a high-kinetic-energy portion of the system's Boltzmann distribution. The cloud then thermalizes at a lower temperature T_f. That process goes on recursively until the Bose-Einstein condensation is achieved.
Source: FRITSCH.[40]

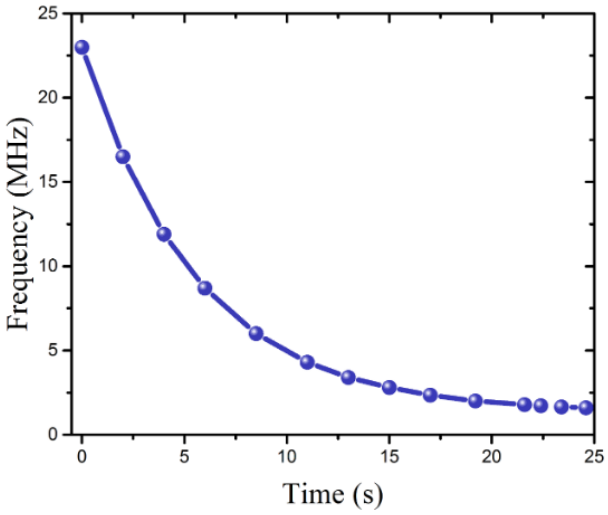

Figure 7 – Frequency (RF) ramp during the evaporation process. As the temperature of the cloud goes lower, the frequency of the radiofrequency signal must also go lower to catch up the fastest atoms of the new Boltzmann distribution, as explained in Fig. 6. The frequency ramp that we employed in our experiments is exponential-like.
Source: FRITSCH.[40]

4.6 Imaging

The imaging system consists of a probing beam and a camera. The probing beam is tilted at 45º from the Ioffe coil's axial, as seen in Fig. 8, which makes possible to measure the three dimensions of the cloud, since the cloud is "cigar-shaped", as seen in the magnetic trap's potential in Eq. 4.1.

However, the cloud inside the magnetic trap is too dense, so the probing beam would not pass through it while inside the trap, making its imaging possible. Fortunately, as the cloud is thermalized in vacuum, it can be released from the trap to expand isothermally without making work for a certain time, in a way that its density would decrease until imaging be possible, but its temperature would remain unchanged. That process is called the *time-of-flight technique*, named after the time that the cloud expands freely.

The camera registers three signals during the imaging procedure. The first signal is the probing beam shot that pass through the cloud, destroying it in the process. The second signal is the probing beam shot alone, measuring its full intensity. The third signal comes from the dark background, with no beam shot. Those three signal generates the normalized intensity of the cloud, as examplified in Fig. 9, which is essentially a measurement of the cloud's optical density.

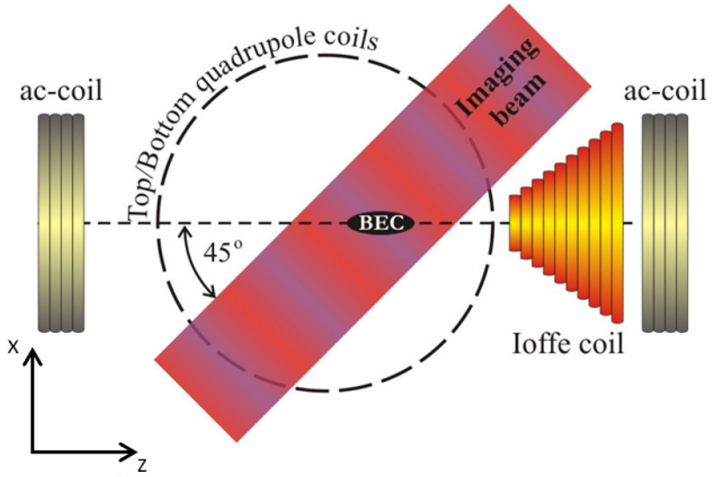

Figure 8 – Scheme of the top view of the science chamber in the BEC1 machine. The position of the atomic clouds is always displaced towards the Ioffe coil, while the angle between the probing beam direction and the Ioffe coil's symmetry axis (z direction) is 45°.
Source: SHIOZAKI.[28]

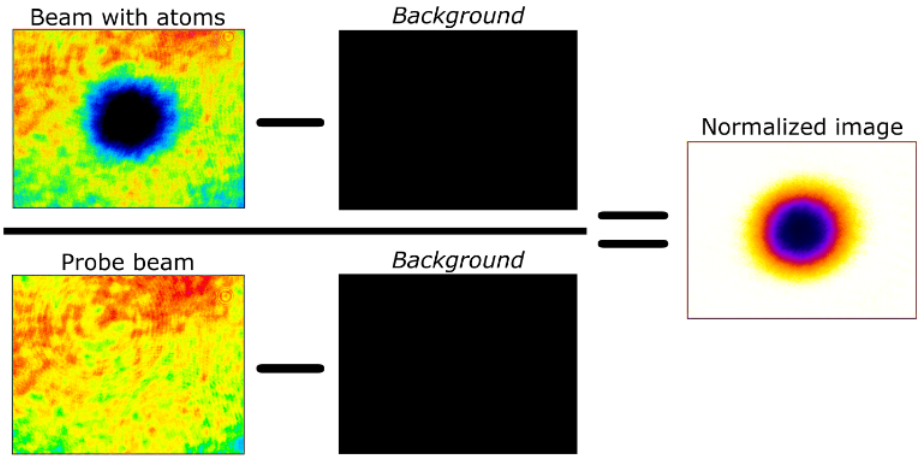

Figure 9 – Getting the normalized-intensity image of an probed cloud. The camera first captures the laser-beam shot that image the cloud, then it captures a second shot to measure the beam's total intensity, and at last it captures the background intensity in darkness.
Source: TAVARES.[43]

The density of the expanded cloud is found by using a non-linear Beer's law,

$$\frac{\mathrm{d}I}{I} = \frac{n(\boldsymbol{r})}{\sigma_0}\mathrm{d}u, \tag{4.2}$$

in which I is the intensity of the probing beam, n is the atomic density of the cloud, $\sigma_0 \simeq 1.36 \times 10^{-13}$ m^2 is the absorption cross-section of a ^{87}Rb atomic cloud and u is the direction of the probing beam. As we have seen in Secs. 2.3 – 2.4, a Bose-condensed gas can be divided into the Bose-Einstein condensate and the thermal cloud surrounding

it, both having different density profiles. According to the Gross-Pitaevskii theory in the Thomas-Fermi limit shown in Sec. 2.3, the Bose-Einstein condensate's density is

$$n_{\mathrm{BE}}(\boldsymbol{r}) = n_{\mathrm{BE}}^{(\max)} \max\left(1 - \frac{(x-x_0)^2}{R_x^2} - \frac{(y-y_0)^2}{R_y^2} - \frac{(z-z_0)^2}{R_z^2}, 0\right), \tag{4.3}$$

in which $\{R_u\}_{u=x,y,z}$ are the u-driection sizes of the condensate. In the case of a freely expanded thermal cloud, we saw in Sec. 2.4 that its density profile is given as

$$n_{\mathrm{th}}(\boldsymbol{r}) = n_{\mathrm{th}}^{(\max)} \exp\left(-\frac{(x-x_0)^2}{S_x^2} - \frac{(y-y_0)^2}{S_y^2} - \frac{(z-z_0)^2}{S_z^2}\right), \tag{4.4}$$

in which $\{S_u\}_{u=x,y,z}$ are the u-direction sizes of the thermal cloud. Eqs. 4.3 and 4.4 are constrained together by the total number of atoms,

$$N = \iiint_{\text{all over the space}} [n_{\mathrm{th}}(\boldsymbol{r}) + n_{\mathrm{BE}}(\boldsymbol{r})]\mathrm{d}^3 r. \tag{4.5}$$

as their are parts of the same atomic cloud.

By integrating Eqs. (4.3) and (4.4) in one of the Cartesian directions, we find the optical density formulae of both thermal and Bose-condensed expanded clouds. Those equations are are fitted to the measured optical density profile of each cloud, which seems tipically like Fig. 10. Once we find the dimensions of the expanded cloud, for both Bose-condensed and thermal parts, we obtain the three-dimensional density profile by substituting the values obtained in Eqs. 4.3 and 4.4, finding also in the process the total number of atoms N from Eq. 4.5 and the system's temperature T by knowing the expansion's time of flight t and using the expression

$$T = \frac{m(S_x S_y S_z)^{2/3}}{kt^2} = \frac{m(S_x S_y^2)^{2/3}}{kt^2}. \tag{4.6}$$

Aware of the technical details of how our experiments are performed, let us proceed the to methodology part in Chap. 5, in which the real contribution of this project starts.

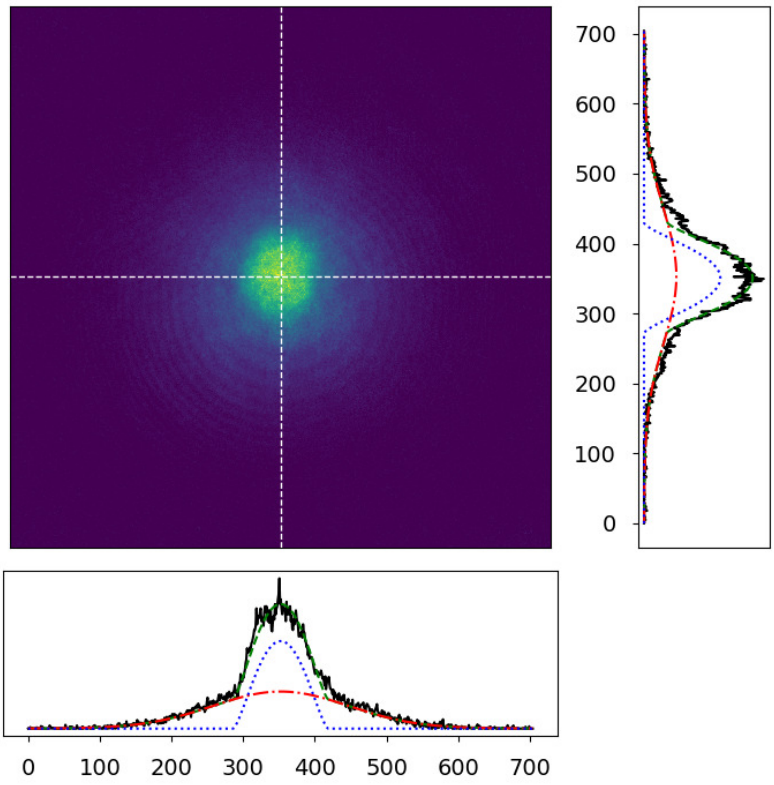

Figure 10 – Two-dimensional fitting of a Bose-condensed cloud image. The dash-dotted red lines are the Gaussian fittings to the thermal-cloud density profile and the dashed green lines are the Thomas-Fermi fittings to the emerging peak caused by the presence of a Bose-Einstein condensate in the sample. The dotted blue lines are used in the calculations to set the symmetry of the image.
Source: Courtesy of Dr. M. Hemmerling.

5 EXPERIMENTAL DATA

We explain in this chapter what were the methods we used to analyzed the results shown in Chap. 6. We start presenting how the harmonic trap's frequencies were determined in Sec. 5.1. Then, we mention in brief the regression procedures to recover the *in situ* profiles of the probed clouds in Sec. 5.2. Finally, we present our methodology to this thermodynamic study in Sec. 5.3.

5.1 Measuring the Trap Frequencies

To measure the Cartesian frequencies of the harmonic trap in each set of experiments we made, we use the following procedures:

- prepare an in-equilibrium atomic cloud in the bottom of the magnetic trap, as explained in Secs. 4.3 – 4.5 and summarized in Fig. 3;
- use the magnetic field of the Ioffe coil seen in the Fig. 8 to displace the trap's bottom upward then release it, making the cloud to move and oscillate accordingly to the natural frequencies of the trap;
- hold the oscillating cloud in the trap for a determined interval of time, known as *hold time*;
- release the cloud from the trap, letting it expand and fall, as explained in Sec. 4.6;
- probe the falling cloud to measure its displacement in the gravity direction;
- repeat the whole process again for different hold times.

The procedure above must be done individually for each Cartesian frequency of the harmonic trap, but since our trap is cylindrically symmetric (two frequencies in different directions are equal), we just need to perform the procedure twice. In the end, the typical profile we have is sinusoidal curve, as the one seen in Fig. 11. The frequency value and its error is found by simply fitting the displacement curve with a sine function with an offset, as the one shown in Eq. (5.1). The angular frequency $2\pi\nu$ in that expression correspond to the trap frequency in a certain direction. The displacement offset d_0, the initial phase φ_0 and the oscillation amplitude A are irrevelant in determining the frequencies.

$$d = d_0 + A\sin(2\pi\nu t + \varphi_0). \tag{5.1}$$

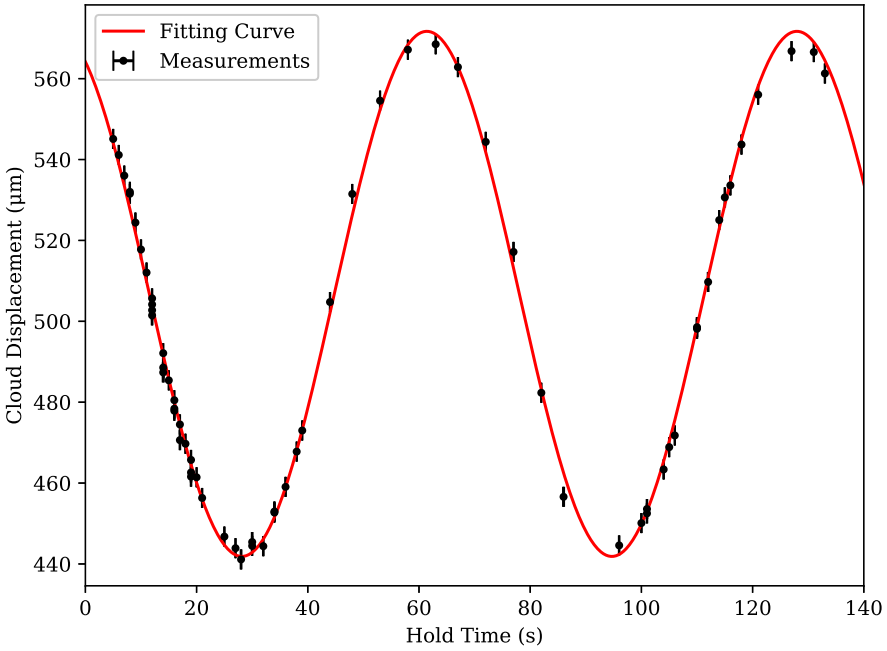

Figure 11 – Typical profile of the the cloud displacement when the measurement of the trap frequencies is been performed. We fit Eq. (5.1) to the curve to the angular frequency of the trap in a given direction.
Source: By the author.

5.2 *In Situ* Properties of the Clouds

Although our experiment apparatus can only image clouds through the time-of--flight technique, as explained in Sec. 4.6, it is necessary to recover the *in situ* properties of those clouds to perform the thermodynamic analysis. Fortunately, the equations of motion of an expanding cloud (either purely thermal and Bose-condensed) are well known and already used for indirect measurements.

In the case of the Bose-Einstein condensate within an atomic cloud, its free expansion follow the equations of motion described by the Castin-Dum theory.[44] In the case of the thermal cloud, its ballistic expansion ensures that it will take a three-dimensional Gaussian shape,[38] as described before in Sec. 2.4.

Our indirect approach to find the *in situ* profiles of the probed clouds is valid because the interval that cloud expands freely (the time of flight) is long enough, in a way that the initial condition are irrevelant to the expansion's dynamical equations, simplifying the analysis.

5.3 Thermodynamic Analysis

Once the *in situ* properties of each probed cloud are obtained, we have the full set of data to start the thermodynamic analysis. For each set of $(N, \mathcal{V})$, we can plot a pressure-

parameter-versus-temperature ($\mathcal{P} \times T$) diagram, such as the one shown in Fig. 12. Those graphs are the starting point of our thermodynamic analysis.

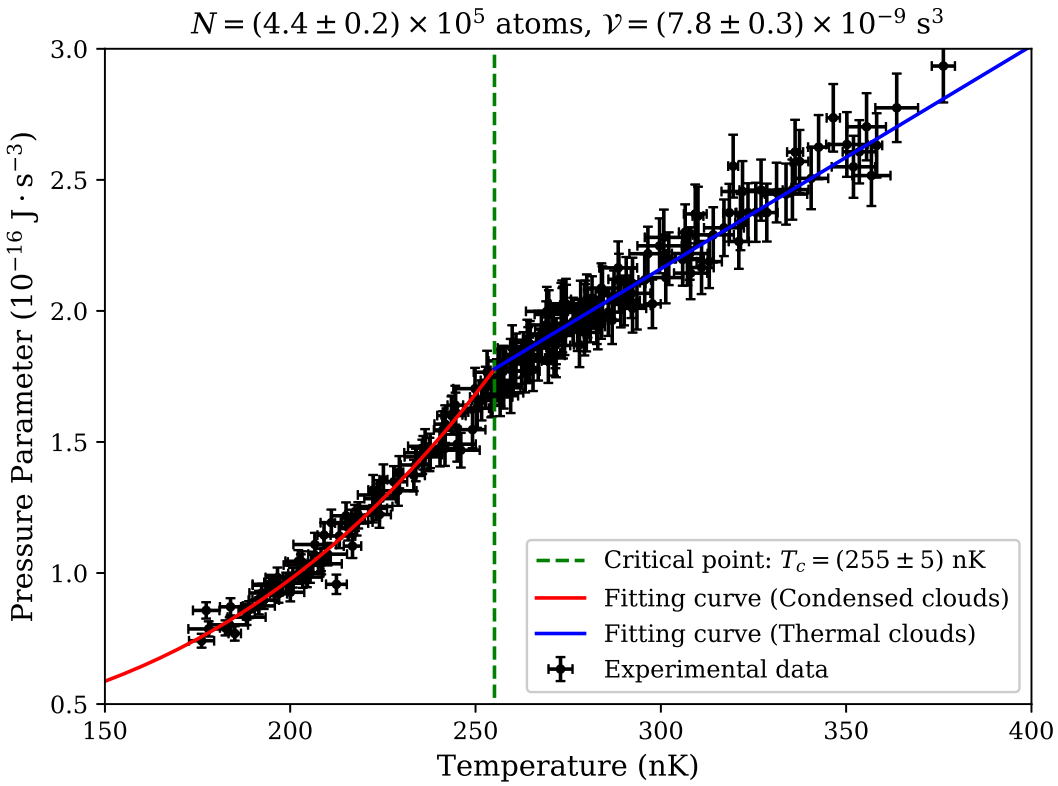

Figure 12 – Graphical representation of the Equation of State for $N = 4.4 \times 10^5$ atoms and $\mathcal{V} = 5.92 \times 10^{-9}$ s^3.
Source: By the author.

Rather than developing a microscopic theory of the thermodynamics of a harmonically trapped, weakly interacting gas around the critical point, we want to give a macroscopic description of its thermodynamic quantities, in a way that they can easily calculated by both experimentalists and theorists. We call this approach a *technical thermodynamics*, in the spirity of the technical thermodynamics tables and empirical formulas that are used by engineers and designers in industry.

Below the critical temperature, the curve can be approximated to a power law, which we relate to the power-of-four behavior observed in the ideal gas in a harmonic potential. Above the critical temperature, the behavior must be linear, in concordance with the Gay-Lussac's law. On those accounts, we developed a simplified model to be fitted to the experimental data, shown in Eq. (5.2).

$$\mathcal{P}(T, \mathcal{V}, N) = \begin{cases} a_0(\mathcal{V}, N) T^{4+a_1(\mathcal{V},N)} + a_2(\mathcal{V}, N), & T < T_c. \\ a_3(\mathcal{V}, N) T + a_4(\mathcal{V}, N), & T > T_c. \end{cases} \tag{5.2}$$

By fitting the model in Eq. (5.2) to the equation-of-state graphs like Fig. (12), we obtain the technical coefficients $\{a_i\}_{i=0,\ldots,4}$ that can represent the behavior of each curve individually. The curve fitted to the experimental points in Fig. 12 is also seen in the plot.

To see if our model is adequate, we compared it with self-consistent calculations of the Hartree-Fock model,[36] which generates theoretical density profiles that are intergrated in Eq. 3.12. As we see the comparison in Fig. 13, the biggest issue with our model is that the critical temperature is underestimated when compared to the Hartree-Fock model's result, which is compartible with more precise measurements of the critical point.[23] Nonetheless, we see that this curve generated with simplified model does agree with the curves of the theoretical predictions within the experimental error, despite the insconsistency in the critical point. Therefore, we conclude that our model can describe satisfactorily the general behavior of the equation of state, both qualitatively and quantitatively, although it cannot give precise information about the Bose-Einstein transition.

With the methodology presented in this chapter, we can now proceed Chap. 6 to see experimental results found during the development of this master's project.

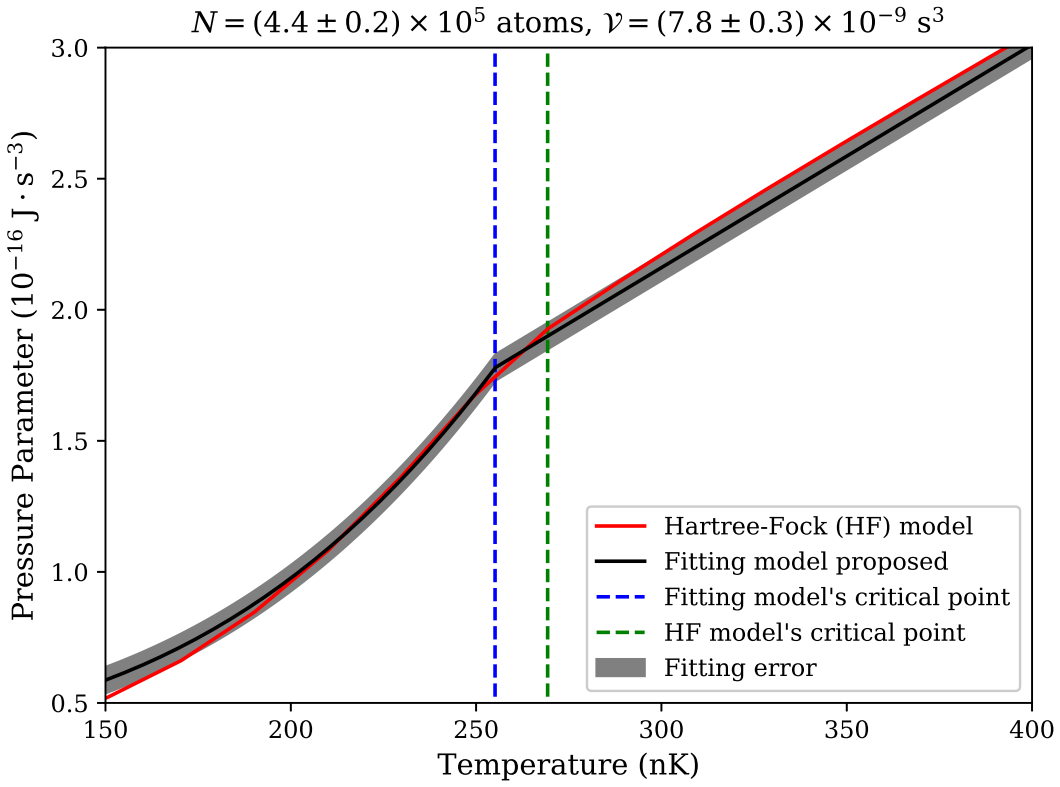

Figure 13 – Comparing the Equation of State's model in Eq. (5.2) with the Hartree-Fock model's expected behavior for $N = 4.4 \times 10^5$ atoms and $\mathcal{V} = 5.92 \times 10^{-9}$ s^3. Source: Courtesy of Dr. M. Hemmerling and Dr. I. Reyes-Ayala.

6 THERMODYNAMIC ANALYSIS

After reviewing the key concepts of quantum gases in Chap. 2, learning the theoretical framework of the GVM in Chap. 5 and knowing the experimental apparatus and methods employed in this project in Chaps. 4 and 5 respectively, we will finally discuss the main outcomes of this research in this chapter.

We begin discussing the results for the technical coefficients of our simplified model in Sec. 6.1. After that, we present and examine the equation-of-state diagrams in Sec. 6.2 generated with the empirical technical coefficients. Next and finally, we use the data of the previous sections to obtain graphs of heat capacity in Section 6.3, graphs of compressibility in Sec. 6.4 and graphs of thermal expansion in Sec. 6.5.

Before we inspect the results, let us review a few aspects of the our methodology that is worth to remember:

- the atomic clouds of our experiments are probed using the time-of-flight technique, which means they are measured after a isothermal expansion against vacuum rather than within the trap (*in situ*);
- the properties of the expanded atomic clouds (size, number of atoms and temperature) are obtained by fitting the bimodal profile (Thomas-Fermi profile for the Bose-condensed component plus the Gaussian profile for the thermal component) to the optical density profile;
- the *in situ* properties of the expanded clouds are recovered by using the Castin-Dum regression[44] (for the Bose-condensed component) and the inverse ballistic expansion (for the thermal component);
- the GVM equation of state is calculated from the recovered *in situ* properties;
- the simplified fitting model for the equation of state was based on the expected behavior for the equation of state of a harmonically trapped ideal gas in the thermodynamic limit

Bearing the information above in mind, let us begin the analysis.

6.1 Technical Coefficients

We start presenting Tab. 1, which shows the range of measured values, setting the validity limits of the simplified model we proposed in Sec. 5.3. For each combination of volume parameter $\mathcal{V}$ and number of atoms N, there is a set of experimental data that generate a $\mathcal{P} \times T$ diagram alike Fig. 12, making three hundred and eighty graphs in total. We fitted Eq. (5.2) to each $\mathcal{P} \times T$ diagram to obtain the technical coefficients $\{a_i\}_{i=0,\dots,4}$ and the model's critical temperature T_c of each measurement set and find their

dependency with $\mathcal{V}$ and N. We depict the a_0 plots in Figs. 14 and 15, the a_1 plots in Figs. 16 and 17, the a_2 plots in Figs. 18 and 19, the a_3 plots in Figs. 20 and 21, the a_4 plots in Figs. 22 and 23, and the T_c plots in Figs. 24 and 25.

It is important to emphasize that this analysis holds solely for points in the neighborhood of the critical point (either above it and below it). Using the technical coefficients obtained from the fittings to calculate the pressure parameter outside the temperature range in Tab. 1 (specially below the minimum value) might lead to wrong values.

Table 1 – Model's limits. Each $(N, \mathcal{V})$ pair corresponds to a $\mathcal{P} \times T$ diagram, to which Eq. (5.2) is fitted, generating the $\{a_i\}$ coefficents and the model's T_c.

Physical Quantity	Minimum Value	Maximum Value	Number of Values
Number of atoms (N)	3.0×10^5	5.5×10^5	20
Volume Parameter ($\mathcal{V}$, s^3)	5.70×10^{-9}	9.68×10^{-9}	19
Temperature (T, units of T_c)	$0.7 \cdot T_c$	$1.3 \cdot T_c$	–

Source: By the author.

On the technical coefficients, it must be noticed that the dimension of the a_0 coefficients is influenced by the value of their correpondent a_1 coefficients, thus the a_0 of each $\mathcal{P} \times T$ diagram for certain N and $\mathcal{V}$ has its own dimension. This fact is completely fine, because the coefficients themselves are devices that we use to reproduce the behavior of the pressure parameter around the Bose-Einstein transition. However, some interesting comments can be made about the physical meaning of the technical coefficient, as we will see in the next subsections.

6.1.1 The a_0 coefficient

In Eq. 6.8, the a_0 coefficient couples the temperature to the equation of state. From Eq. 3.10, the pressure parameter of a harmonically trapped, ideal gas is

$$\mathcal{P}(T, \bar{\omega}, \mu) = kT \left(\frac{kT}{\hbar}\right)^3 g_4(e^{\mu/(kT)}), \tag{6.1}$$

therefore the a_0 coefficient in the ideal case is

$$a_0^{\text{ideal gas}} = \frac{k^4}{\hbar^3} g_4(e^{\mu/(kT)}). \tag{6.2}$$

For $T < T_c$ in the ideal case, the chemical potential becomes $\mu = 0$, making the fugacity $e^{\mu/(kT)}$ a constant and $a_0^{\text{ideal gas}}$ independent of both N and $\mathcal{V}$. However, the graphs in Figs. 14 and 15 shows that the real case has a very small dependence on those quantities, although the values remain around the amount of 3.5×10^{10}, which is a little higher than ideal case's $g_4(1)k^4/\hbar^3 \overset{N}{\approx} 3.3 \times 10^{10}$.

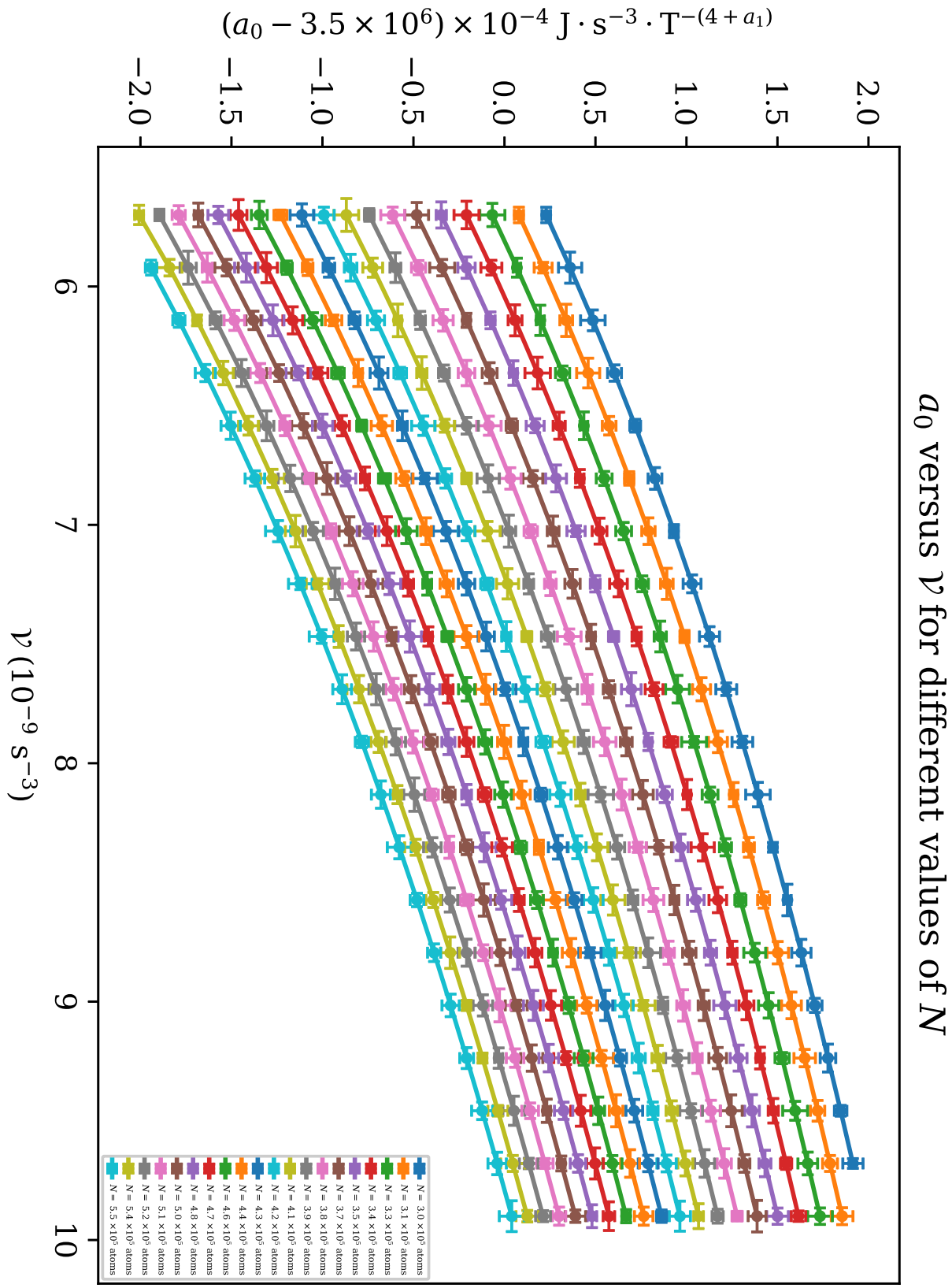

Figure 14 – Plots of the a_0 coefficient versus the volume parameter $\mathcal{V}$.
Source: By the author.

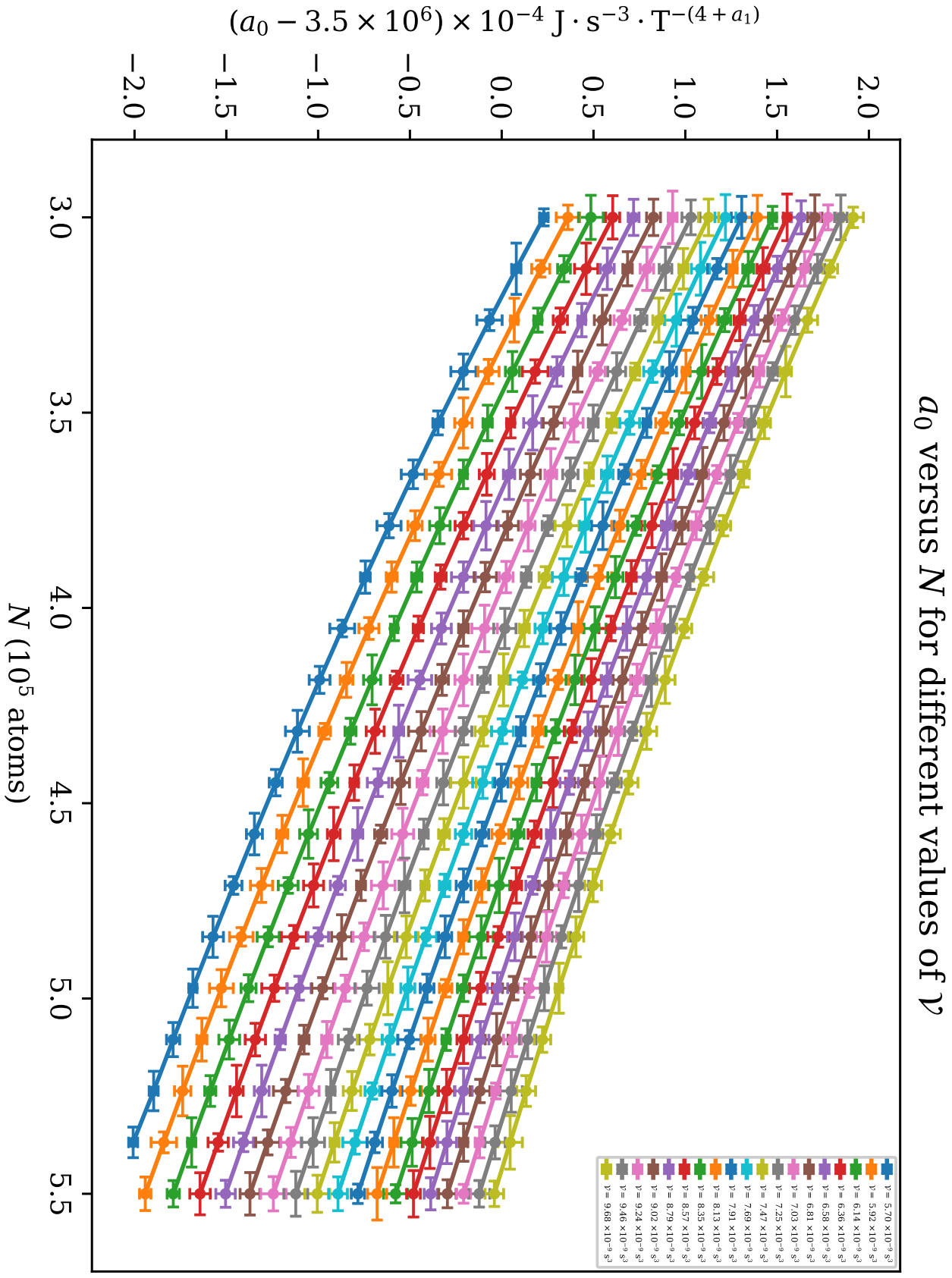

Figure 15 – Plots of the a_0 coefficient versus the number of atoms N.
Source: By the author.

6.1.2 The a_1 coefficient

In the ideal case, the pressure parameter depends on the fourth power of the temperature, which is comparable to the behavior of a photon gas. In the real case however, as seen in Figs. 16 and 17, we observed a decrease in the temperature's power, computed by the a_1 coefficient. The reason is very obvious in our opinion: as mentioned before in Sec. 2.4, the thermal clouds influences the Bose-Einstein condensate's behavior, and since the equation-of-state's power has decreased towards to classical gas' straight line, we see that the a_1 gives a macroscopic description of how the thermal atoms are affecting the condensed ones.

In Fig. 16, the temperature's power decreases as the volume parameter increases, since the available space for the atoms to occupy is larger for greater volume parameters, or equivalently less-confining potentials. In that case, the tempearture's power is closer the ideal gas' power of four, as the atoms are more spread throughout the space and interact less. Conversely, in Fig. 17, the temperature's power decreases as the number of atoms decreases, for a very clear reason: less atoms, less interactions, so the temperature's power is closer to four.

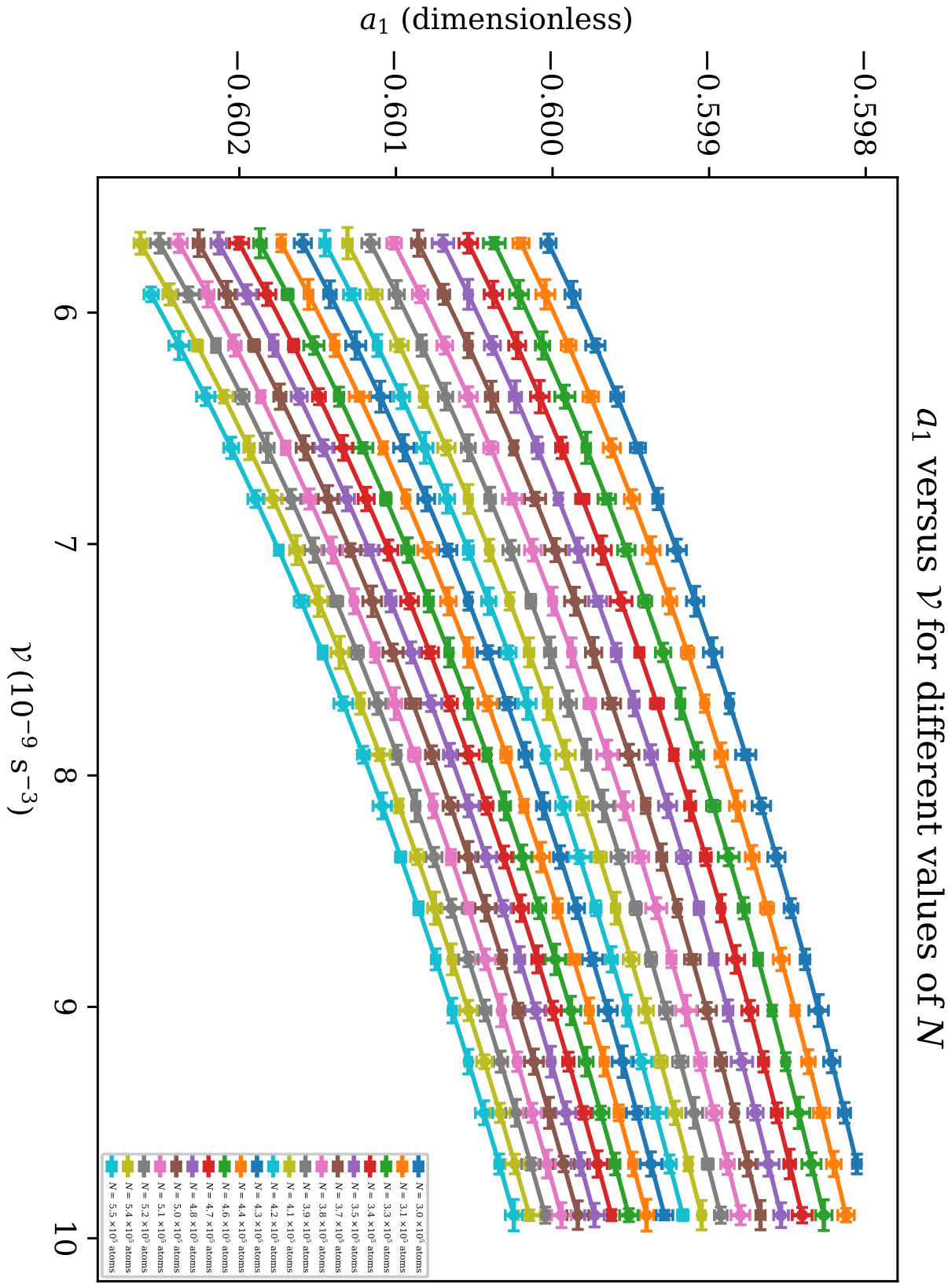

Figure 16 – Plots of the a_1 coefficient versus the volume parameter $\mathcal{V}$.
Source: By the author.

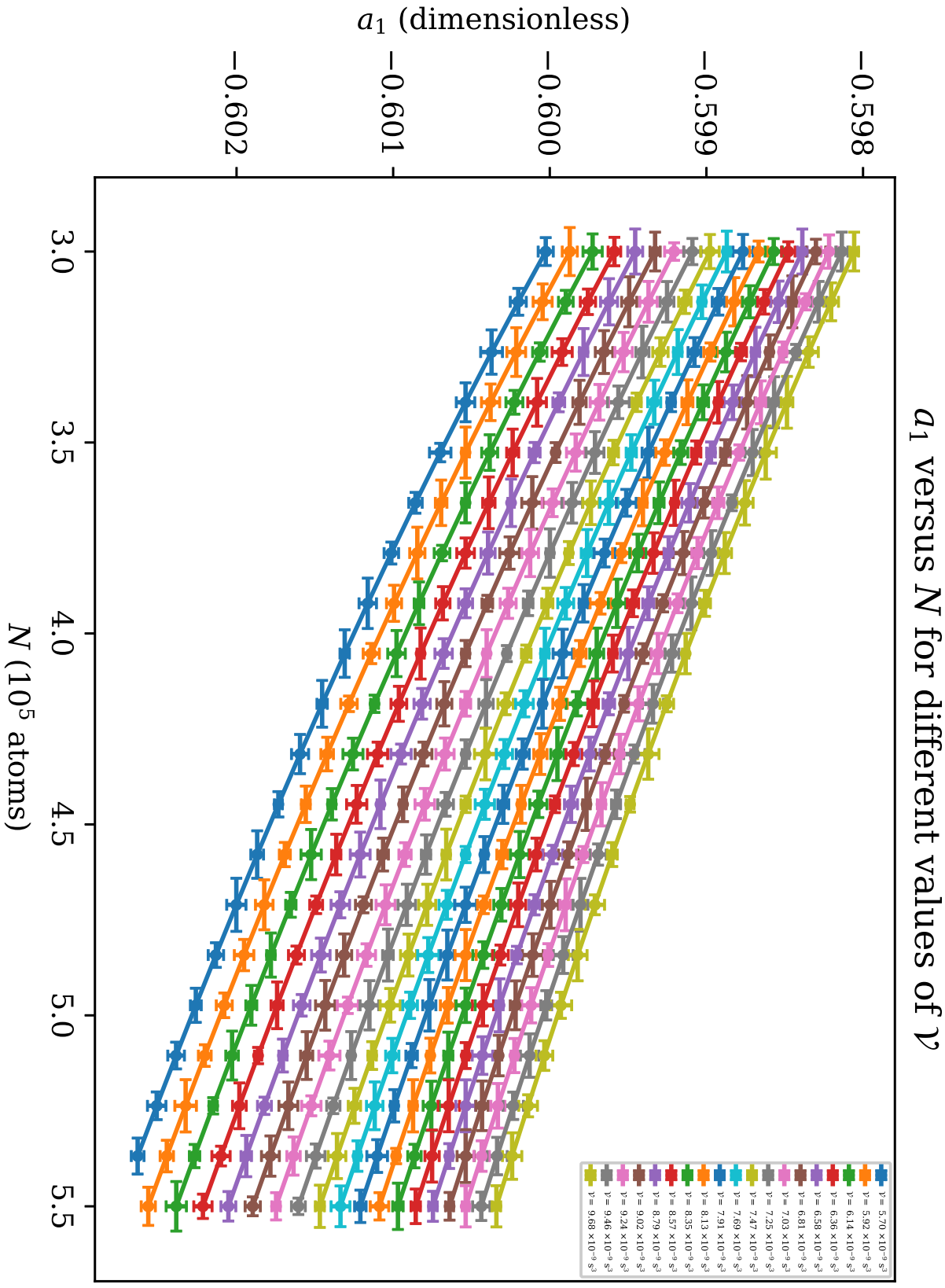

Figure 17 – Plots of the a_1 coefficient versus the number of atoms N.
Source: By the author.

6.1.3 The a_2 coefficient

Setting $T = 0$ in the $T < T_c$ part of Eq. (6.8), we see that a_2 corresponds to the zero-point pressure parameter. At that limit, the pressure parameter comes solely from the ground-state energy of the oscillator and inter-particle interactions. Looking only at the ground-state energy, we have

$$E_0 = \frac{N\hbar}{2}(\omega_x + \omega_y + \omega_z), \tag{6.3}$$

which is directly proportional to the trap frequencies. On one hand, the average frequency of the trap increases as $\mathcal{V}$ decreases, thus increasing the zero-point energy and the zero-point pressure parameter, as observed in Fig. 18. On the other hand, the total zero-point energy increases as the total number of atoms N increases, increasing the ground-state level, which is seen clearly in Fig. 19.

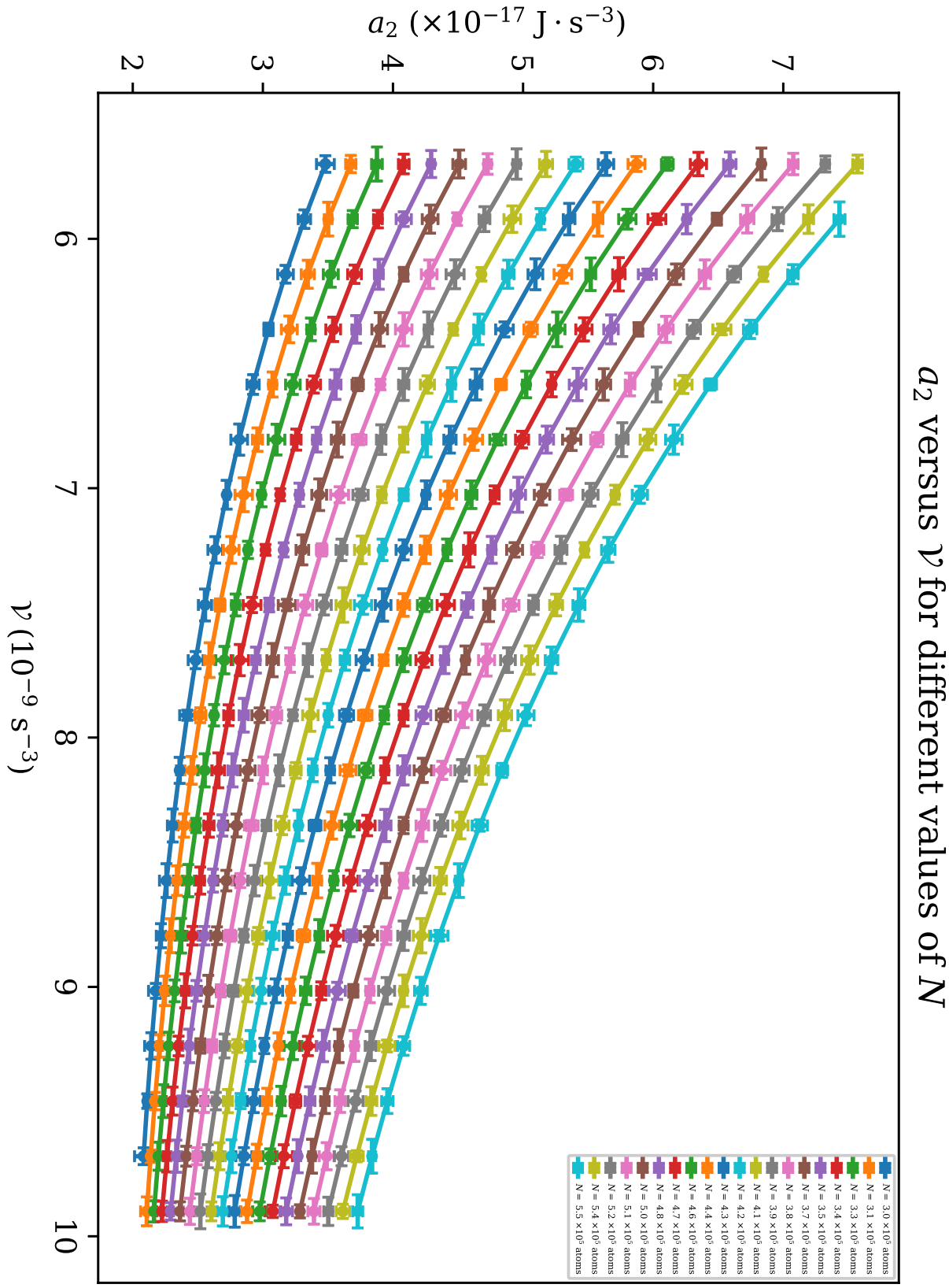

Figure 18 – Plots of the a_2 coefficient versus the volume parameter $\mathcal{V}$.
Source: By the author.

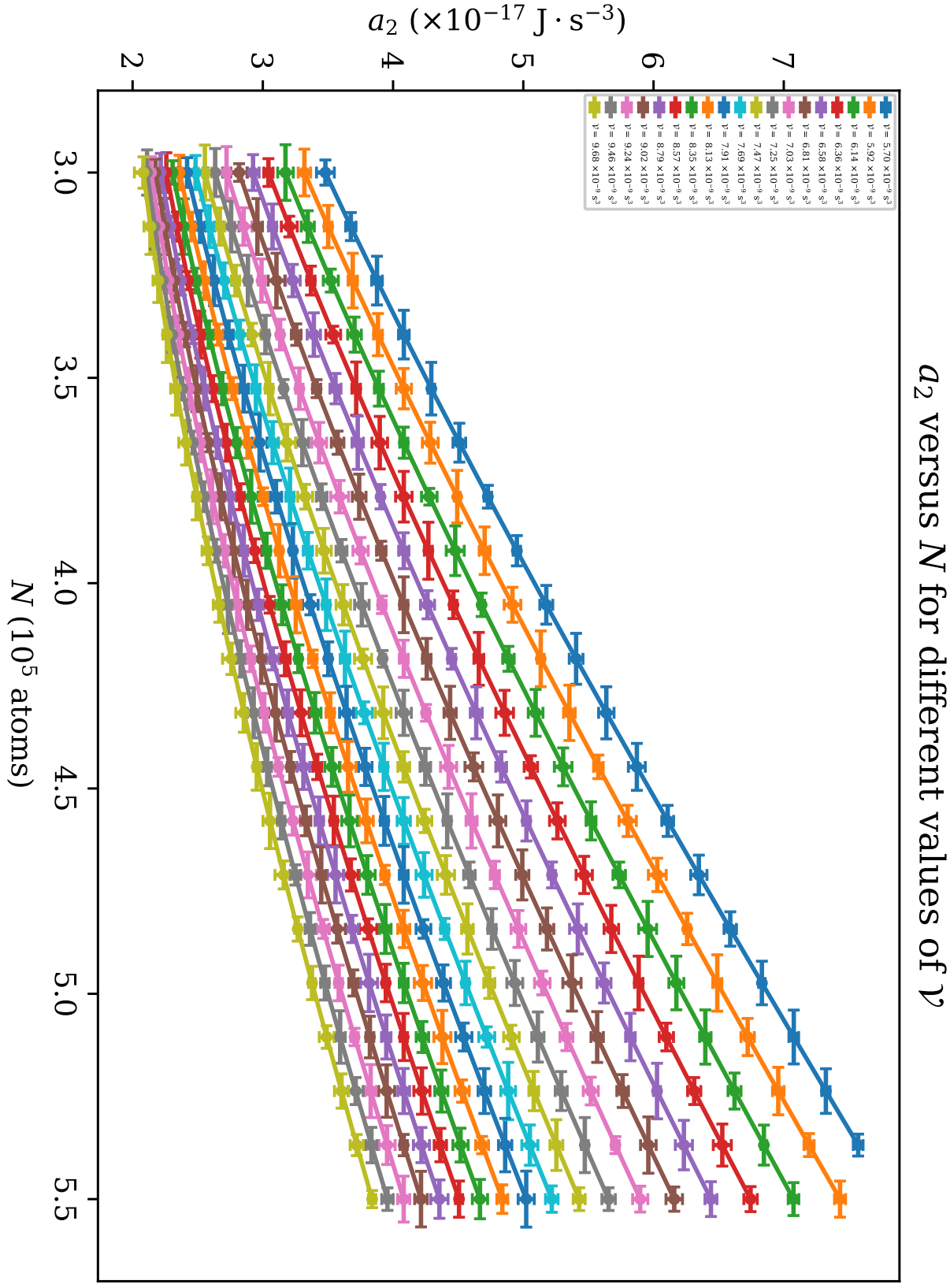

Figure 19 – Plots of the a_2 coefficient versus the number of atoms N.
Source: By the author.

6.1.4 The a_3 coefficient

Graphs of the a_3 coeffient are presented in Figs. 20 and 21. It is equivalent to the slope of the Gay-Lussac's law for classical gases, which is

$$a_3^{\text{ideal gas}} = \frac{Nk}{\mathcal{V}}. \tag{6.4}$$

The indirect dependence on $\mathcal{V}$ in Fig. 20 and direct dependence on N in Fig. 21 are evident, and it can see even more clearly when we differentiate the equation of state to obtain the heat-capacity curves, seen in Fig. 61. The coefficient is around $3Nk$, the value expected to an ideal classical gas in a harmonic potential. That results shows that interaction in the system are small enough to be described by the ideal gas' equation of state for $T > T_c$, even though small but expected deviations are observed. For the sake of simplicity and demonstration of the principle, our mathematical modeling is satisfactory.

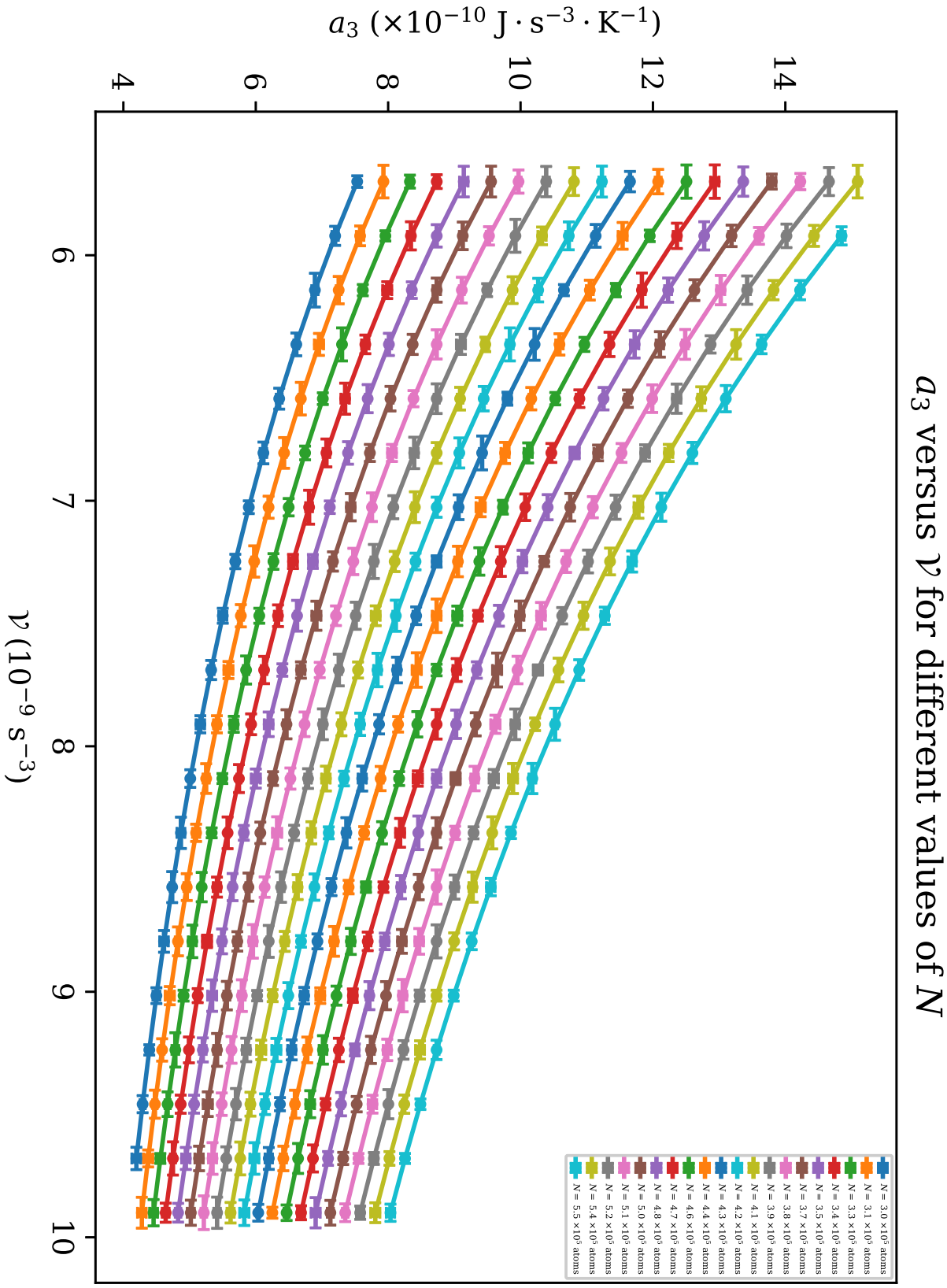

Figure 20 – Plots of the a_3 coefficient versus the volume parameter $\mathcal{V}$.
Source: By the author.

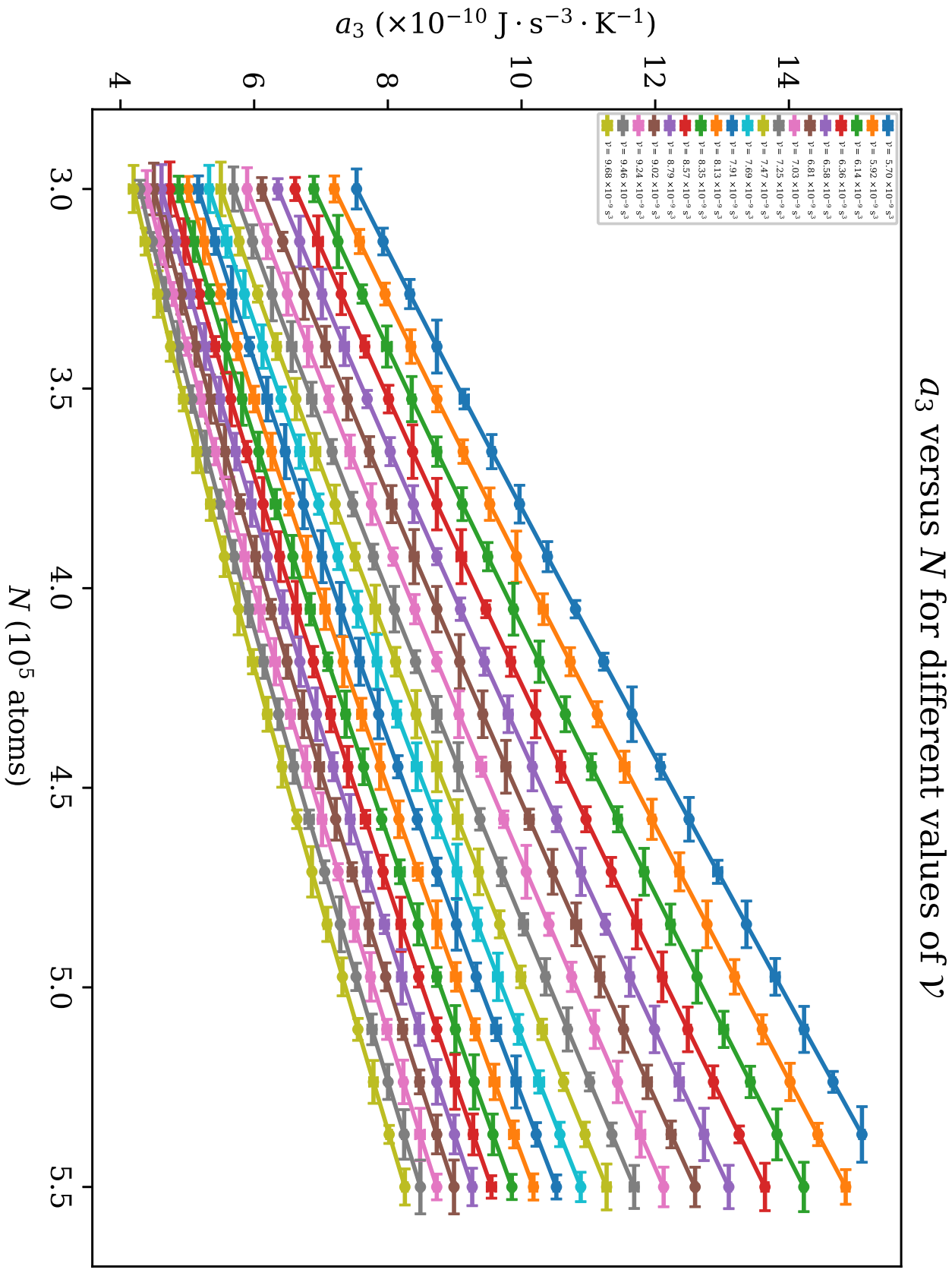

Figure 21 – Plots of the a_3 coefficient versus the number of atoms N.
Source: By the author.

6.1.5 The a_4 coefficient

Setting $T = 0$ in the $T > T_c$ part of Eq. (6.8), we see that a_2 corresponds to the zero-point pressure parameter in the classical case. The $T > T_c$ part of our fitting model is roughly equivalent to the classical van der Waals equation, which for a gas in a box of volume V is written as

$$P = \frac{NkT}{V - b} - \frac{a}{V^2}, \tag{6.5}$$

which $a > 0$ is a measure of the particle-particle attraction and $b > 0$ is total volume occupied by the particles, both extensive quantities. The a_4 coefficient corresponds directly to the temperature-independent term $-a/V^2$: first, it is always negative, as observed in Figs. 22 and 23; second, it increases as $\mathcal{V}$ increases, according to the curves in Fig. 22, lessening the inter-particle attraction; third, it decreases as N increases, in agreement with the behavior seen in Fig. 22, incrementing the inter-particle attraction. It is worthed mentioning in the third case that the van der Waals's a coefficient can be rewritten as

$$a = N^2 a'. \tag{6.6}$$

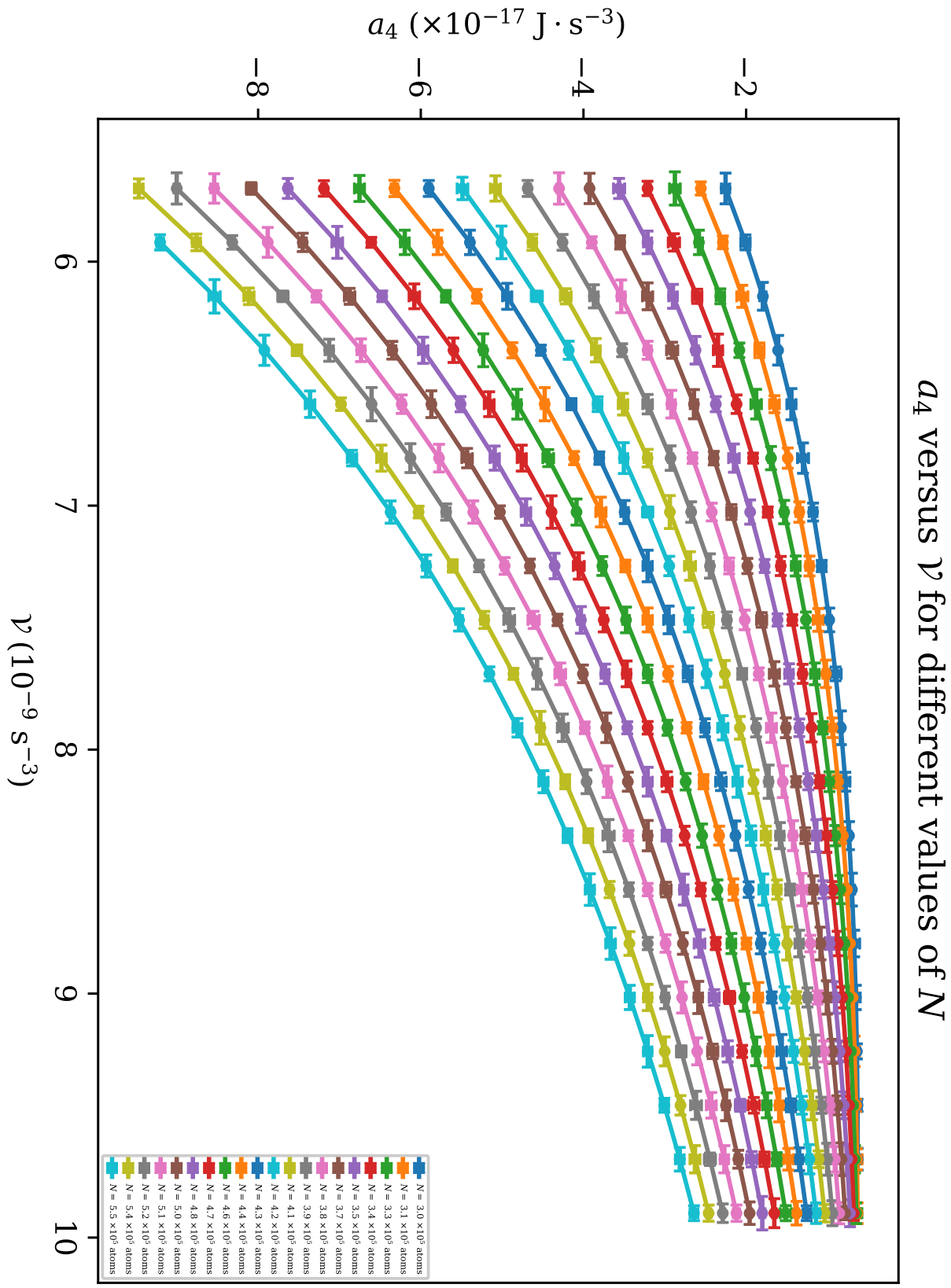

Figure 22 – Plots of the a_4 coefficient versus the volume parameter $\mathcal{V}$.
Source: By the author.

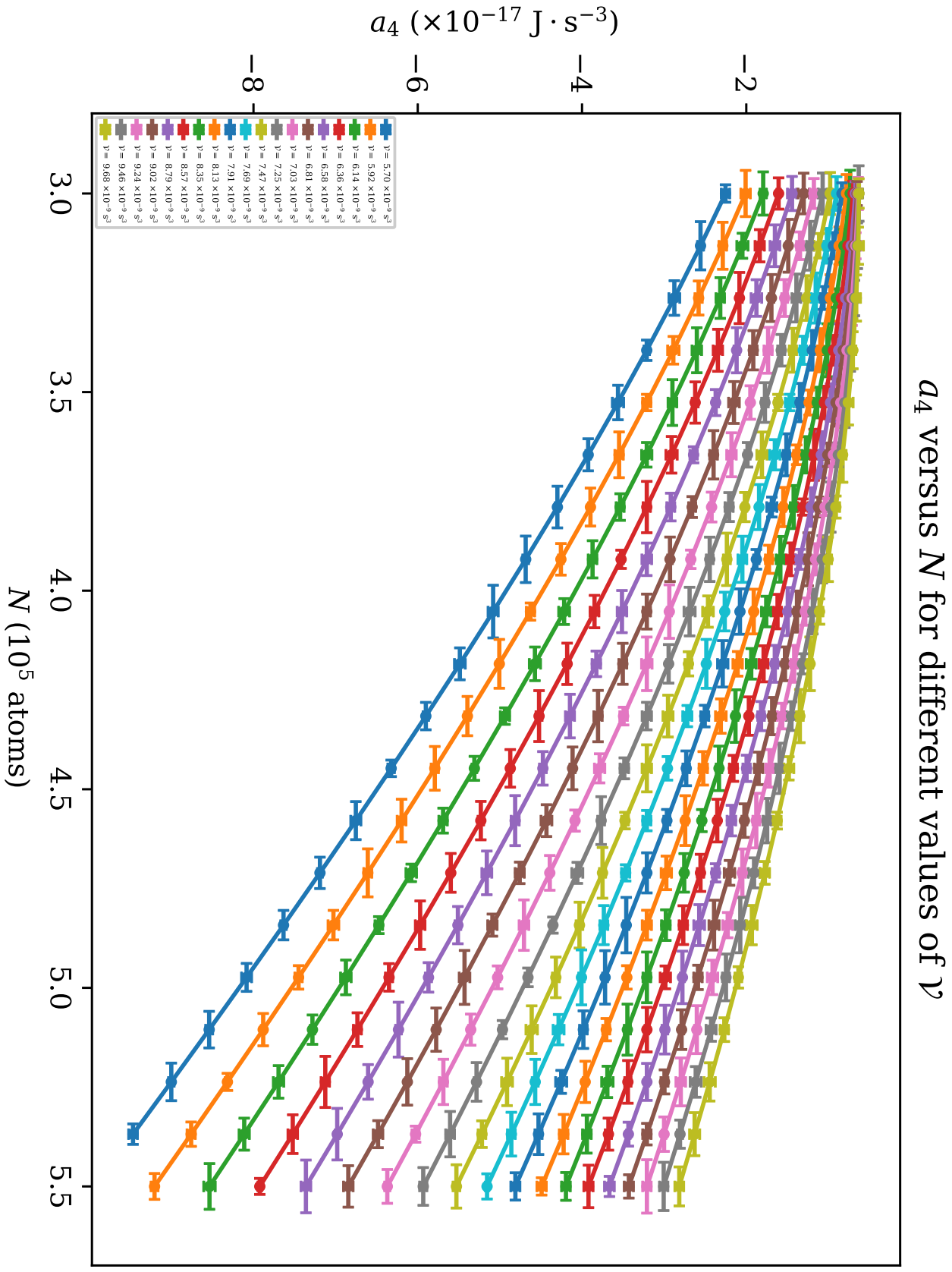

Figure 23 – Plots of the a_4 coefficient versus the number of atoms N.
Source: By the author.

6.1.6 The model's critical temperature

Diagrams of the critical temperature are observed in Figs. 24 and 25, which are the only downside of our model, since it cannot predict the actual cirtical point precisely. Nonetheless, let us check again the critical temperature of an ideal gas in a harmonic trap in Eq. (6.7),

$$T_c = \frac{\hbar}{k}\left(\frac{1}{g_3(1)}\frac{N}{\mathcal{V}}\right)^{1/3}. \tag{6.7}$$

Even though the model's critical temperature is physically imprecise, deviating generally in $\sim 7\%$ from the actual value, that quantity is still physically consistent with the ideal case, as T_c decreases for increasing values of $\mathcal{V}$ and increases for increasing values of N. In that perspective, a future correction in the fitting model to force its critical temperature to match the actual critical temperature would only improve the precision of finding the critical poitn, but it would change the behavior of the other technical coefficients described before the Subsecs. 6.1.1 – 6.1.5, as the shape of the curves would remain unchanged overall, just like their physical meanings.

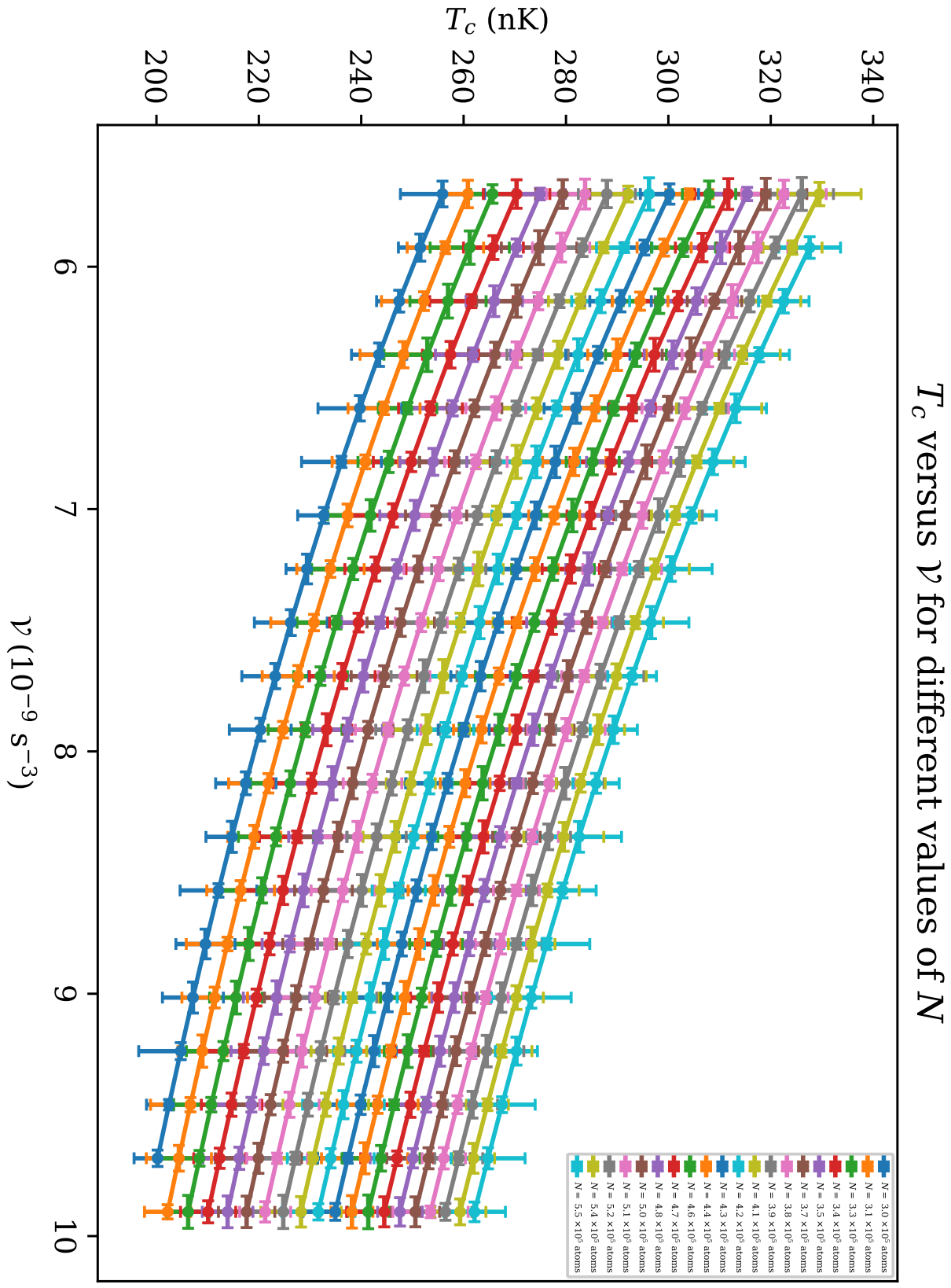

Figure 24 – Plots of the critical temperature T_c versus the volume parameter $\mathcal{V}$.
Source: By the author.

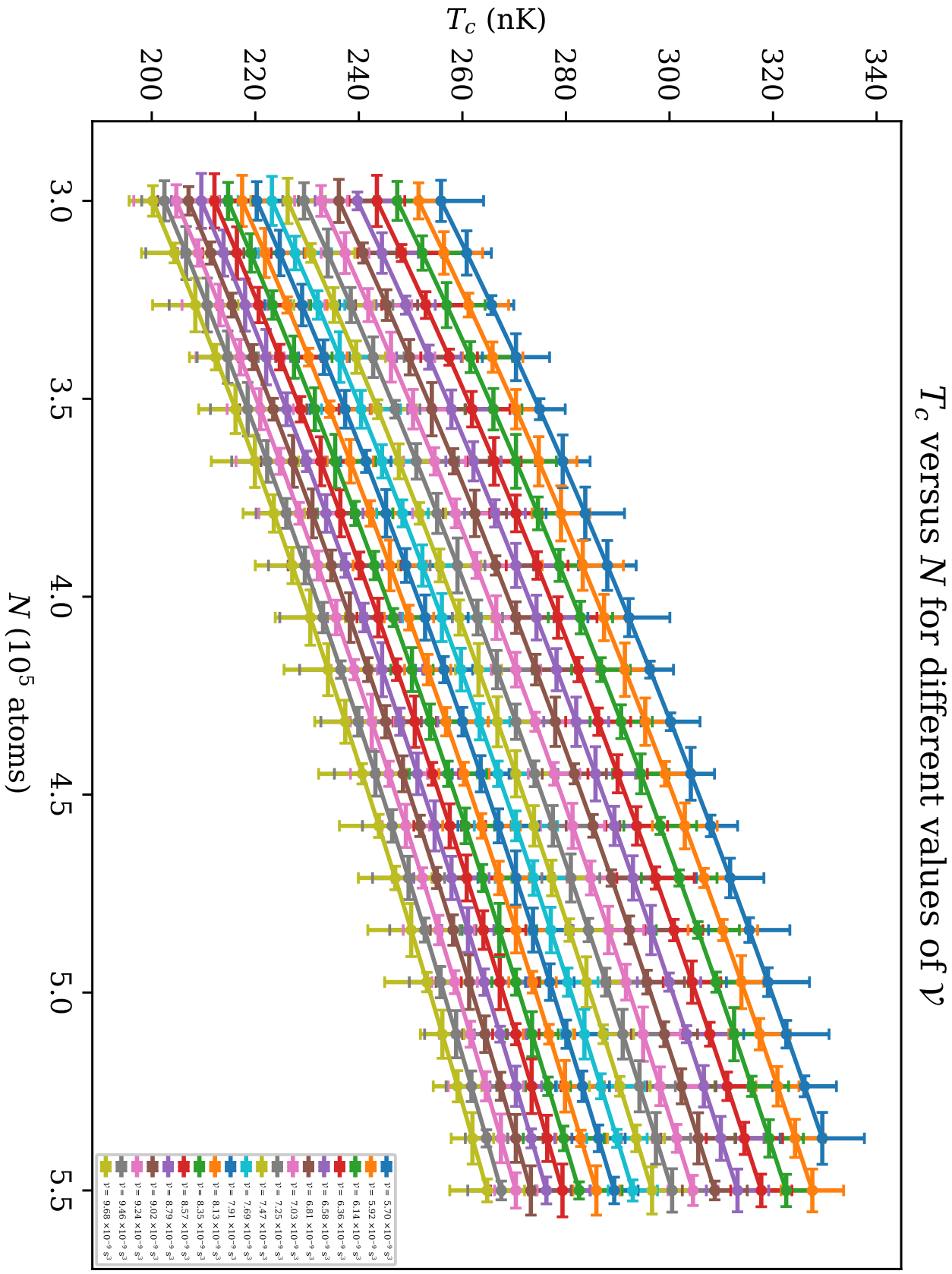

Figure 25 – Plots of the critical temperature T_c versus the number of atoms N.
Source: By the author.

With the technical coefficient graphs, we can determine all the *thermodynamic susceptibilities* of the harmonically trapped gas, which are necessary for a complete thermodynamic description of that inhomogeneous system. We present and analyze the curves of Equation of State ($\mathcal{P}$) in Sec. 6.2, the curves of heat capacity at constant volume parameter ($C_{\mathcal{V}}$) in Sec. 6.3, the curves of isothermal compressibility ($\mathcal{K}_T$) in Sec. 6.4 and the curves of thermal expansion at constant pressure parameter ($\beta_{\mathcal{P}}$) in Sec. 6.5.

6.2 Equation of State

Once we determined the model's parameters, we can generate smooth equation-of-state curves that represent our experimental data. For the brevity's sake, let us write the model in Eq. (5.2) again:

$$\mathcal{P}(T,\mathcal{V},N) = \begin{cases} a_0(\mathcal{V},N)T^{4+a_1(\mathcal{V},N)} + a_2(\mathcal{V},N), & T < T_c. \\ a_3(\mathcal{V},N)T + a_4(\mathcal{V},N), & T > T_c. \end{cases} \tag{6.8}$$

Using Eq. (6.8) and the graphs in Sec. 6.1, we plotted the $\mathcal{P}\times T$ graphs shown in Appx. D, with a sample of them seen in Fig. 41. As we mentioned before in Sec. 5.3, the plots become a straight line above the critical temperature, in accordance with the Gay-Lussac's law for classical gases.

Moreover, the plots shown in this section are also in agreement with previous GVM measurements.[27] Nonetheless, since our model is limited to the range of values shown in Tab. 1, we cannot estimate the equation of state at zero temperature as done before elsewhere.[29]

More importantly, the graphs in Appx. D are smooth enough to be differentiated, oppositely to the untreated $\mathcal{P}\times T$ curves alike Fig. 12. That property is crucial in this analysis, because the other thermodynamic susceptibilities ($C_{\mathcal{V}}$, $\mathcal{K}_T$ and $\beta_{\mathcal{P}}$) necessary to complete our investigation are essentially derivatives. A complete and reliable thermodynamic study would not be possible without that.

In the literature, other publications were able also to determine experimentally the equation of state of a ultracold Fermi gas using the Local-Density Approximation (LDA).[2,45] Nonetheless, the experiments described in these papers used box-potential traps, which means the density of their atomic clouds were constant, differently from our experiments. Hence, despite the fact we rely on models to fit and recover the *in situ* profiles of our probed clouds, it is important to notice that our methods describe a non-uniform system, completely more complex than a constant-density system, and still our analysis tools are mathematically simpler than the LDA's framework.

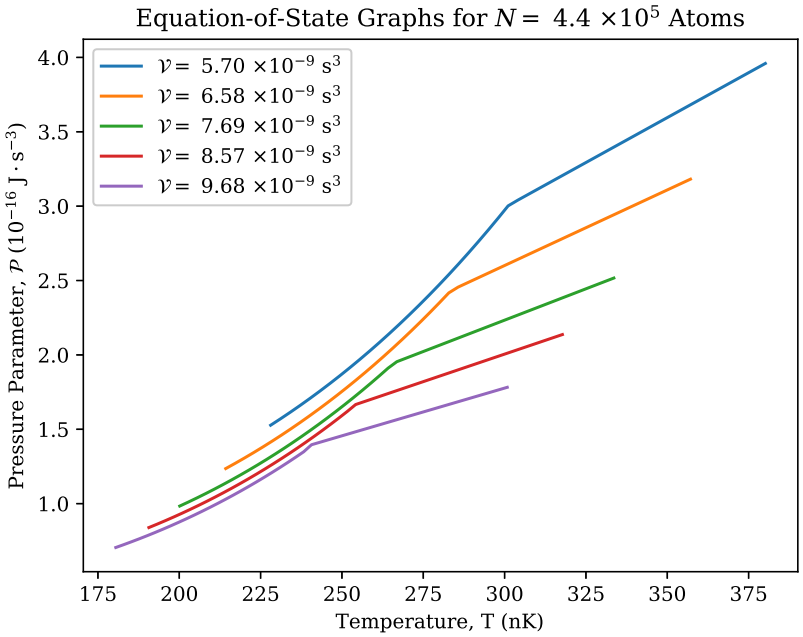

Figure 26 – A few equation-of-State graphs generated with the fitted data for clouds of $N = 4.4 \times 10^5$ atoms. See Appx. D for more curves.
Source: By the author.

6.3 Heat Capacity at Constant Volume Parameter

To see how the quantity aforementioned is found, let us recall firstly that we already know a fine approximation for the internal energy, given as

$$E(\mathcal{P}, \mathcal{V}) \approx 3\mathcal{P}\mathcal{V}, \tag{6.9}$$

as seen before in Eq. (3.11). On that account, according to the differential formulation of the first law of thermodynamics, the *heat capacity at constant volume parameter* is

$$C_{\mathcal{V}} = \left.\frac{\partial E}{\partial T}\right|_{\mathcal{V},N} \overset{(6.9)}{=} 3\mathcal{V} \left.\frac{\partial \mathcal{P}}{\partial T}\right|_{\mathcal{V},N}. \tag{6.10}$$

Therefore, replacing Eq. (5.2) into Eq. (6.10) yields the formula

$$C_{\mathcal{V}}(T, \mathcal{V}, N) = \begin{cases} 3[4 + a_2(\mathcal{V}, N)]\mathcal{V} a_1(\mathcal{V}, N) T^{3+a_2(\mathcal{V},N)}, & T < T_c, \\ 3a_3(\mathcal{V}, N)\mathcal{V}, & T > T_c, \end{cases} \tag{6.11}$$

which was used to generate heat-capacity plots as we see in Fig. 61. The rest of the curves are found in Appx. E.

As we know, the model's critical temperatures are underestimated, thus the peaks of the real critical points are slightly shifted to the right in the graphs. Notwithstanding,

we still see the graphs are physically consistent, as the heat capacity drops to $3Nk$ above and beyond the critical temperature in all the plots, as predicted for a classical gas in a harmonic potential.

Furthermore, the graphs in Appx. E are also consistent with past measurements using the GVM,[28] as well as measurements of the heat capacity that did not rely on the GVM, but were made with atomic clouds held a constant-frequency harmonic trap. This proves that our methods have been being adequate so far, not only compared to other GVM measurments, but also to different approaches.

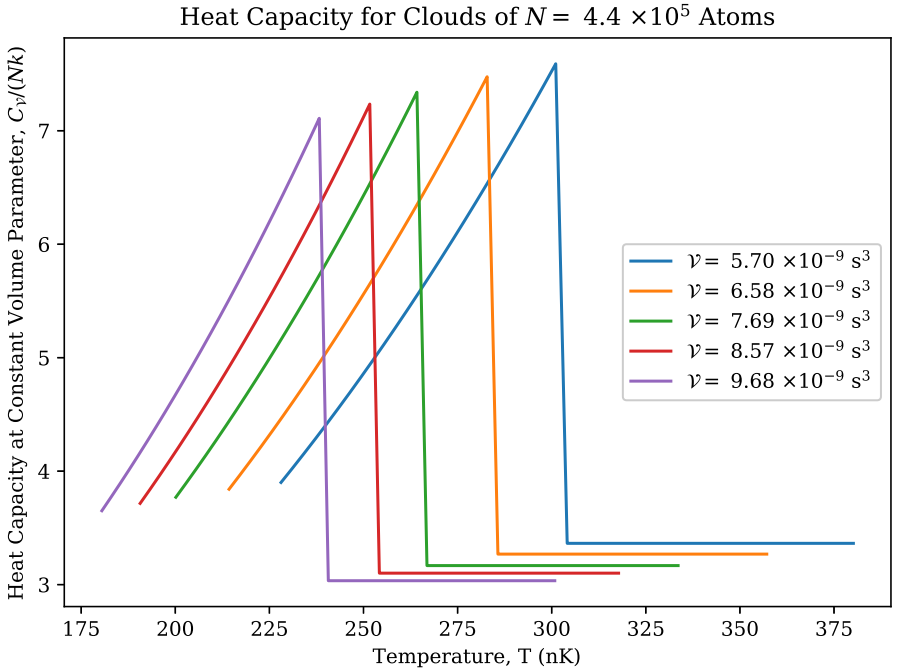

Figure 27 – A few plots of the heat capacity at constant volume parameter $C_\mathcal{V}$ for clouds of $N = 4.4 \times 10^5$ atoms. See Appx. E for more curves.
Source: By the author.

6.4 Isothermal Compressibility

Let us look now at first of the two susceptibilties of the gas that depend on variations of the volume parameter, the *compressibility parameter at constant temperature*:

$$\mathcal{K}_T \equiv -\frac{1}{\mathcal{V}} \frac{\partial \mathcal{V}}{\partial \mathcal{P}}\bigg|_{T,N} . \tag{6.12}$$

Both quantities can be easily obtained by differentiating partially Eq. (5.2) with respect to $\mathcal{V}$, keeping T constant. The partial derivatives of the technical coefficients are obtained by differentiating numerically the curves in Figs. 14, 16, 18, 20 and 22. Therefore, the $\mathcal{K}_T$ plots are shown in Fig. 81 and Appx. G. The values of temperature of each $\mathcal{K}_T$ curve, as well as the values of pressure parameter of each $\beta_\mathcal{P}$ curve, correspond to the set of T_c of

all combinations of N and $\mathcal{V}$ we measured. Furthermore, the real critical point of each curve is also slightly shifted to the right.

In the case of the $\mathcal{K}_T$ plots, the classical behavior is observed on the left-hand side of the critical-point peaks, where the curves overlap following the $\mathcal{P}^{-1}$ behavior, as expected. The overall behavior of the plots agrees with previous results relying on the GVM published in the recent past.[30] No measurement of the compressibility relying on the LDA has been reported in the literature yet, as far as we know. That fact clearly puts the GVM head in the thermodynamic research of quantum gases compared to the LDA.

Differently from the isothermal compressibility κ_T for a homogeneous ideal gas, which diverges at $T = T_c$, Reyes-Ayala and co-workers[46] have demonstrated analitically that isothermal compressibility $\mathcal{K}_T$ of a harmonically trapped gas is continuous around the transition. However, its derivative with respect to T is discontinuous at the critical point. That behavior is notorious, for it shows that the critical behavior of a harmonically confined gas belongs to the universility class of the spherical model. Although that system is supposed to be in the 3D XY model, that finding illustrates that how different the Bose-Einstein transition is in a inhomogeneous case compared to the homogeneous case.

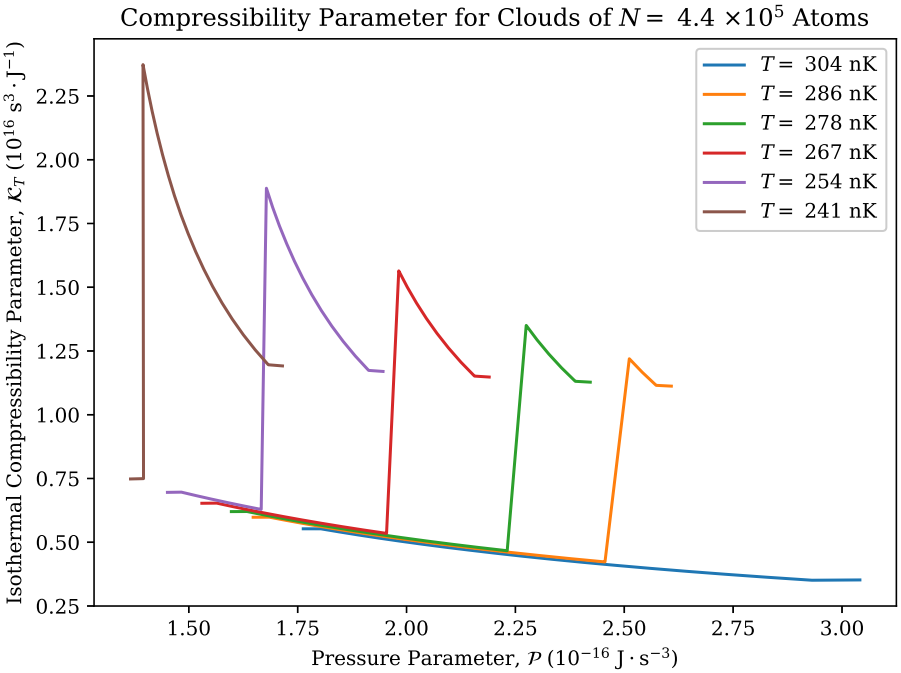

Figure 28 – A few plots of the isothermal compressibility parameter $\mathcal{K}_T$ for clouds of $N = 4.4 \times 10^5$ atoms. See Appx. G for more curves.
Source: By the author.

6.5 Thermal Expansion at Constant Pressure Parameter

After analyzing the $\mathcal{K}_T$ curves in Sec. 6.4, let us see the second of the two susceptibilties of the gas that depend on variations of the volume parameter, the *thermal-expansion*

parameter at constant pressure parameter:

$$\beta_{\mathcal{P}} \equiv \frac{1}{\mathcal{V}} \left.\frac{\partial \mathcal{V}}{\partial T}\right|_{\mathcal{P},N} . \tag{6.13}$$

We used essentially the same methodology described in Sec. sec:KT-res to generate the quantity in 6.13. The only differences here are that Eq. (5.2) was differentiated with respect to T keeping $\mathcal{P}$ constant, and the values of pressure parameter used in this stage correspond to the list of $\mathcal{P}_c$ values obtained with our model. The $\beta_{\mathcal{P}}$ plots are presented in Fig. 101 and Appx. F.

The $\beta_{\mathcal{P}}$ plots we found here are concordant with the outcomes of past investigations.[31] The quantum-mechanical behavior of a Bose-condensed gas is seen on the right-hand side of the critical-point peaks, as the thermal expansion drops to zero and gas ceases to expand, as expected again.

Again, no measurement of the thermal expansion has been published yet in the literature, giving the GVA a clear advantage next to the LDA.

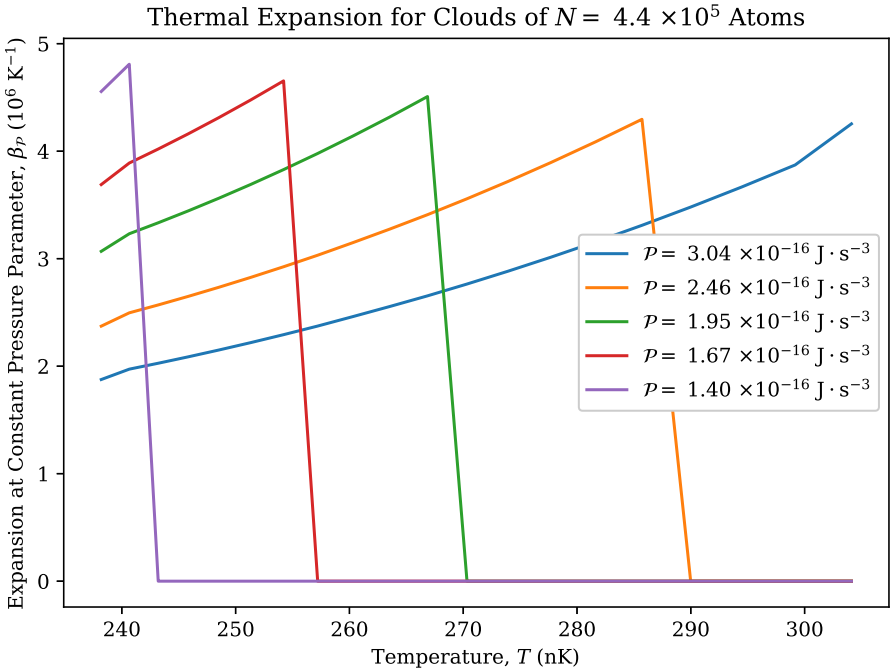

Figure 29 – A few plots of the thermal expansion at constant pressure parameter $\beta_{\mathcal{P}}$ for clouds of $N = 4.4 \times 10^5$ atoms. See Appx. F for more curves.
Source: By the author.

7 CONCLUSIONS

So far, the thermodynamic susceptibilities we found using our simplified model satisfy the expectation. We could reproduce the results of independent studies that found the equation of state,[27] the heat capacity,[28] the compressibility[30] and the thermal expansion.[31] That fact ensures the robustness and reliability of our methods.

Moreover, the curves of heat capacity that we obtained empiracally are comparable to measurements of atomic clouds in a constant-frequency harmonic trap using approaches other than the GVM.[22,24] Besides, our results are in agreement with the theoretical calculations presented in one of our Mexican collaborators' papers.[47] Therefore, we observe that our combination of the GVM with the simplified model we proposed is concordant with the results already existent in the literature.

Besides, we should have to find the heat capacity at constant pressure ($C_{\mathcal{P}}$) to achieve a complete thermodynamic description in usual conditions. However, we had Eq. (6.9) since the beginning to determine the internal energy of the system. Hence, as we have E, $C_{\mathcal{V}}$, $\mathcal{K}_T$ and $\beta_{\mathcal{P}}$, the thermodynamic description of the our gas is now complete and we can generate any other thermodynamic potential wih those four quantities.

As a final result, we have sucessfully demonstrated that it is possible to give a full description of the thermodynamics of a harmonically trapped Bose gas around its critical points using the Global-Variable Method and a simplified model to its equation of state. We described a methodology to give a full thermodynamic description to an ultracold gas in a harmonic trap around the Bose-Einstein transition. We used the global-variable formalism to describe the thermodynamic quantitites of the system, allowing us to perform global measurements on our samples, rather than usual local-measurement techniques presented in the literature. To accomplish this study, we developed an empirical model to fit the global equation of state, which was essential to find the susceptibilities. Although we made this investigation with a Bose gas, our methodology applies also to non-atomic gases, Fermi gases and Bose-Fermi mixtures.

By using the gas in a harmonic potential as a toy model to non-uniform systems, we think that our methodology might contribute to the understanding of nonhomogeneous systems of greater complexity, including out-of-equilibrium systems. Moreover, we believe that our findings provide technical tools to the the further advance of the emerging field of quantum thermal engines, which may lead to a new industrial revolution, just as the development of classical thermal engines did in the 19th century.

REFERENCES

1 KETTERLE, W.; DALLIN, D.; STAMPER-KURN, D. M. **Making, probing and understanding Bose-Einstein condensates**. 1999. Available from: https://arxiv.org/pdf/cond-mat/9904034.pdf. Acessible at: 23 Jan. 2020.

2 NASCIMBÈNE, S. *et al.* Exploring the thermodynamics of a universal Fermi gas. **Nature**, Nature Publishing Group, v. 463, n. 7284, p. 1057–1060, 2010.

3 ROMERO-ROCHÍN, V. Equation of state of an interacting Bose gas confined by a harmonic trap: the role of the "harmonic" pressure. **Physical Review Letters**, APS, v. 94, n. 13, p. 130601, 2005.

4 ROMERO-ROCHÍN, V.; BAGNATO, V. S. Thermodynamics of an ideal gas of bosons harmonically trapped: equation of state and susceptibilities. **Brazilian Journal of Physics**, SciELO Brasil, v. 35, n. 3a, p. 607–613, 2005.

5 BOSE, S. N. Plancks gesetz und lichtquantenhypothese. **Zeitschrift für Physik**, v. 26, p. 178–181, 1924.

6 EINSTEIN, A. Quantentheorie des einatomigen idealen gases. **Sitzungsberichte der Preussischen Akademie der Wissenschaften**: sitzung der physikalisch-mathematischen, 1924. Available from: https://echo.mpiwg-berlin.mpg.de/ECHOdocuView?url=/permanent/echo/einstein/sitzungsberichte/PG8B073X/index.meta. Accessible at: 13 Sept. 2021.

7 EINSTEIN, A. Quantentheorie des einatomigen idealen gases. **Sitzungsberichte der Preussischen Akademie der Wissenschaften**: sitzung der physikalisch-mathematischen, 1925. Available from: http://digitalcollections.library.cmu.edu/awweb/awarchive?type=file&item=393674. Accessible at: 13 Sept. 2021.

8 UHLENBECK, G. E. **Over statistische methoden in der theorie der quanta**. 1927. 98 p. Ph. D. Thesis (Doctor in Science) — Universiteit Leiden, Leiden, 1927.

9 KAHN, B.; ; UHLENBECK, G. E. On the theory of condensation. **Physica**, Elsevier, v. 5, n. 5, p. 399–416, 1938.

10 LONDON, F. On the Bose-Einstein condensation. **Physical Review**, APS, v. 54, n. 11, p. 947, 1938.

11 ANDERSON, M. H. *et al.* Observation of Bose-Einstein condensation in a dilute atomic vapor. **Science**, American Association for the Advancement of Science, v. 269, n. 5221, p. 198–201, 1995.

12 DAVIS, K. B. *et al.* Bose-Einstein condensation in a gas of sodium atoms. **Physical Review Letters**, APS, v. 75, n. 22, p. 3969, 1995.

13 BRADLEY, C. C. *et al.* Evidence of Bose-Einstein condensation in an atomic gas with attractive interactions. **Physical Review Letters**, APS, v. 75, n. 9, p. 1687, 1995.

14 FRIED, D. G. *et al.* Bose-Einstein condensation of atomic hydrogen. **Physical Review Letters**, APS, v. 81, n. 18, p. 3811, 1998.

15 SANTOS, F. P. *et al.* Bose-Einstein condensation of metastable helium. **Physical Review Letters**, APS, v. 86, n. 16, p. 3459, 2001.

16 MODUGNO, G. *et al.* Bose-Einstein condensation of potassium atoms by sympathetic cooling. **Science**, American Association for the Advancement of Science, v. 294, n. 5545, p. 1320–1322, 2001.

17 WEBER, T. *et al.* Bose-Einstein condensation of cesium. **Science**, American Association for the Advancement of Science, v. 299, n. 5604, p. 232–235, 2003.

18 GRIESMAIER, A. *et al.* Bose-Einstein condensation of chromium. **Physical Review Letters**, APS, v. 94, n. 16, p. 160401, 2005.

19 FUKUHARA, T.; SUGAWA, S.; TAKAHASHI, Y. Bose-Einstein condensation of an ytterbium isotope. **Physical Review A**, APS, v. 76, n. 5, p. 051604, 2007.

20 LU, M. *et al.* Strongly dipolar Bose-Einstein condensate of dysprosium. **Physical Review Letters**, APS, v. 107, n. 19, p. 190401, 2011.

21 AIKAWA, K. *et al.* Bose-Einstein condensation of erbium. **Physical Review Letters**, APS, v. 108, n. 21, p. 210401, 2012.

22 ENSHER, J. R. *et al.* Bose-Einstein condensation in a dilute gas: measurement of energy and ground-state occupation. **Physical Review Letters**, APS, v. 77, n. 25, p. 4984, 1996.

23 GERBIER, F. *et al.* Critical temperature of a trapped, weakly interacting Bose gas. **Physical Review Letters**, APS, v. 92, n. 3, p. 030405, 2004.

24 GERBIER, F. *et al.* Experimental study of the thermodynamics of an interacting trapped Bose-Einstein condensed gas. **Physical Review A**, APS, v. 70, n. 1, p. 013607, 2004.

25 MEYRATH, T. P. *et al.* Bose-Einstein condensate in a box. **Physical Review A**, APS, v. 71, n. 4, p. 041604, 2005.

26 MAGALHÃES, K. M. F. **Obtenção da degenerescência quântica em sódio aprisionado**. 2004. Tese (Doutorado em Ciências) — Instituto de Física de São Carlos, Universidade de São Paulo, São Carlos, 2004.

27 SILVA, R. R. *et al.* Definition and measurement of global thermodynamic variables for laser-cooled trapped gas. **Laser Physics**, Springer, v. 16, n. 4, p. 687–692, 2006.

28 SHIOZAKI, R. F. **Quantum turbulence and thermodynamics on a trapped Bose-Einstein condensate**. 2013. Tese (Doutorado em Ciências) — Instituto de Física de São Carlos, Universidade de São Paulo, São Carlos, 2013.

29 CASTILHO, P. C. M. *et al.* Equation of state for a trapped quantum gas: remnant of zero-point energy effects. **New Journal of Physics**, IOP Publishing, v. 18, n. 2, p. 023014, 2016.

30 POVEDA-CUEVAS, F. J. *et al.* Isothermal compressibility determination across Bose-Einstein condensation. **Physical Review A**, APS, v. 92, n. 1, p. 013638, 2015.

31 MERCADO-GUTIÉRREZ, E. D.; POVEDA-CUEVAS, F. J.; BAGNATO, V. S. Thermal global expansion coefficient measurement for a harmonic trapped gas across Bose-Einstein condensation. **Brazilian Journal of Physics**, Springer, v. 48, n. 6, p. 539–542, 2018.

32 FRITSCH, A. R. *et al.* Thermodynamic measurement of the sound velocity of a Bose gas across the transition to Bose-Einstein condensation. **Journal of Statistical Mechanics**: theory and experiment, IOP Publishing, v. 2018, n. 5, p. 053108, 2018.

33 GROSSMANN, S.; HOLTHAUS, M. On Bose-Einstein condensation in harmonic traps. **Physics Letters A**, Elsevier, v. 208, n. 3, p. 188–192, 1995.

34 SHIOZAKI, R. F. *et al.* Measuring the heat capacity in a Bose-Einstein condensation using global variables. **Physical Review A**, APS, v. 90, n. 4, p. 043640, 2014.

35 HUANG, K. **Statistical mechanics**. New York: John Willey & Sons, 1963.

36 PETHICK, C. J.; SMITH, H. **Bose-Einstein condensation in dilute gases**. Cambridge, United Kingdom: Cambridge University Press, 2003.

37 FERMI, E. *et al.* Motion of neutrons in hydrogenous substances. **Ricerca Scientifica**, v. 7, n. 2, p. 13–52, 1936.

38 YOU, L.; HOLLAND, M. Ballistic expansion of trapped thermal atoms. **Physical Review A**, APS, v. 53, n. 1, p. R1, 1996.

39 SANDOVAL-FIGUEROA, N.; ROMERO-ROCHÍN, V. Thermodynamics of trapped gases: generalized mechanical variables, equation of state, and heat capacity. **Physical Review E**, APS, v. 78, n. 6, p. 061129, 2008.

40 FRITSCH, A. R. **Thermodynamics of a Bose gas: sound velocity from global variables and equivalence with other approaches**. 2016. Tese (Doutorado em Ciências) — Instituto de Física de São Carlos, Universidade de São Paulo, São Carlos, 2016.

41 TAVARES, P. E. S. **Consequências das excitações oscilatórias em condensados de Bose-Einstein**. 2012. Dissertação (Mestrado em Ciências) — Instituto de Física de São Carlos, Universidade de São Paulo, São Carlos, 2012.

42 STECK, D. A. **Rubidium 87 D line data**. 2001. Available from: https://steck.us/alkalidata/rubidium87numbers.pdf. Accessible at: 23 Jan. 2020.

43 TAVARES, P. E. S. **Excitations in Bose-Einstein condensates: collective modes, quantum turbulence and matter wave statistics**. 2016. Tese (Doutorado em Ciências) — Instituto de Física de São Carlos, Universidade de São Paulo, São Carlos, 2016.

44 CASTIN, Y.; DUM, R. Bose-Einstein condensates in time dependent traps. **Physical Review Letters**, APS, v. 77, n. 27, p. 5315, 1996.

45 KU, M. J. H. *et al.* Revealing the superfluid lambda transition in the universal thermodynamics of a unitary Fermi gas. **Science**, American Association for the Advancement of Science, v. 335, n. 6068, p. 563–567, 2012.

46 REYES-AYALA, I. *et al.* Critical properties of weakly interacting Bose gases as modified by a harmonic confinement. **Journal of Statistical Mechanics**: theory and experiment, IOP Publishing, v. 2017, n. 7, p. 073101, 2017.

47 POVEDA-CUEVAS, F. J. *et al.* Global thermodynamics of confined inhomogeneous dilute gases: a semi-classical approach. **AIP Conference Proceedings**, v. 1950, n. 1, p. 030006, 2018.

APPENDIX A – DENSITY OF STATES IN EQUATION (2.12)

Let us write again the density-of-states integral, shown previously in Eq. (2.12):

$$\varrho(\varepsilon) = \frac{2\pi(2m)^{3/2}}{(2\pi\hbar)^3} \iiint_{D_\varepsilon} \sqrt{\varepsilon - U(\boldsymbol{r})}\mathrm{d}^3 r \tag{A.1}$$

For the sake of generality, let us solve Eq. (A.1) with a general power-law potential,

$$U(\boldsymbol{r}) = U_x \left(\frac{x}{a_x}\right)^{2\nu_x} + U_y \left(\frac{y}{a_y}\right)^{2\nu_y} + U_z \left(\frac{z}{a_z}\right)^{2\nu_z} \quad \nu_i \in \mathbb{Z}_{\neq 0},\ i = x, y, z \tag{A.2}$$

whose correspondent integration domain D_ε is

$$D_\varepsilon : \begin{cases} |x| \leq a_x \left[\dfrac{\varepsilon - U_y(y/a_y)^{2\nu_y} - U_z(z/a_z)^{2\nu_z}}{U_x}\right]^{1/(2\nu_x)} \\ |y| \leq a_y \left[\dfrac{\varepsilon - U_z(z/a_z)^{2\nu_z}}{U_y}\right]^{1/(2\nu_y)} \\ |z| \leq a_z \left(\dfrac{\varepsilon}{U_x}\right)^{1/(2\nu_z)} \end{cases} \tag{A.3}$$

Fortunately, there is an analytical solution in this case, and it can be achieved with the mathematical result

$$\int_{-\sqrt[2C]{A/B}}^{\sqrt[2C]{A/B}} (A - B\xi^{2C})^D \mathrm{d}\xi = \frac{2A^{D+1/(2C)}}{B^{1/(2C)}} {}_2F_1\left(\frac{1}{2C}, -D; 1 + \frac{1}{2C}; 1\right), \tag{A.4}$$

in which the gamma function is defined as

$$\Gamma(\xi) \equiv \int_0^\infty \tau^{\xi-1} e^{-\tau} \mathrm{d}\tau; \quad \mathrm{Re}(\xi) > 0. \tag{A.5}$$

and the hypergeometric function is given as

$${}_2F_1(a, b; c; \xi) \equiv \frac{\Gamma(c)}{\Gamma(b)\Gamma(c-b)} \int_0^1 \frac{\tau^{b-1}(1-\tau)^{c-b-1}}{(1-\tau\xi)^a} \mathrm{d}\tau, \tag{A.6}$$

Therefore, the solution of Eq. (A.1) with the potential in Eq. (A.2) is

$$\varrho_{\mathrm{PL}}(\varepsilon) = \frac{16\pi(2m)^{3/2}a_x a_y a_z}{(2\pi\hbar)^3}\sqrt{\frac{\varepsilon^{1+1/\nu_x+1/\nu_y+1/\nu_z}}{U_x^{1/\nu_x}U_y^{1/\nu_y}U_z^{1/\nu_z}}}f(\nu_x,\nu_y,\nu_z), \tag{A.7}$$

in which

$$\begin{aligned} f(\nu_x,\nu_y,\nu_z) \equiv {}& {}_2F_1\left(\frac{1}{2\nu_x},-\frac{1}{2};1+\frac{1}{2\nu_x};1\right){}_2F_1\left(\frac{1}{2\nu_y},-\frac{1}{2}\left(1+\frac{1}{\nu_x}\right);1+\frac{1}{2\nu_y};1\right)\cdot \\ & \cdot {}_2F_1\left(\frac{1}{2\nu_z},-\frac{1}{2}\left(1+\frac{1}{\nu_x}+\frac{1}{\nu_y}\right);1+\frac{1}{2\nu_z};1\right). \end{aligned} \tag{A.8}$$

However, we are interested only in two special cases of Eq. (A.7), which are the density of states with a box potential,

$$\varrho_{\mathrm{box}}(\varepsilon) = \lim_{\substack{\nu_x\to\infty\\ \nu_y\to\infty\\ \nu_z\to\infty}}\varrho_{\mathrm{PL}}(\varepsilon) = \frac{1}{2\pi}\left(\frac{2m}{\hbar^2}\right)^{3/2}V\varepsilon^{1/2}, \tag{A.9}$$

and the the density of states with a harmonic potential,

$$\varrho_{\mathrm{HP}}(\varepsilon) = \lim_{\substack{\nu_x\to 2\\ \nu_y\to 2\\ \nu_z\to 2}}\varrho_{\mathrm{PL}}(\varepsilon) = \frac{\varepsilon^2}{2(\hbar\bar{\omega})^3}. \tag{A.10}$$

APPENDIX B – PARTITION FUNCTIONS IN SECTION 3.1

Let us write again the canonical partition function integral:

$$Z = \frac{1}{(2\pi\hbar)^{3N} N!} \int_D \mathrm{d}^3 r_1 \mathrm{d}^3 p_1 \cdots \mathrm{d}^3 r_N \mathrm{d}^3 p_N \; e^{-H(\{\boldsymbol{r_i}\},\{\boldsymbol{p_i}\})/(kT)}, \tag{B.1}$$

Moreover, let us recall of an important mathematical result, the Gaussian integral:

$$\int_{-\infty}^{\infty} e^{-aw^2} \mathrm{d}w = \sqrt{\frac{\pi}{a}}; \quad a \in \mathbb{R}. \tag{B.2}$$

On the one hand, the Hamiltonian of a gas of N particles in a box of volume V is

$$H(\{\boldsymbol{r_i}\},\{\boldsymbol{p_i}\}) = \begin{cases} \displaystyle\sum_{i=1}^{N} \frac{\|\boldsymbol{p_i}\|^2}{2m} & \text{inside the box of volume } V. \\ 0 & \text{outside the box of volume } V. \end{cases} \tag{B.3}$$

Hence, while the space triple integral is obviously V, each three momentum integrals is

$$I_p = \int_{-\infty}^{\infty} e^{-(p^2)/(2mkT)} \mathrm{d}p = \sqrt{2\pi m k T}. \tag{B.4}$$

Therefore, from Eqs. (B.1) and (B.4), the canonical partition function of a classical gas in a box of volume V is

$$Z_{\text{box}} = \frac{(I_p^3 V)^N}{(2\pi\hbar)^{3N} N!} = \frac{1}{N!} \left(\frac{kT}{\hbar\bar{\omega}} \right)^{3N}, \tag{B.5}$$

as shown in Eq. (3.2).

On the other hand, the Hamiltonian of a gas of N particles in a typical harmonic potential is

$$H(\{\boldsymbol{r_i}\},\{\boldsymbol{p_i}\}) = \sum_{i=1}^{N} \frac{\|\boldsymbol{p_i}\|^2}{2m} + \sum_{i=1}^{N} \sum_{w=x,y,z} \frac{m\omega_w^2 w^2}{2}, \tag{B.6}$$

In this case, while the momentum integrals are exactly like Eq. (B.4), the space integrals are

$$I_w = \int_{-\infty}^{\infty} e^{-(\omega_w^2 w^2)/(2kT)} \mathrm{d}w = \sqrt{\frac{2\pi kT}{m\omega_w^2}}; \quad w = x, y, z. \tag{B.7}$$

As a result, canonical partition function of a classical gas in a harmonic potential is

$$Z_{\text{HP}} = \frac{(I_p^3 I_x I_y I_z)^N}{(2\pi\hbar)^{3N} N!} = \frac{1}{N!}\left(\frac{kT}{\hbar\bar{\omega}}\right)^{3N} ; \quad \bar{\omega} \equiv \sqrt{\omega_x \omega_y \omega_z}, \tag{B.8}$$

as presented in Eq. (3.3).

APPENDIX C – DERIVATION OF EQUATION (3.12)

Let us consider a gas of N particles whose positions and momenta are represented as $\{\boldsymbol{r_i}\}$ and $\{\boldsymbol{p_i}\}$, $i = 1, \cdots, N$, respectively. The Hamiltonian of that system is

$$H(\{\boldsymbol{r_i}\}, \{\boldsymbol{p_i}\}) = K(\{\boldsymbol{p_i}\}) + U(\{\boldsymbol{r_i}\}) \tag{C.1}$$

in which K is the total kinetic energy and U the total potential energy. Therefore, if the gas is in thermal equilibrium at temperature T, we can write its canonical partition function in the form

$$Z = \mathrm{tr}(e^{H(\{\boldsymbol{r_i}\},\{\boldsymbol{p_i}\})/(kT)}), \tag{C.2}$$

in which the trace operator tr represents a generic computation over the states of the system. We can readily see that $e^{H/(kT)} = e^{K/(kT)}e^{U/(kT)}$ is a Kronecker product, hence $\mathrm{tr}(e^{H/(kT)}) = \mathrm{tr}(e^{K/(kT)})\mathrm{tr}(e^{U/(kT)})$. Consequently, we can define partition functions for K and U as

$$Z_p = \mathrm{tr}(e^{K(\{\boldsymbol{p_i}\})/(kT)}) \quad \text{and} \quad Z_r = \mathrm{tr}(e^{U(\{\boldsymbol{r_i}\})/(kT)}), \tag{C.3}$$

respectively. As a result, the Helmholtz potential of the gas is

$$F = -kT\log(Z) \overset{\text{Eq. (C.3)}}{=} -kT\log(Z_p) - kT\log(Z_r) \tag{C.4}$$

For the sake of simplicity, we will consider a spherically symmetric harmonic potential, whose expression is

$$U(\{\boldsymbol{r_i}\}) = \frac{1}{2}m\omega^2\sum_{i=1}^{N} r_i^2 \tag{C.5}$$

According to Eq. (3.7), the volume parameter of a system subjected to the external potential in Eq. (C.5) is $\mathcal{V} \equiv \omega^{-3}$. That being so, the pressure parameter of the system is $\mathcal{P} = (\partial F/\partial \mathcal{V})_{T,N}$, as stated in Eq. (3.9). We must notice that K has no dependence on $\mathcal{V}$, therefore the term $\log(Z_p)$ will vanish in the derivative. On that account, we write

$$\begin{aligned}\mathcal{P} &= -\left.\frac{\partial F}{\partial \mathcal{V}}\right|_{T,N} \\ &= \frac{kT}{Z_r}\mathrm{tr}\left(\left.\frac{e^{U(\{\boldsymbol{r_i}\})/(kT)}}{\partial \mathcal{V}}\right|_{T,N}\right) \\ &= \frac{kT}{Z_r}\mathrm{tr}\left(\frac{2}{3\mathcal{V}}U(\boldsymbol{r})e^{U(\{\boldsymbol{r_i}\})/(kT)}\right) \\ &= \frac{2kT}{3\mathcal{V}}\mathrm{tr}\left(U(\boldsymbol{r})\frac{e^{U(\{\boldsymbol{r_i}\})/(kT)}}{Z_r}\right)\end{aligned} \tag{C.6}$$

Here we introduce the *density matrix*, given as

$$n \equiv \frac{e^{H(\{\boldsymbol{r_i}\},\{\boldsymbol{p_i}\})/(kT)}}{\mathrm{tr}(e^{H(\{\boldsymbol{r_i}\},\{\boldsymbol{p_i}\})/(kT)})} = \frac{e^{H(\{\boldsymbol{r_i}\},\{\boldsymbol{p_i}\})/(kT)}}{Z}. \tag{C.7}$$

From Eq. (C.7), we observe that term $e^{U/(kT)/Z_r} \equiv n_r$ in Eq. (C.6) is a density matrix of the position space, thus we find that

$$\mathcal{P} = \frac{2kT}{3\mathcal{V}}\mathrm{tr}\left(U(\boldsymbol{r})n_r\right), \tag{C.8}$$

In the continuous-spectrum approximation, the trace operator becomes a volume integral, therefore we obtain finally

$$\mathcal{P} = \frac{2}{3\mathcal{V}}\iiint_{D_U} n(\boldsymbol{r})U(\boldsymbol{r})\mathrm{d}^3r \tag{C.9}$$

in which $n(\boldsymbol{r})$ is the density of particles per unit volume of the gas and D_U is integration domain defined by the potential energy U.

APPENDIX D – EQUATION-OF-STATE DIAGRAMS

The complete set of equation-of-state graphs mentioned in Sec. 6.2 are shown here.

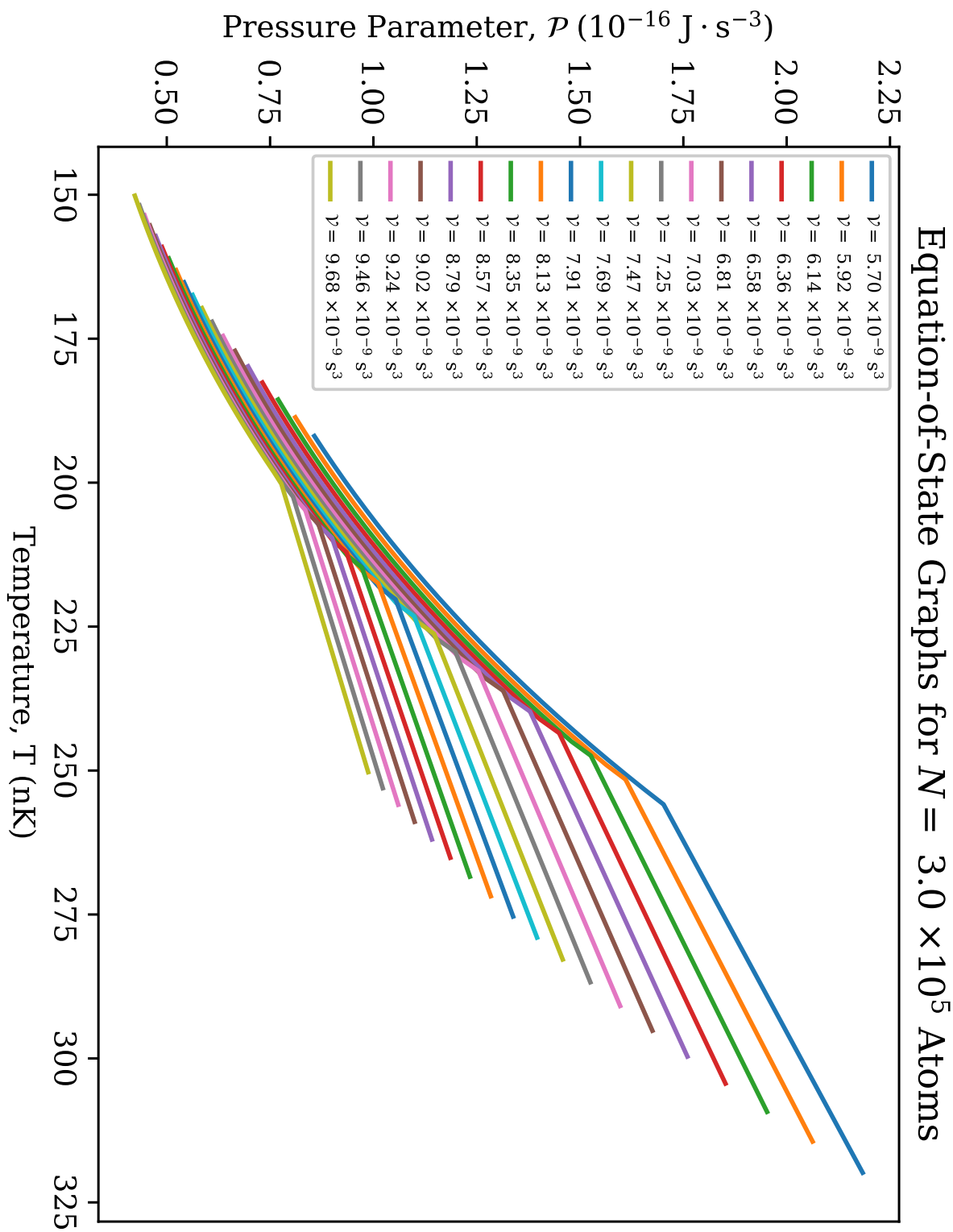

Figure 30 – Equation-of-State graphs generated with the fitted data for clouds of $N = 3.0 \times 10^5$ atoms.
Source: By the author.

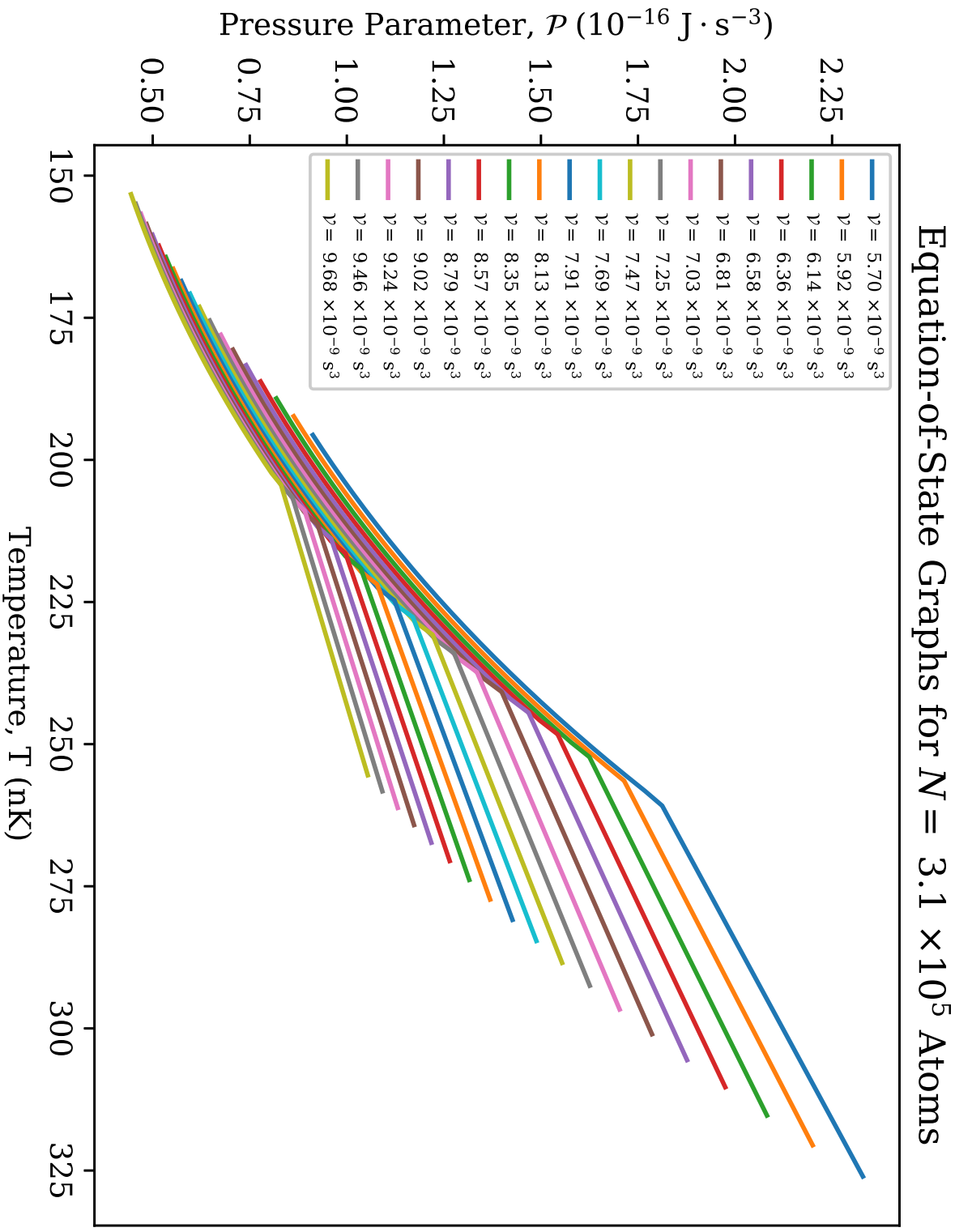

Figure 31 – Equation-of-State graphs generated with the fitted data for clouds of $N = 3.1 \times 10^5$ atoms.
Source: By the author.

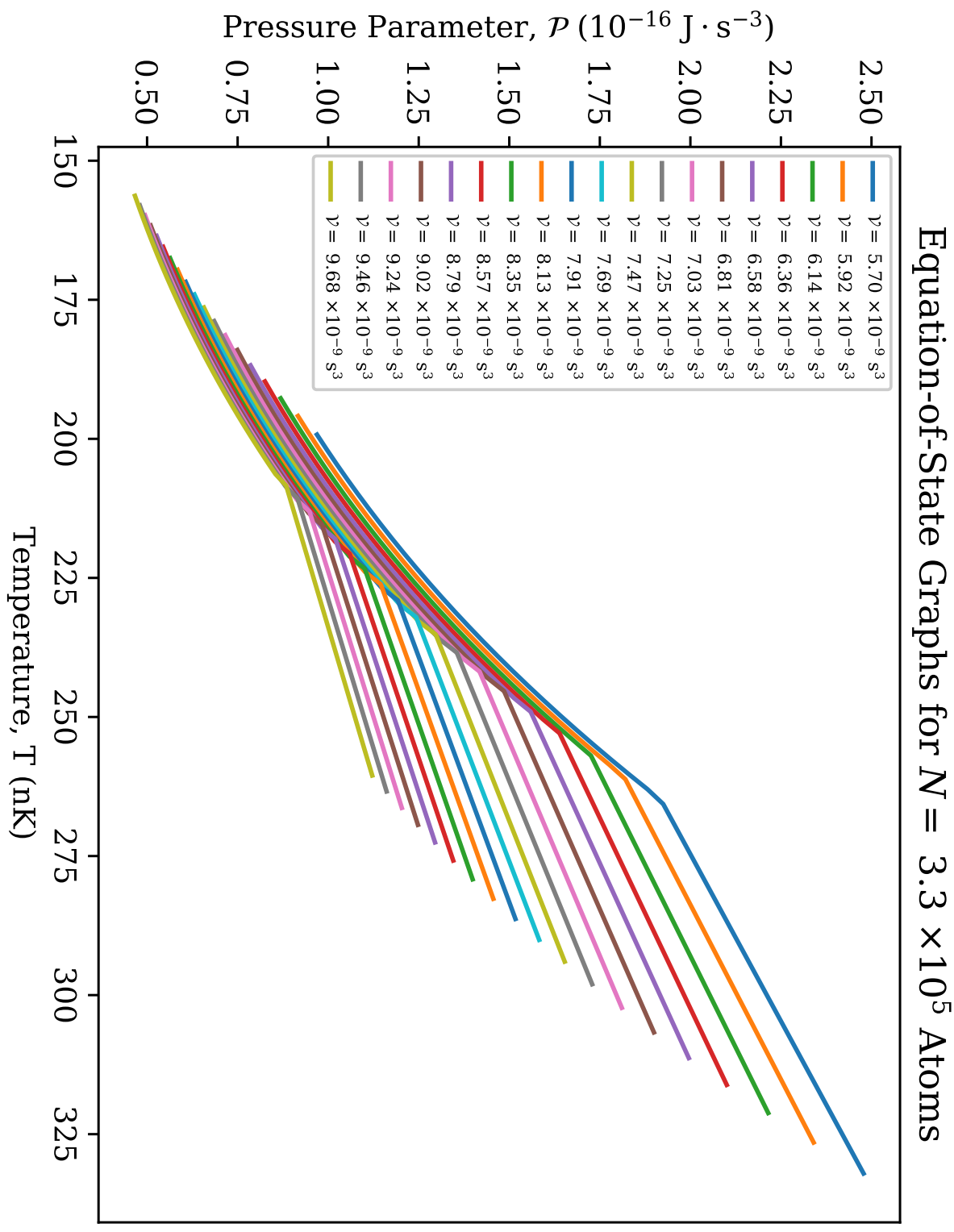

Figure 32 – Equation-of-State graphs generated with the fitted data for clouds of $N = 3.3 \times 10^5$ atoms.
Source: By the author.

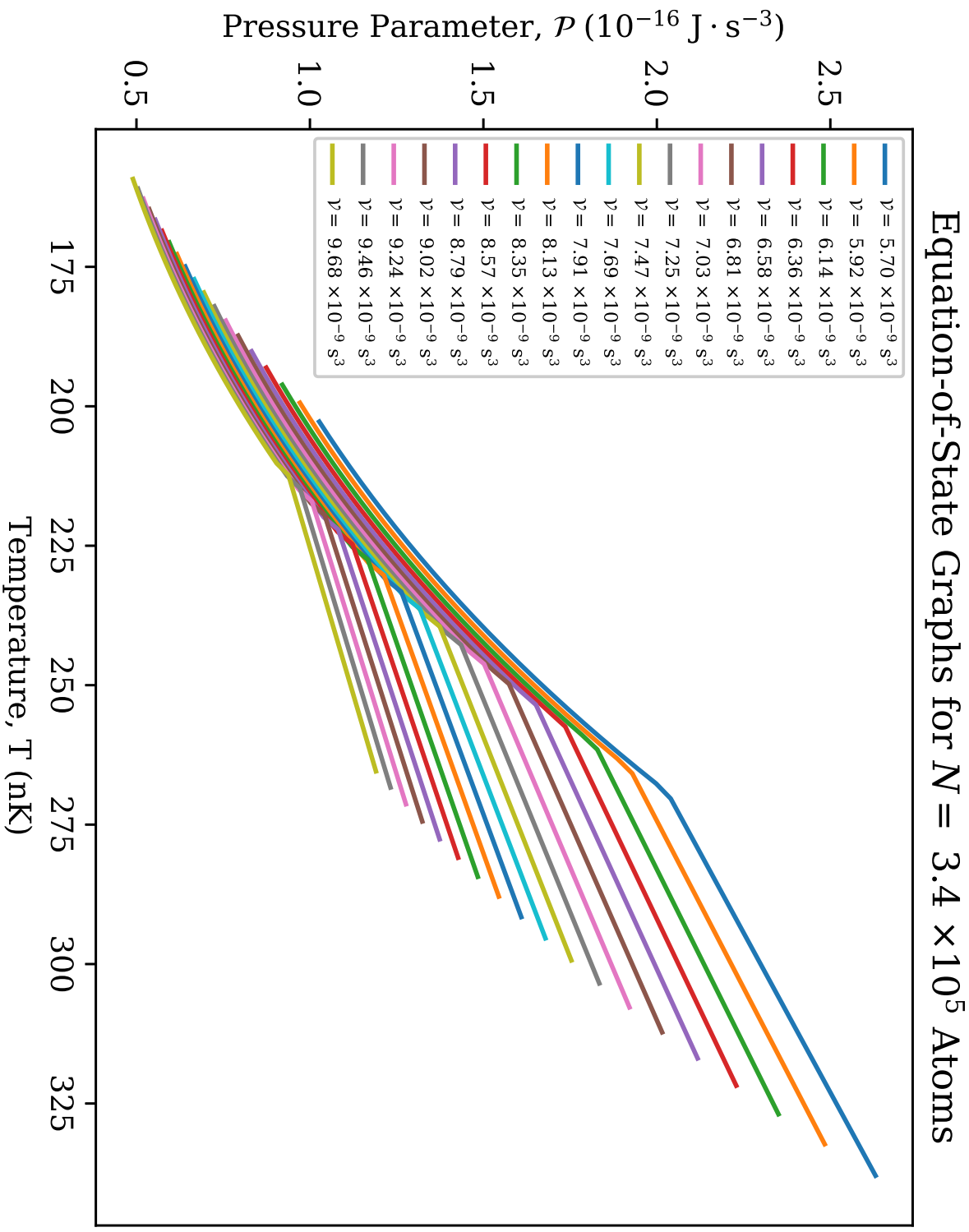

Figure 33 – Equation-of-State graphs generated with the fitted data for clouds of $N = 3.4 \times 10^5$ atoms.
Source: By the author.

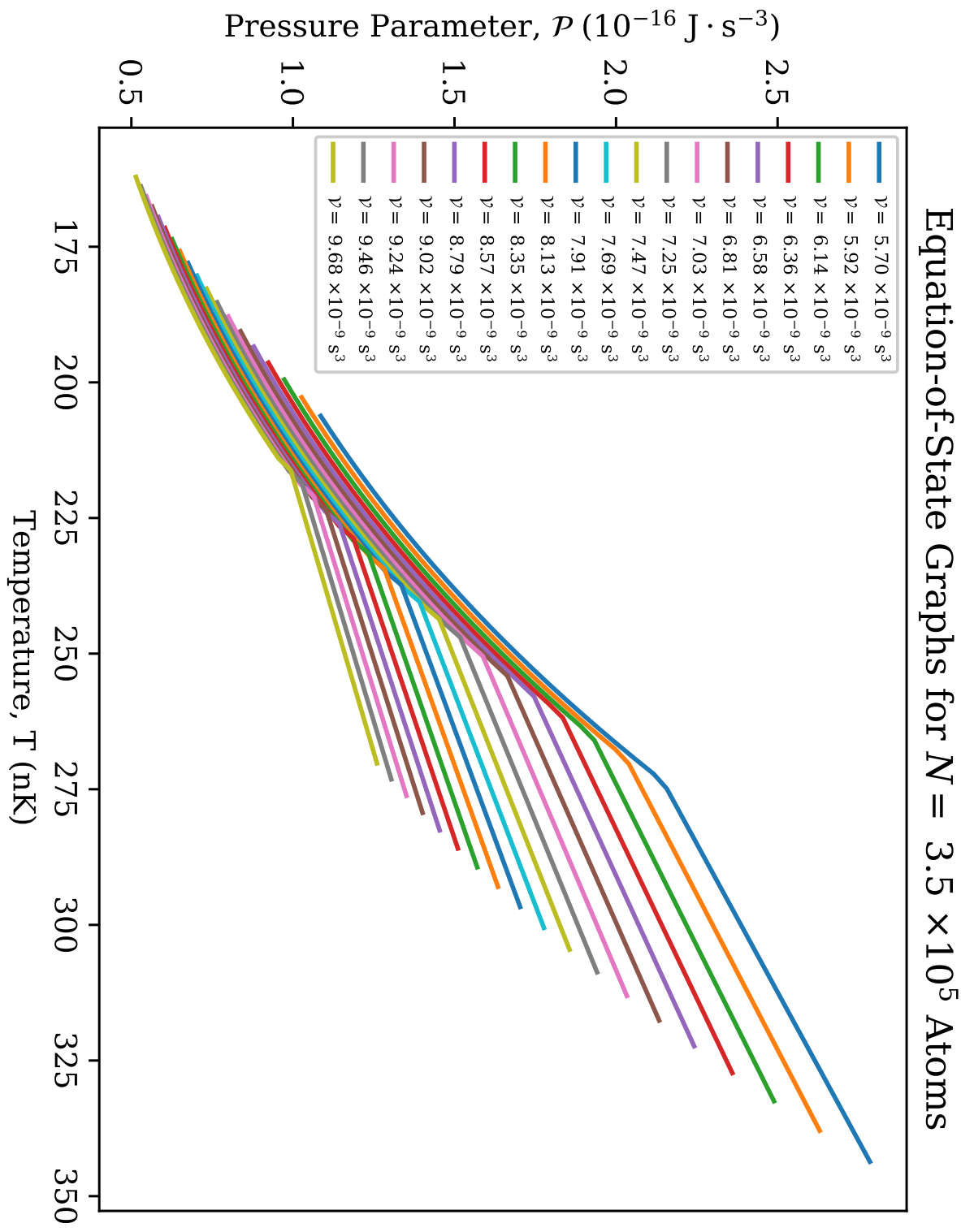

Figure 34 – Equation-of-State graphs generated with the fitted data for clouds of $N = 3.5 \times 10^5$ atoms.
Source: By the author.

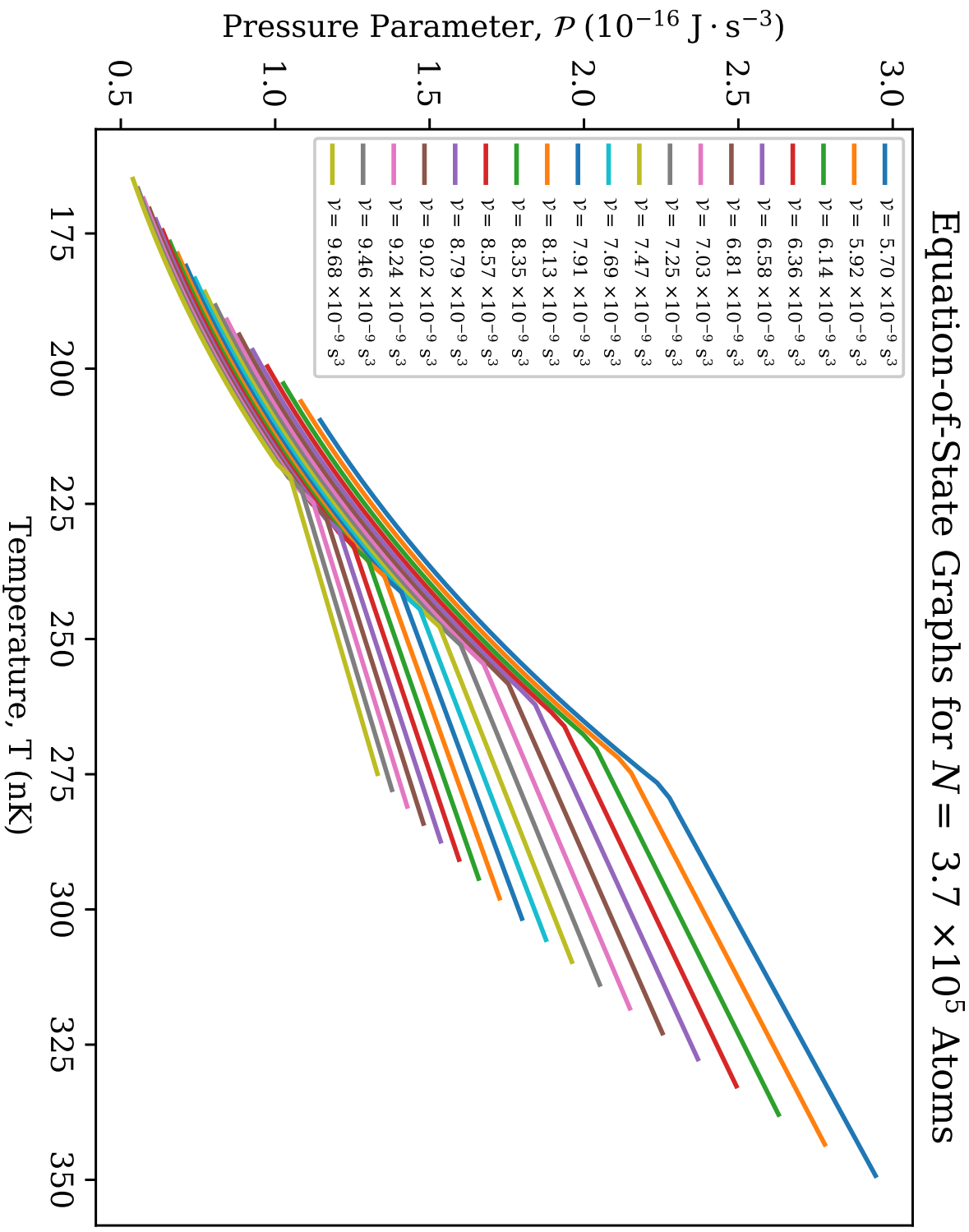

Figure 35 – Equation-of-State graphs generated with the fitted data for clouds of $N = 3.7 \times 10^5$ atoms.
Source: By the author.

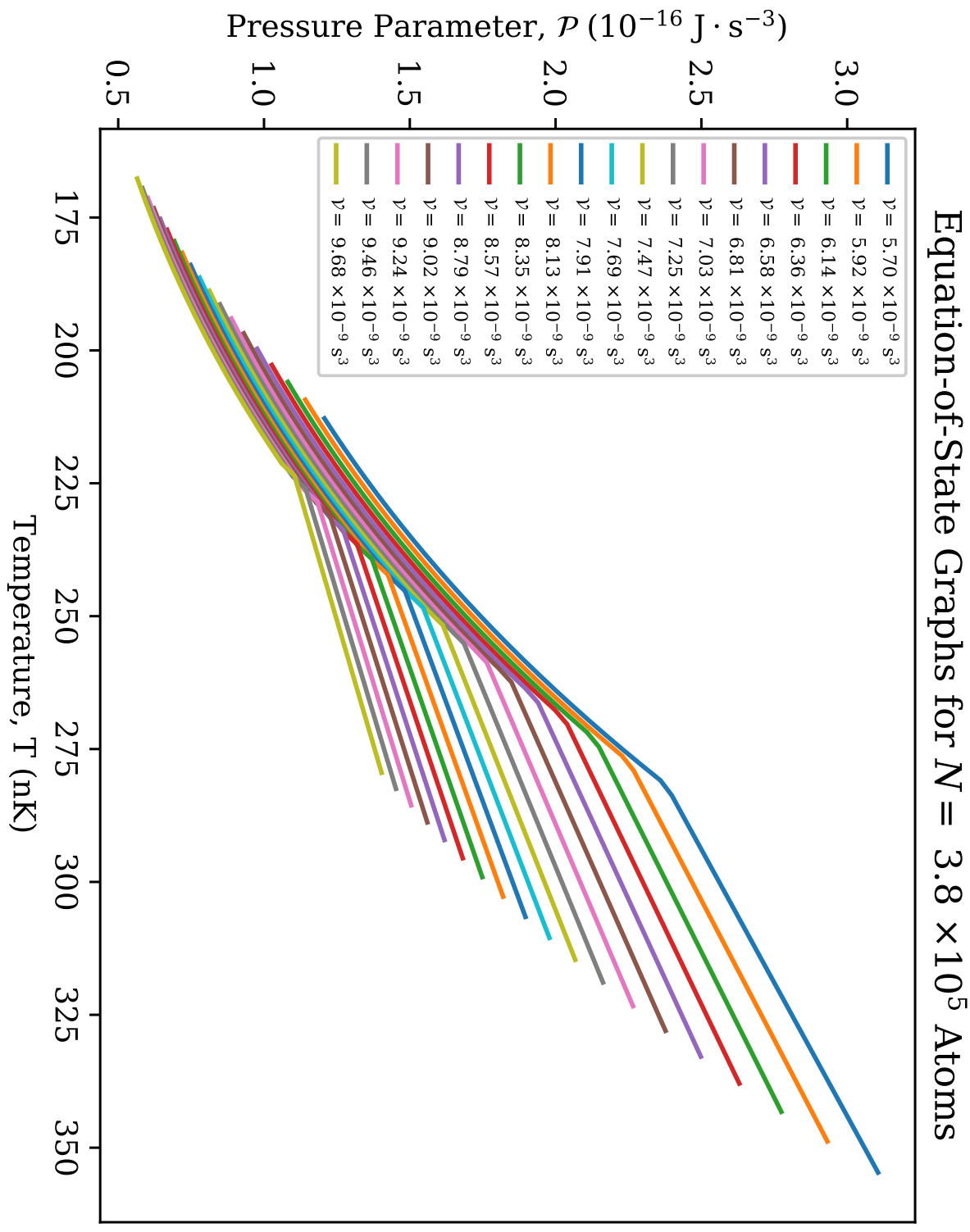

Figure 36 – Equation-of-State graphs generated with the fitted data for clouds of $N = 3.8 \times 10^5$ atoms.
Source: By the author.

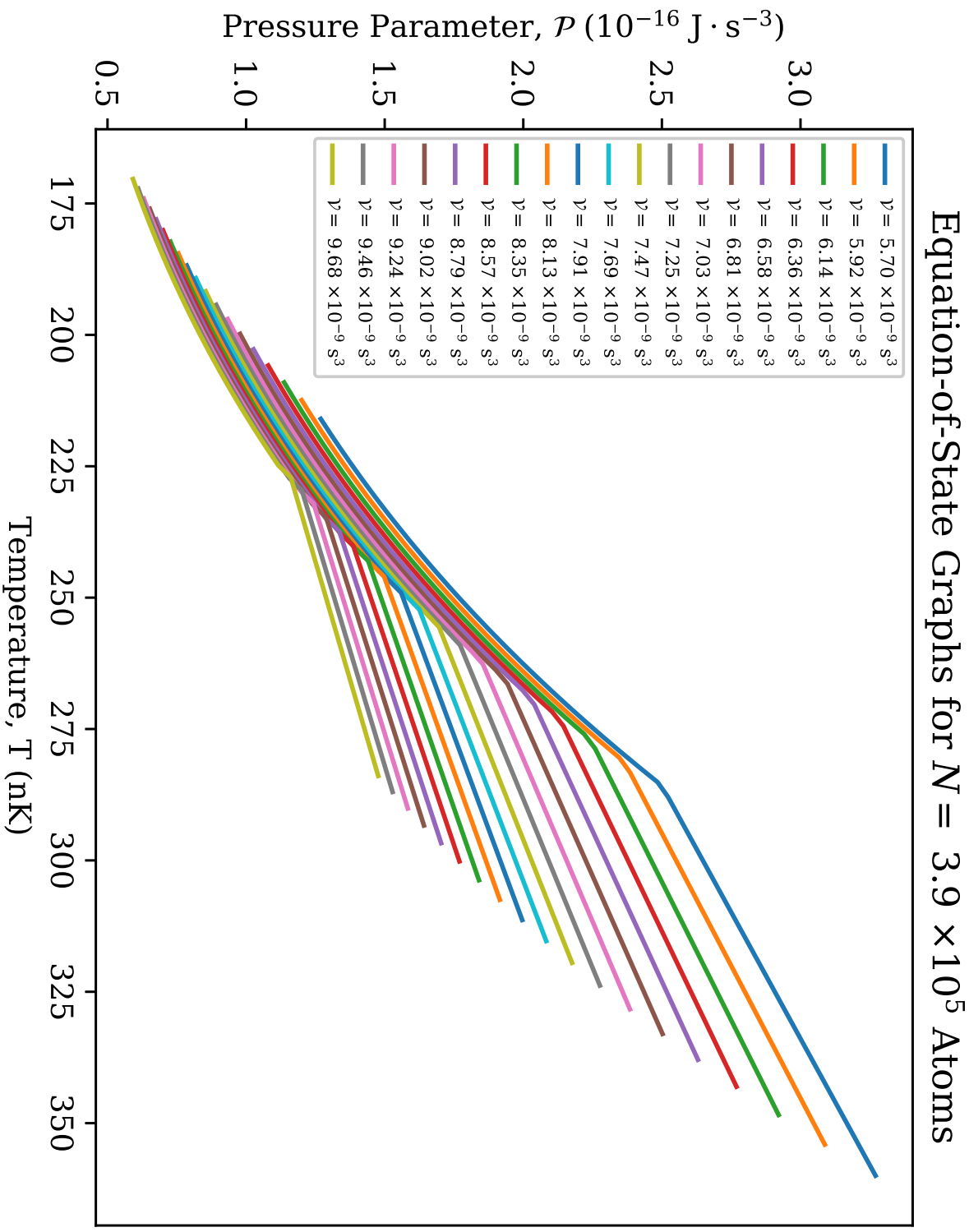

Figure 37 – Equation-of-State graphs generated with the fitted data for clouds of $N = 3.9 \times 10^5$ atoms.
Source: By the author.

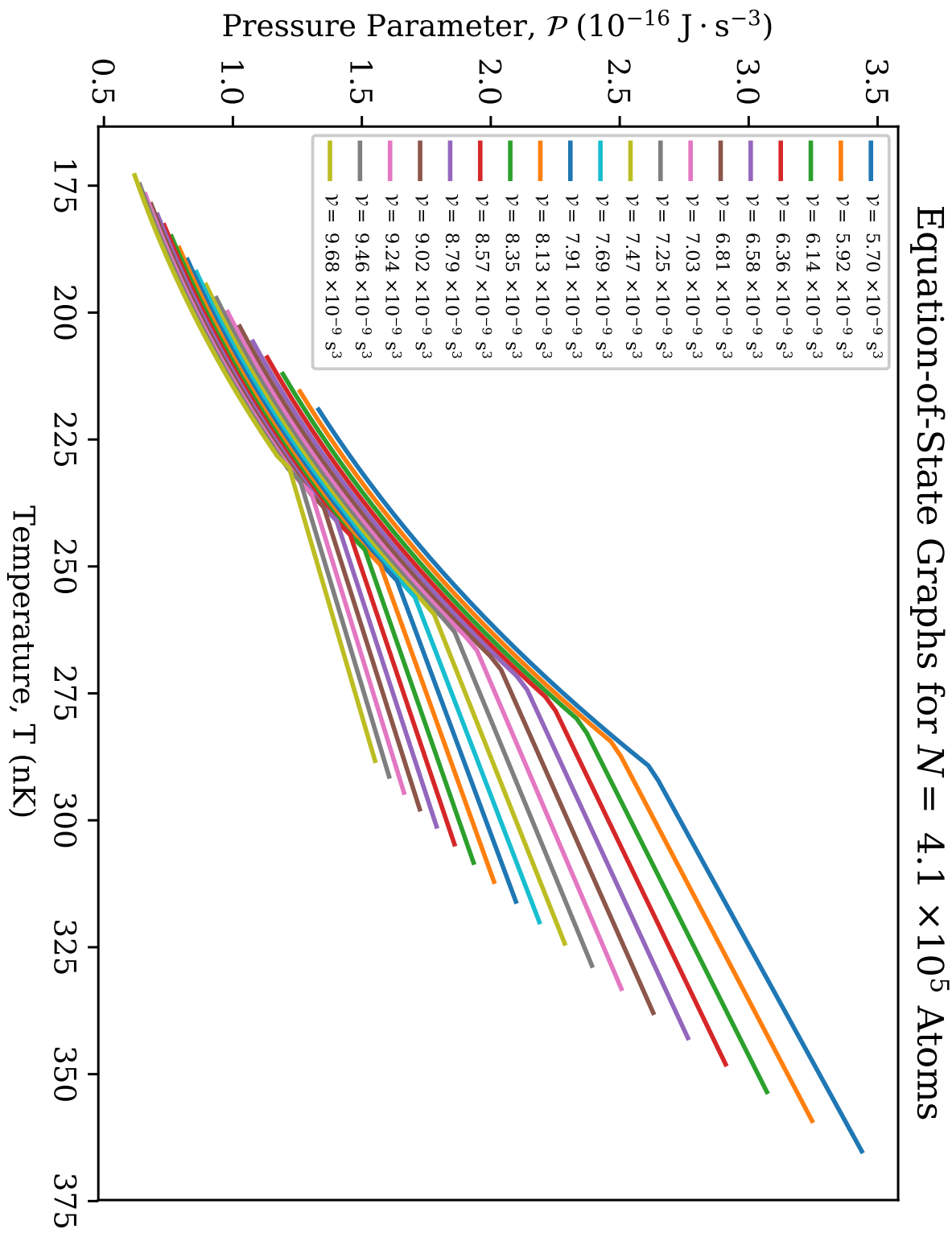

Figure 38 – Equation-of-State graphs generated with the fitted data for clouds of $N = 4.1 \times 10^5$ atoms.
Source: By the author.

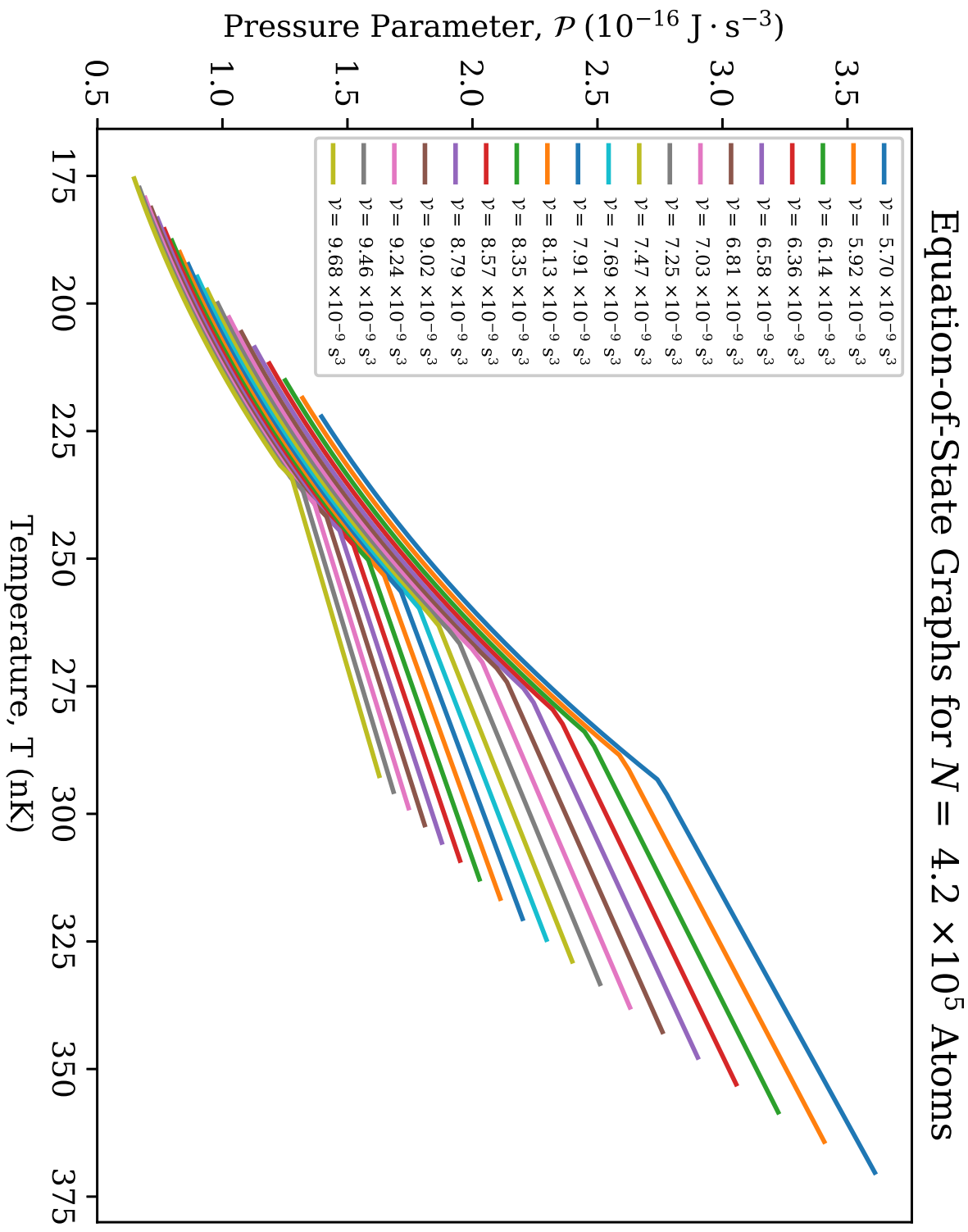

Figure 39 – Equation-of-State graphs generated with the fitted data for clouds of $N = 4.2 \times 10^5$ atoms.
Source: By the author.

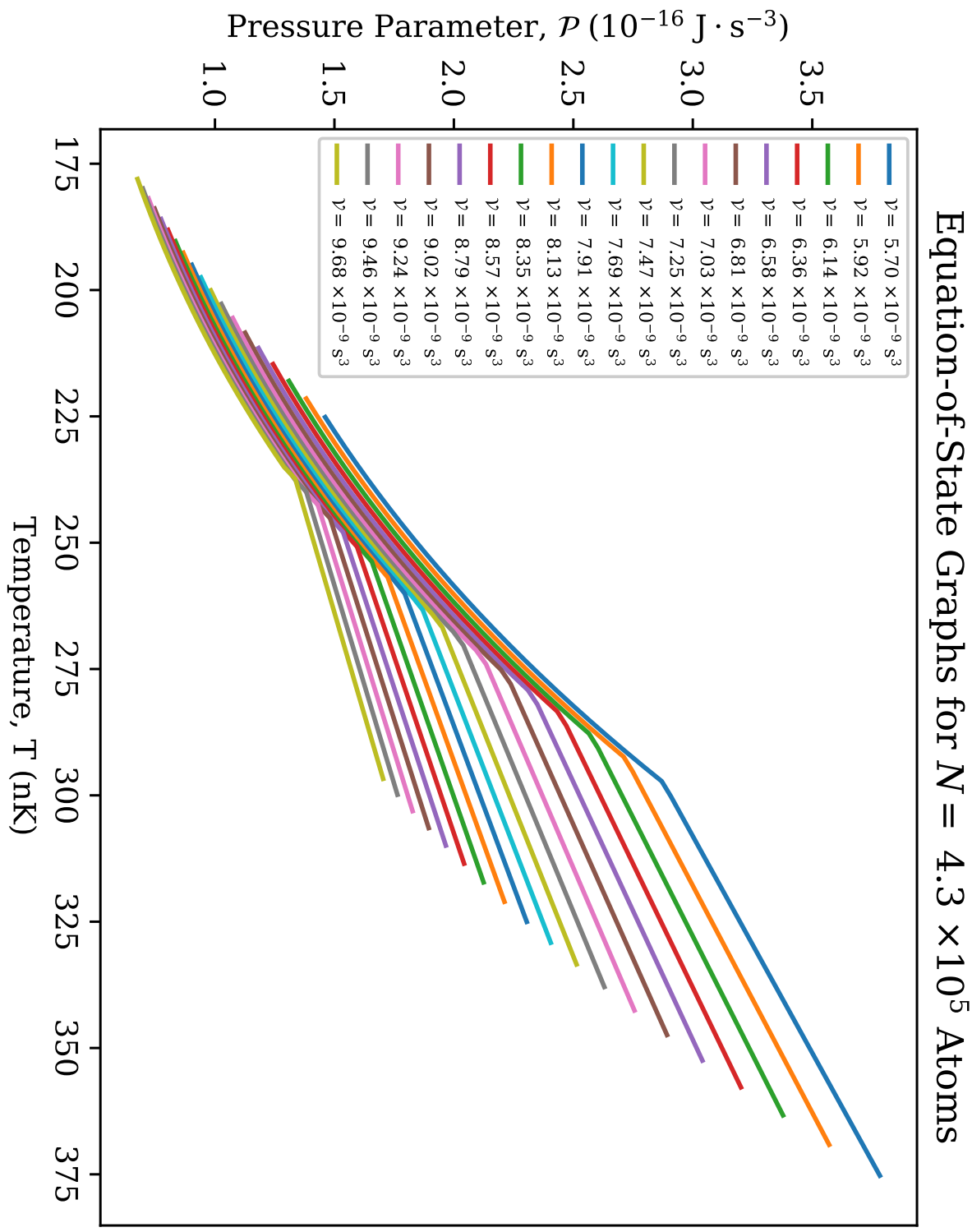

Figure 40 – Equation-of-State graphs generated with the fitted data for clouds of $N = 4.3 \times 10^5$ atoms.
Source: By the author.

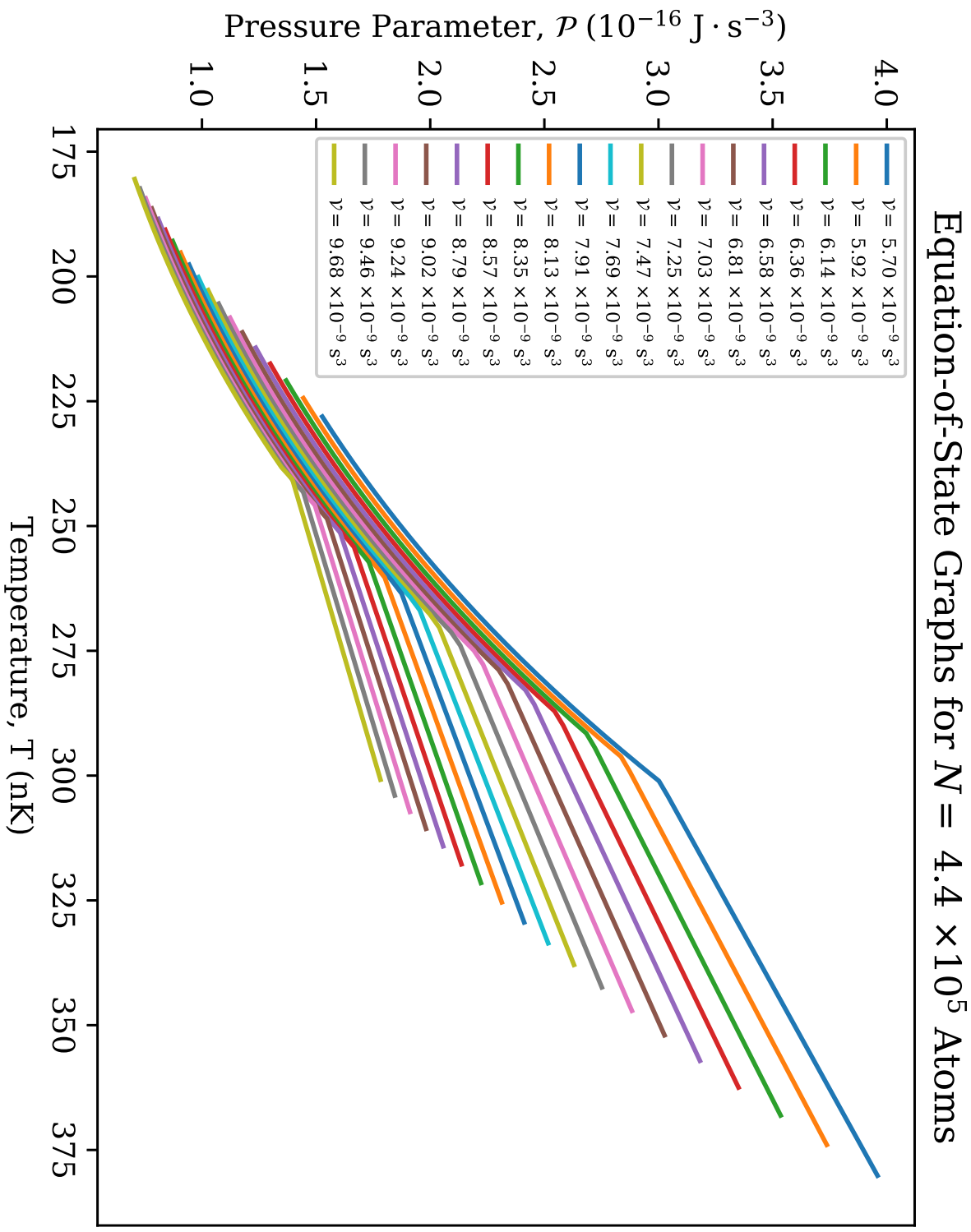

Figure 41 – Equation-of-State graphs generated with the fitted data for clouds of $N = 4.4 \times 10^5$ atoms.
Source: By the author.

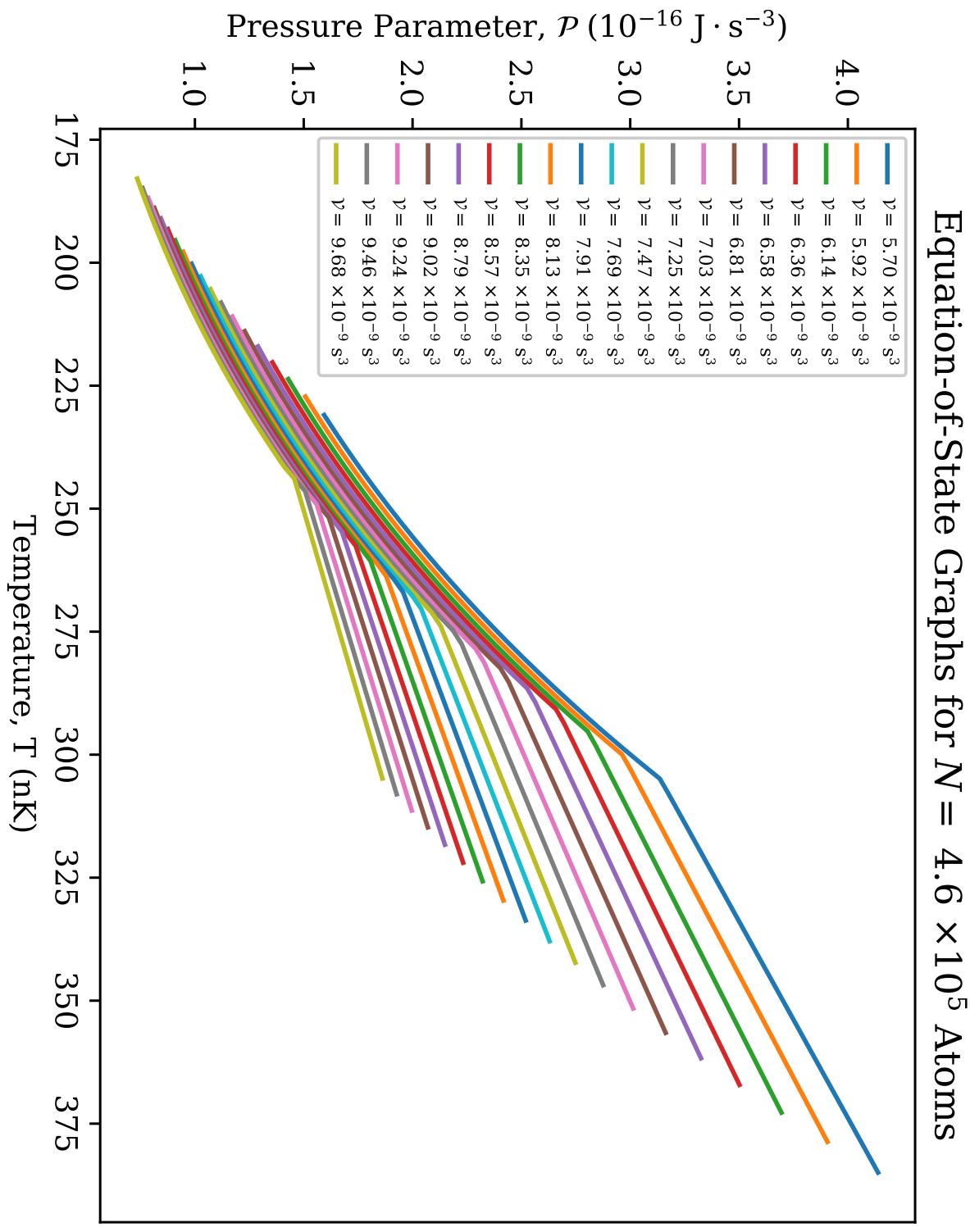

Figure 42 – Equation-of-State graphs generated with the fitted data for clouds of $N = 4.6 \times 10^5$ atoms.
Source: By the author.

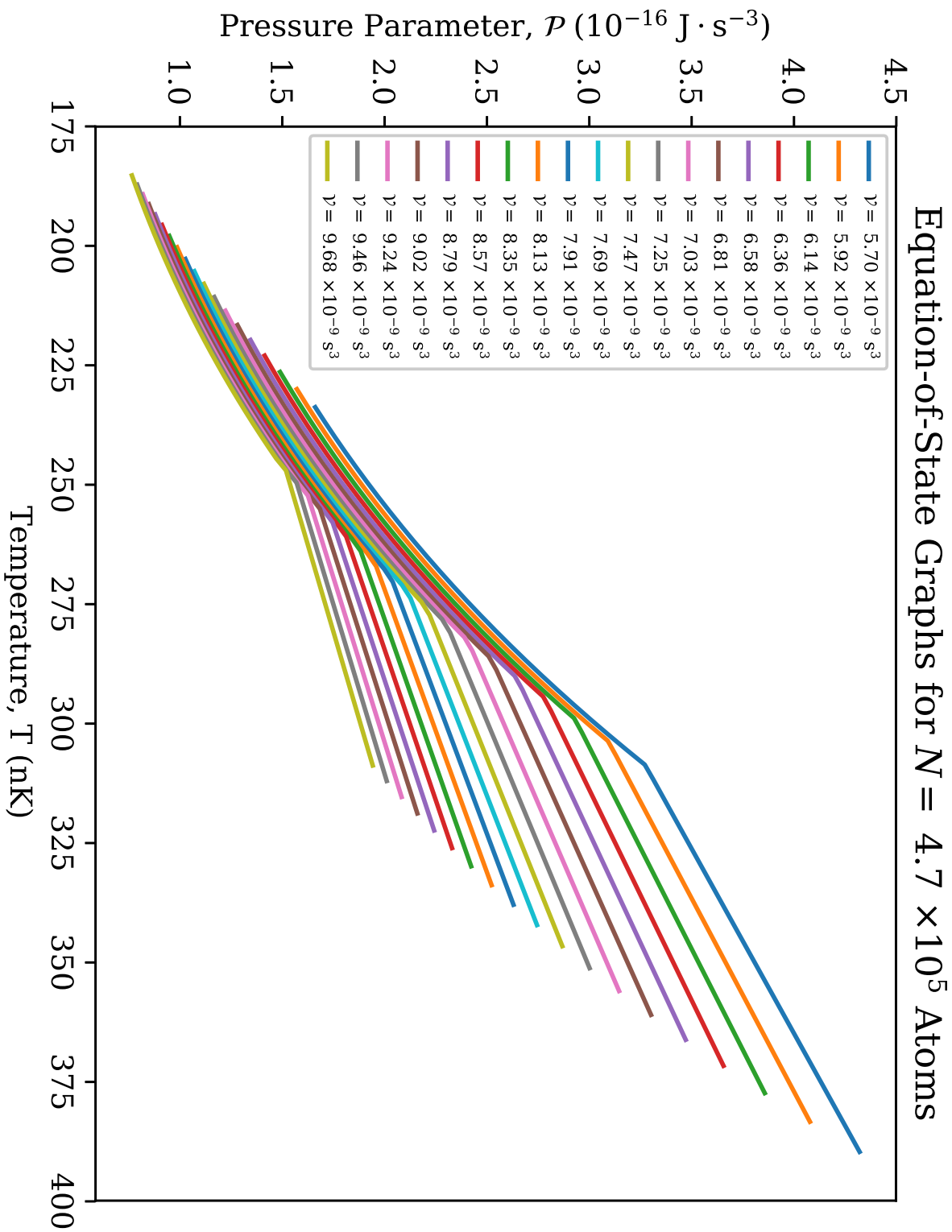

Figure 43 – Equation-of-State graphs generated with the fitted data for clouds of $N = 4.7 \times 10^5$ atoms.
Source: By the author.

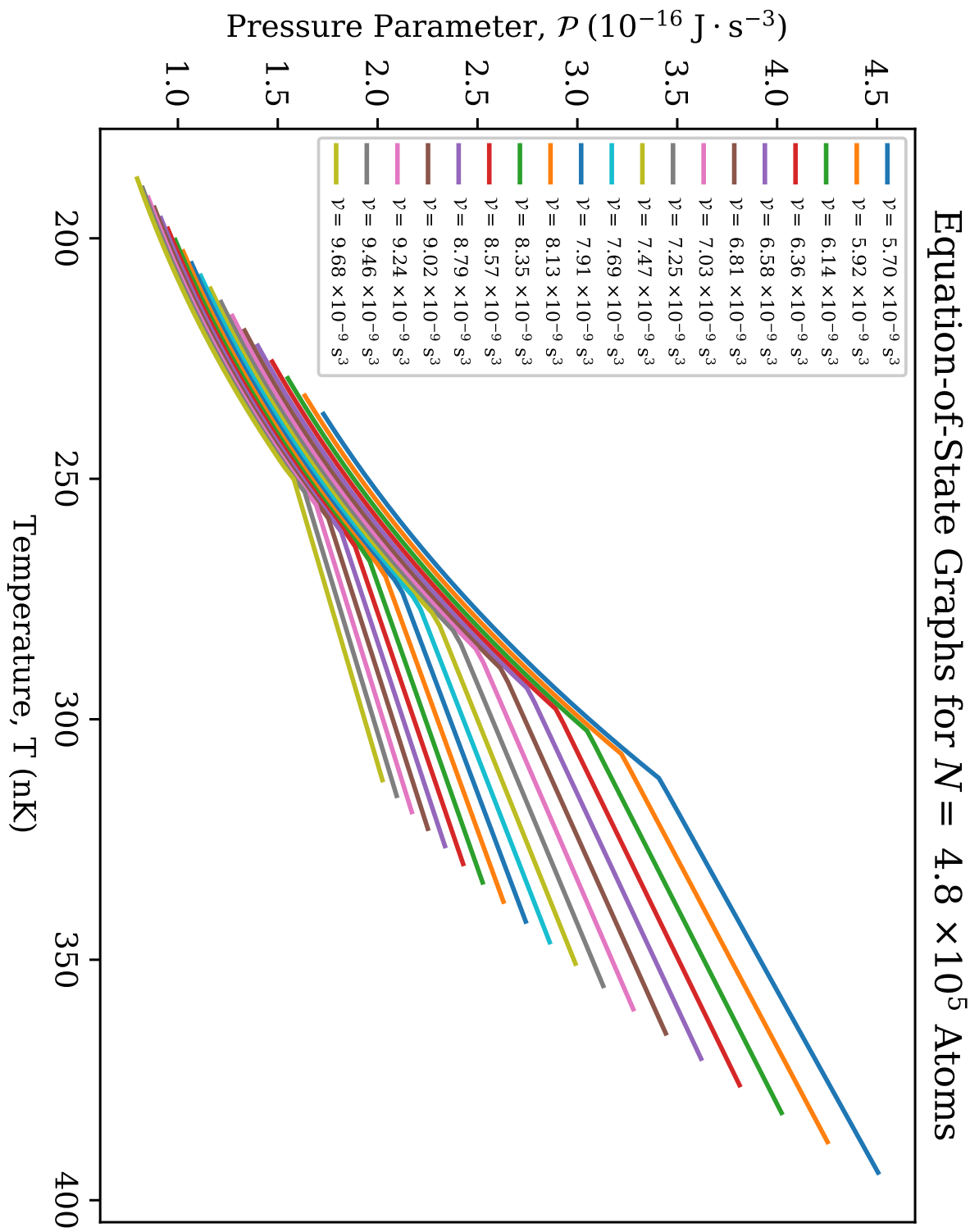

Figure 44 – Equation-of-State graphs generated with the fitted data for clouds of $N = 4.8 \times 10^5$ atoms.
Source: By the author.

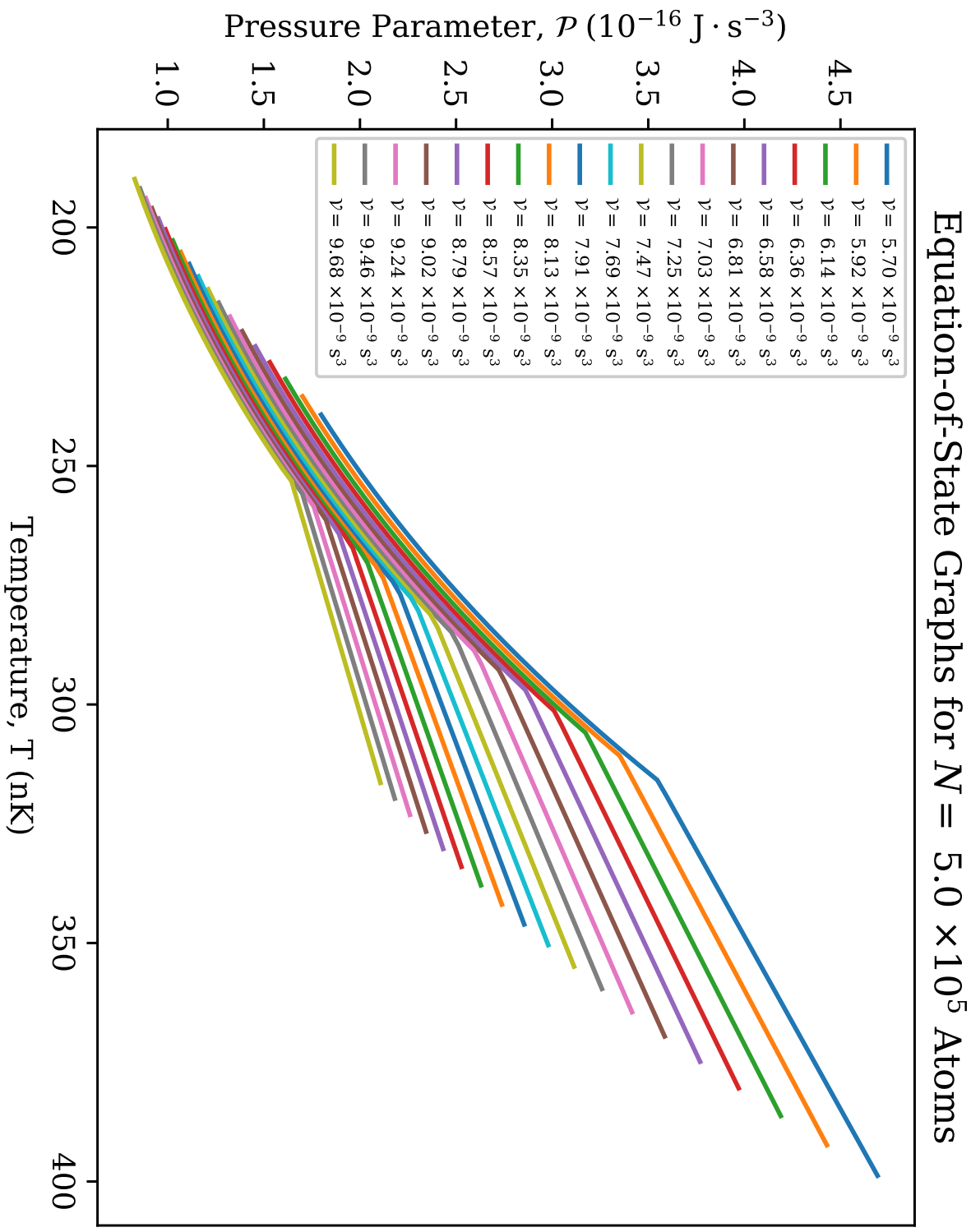

Figure 45 – Equation-of-State graphs generated with the fitted data for clouds of $N = 5.0 \times 10^5$ atoms.
Source: By the author.

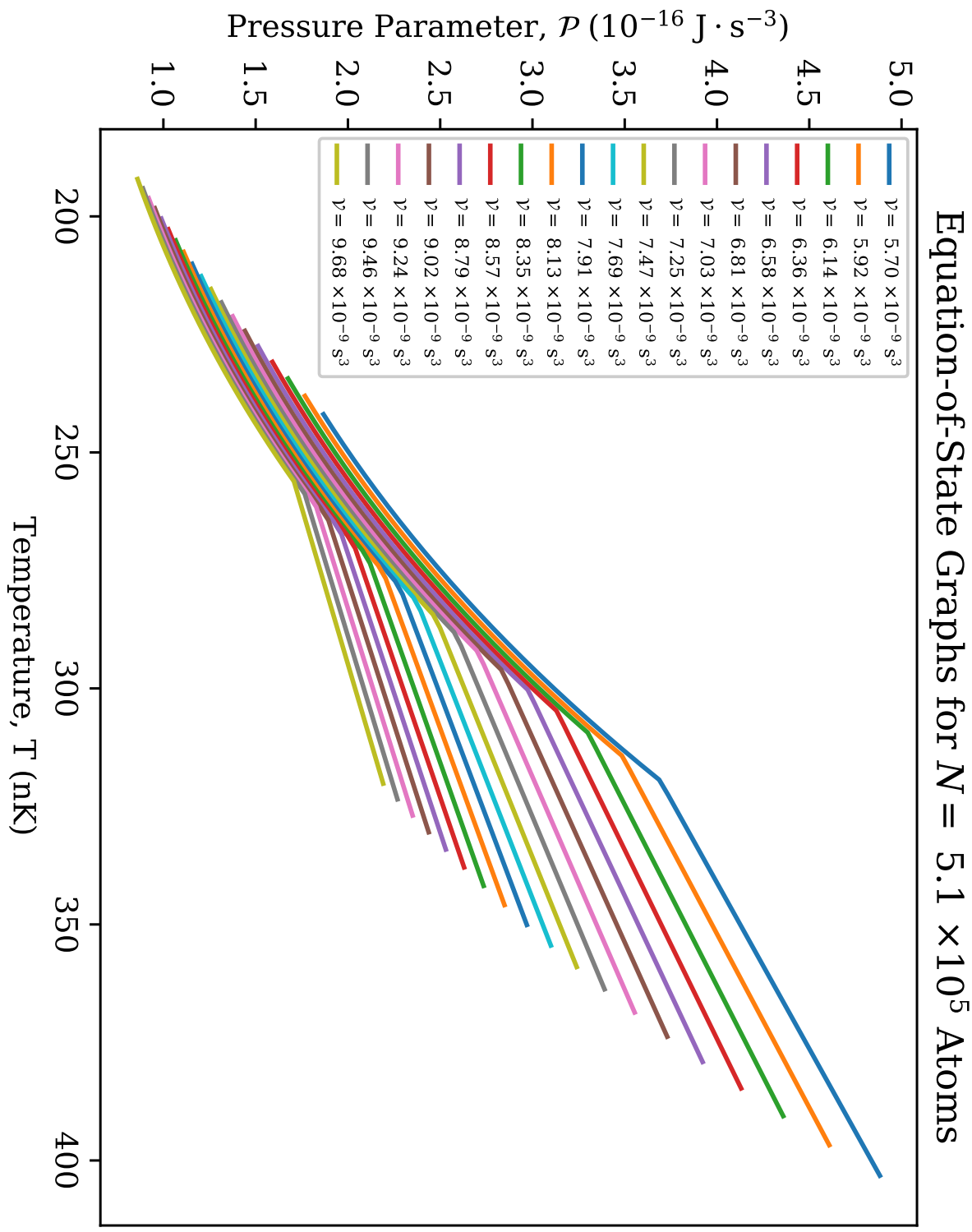

Figure 46 – Equation-of-State graphs generated with the fitted data for clouds of $N = 5.1 \times 10^5$ atoms.
Source: By the author.

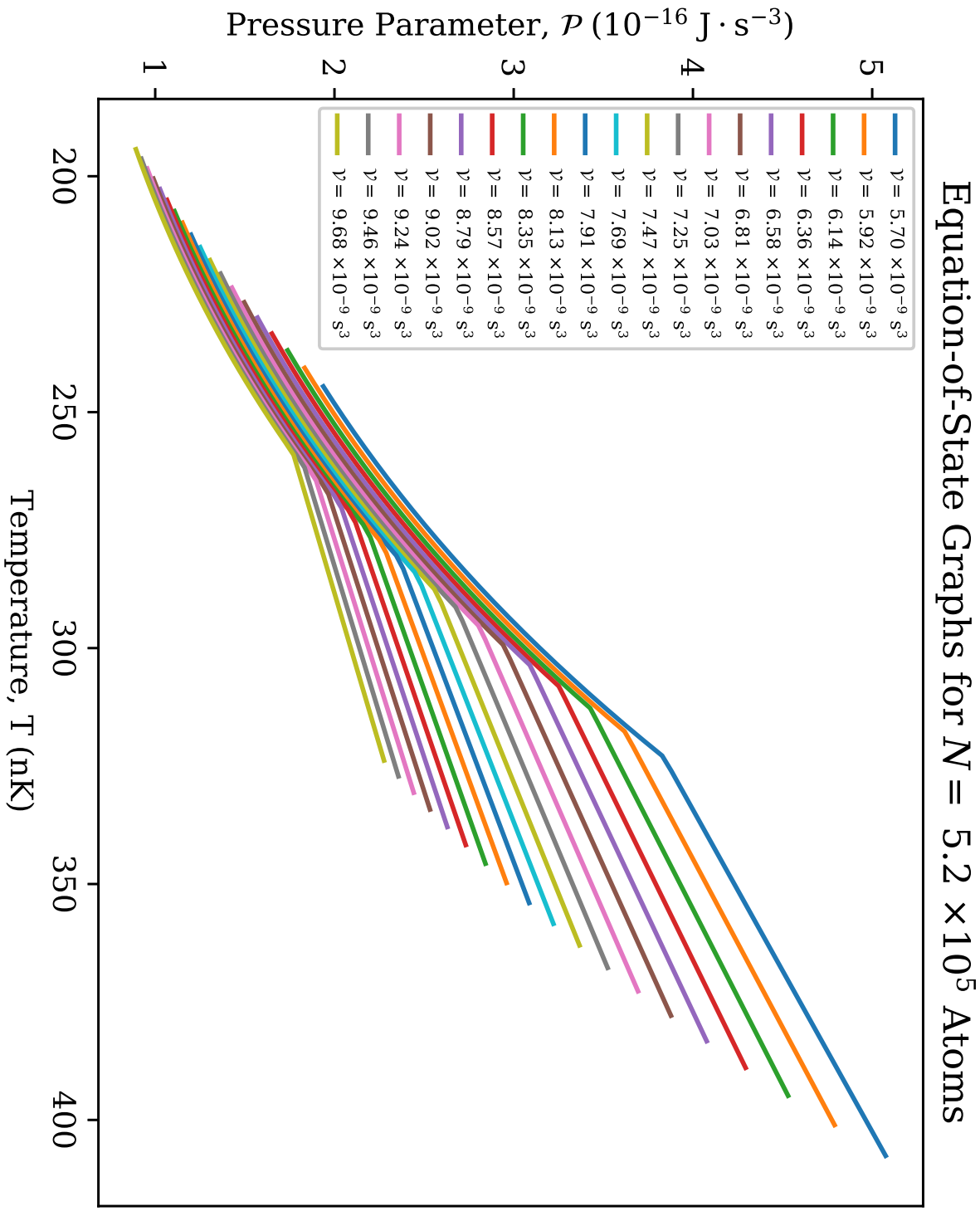

Figure 47 – Equation-of-State graphs generated with the fitted data for clouds of $N = 5.2 \times 10^5$ atoms.
Source: By the author.

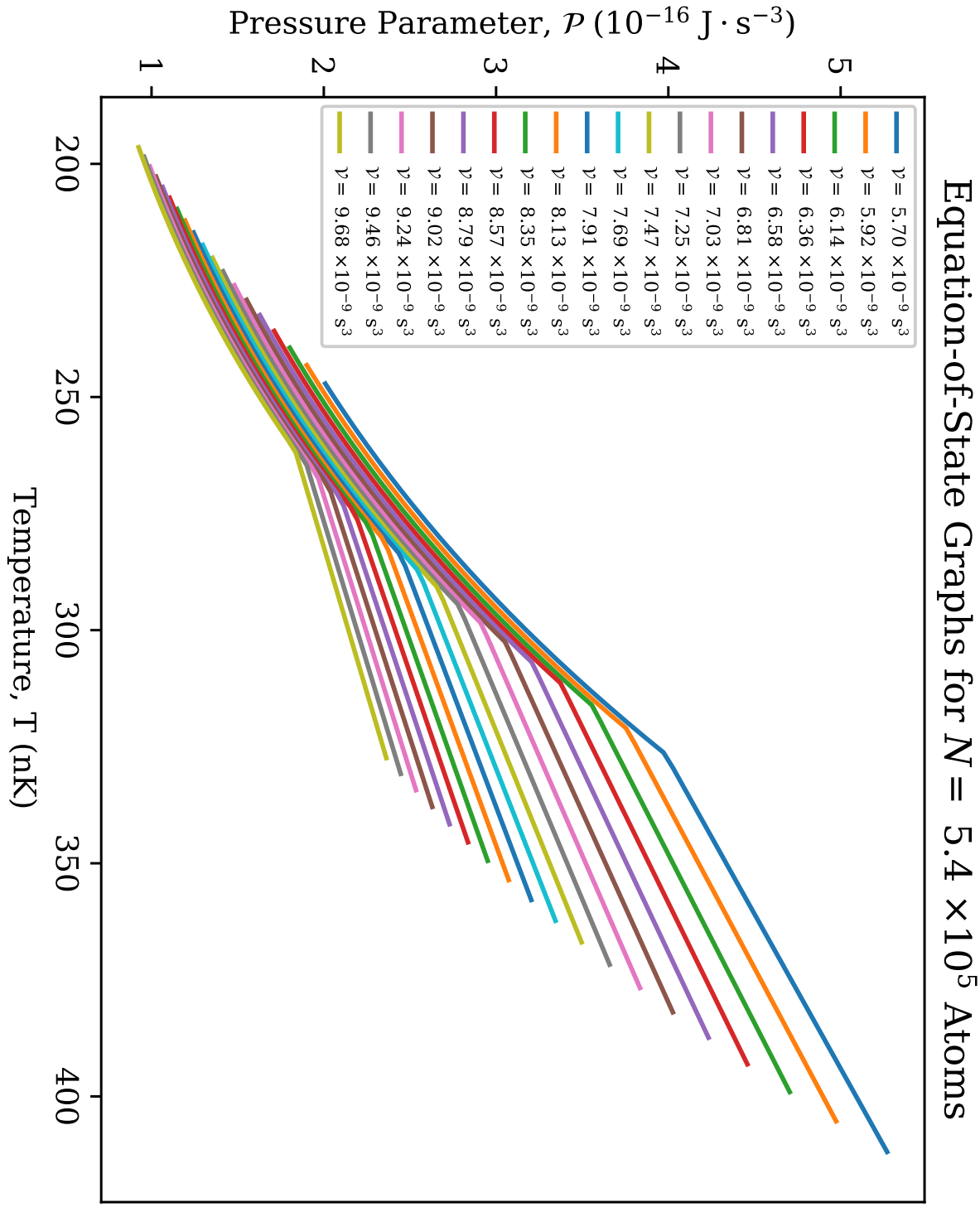

Figure 48 – Equation-of-State graphs generated with the fitted data for clouds of $N = 5.4 \times 10^5$ atoms.
Source: By the author.

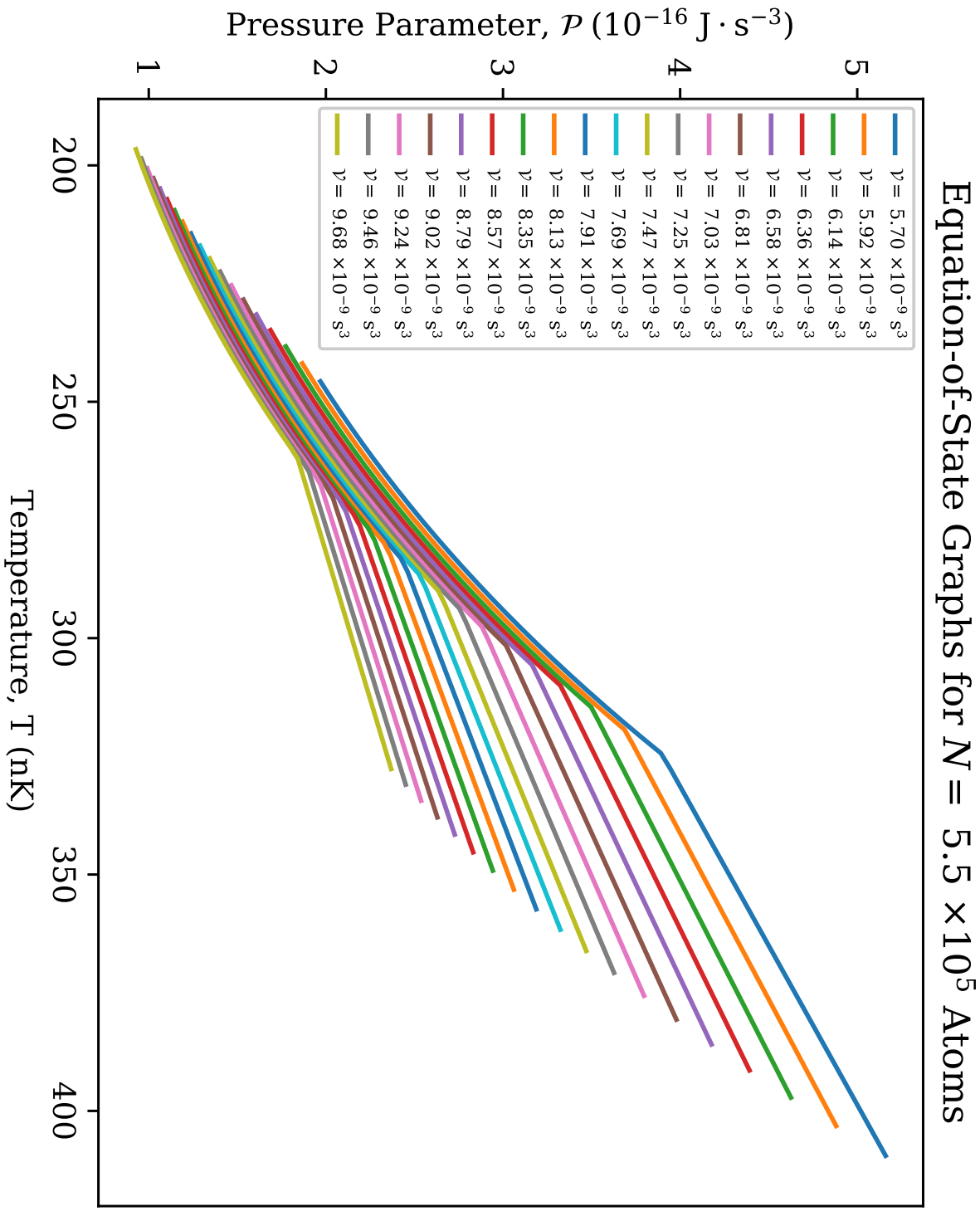

Figure 49 – Equation-of-State graphs generated with the fitted data for clouds of $N = 5.5 \times 10^5$ atoms.
Source: By the author.

APPENDIX E – HEAT-CAPACITY DIAGRAMS

The complete set of heat-capacity graphs mentioned in Sec. 6.3 are shown here.

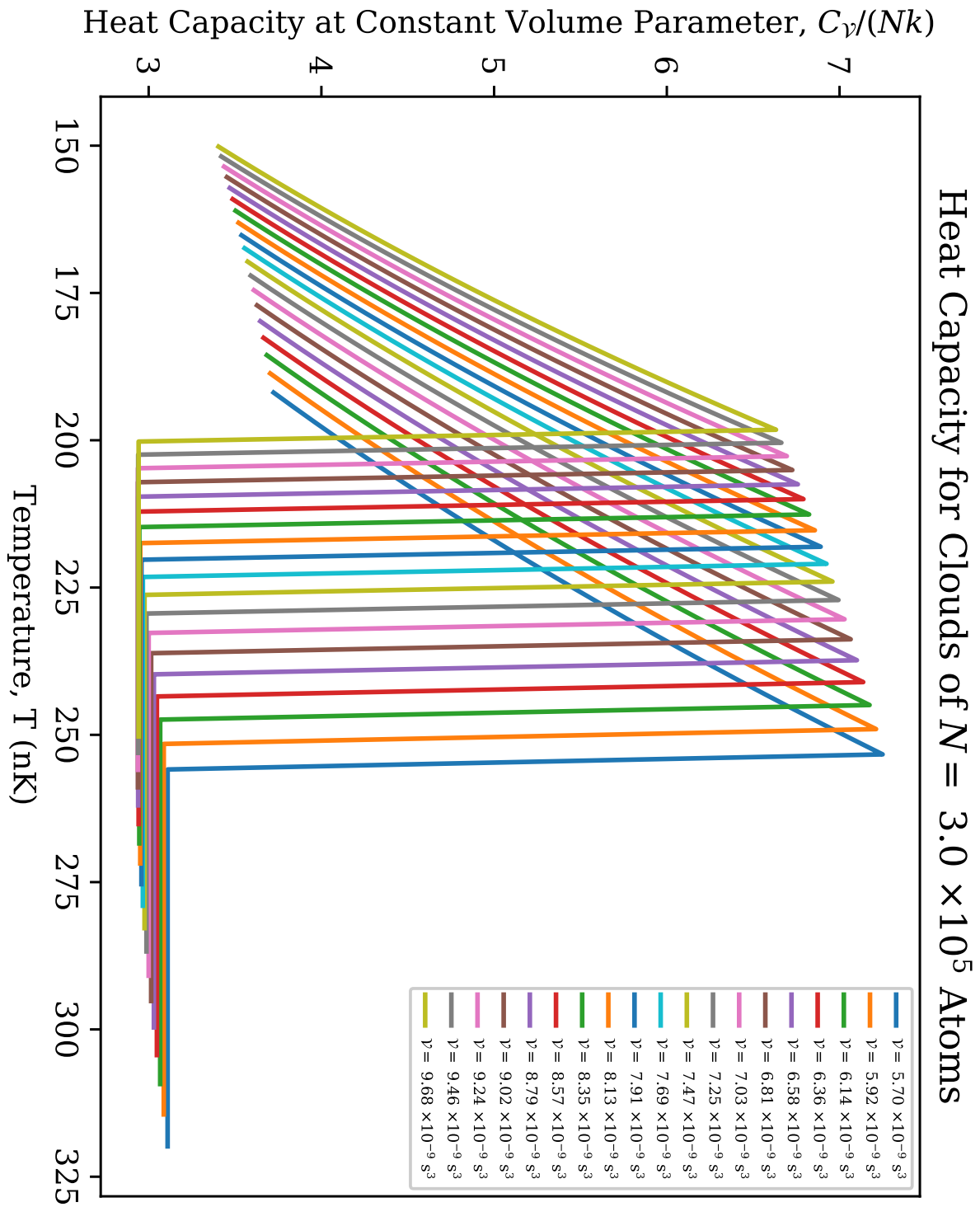

Figure 50 – Plots of the heat capacity at constant volume parameter $C_\mathcal{V}$ for clouds of $N = 3.0 \times 10^5$ atoms.
Source: By the author.

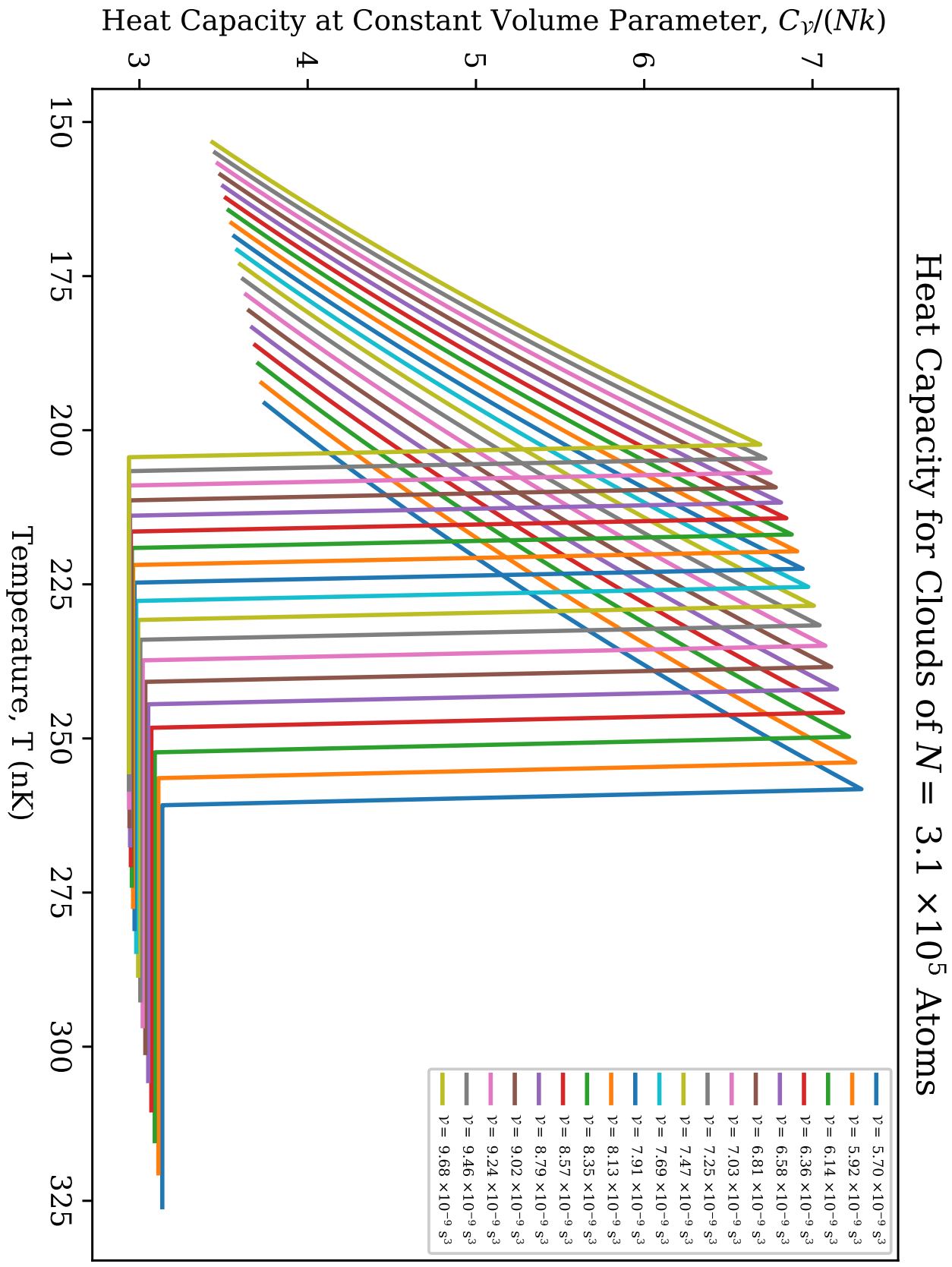

Figure 51 – Plots of the heat capacity at constant volume parameter C_ν for clouds of $N = 3.1 \times 10^5$ atoms.
Source: By the author.

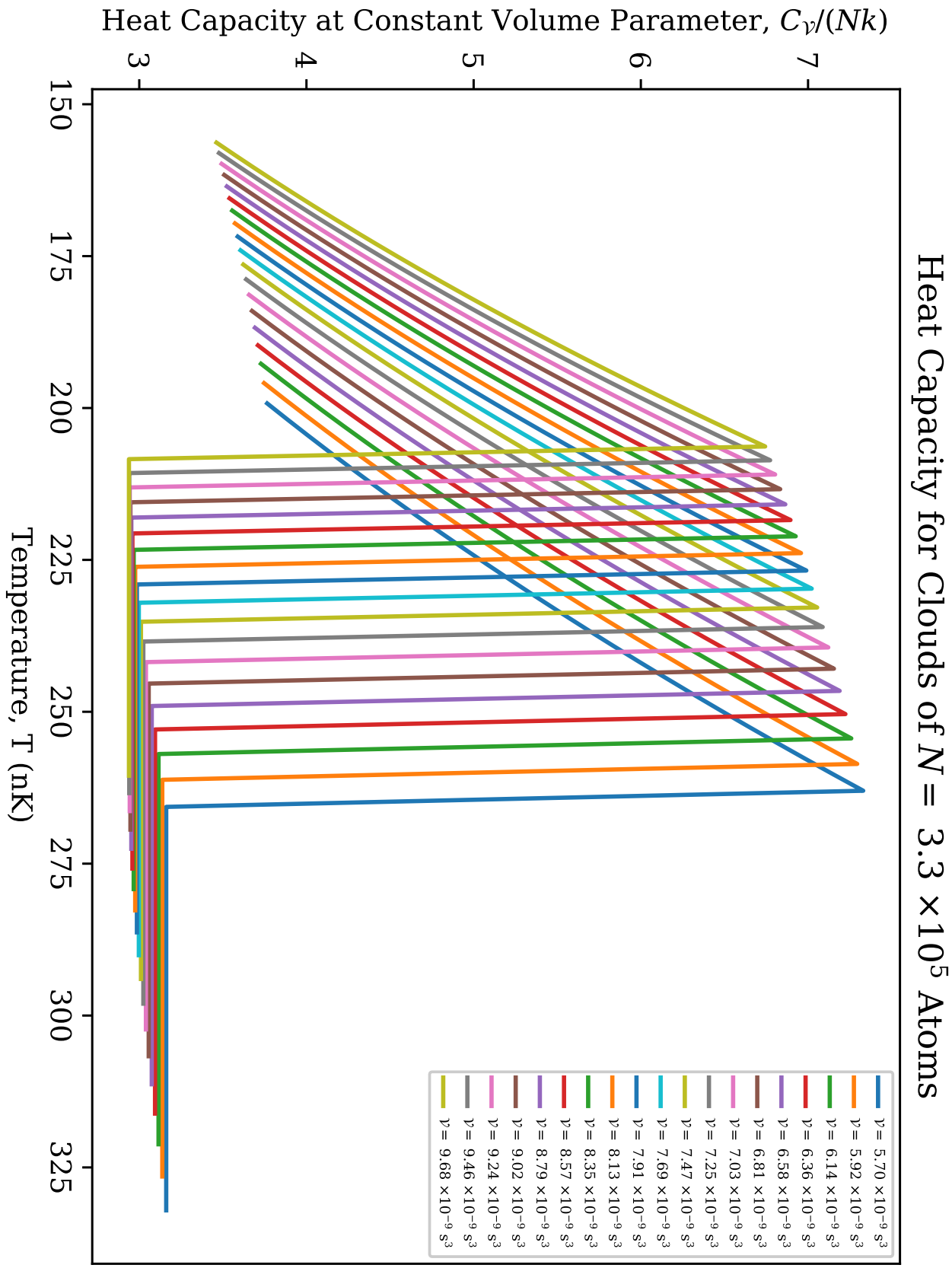

Figure 52 – Plots of the heat capacity at constant volume parameter $C_\mathcal{V}$ for clouds of $N = 3.3 \times 10^5$ atoms.
Source: By the author.

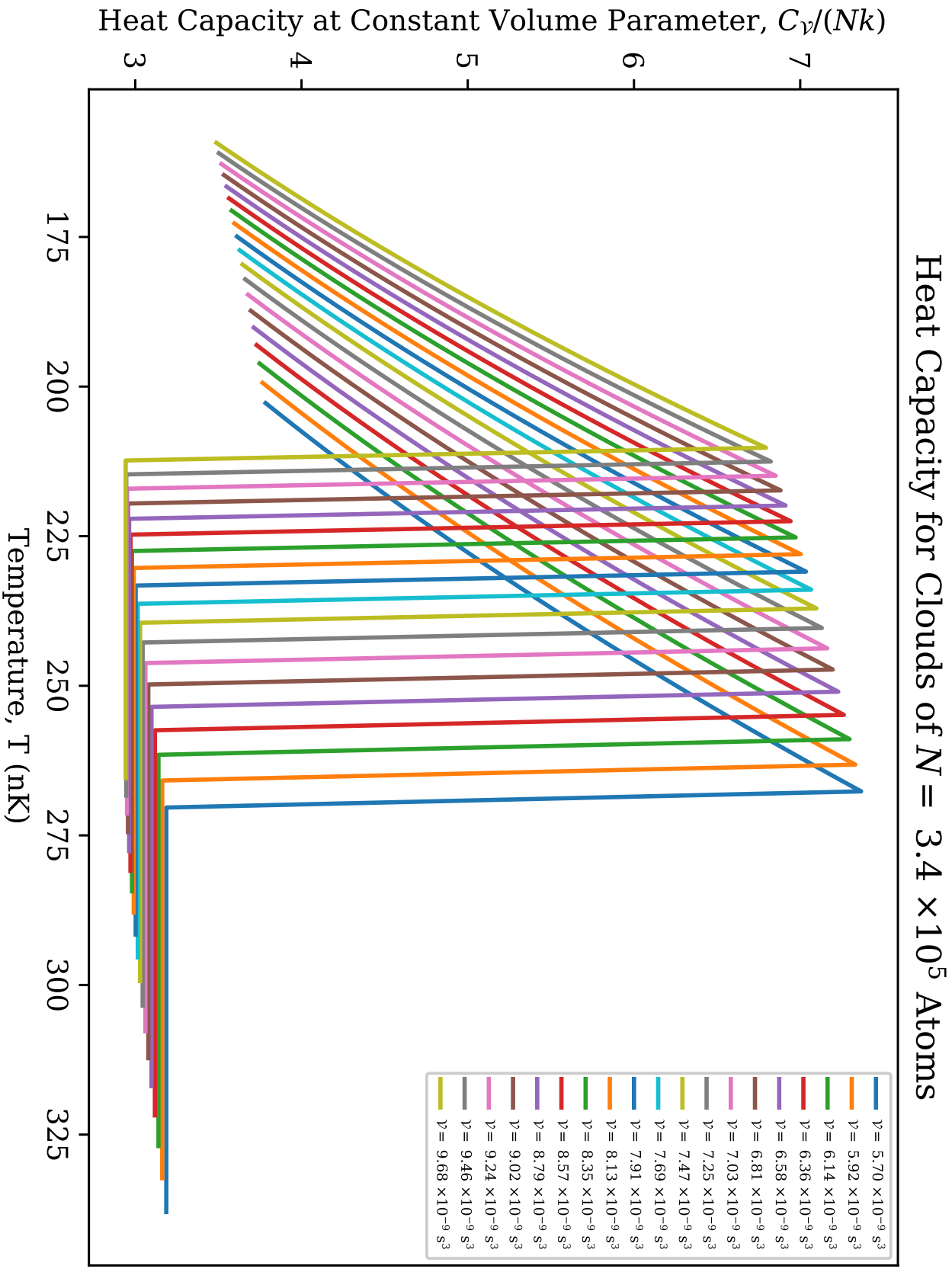

Figure 53 – Plots of the heat capacity at constant volume parameter C_ν for clouds of $N = 3.4 \times 10^5$ atoms.
Source: By the author.

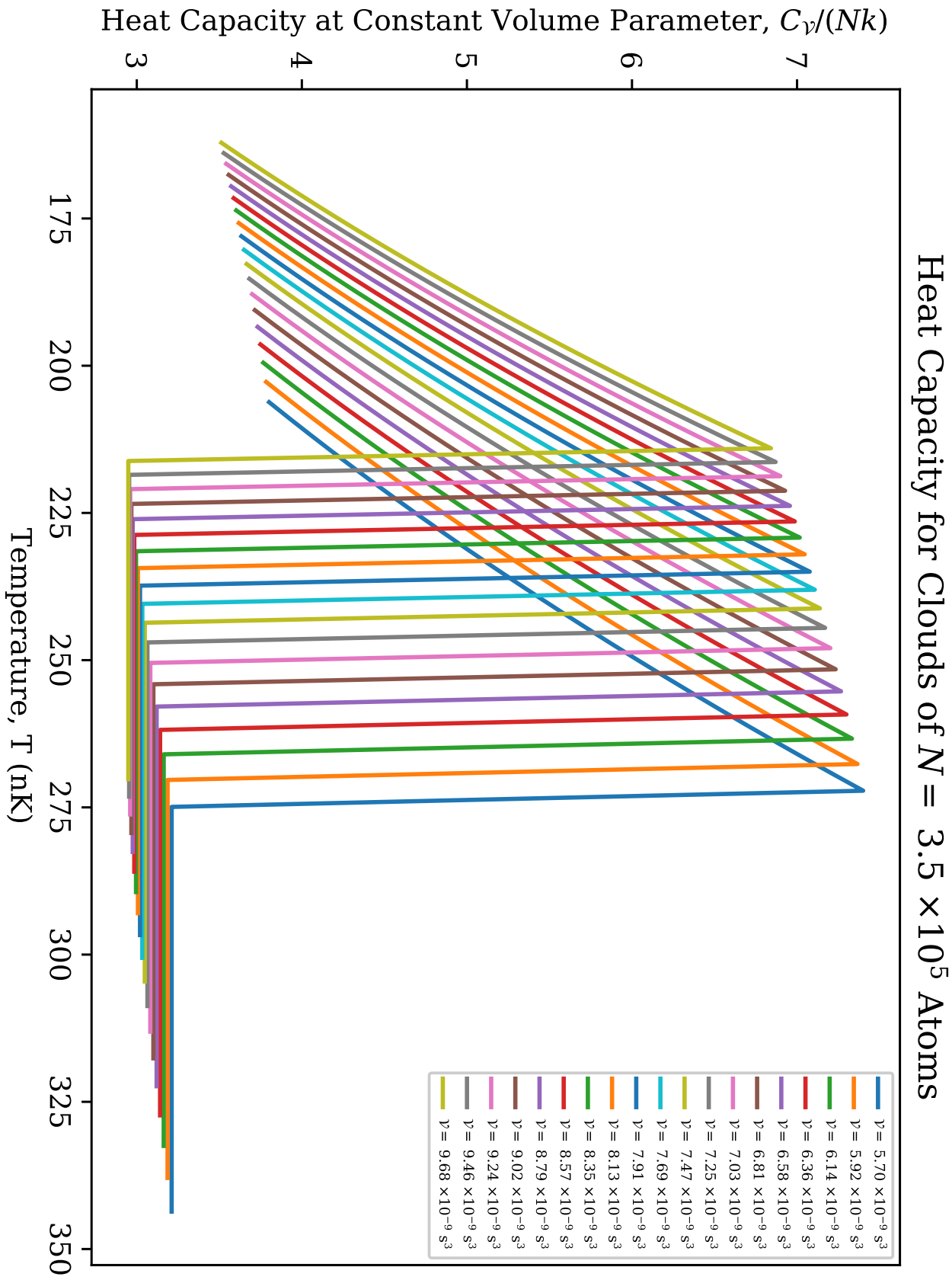

Figure 54 – Plots of the heat capacity at constant volume parameter $C_\mathcal{V}$ for clouds of $N = 3.5 \times 10^5$ atoms.
Source: By the author.

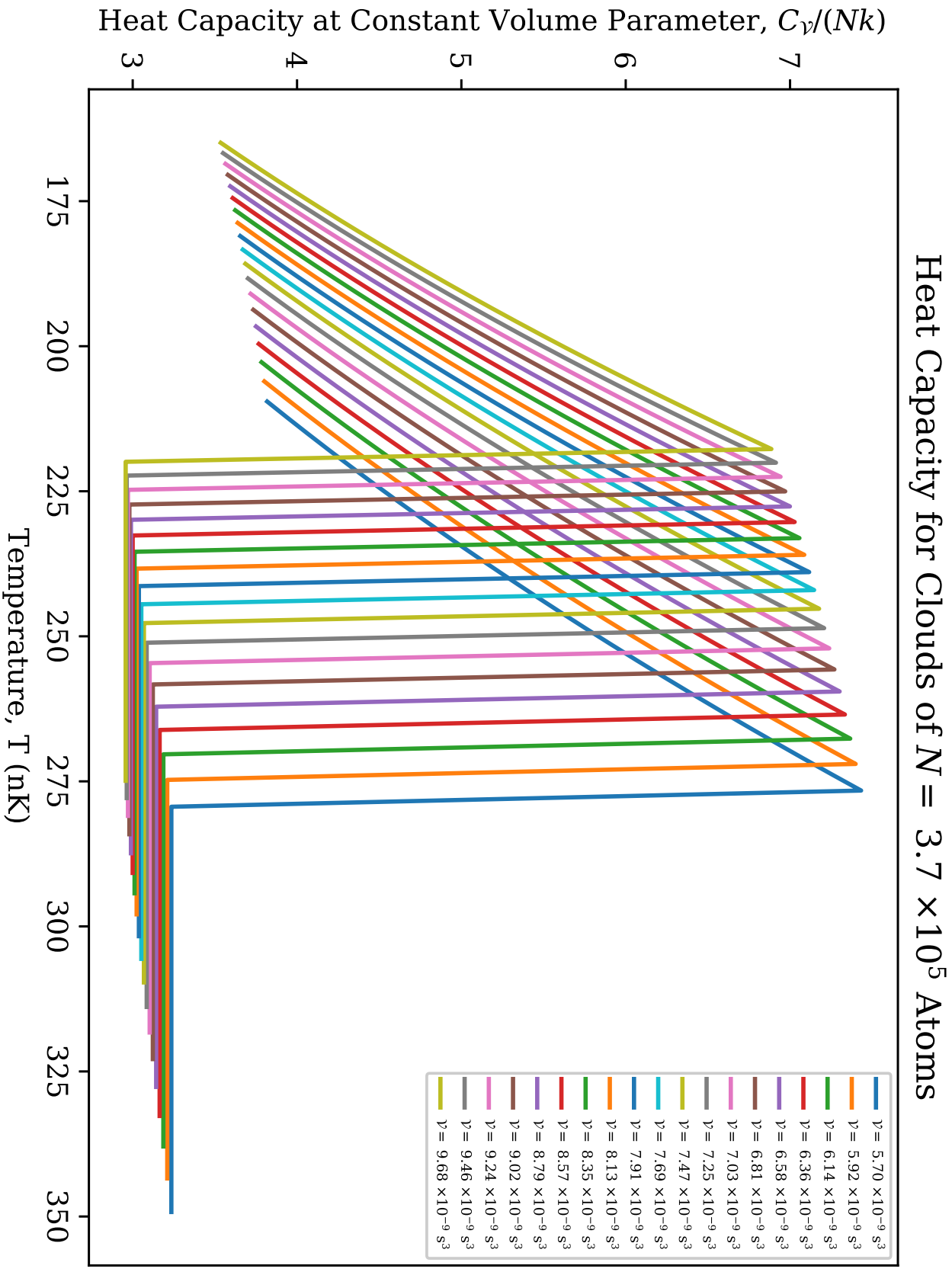

Figure 55 – Plots of the heat capacity at constant volume parameter C_ν for clouds of $N = 3.7 \times 10^5$ atoms.
Source: By the author.

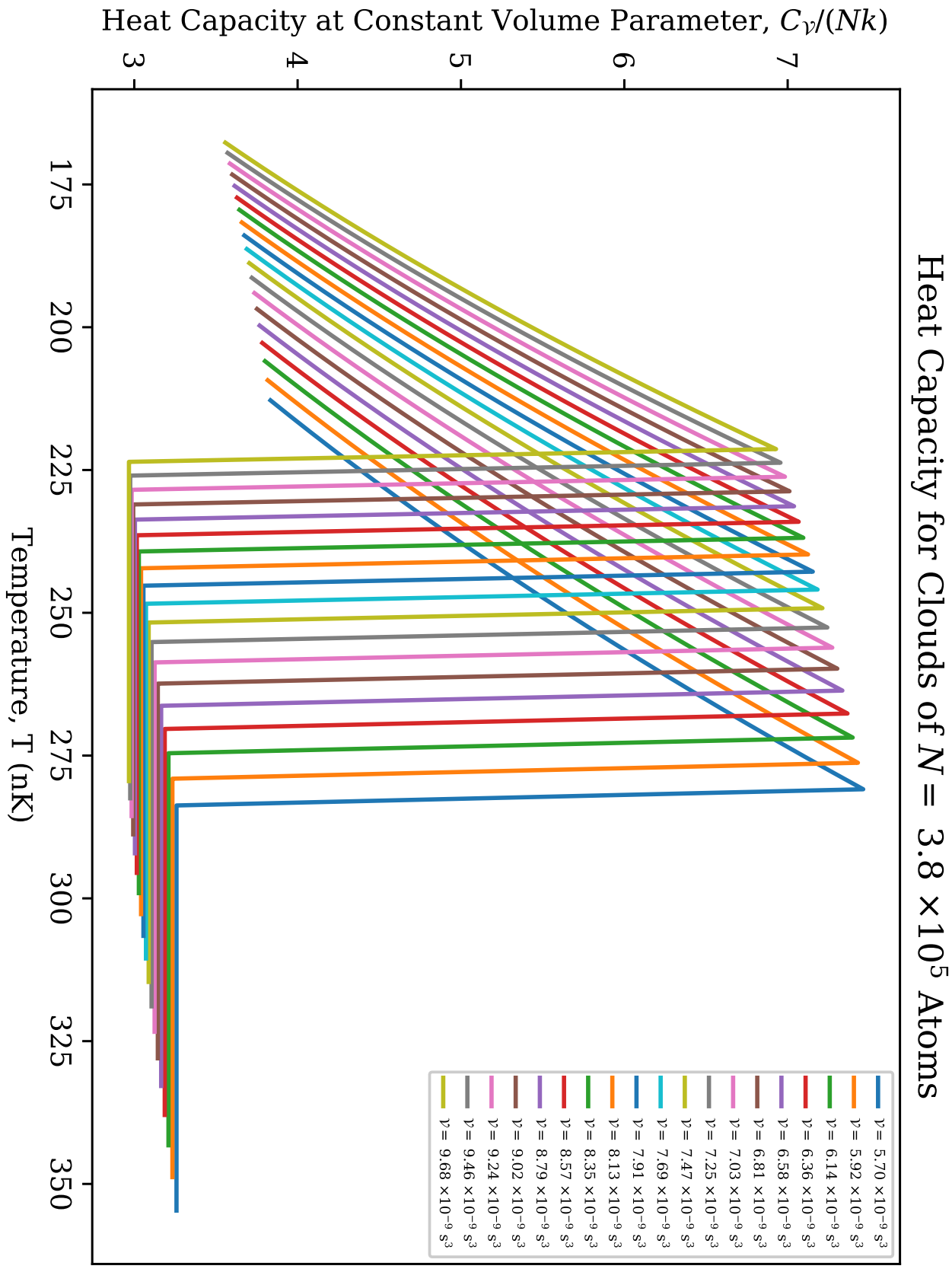

Figure 56 – Plots of the heat capacity at constant volume parameter $C_\mathcal{V}$ for clouds of $N = 3.8 \times 10^5$ atoms.
Source: By the author.

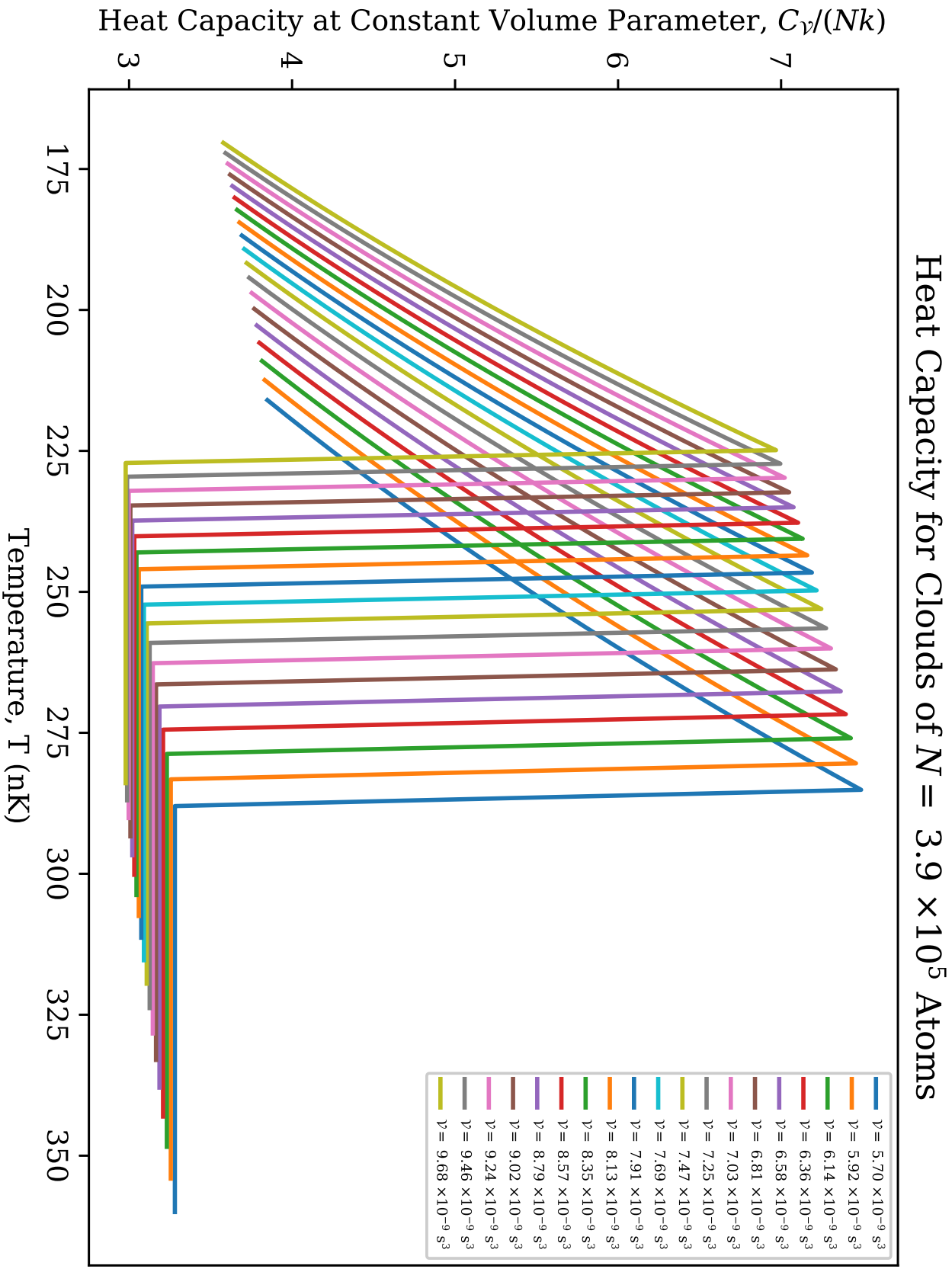

Figure 57 – Plots of the heat capacity at constant volume parameter C_ν for clouds of $N = 3.9 \times 10^5$ atoms.
Source: By the author.

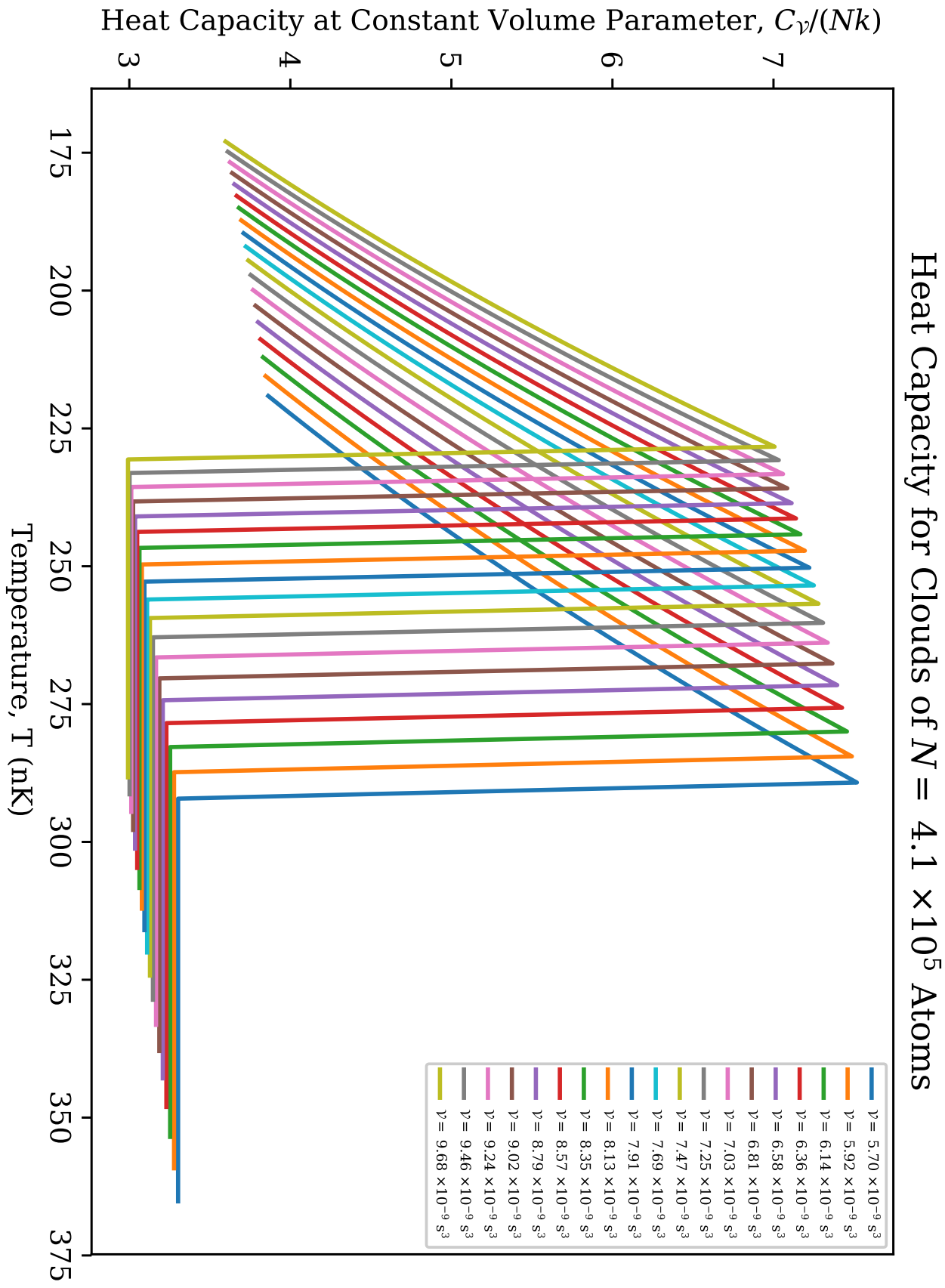

Figure 58 – Plots of the heat capacity at constant volume parameter $C_\mathcal{V}$ for clouds of $N = 4.1 \times 10^5$ atoms.
Source: By the author.

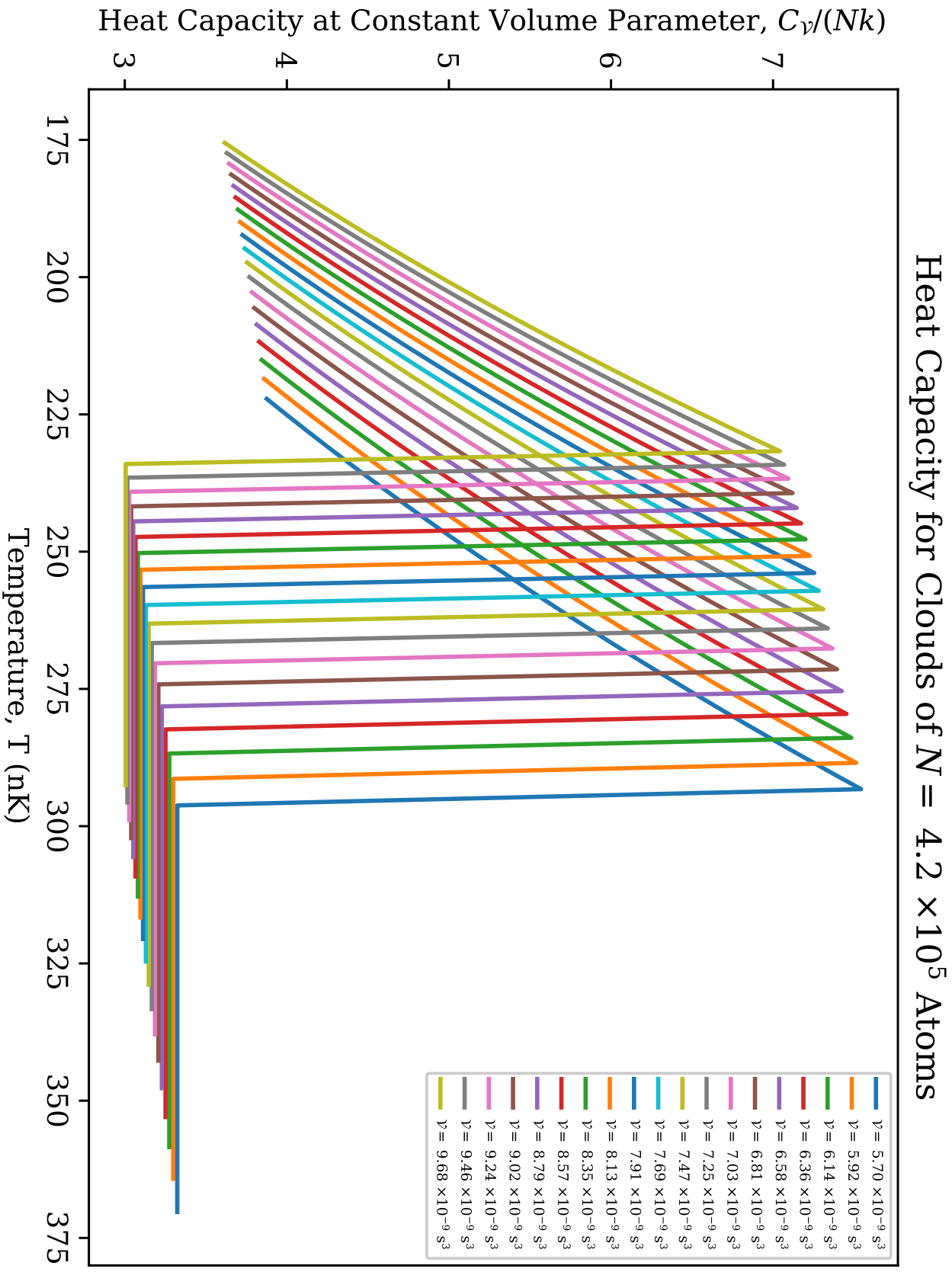

Figure 59 – Plots of the heat capacity at constant volume parameter C_ν for clouds of $N = 4.2 \times 10^5$ atoms.
Source: By the author.

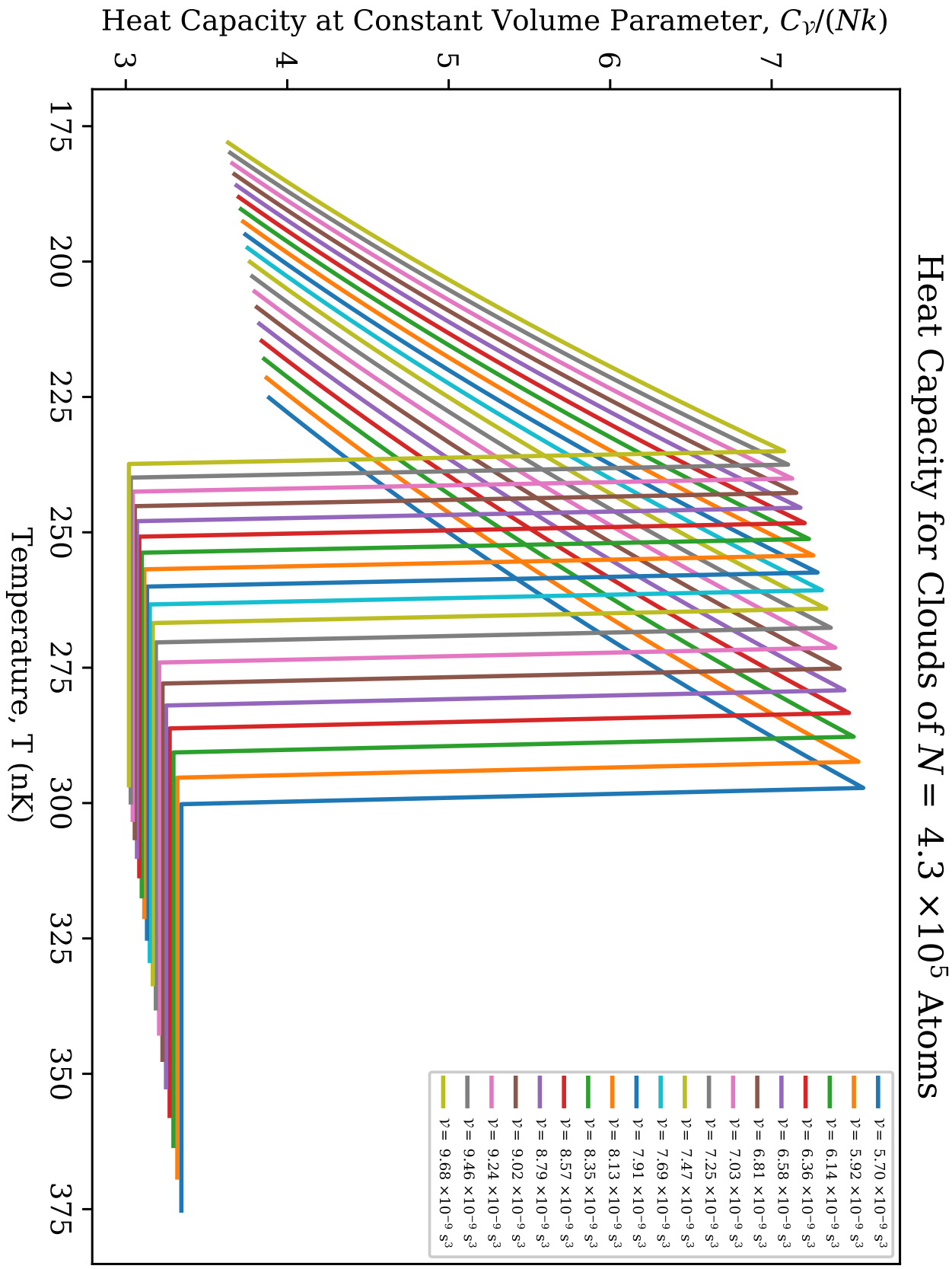

Figure 60 – Plots of the heat capacity at constant volume parameter $C_\mathcal{V}$ for clouds of $N = 4.3 \times 10^5$ atoms.
Source: By the author.

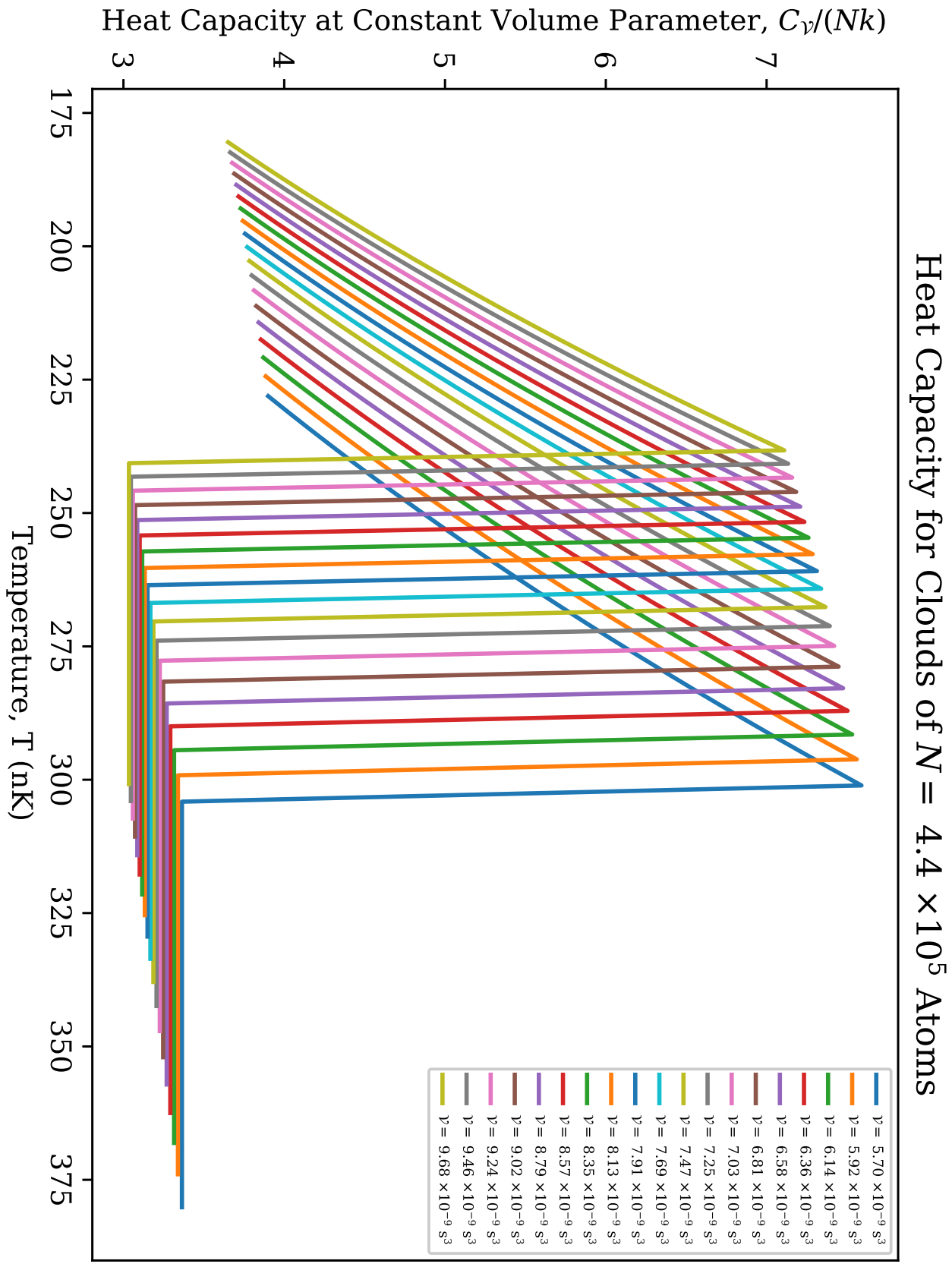

Figure 61 – Plots of the heat capacity at constant volume parameter C_ν for clouds of $N = 4.4 \times 10^5$ atoms.
Source: By the author.

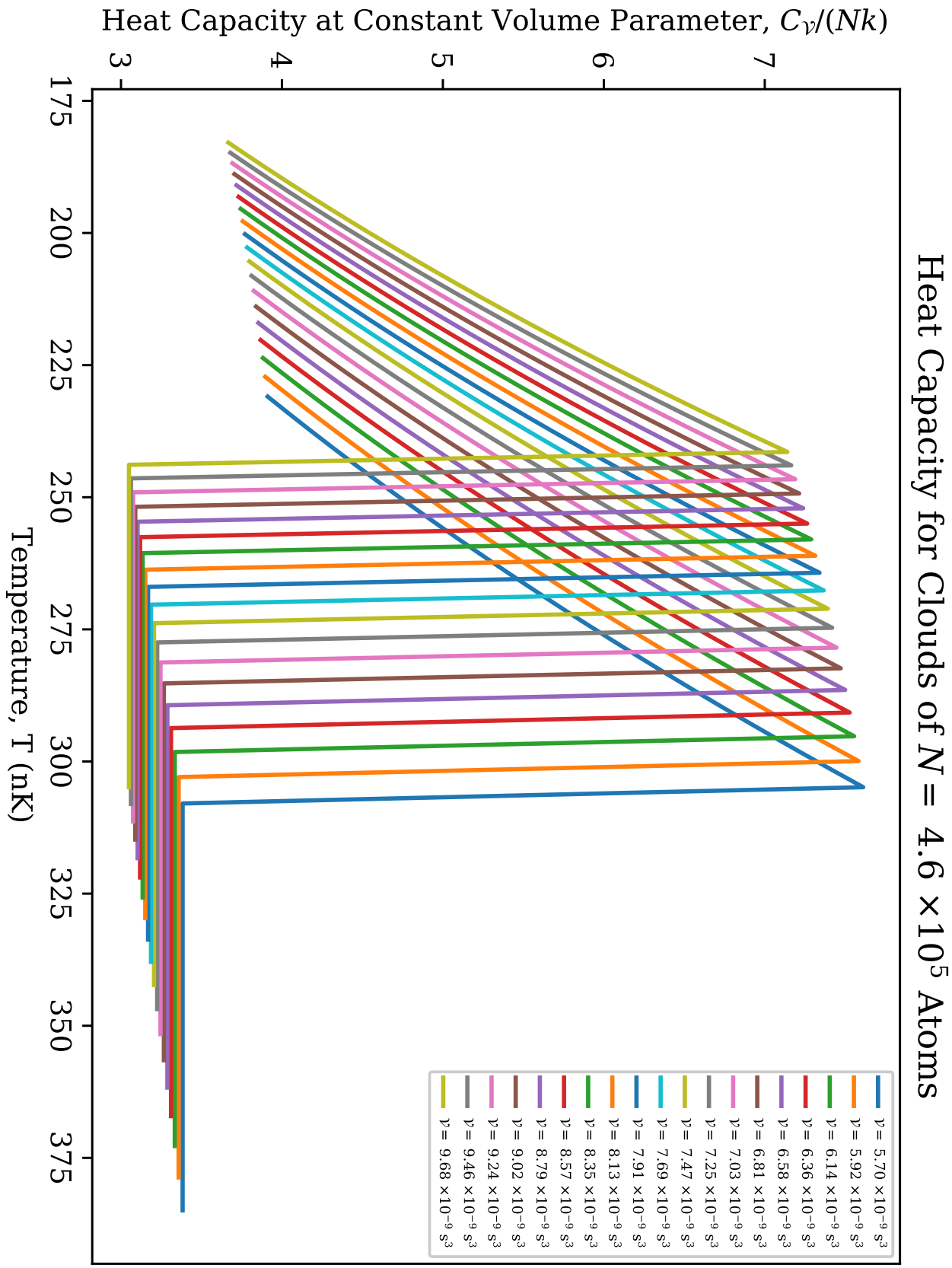

Figure 62 – Plots of the heat capacity at constant volume parameter $C_\mathcal{V}$ for clouds of $N = 4.6 \times 10^5$ atoms.
Source: By the author.

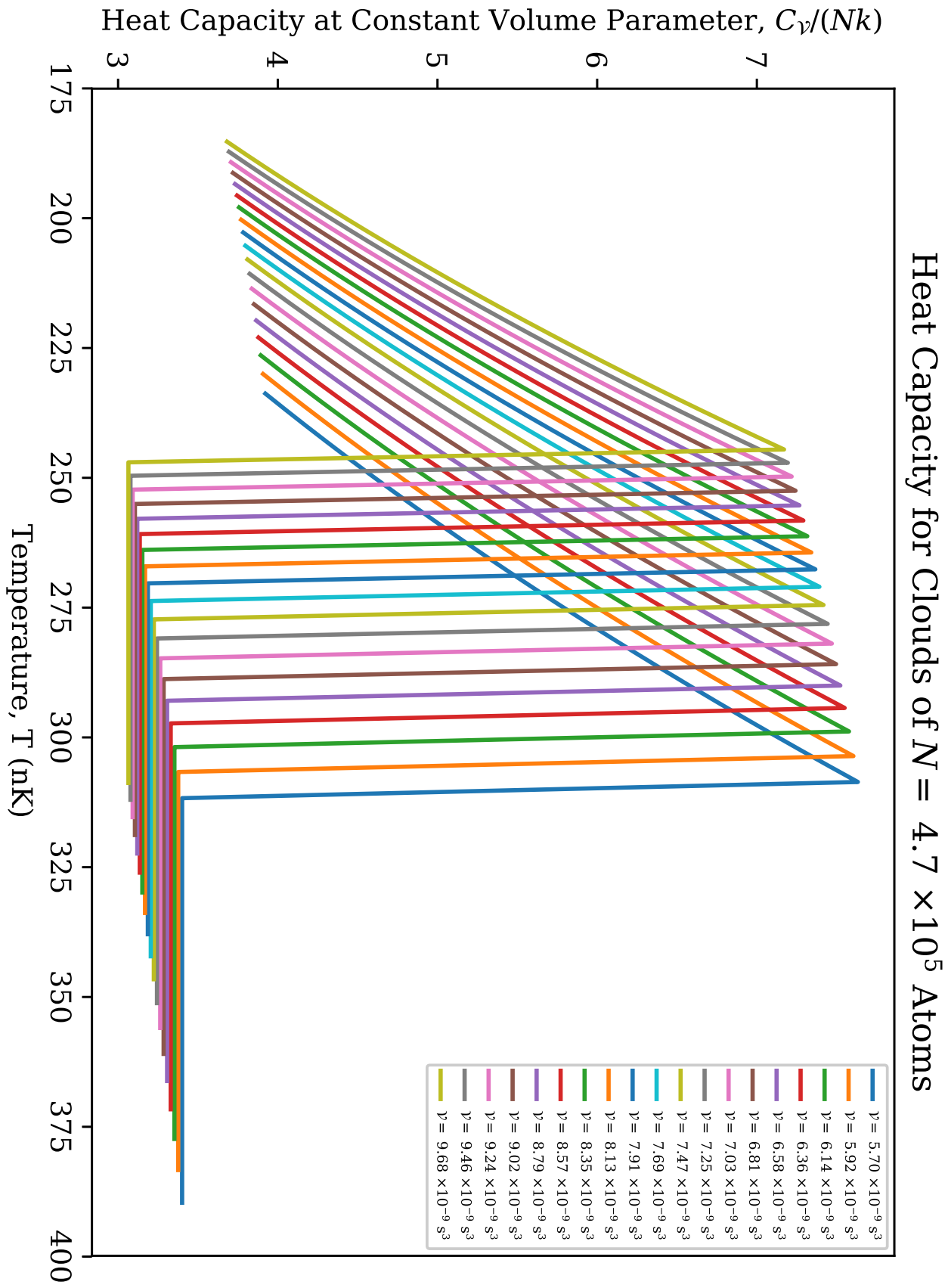

Figure 63 – Plots of the heat capacity at constant volume parameter C_ν for clouds of $N = 4.7 \times 10^5$ atoms.
Source: By the author.

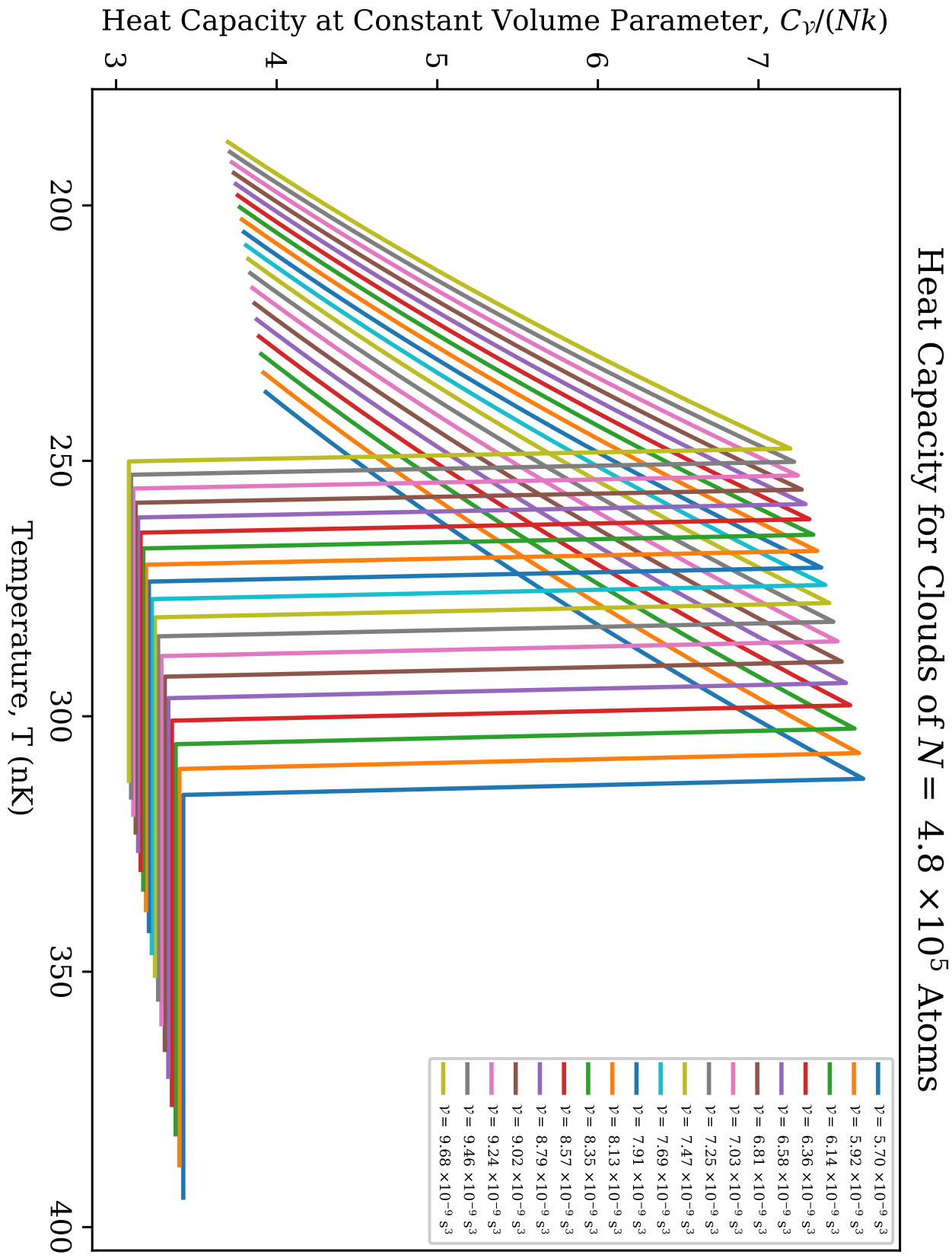

Figure 64 – Plots of the heat capacity at constant volume parameter C_ν for clouds of $N = 4.8 \times 10^5$ atoms.
Source: By the author.

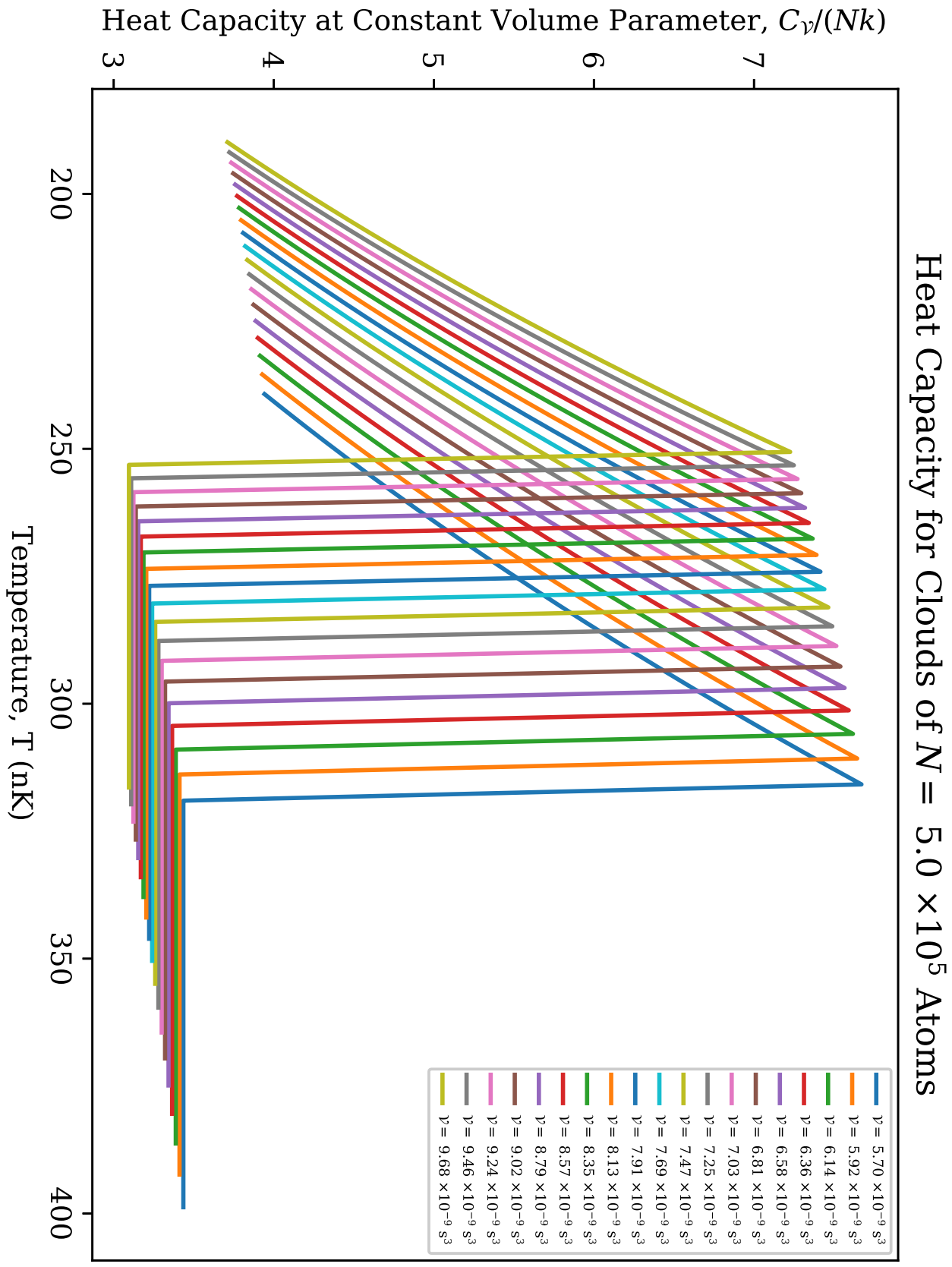

Figure 65 – Plots of the heat capacity at constant volume parameter C_ν for clouds of $N = 5.0 \times 10^5$ atoms.
Source: By the author.

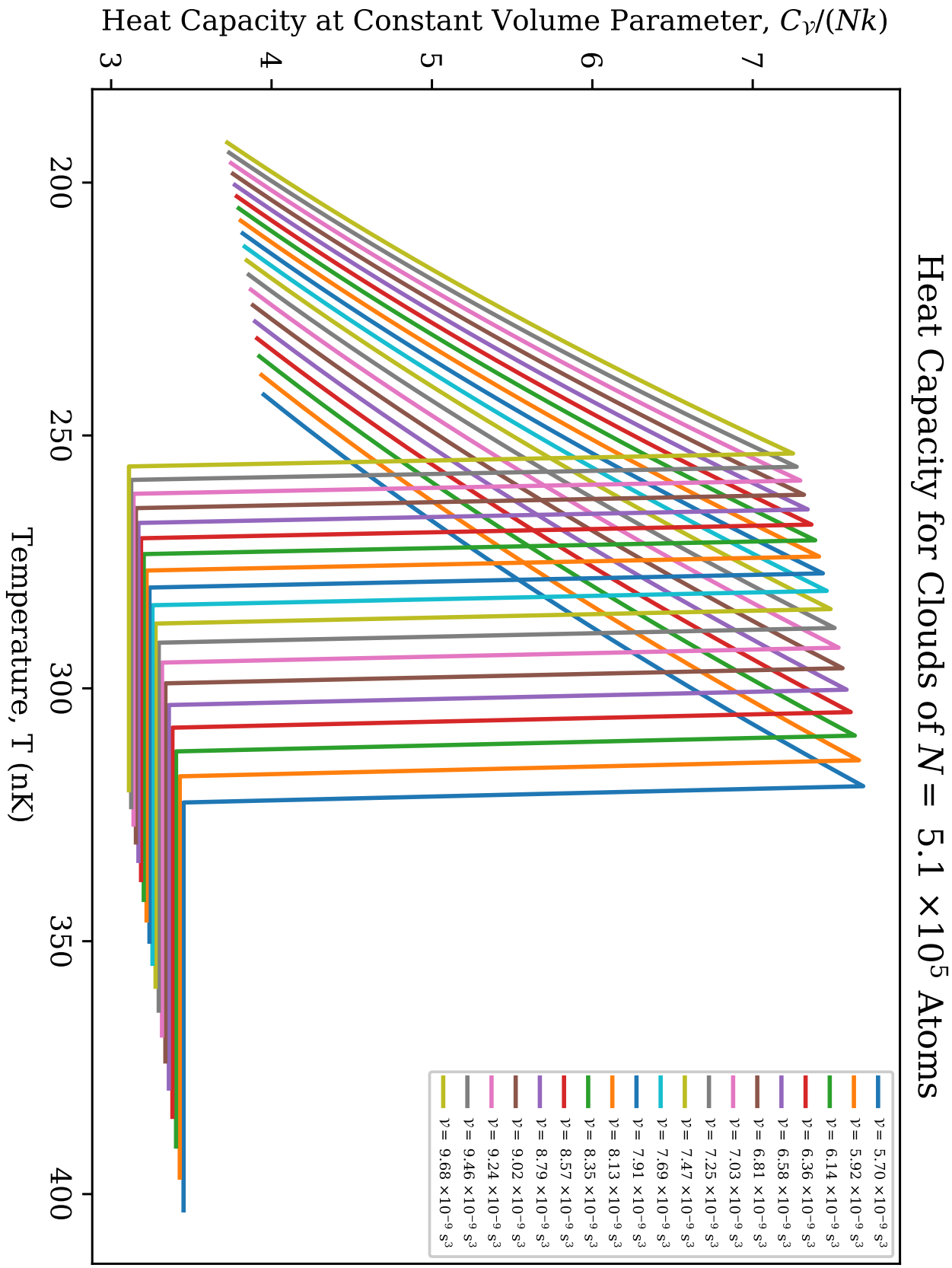

Figure 66 – Plots of the heat capacity at constant volume parameter C_ν for clouds of $N = 5.1 \times 10^5$ atoms.
Source: By the author.

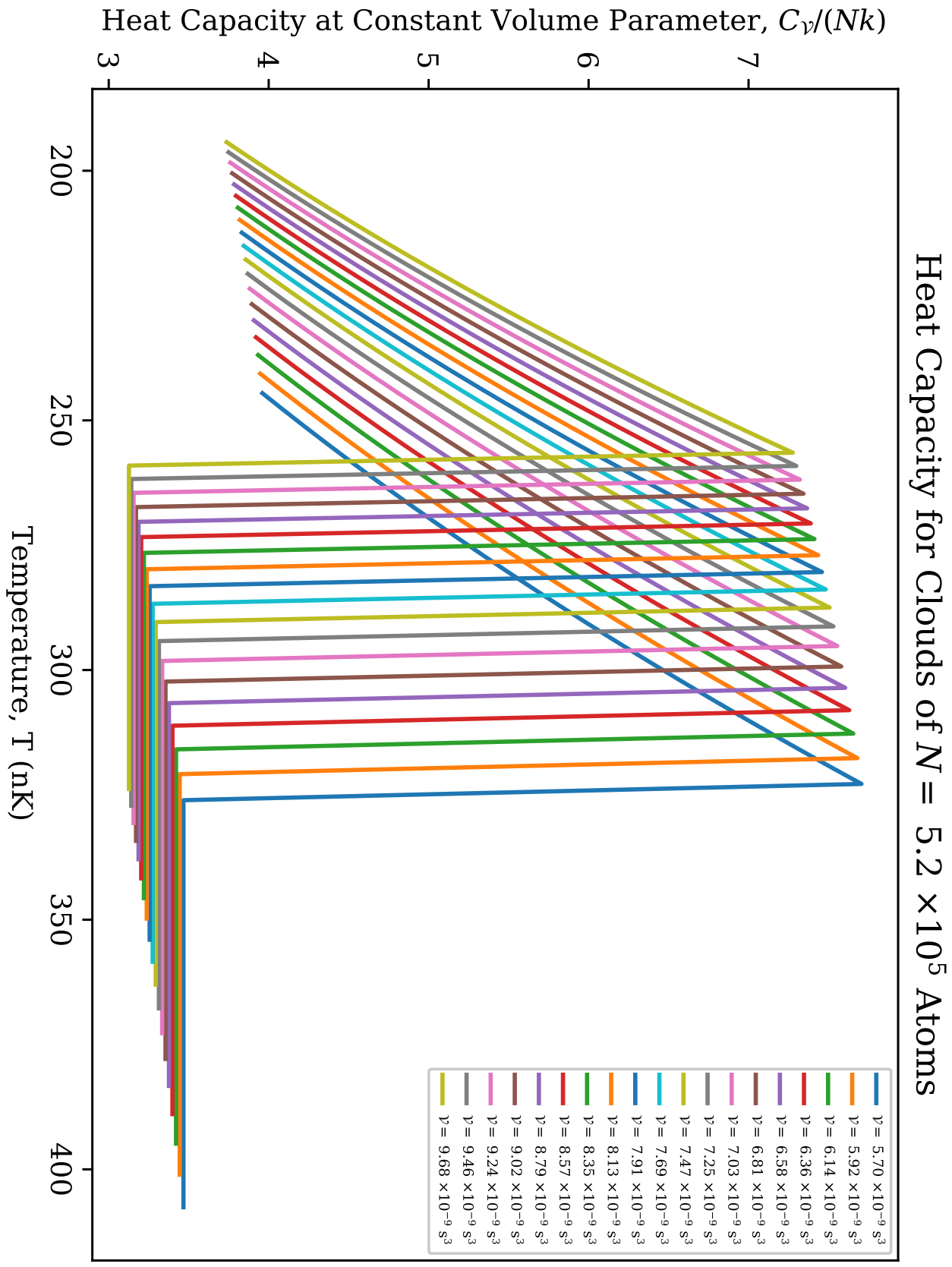

Figure 67 – Plots of the heat capacity at constant volume parameter C_ν for clouds of $N = 5.2 \times 10^5$ atoms.
Source: By the author.

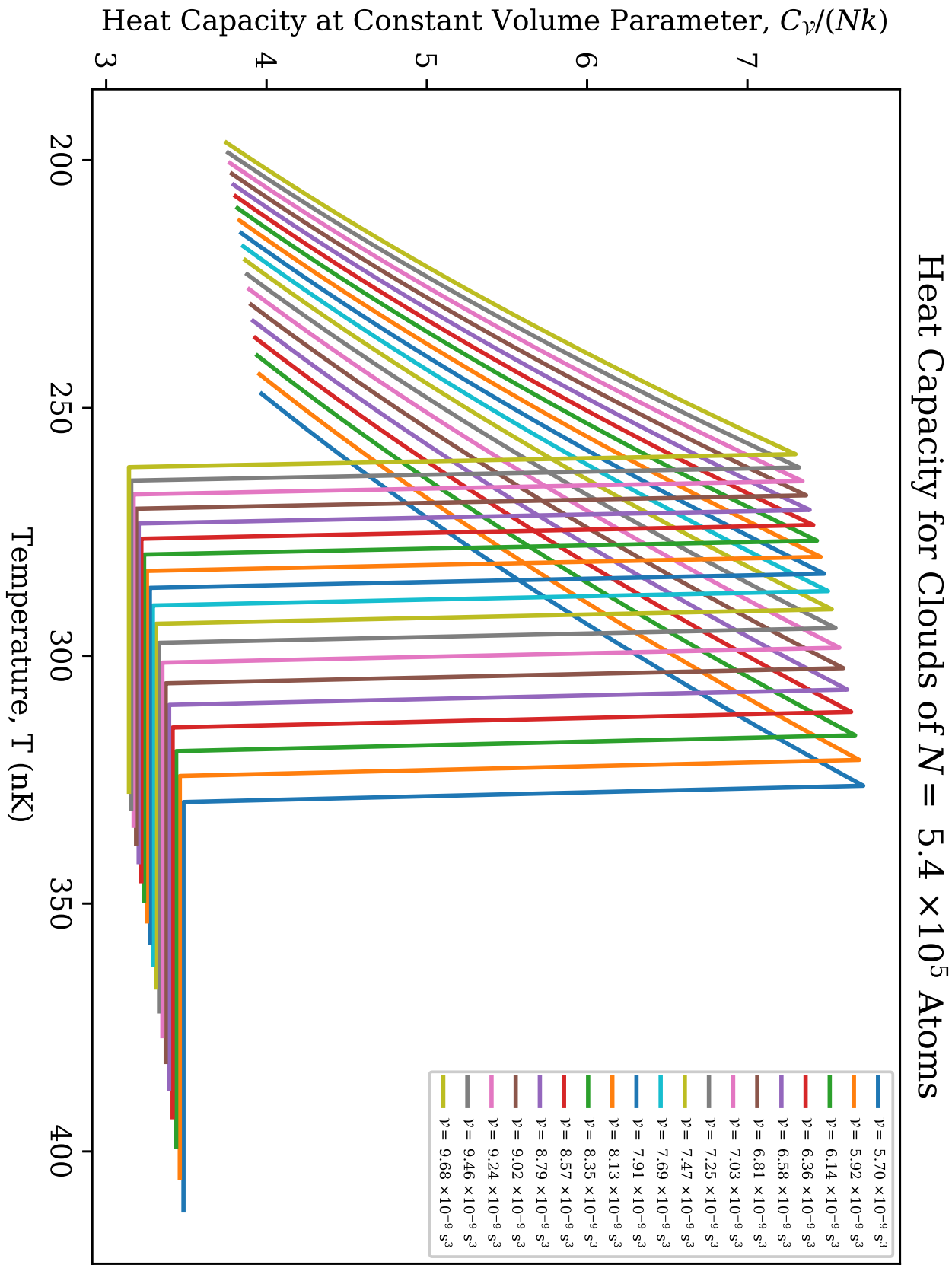

Figure 68 – Plots of the heat capacity at constant volume parameter $C_\mathcal{V}$ for clouds of $N = 5.4 \times 10^5$ atoms.
Source: By the author.

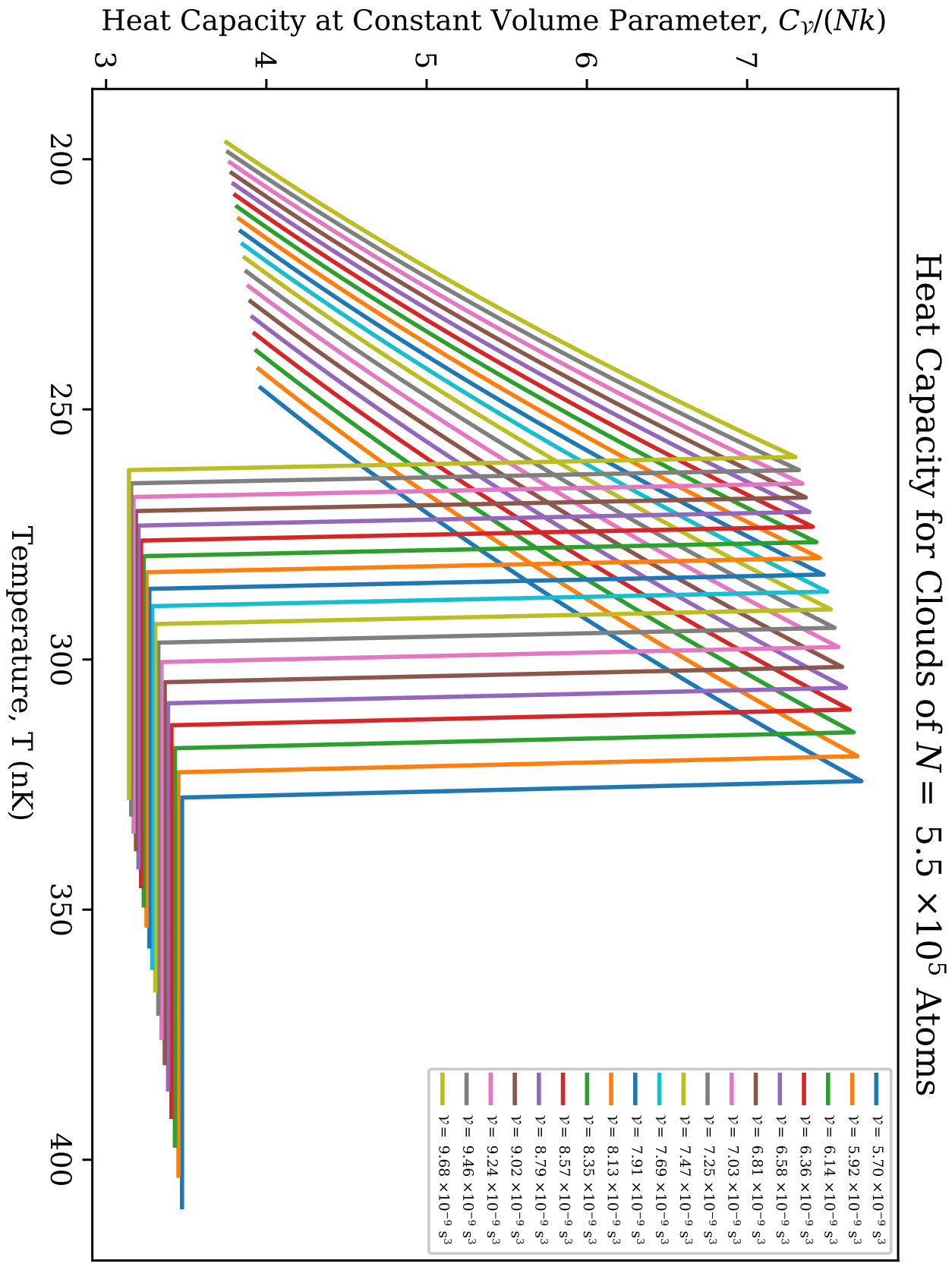

Figure 69 – Plots of the heat capacity at constant volume parameter C_ν for clouds of $N = 5.5 \times 10^5$ atoms.
Source: By the author.

APPENDIX F – COMPRESSIBILITY DIAGRAMS

The complete set of compressibility graphs mentioned in Sec. 6.4 are shown here.

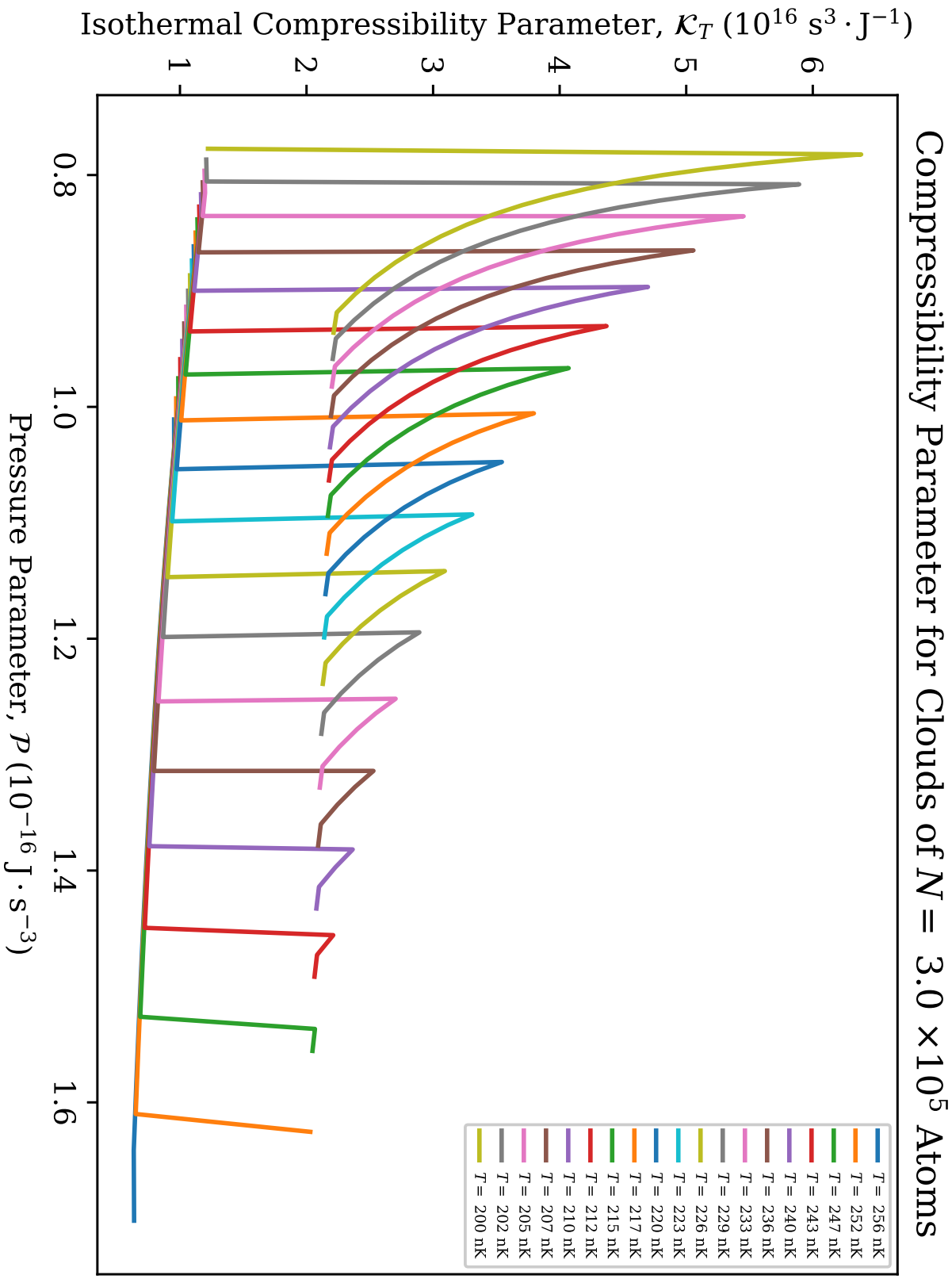

Figure 70 – Plots of the isothermal compressibility parameter $\mathcal{K}_T$ for clouds of $N = 3.0 \times 10^5$ atoms.
Source: By the author.

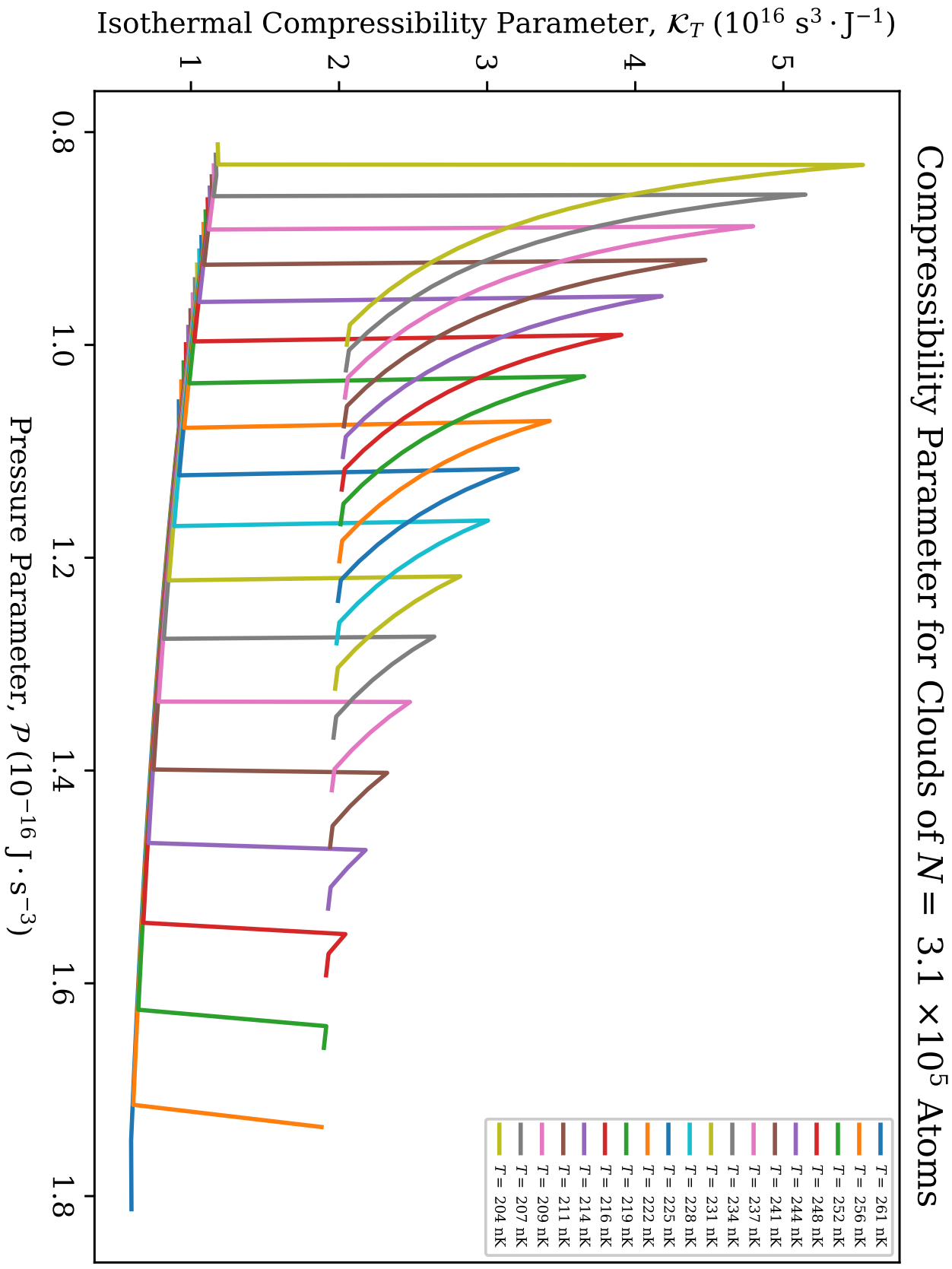

Figure 71 – Plots of the isothermal compressibility parameter $\mathcal{K}_T$ for clouds of $N = 3.1 \times 10^5$ atoms.
Source: By the author.

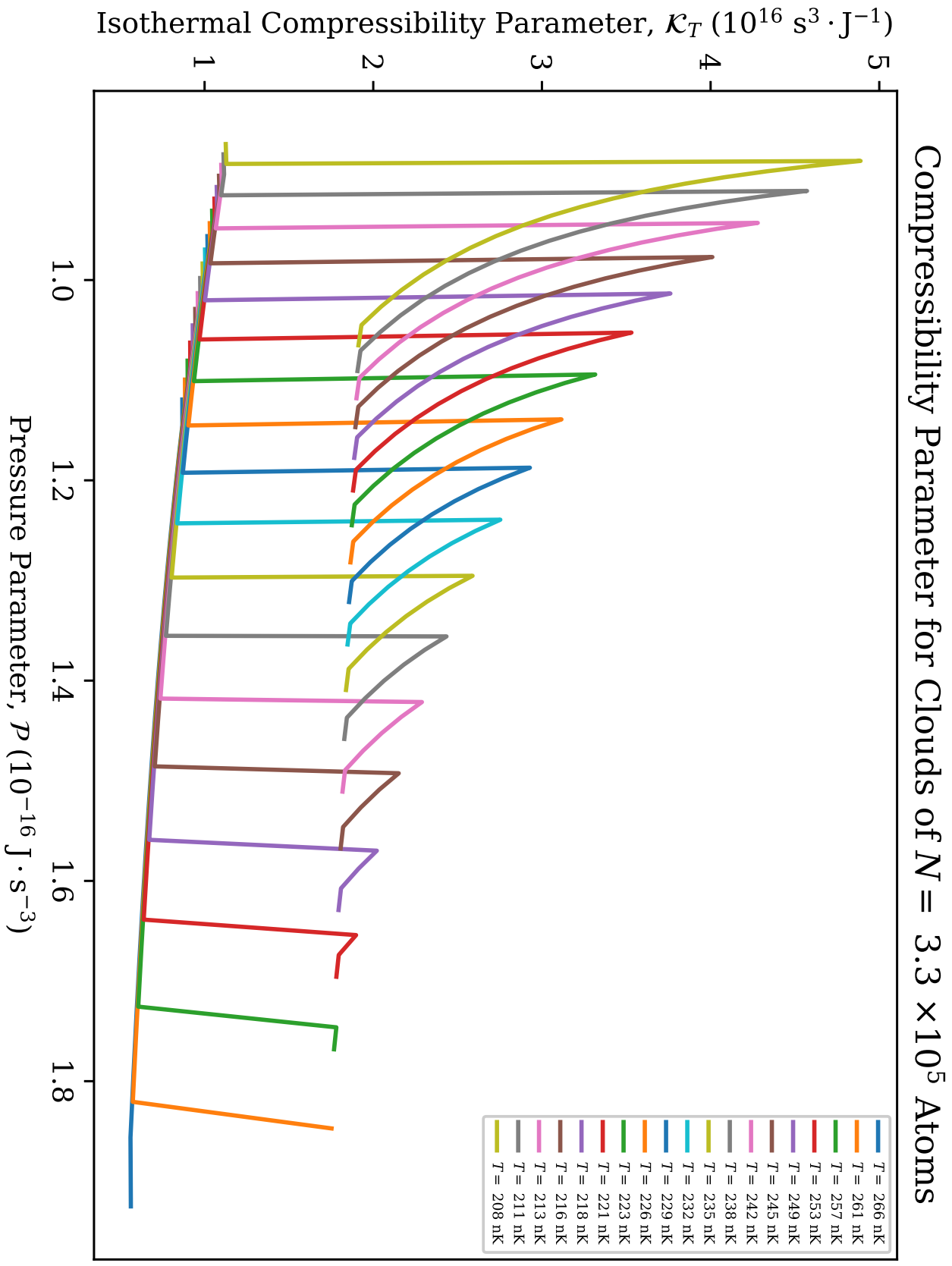

Figure 72 – Plots of the isothermal compressibility parameter $\mathcal{K}_T$ for clouds of $N = 3.3 \times 10^5$ atoms.
Source: By the author.

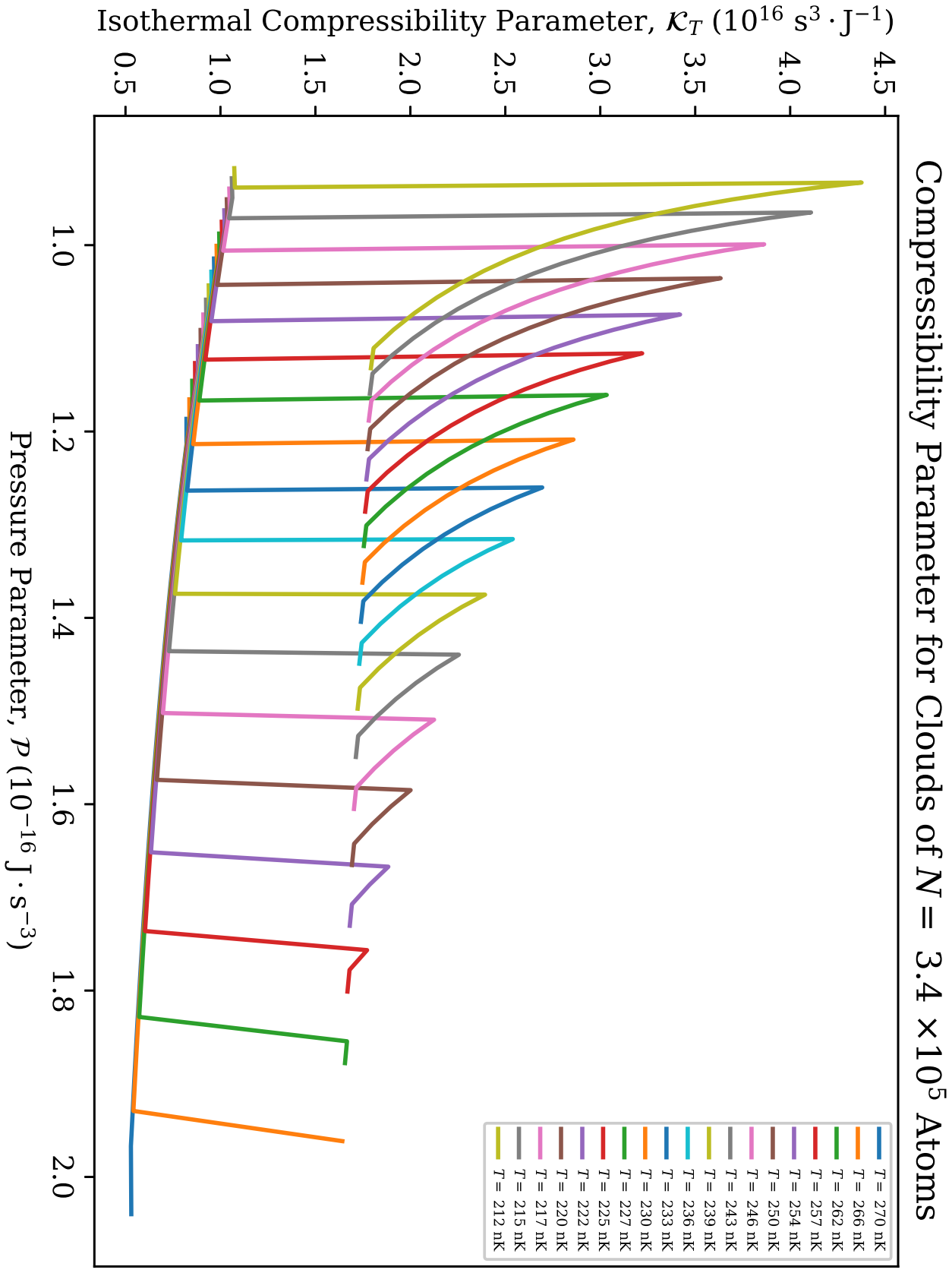

Figure 73 – Plots of the isothermal compressibility parameter $\mathcal{K}_T$ for clouds of $N = 3.4 \times 10^5$ atoms.
Source: By the author.

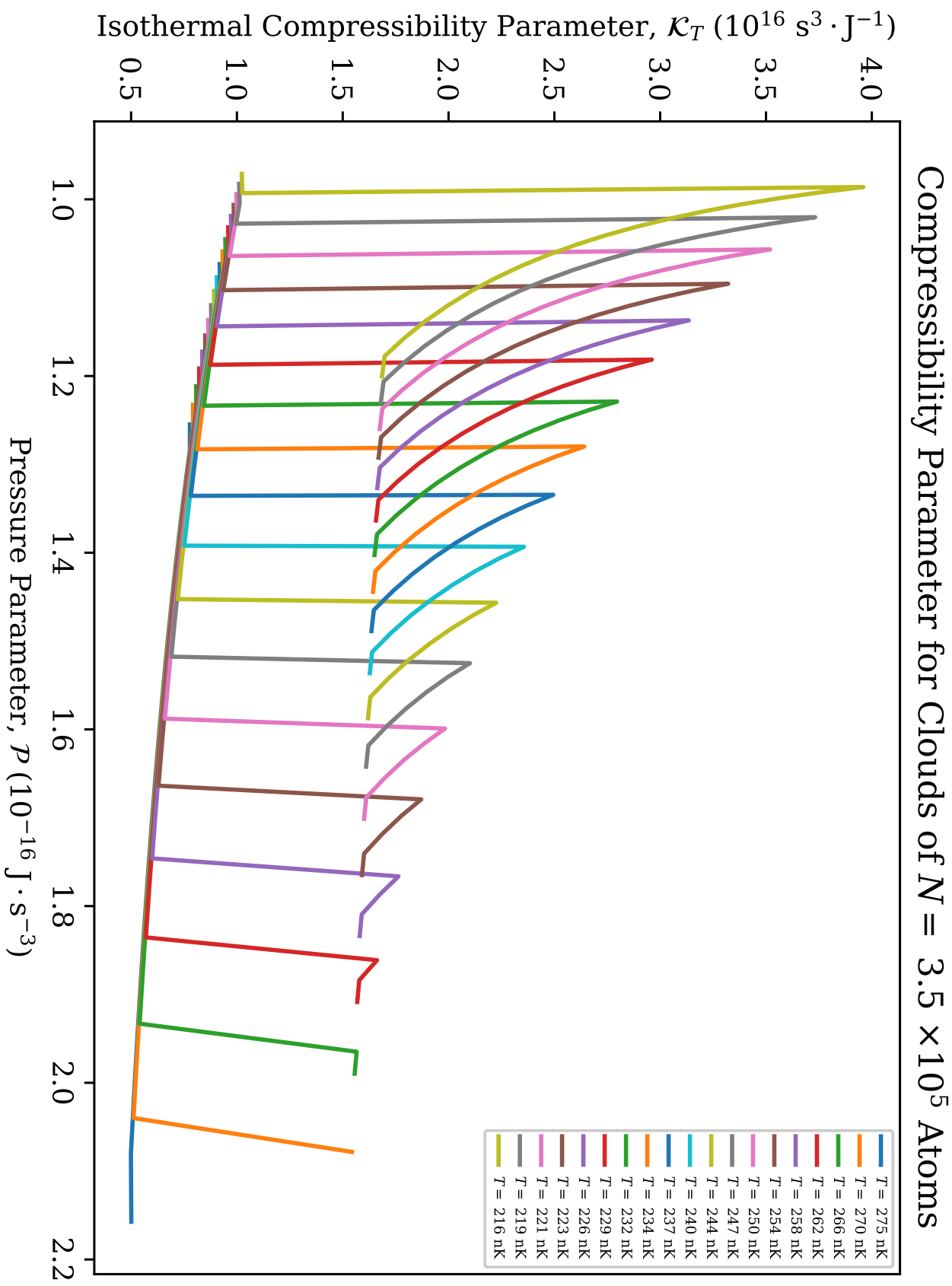

Figure 74 – Plots of the isothermal compressibility parameter $\mathcal{K}_T$ for clouds of $N = 3.5 \times 10^5$ atoms.
Source: By the author.

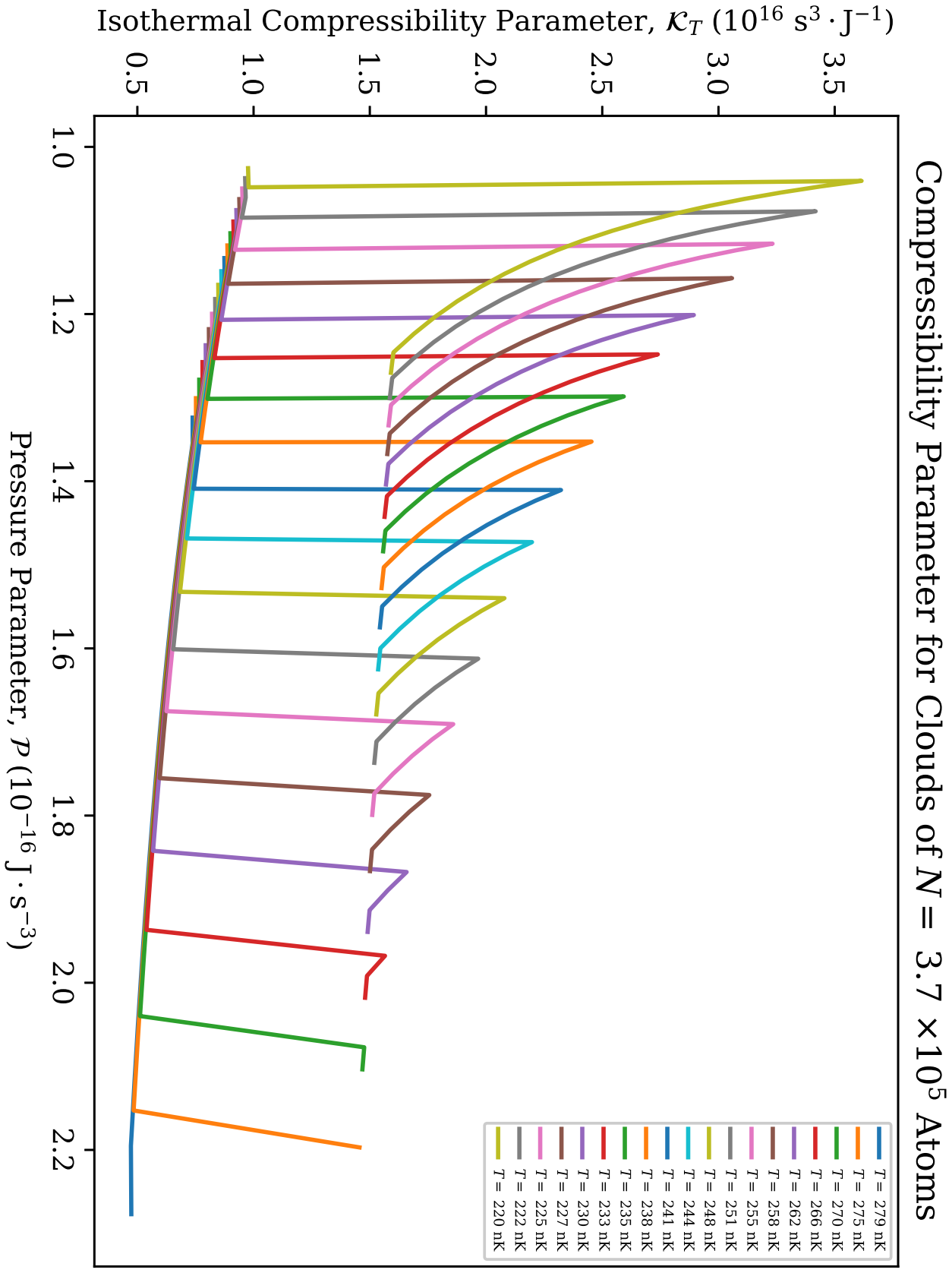

Figure 75 – Plots of the isothermal compressibility parameter $\mathcal{K}_T$ for clouds of $N = 3.7 \times 10^5$ atoms.
Source: By the author.

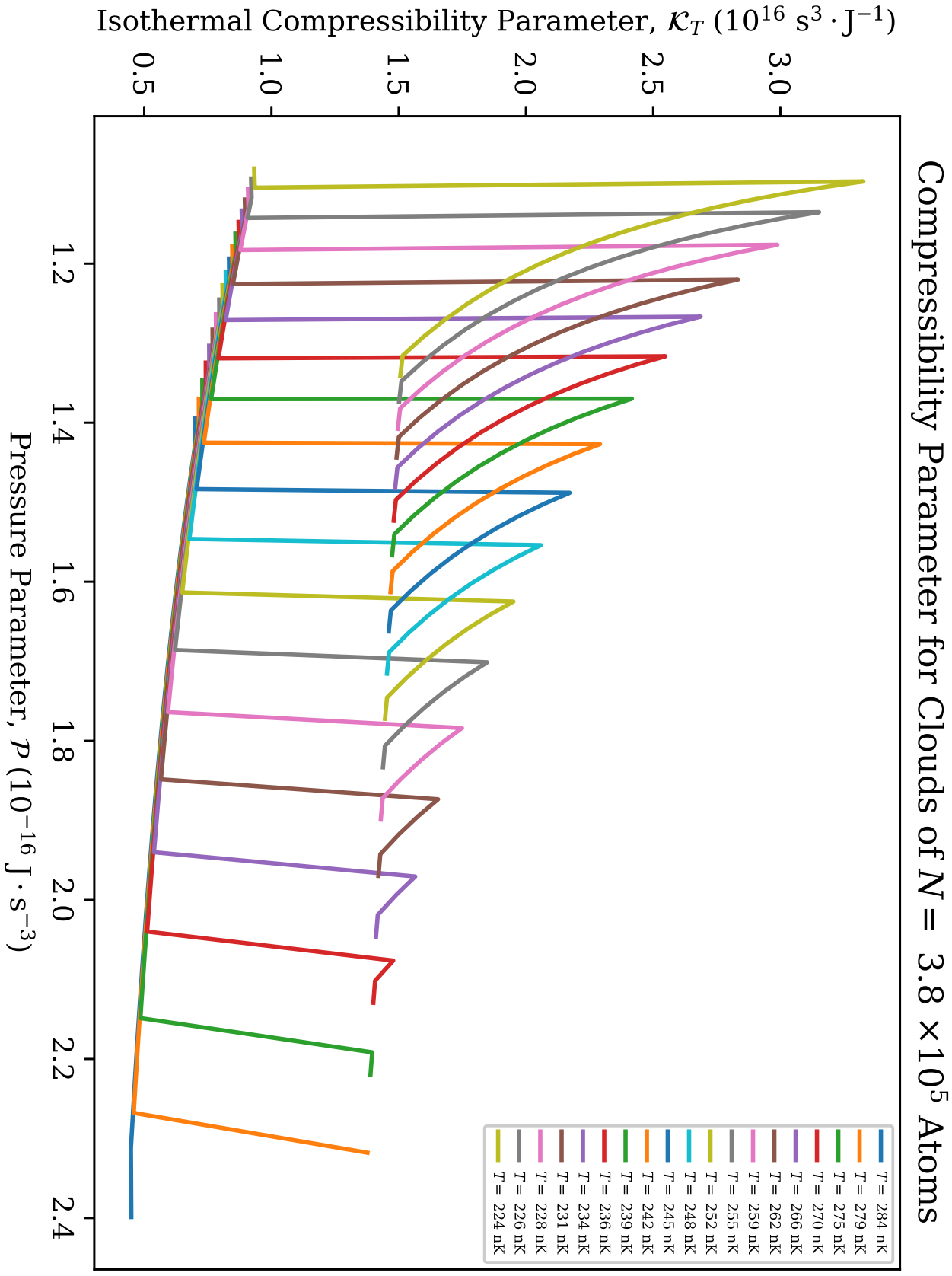

Figure 76 – Plots of the isothermal compressibility parameter $\mathcal{K}_T$ for clouds of $N = 3.8 \times 10^5$ atoms.
Source: By the author.

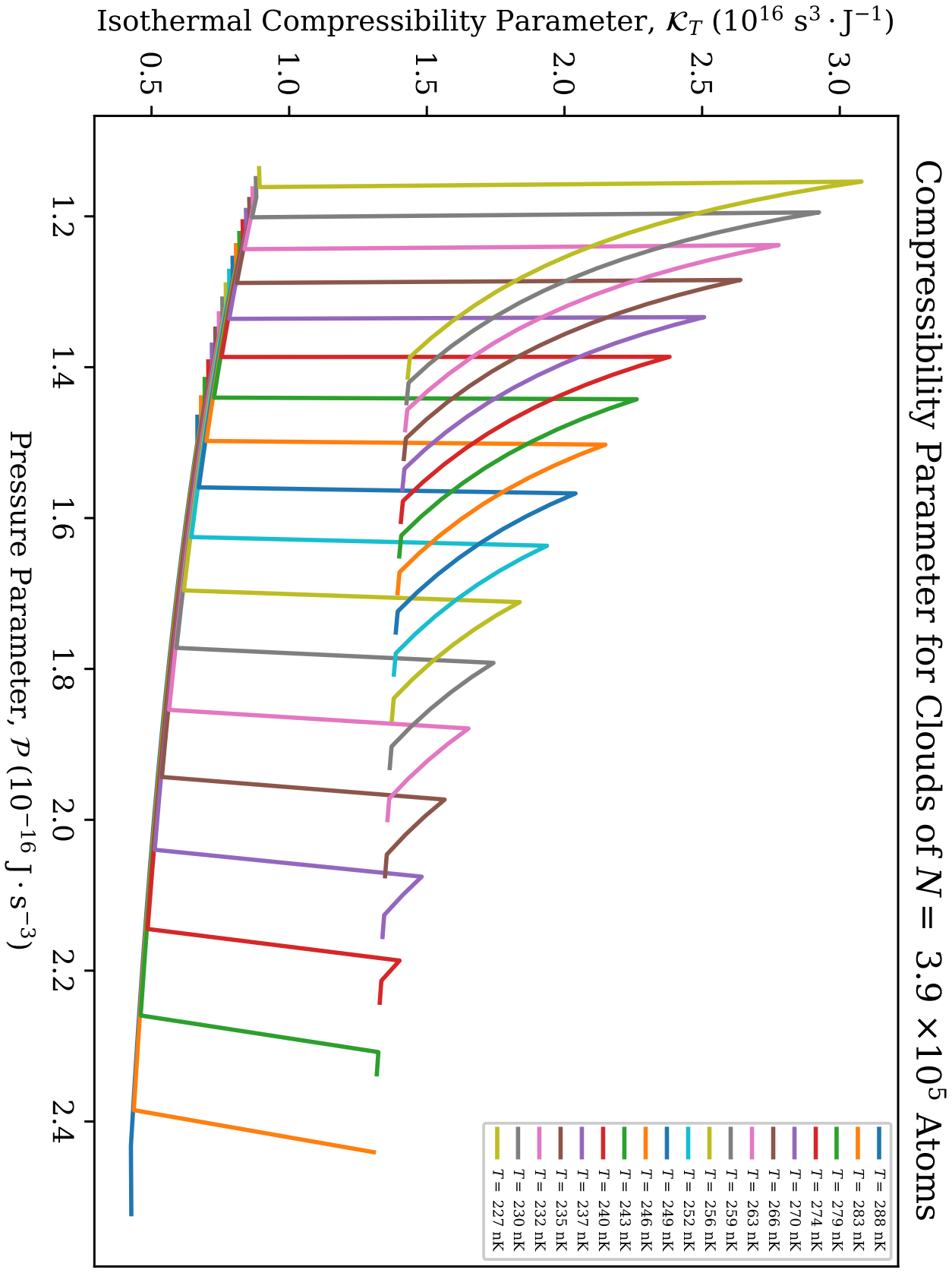

Figure 77 – Plots of the isothermal compressibility parameter $\mathcal{K}_T$ for clouds of $N = 3.9 \times 10^5$ atoms.
Source: By the author.

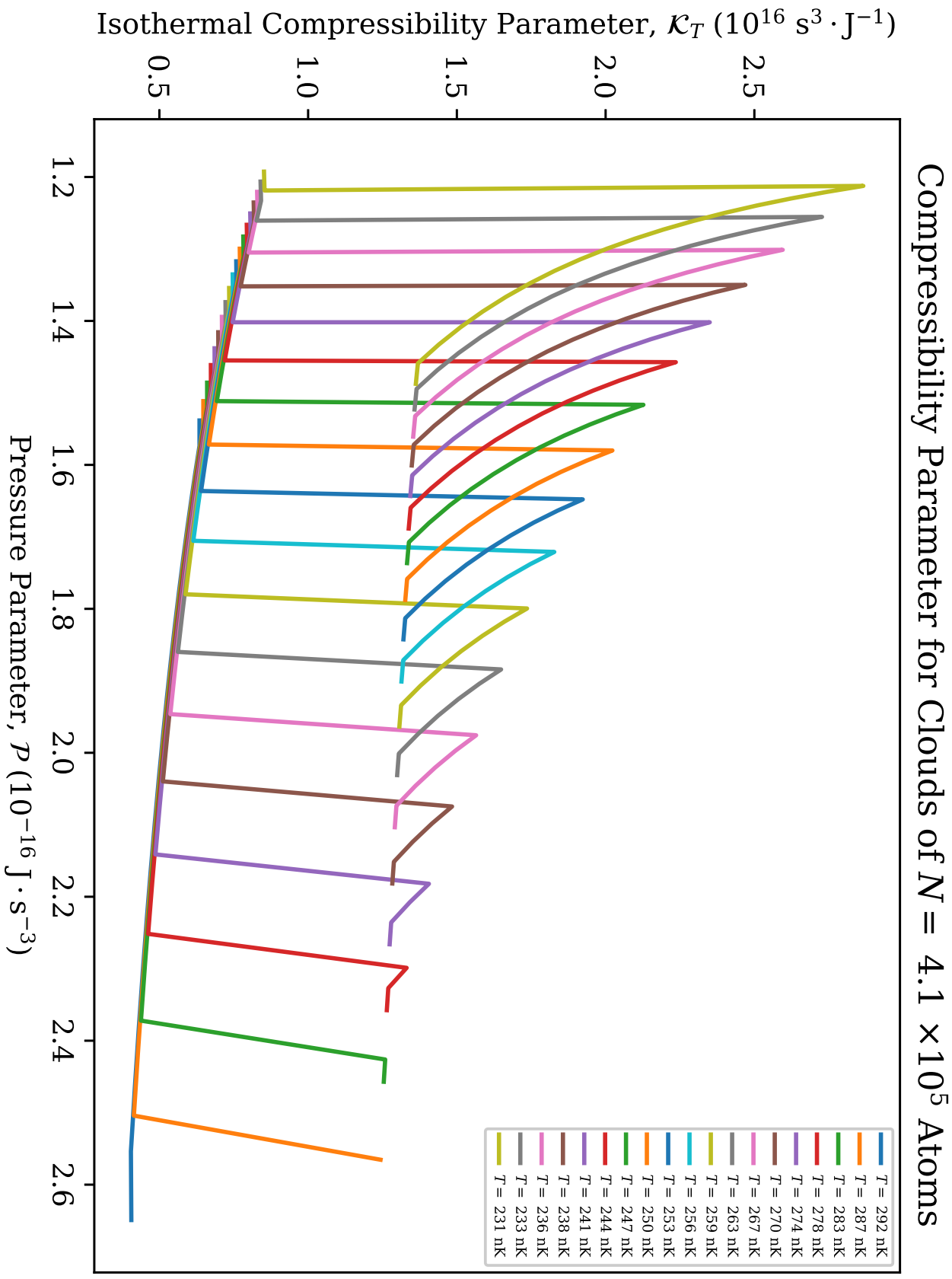

Figure 78 – Plots of the isothermal compressibility parameter $\mathcal{K}_T$ for clouds of $N = 4.1 \times 10^5$ atoms.
Source: By the author.

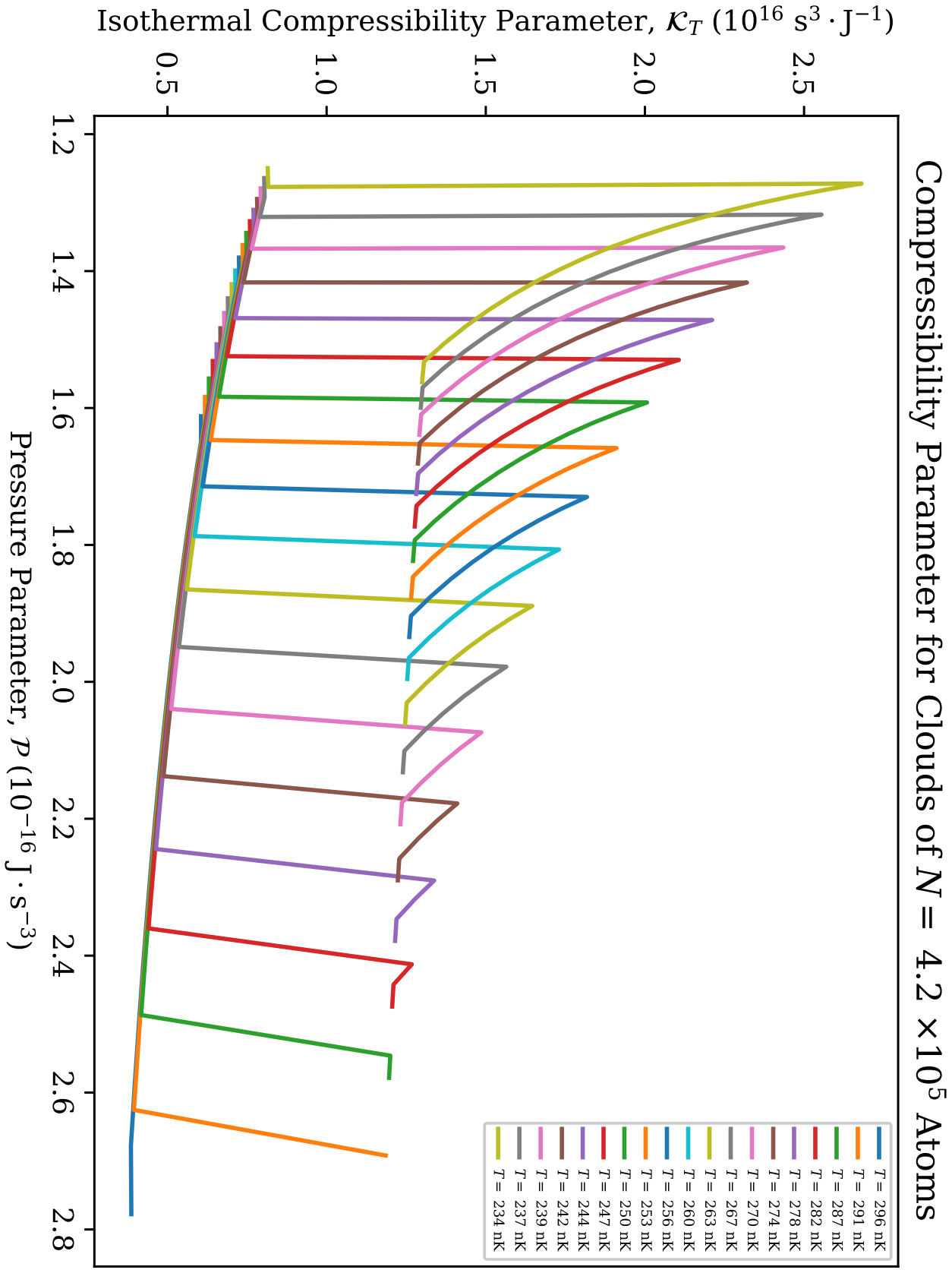

Figure 79 – Plots of the isothermal compressibility parameter $\mathcal{K}_T$ for clouds of $N = 4.2 \times 10^5$ atoms.
Source: By the author.

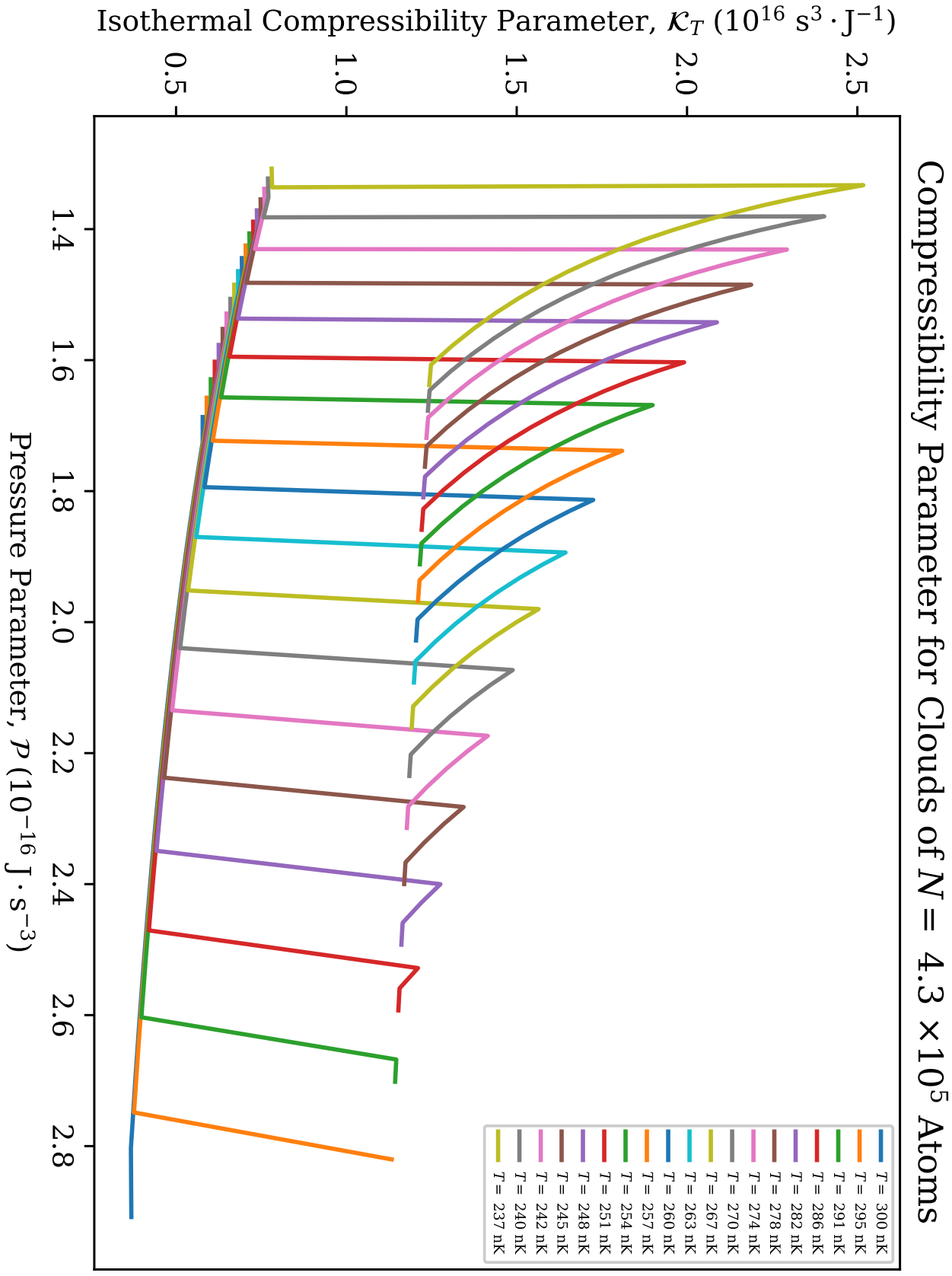

Figure 80 – Plots of the isothermal compressibility parameter $\mathcal{K}_T$ for clouds of $N = 4.3 \times 10^5$ atoms.
Source: By the author.

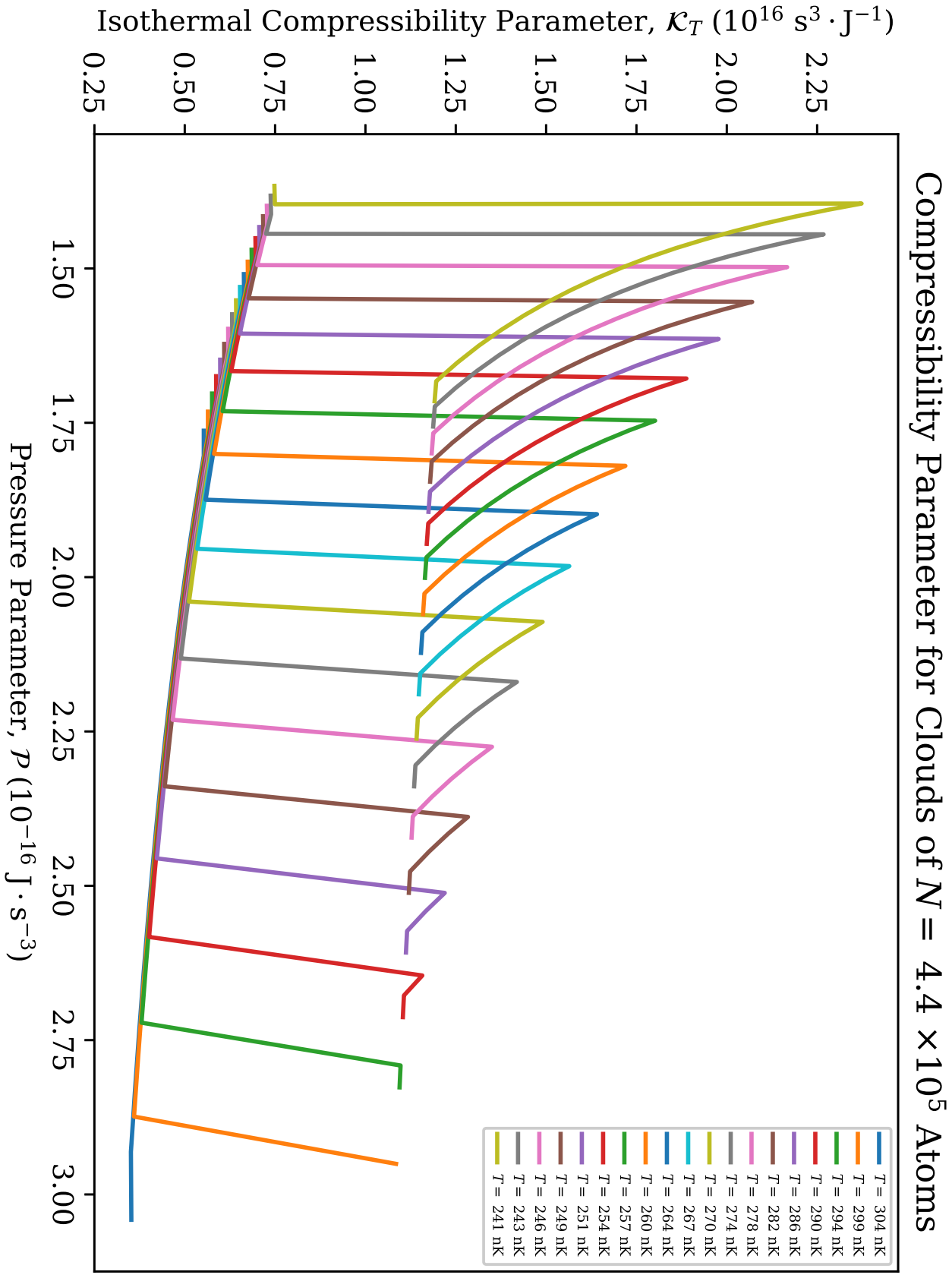

Figure 81 – Plots of the isothermal compressibility parameter $\mathcal{K}_T$ for clouds of $N = 4.4 \times 10^5$ atoms.
Source: By the author.

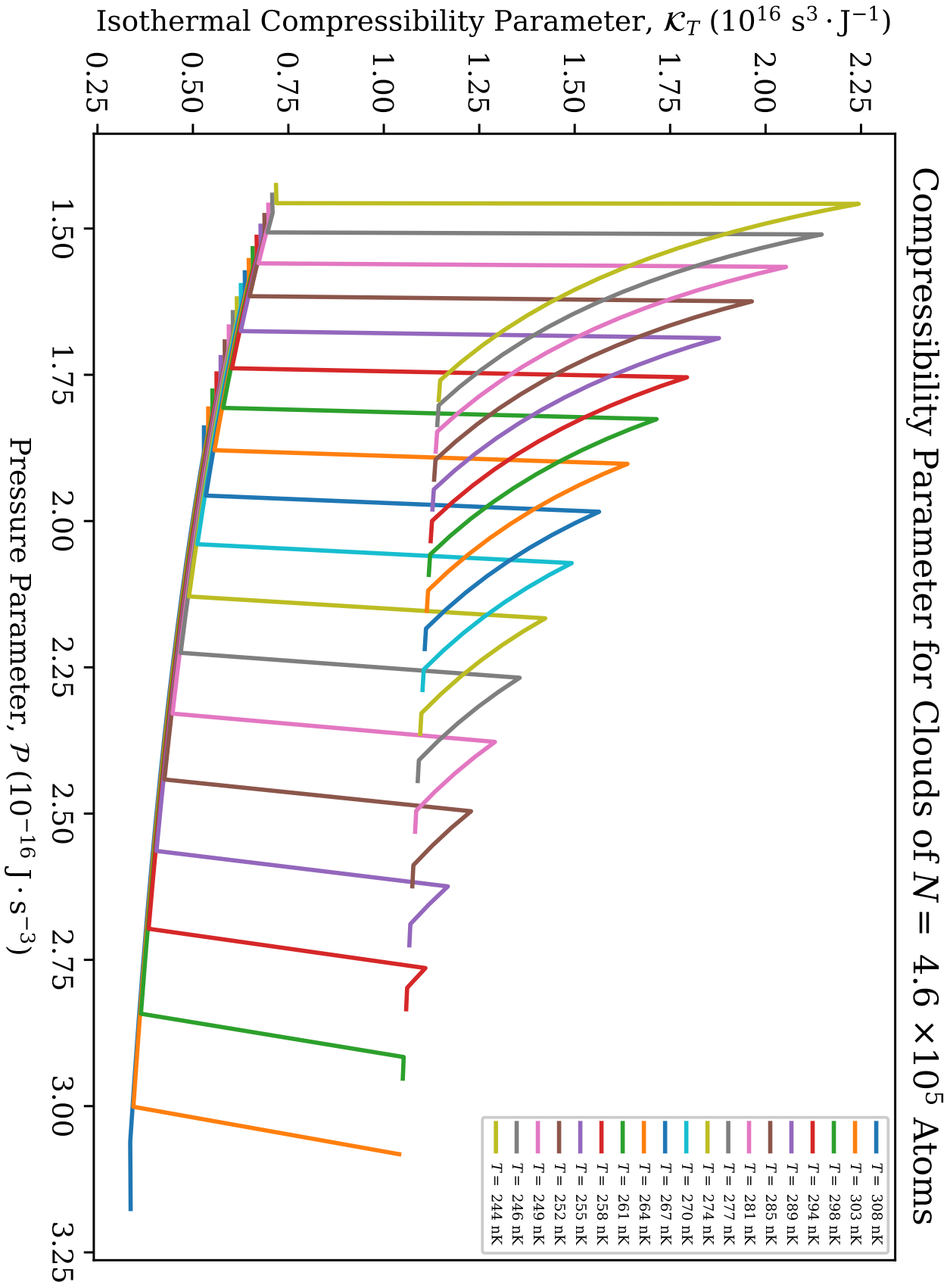

Figure 82 – Plots of the isothermal compressibility parameter $\mathcal{K}_T$ for clouds of $N = 4.6 \times 10^5$ atoms.
Source: By the author.

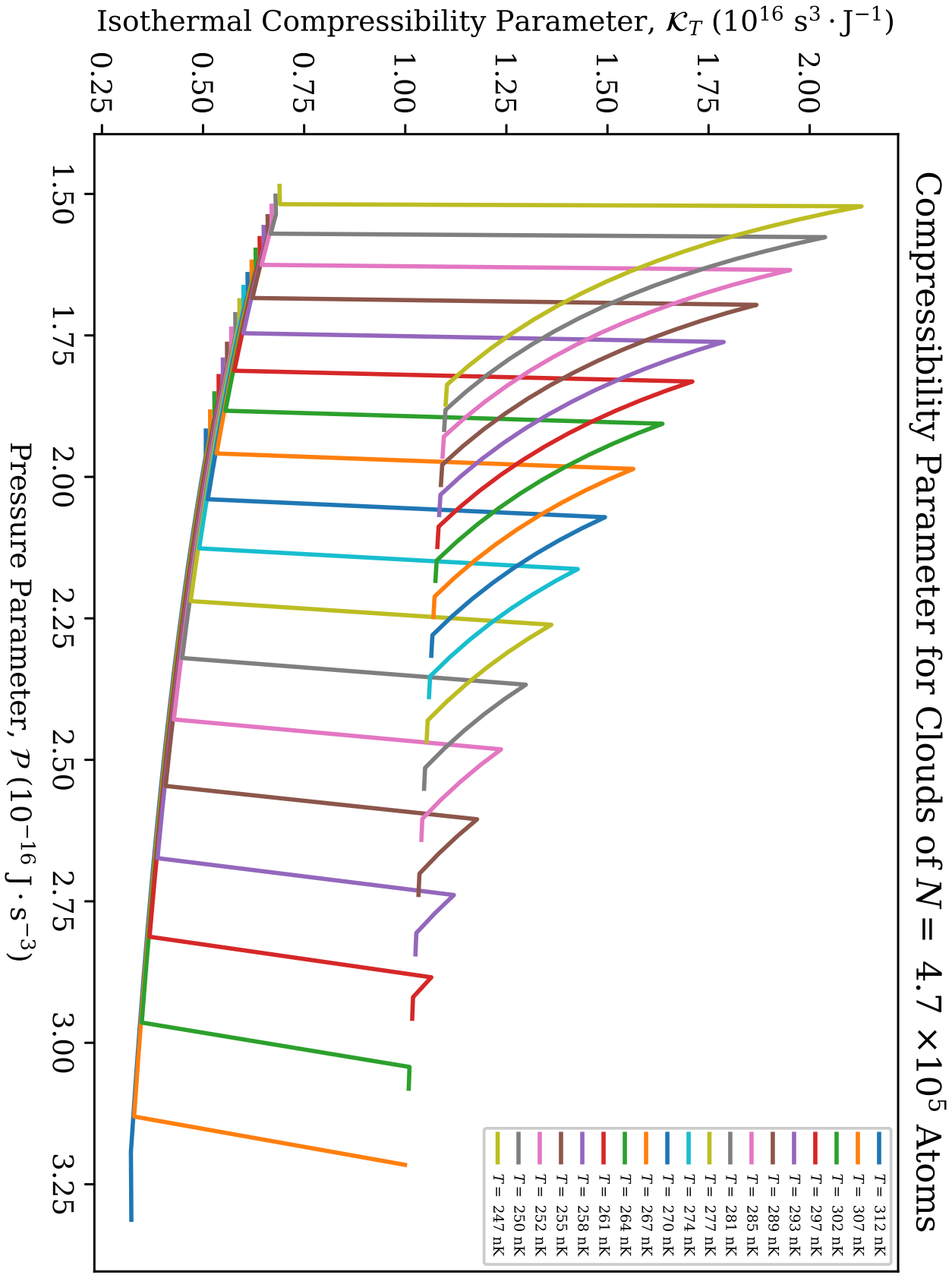

Figure 83 – Plots of the isothermal compressibility parameter $\mathcal{K}_T$ for clouds of $N = 4.7 \times 10^5$ atoms.
Source: By the author.

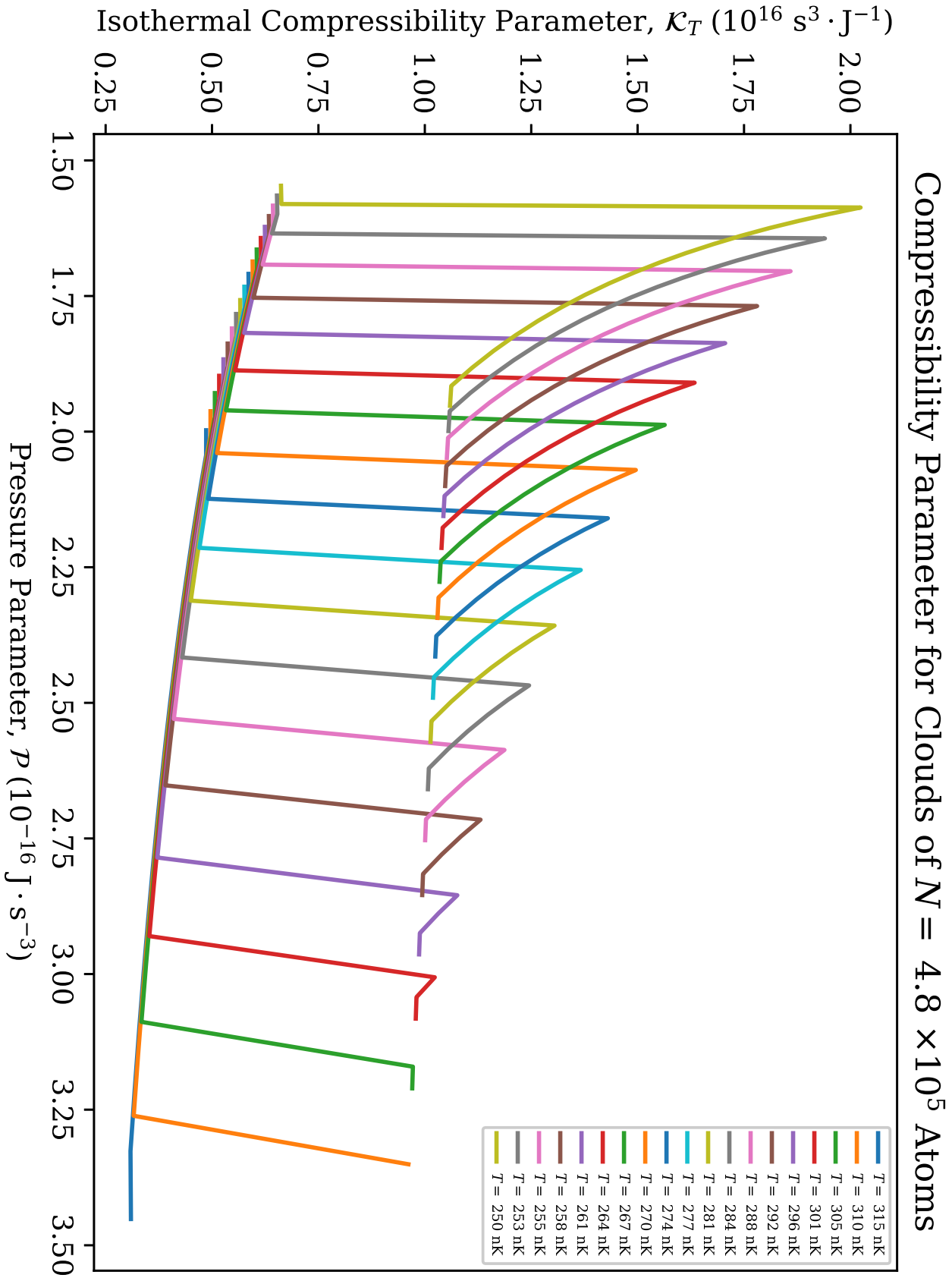

Figure 84 – Plots of the isothermal compressibility parameter $\mathcal{K}_T$ for clouds of $N = 4.8 \times 10^5$ atoms.
Source: By the author.

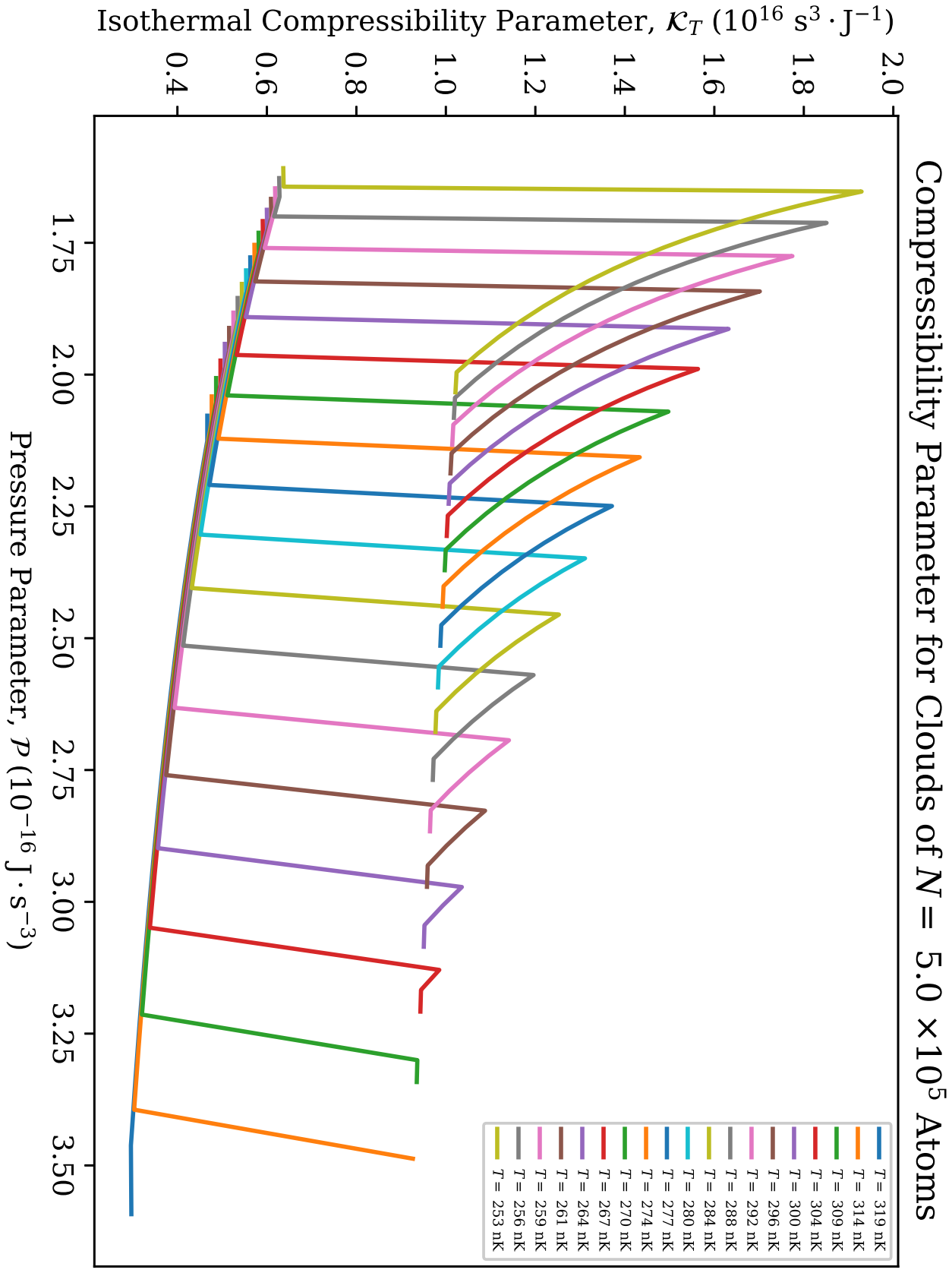

Figure 85 – Plots of the isothermal compressibility parameter $\mathcal{K}_T$ for clouds of $N = 5.0 \times 10^5$ atoms.
Source: By the author.

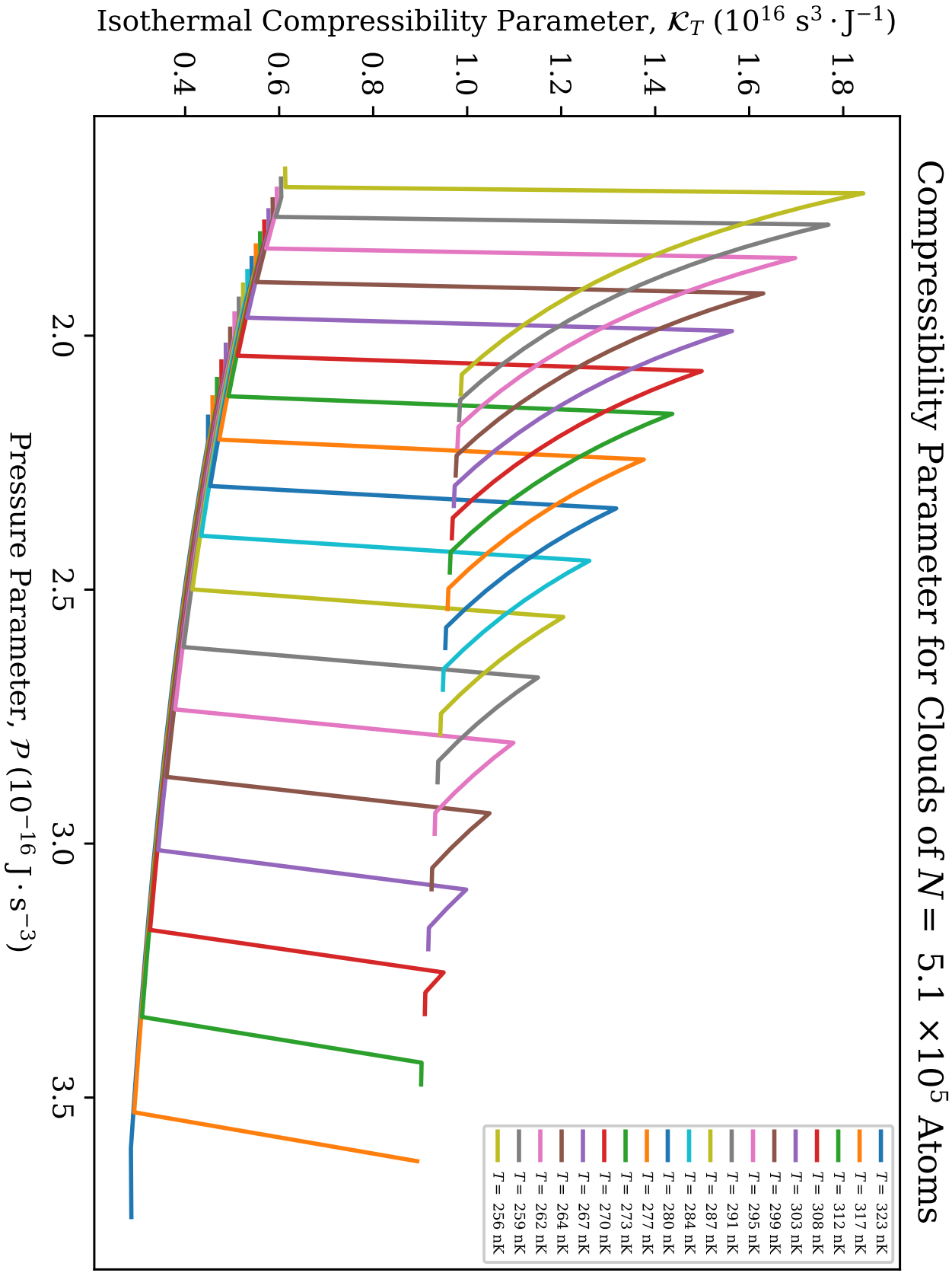

Figure 86 – Plots of the isothermal compressibility parameter $\mathcal{K}_T$ for clouds of $N = 5.1 \times 10^5$ atoms.
Source: By the author.

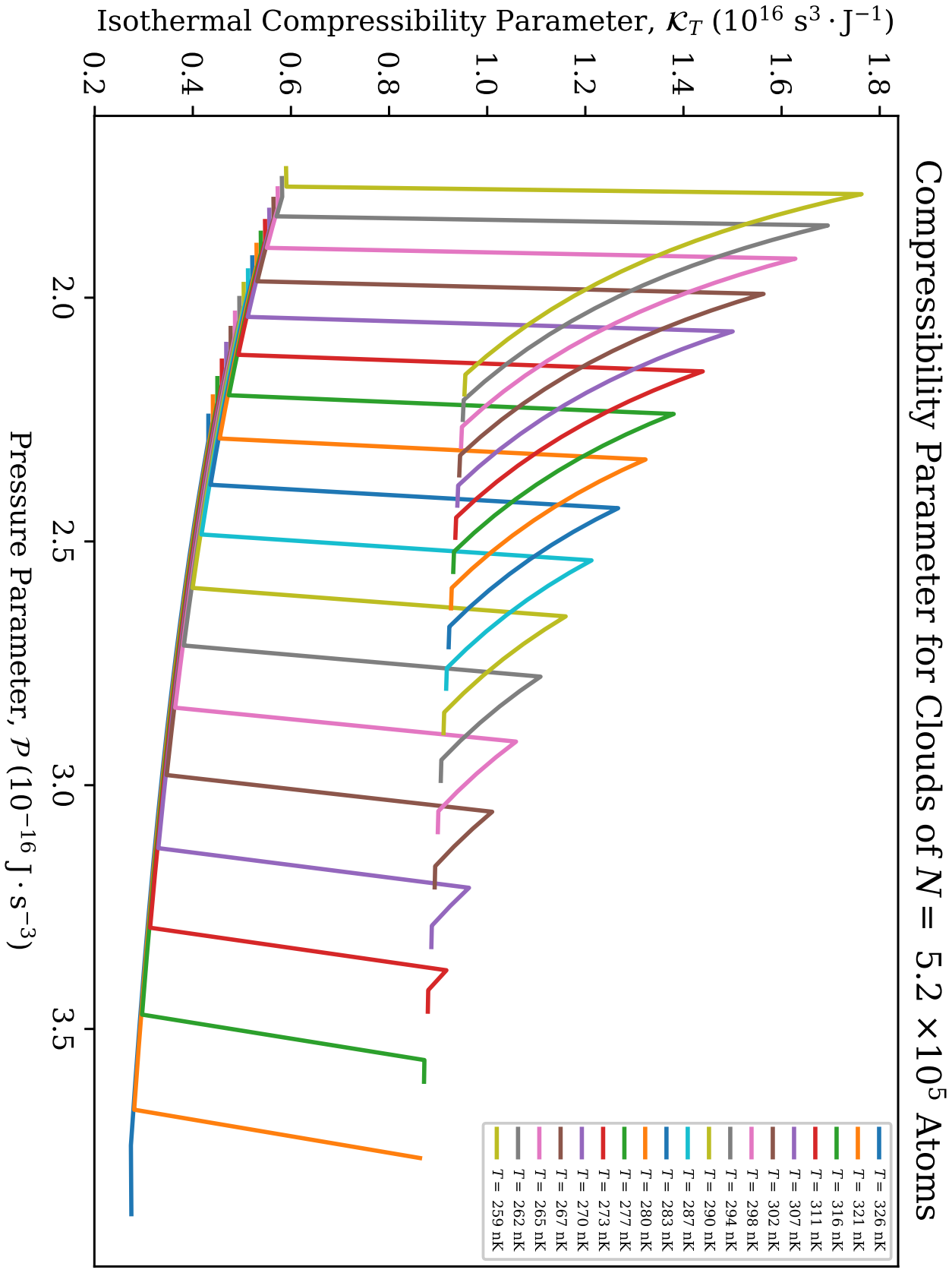

Figure 87 – Plots of the isothermal compressibility parameter $\mathcal{K}_T$ for clouds of $N = 5.2 \times 10^5$ atoms.
Source: By the author.

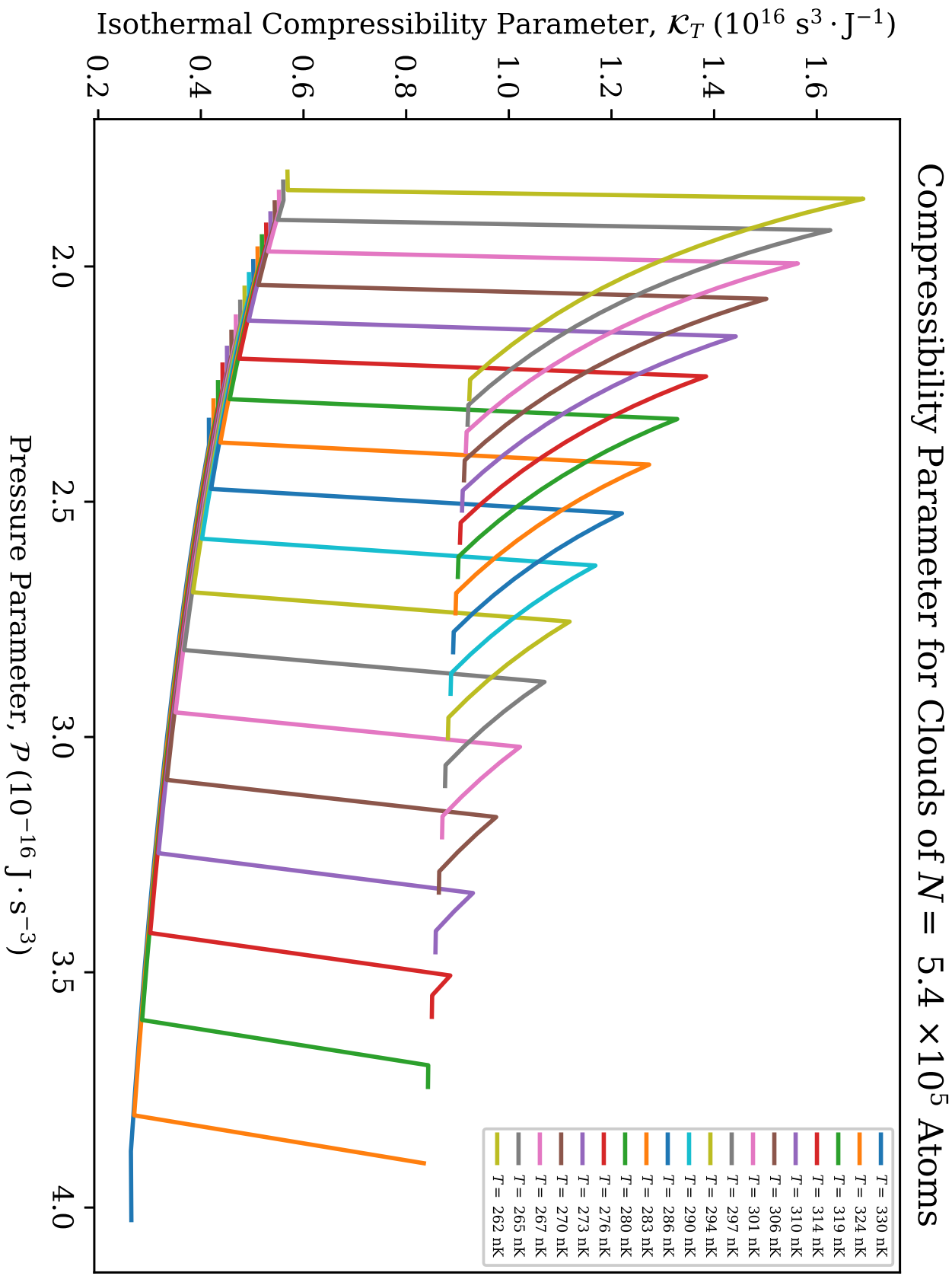

Figure 88 – Plots of the isothermal compressibility parameter $\mathcal{K}_T$ for clouds of $N = 5.4 \times 10^5$ atoms.
Source: By the author.

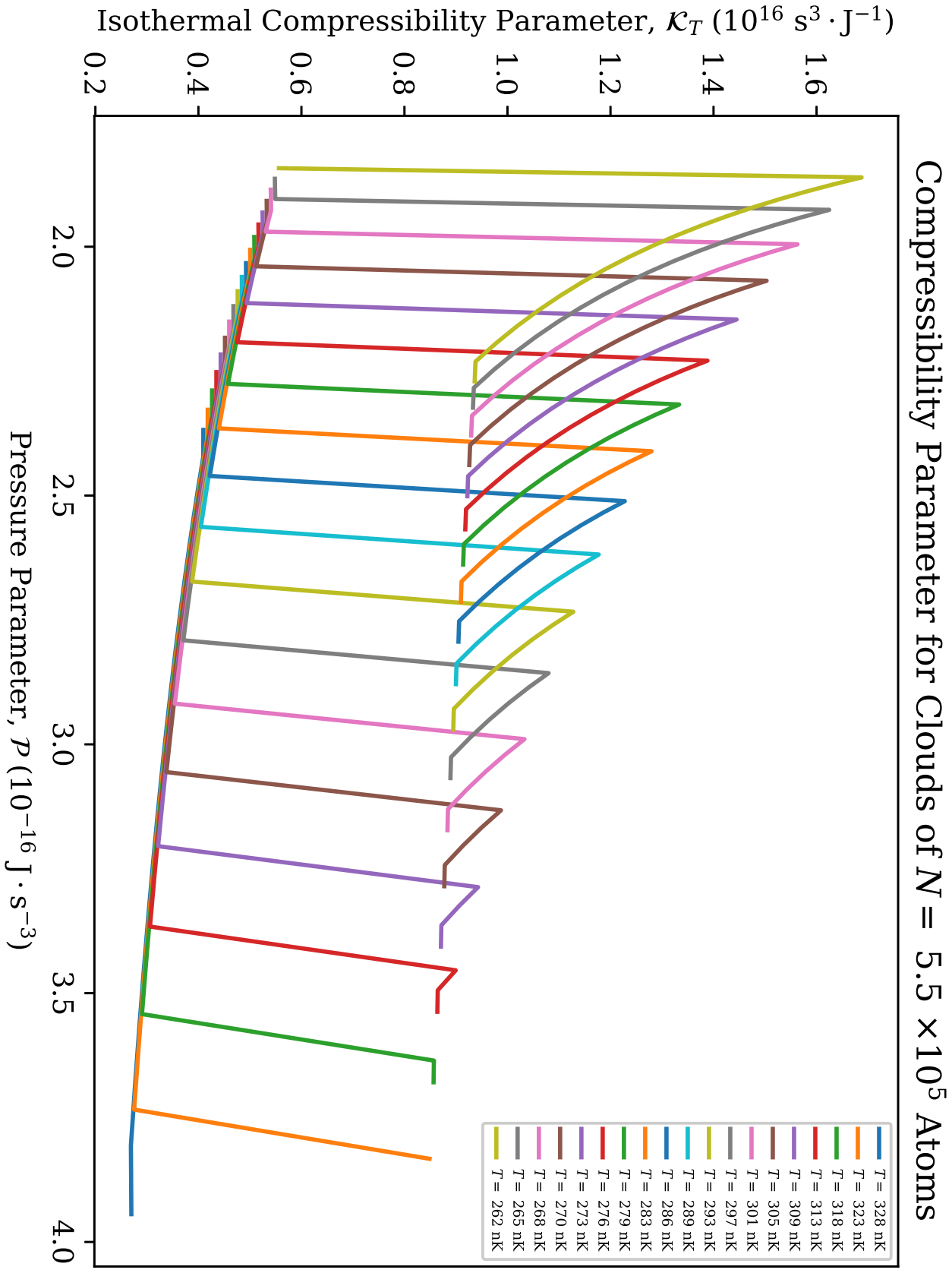

Figure 89 – Plots of the isothermal compressibility parameter $\mathcal{K}_T$ for clouds of $N = 5.5 \times 10^5$ atoms.
Source: By the author.

APPENDIX G – THERMAL-EXPANSION DIAGRAMS

The complete set of thermal-expansion plots mentioned in Sec. 6.4 are shown here.

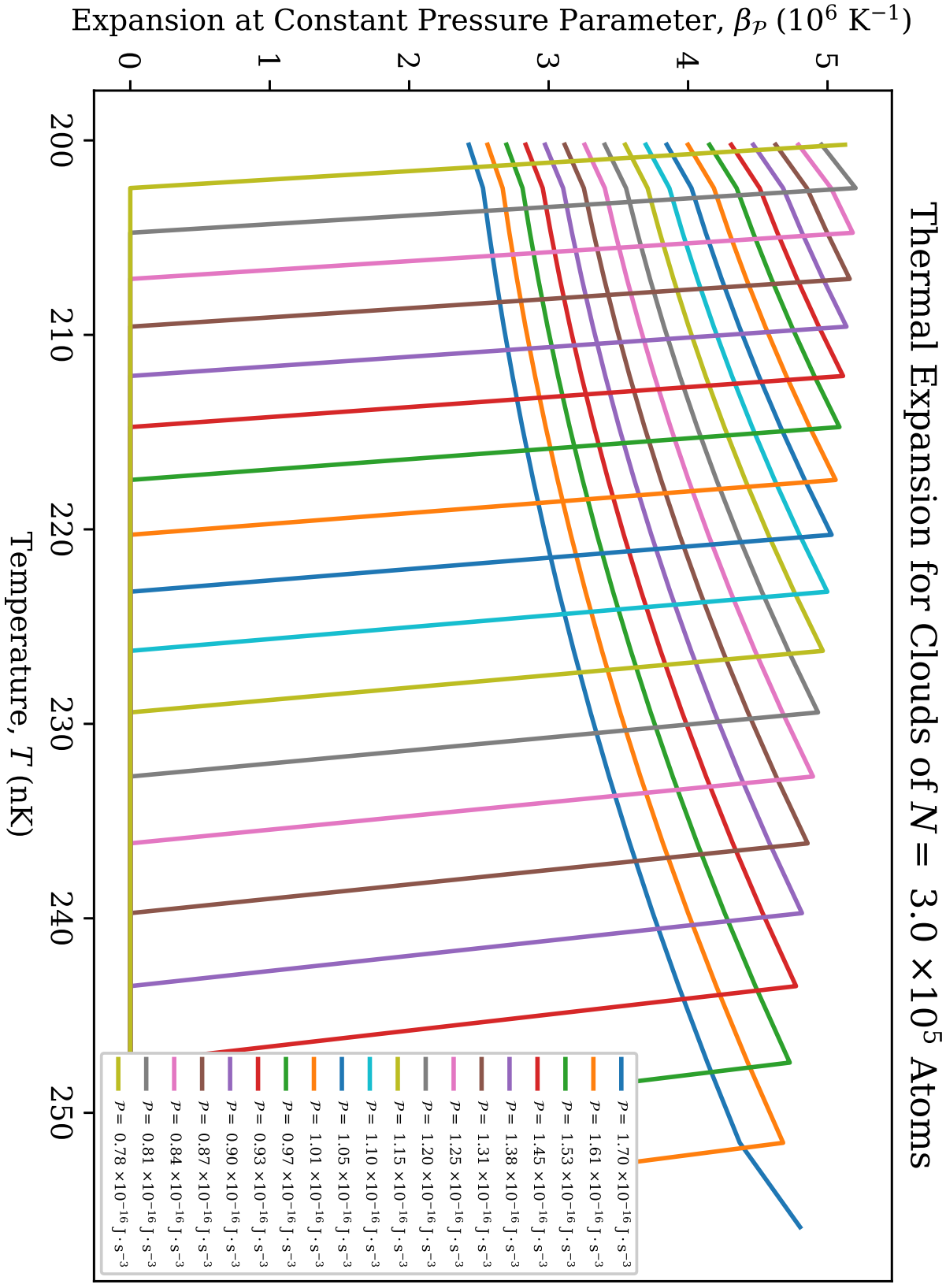

Figure 90 – Plots of the thermal expansion at constant pressure parameter $\beta_{\mathcal{P}}$ for clouds of $N = 3.0 \times 10^5$ atoms.
Source: By the author.

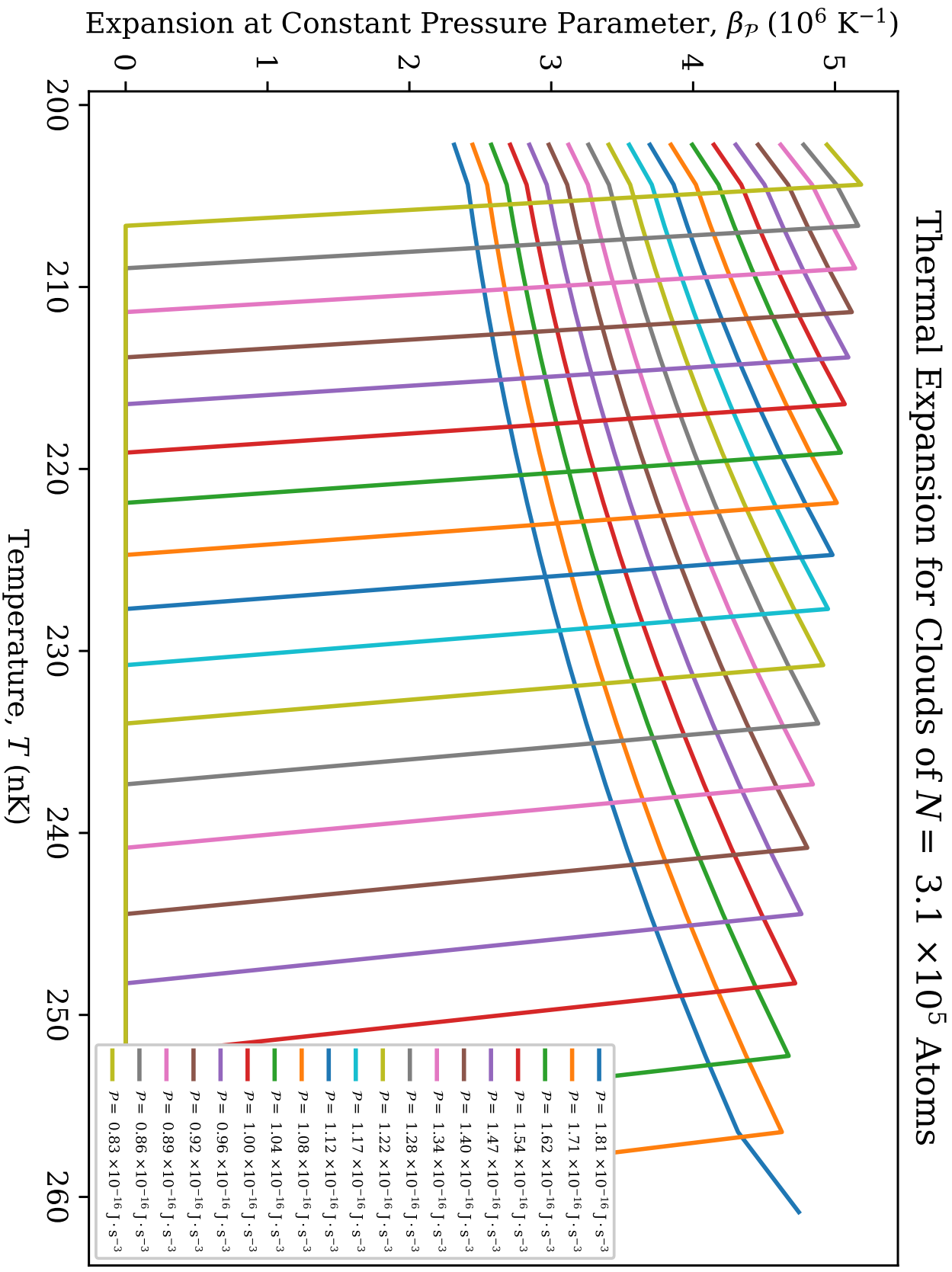

Figure 91 – Plots of the thermal expansion at constant pressure parameter $\beta_{\mathcal{P}}$ for clouds of $N = 3.1 \times 10^5$ atoms.
Source: By the author.

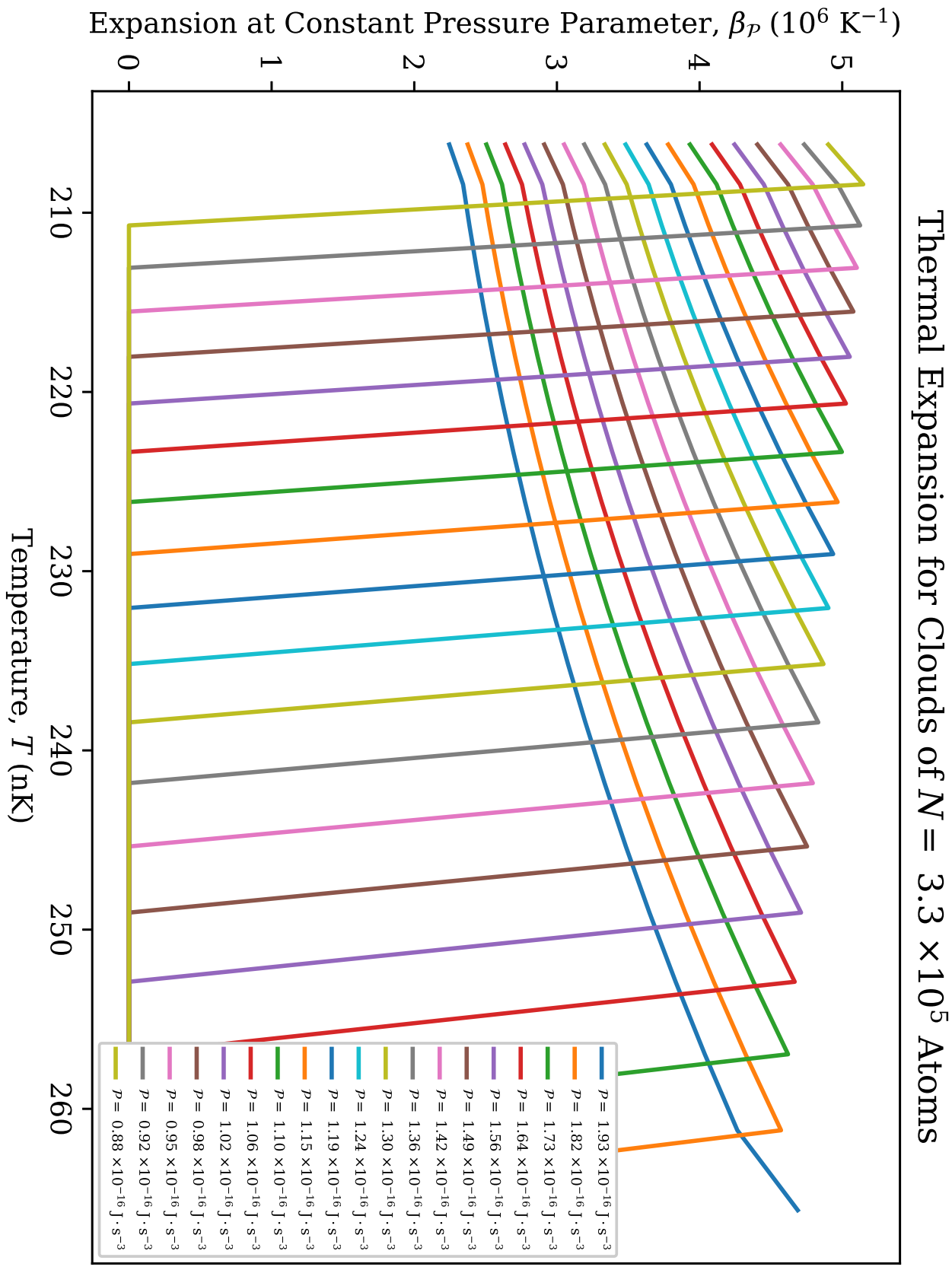

Figure 92 – Plots of the thermal expansion at constant pressure parameter $\beta_\mathcal{P}$ for clouds of $N = 3.3 \times 10^5$ atoms.
Source: By the author.

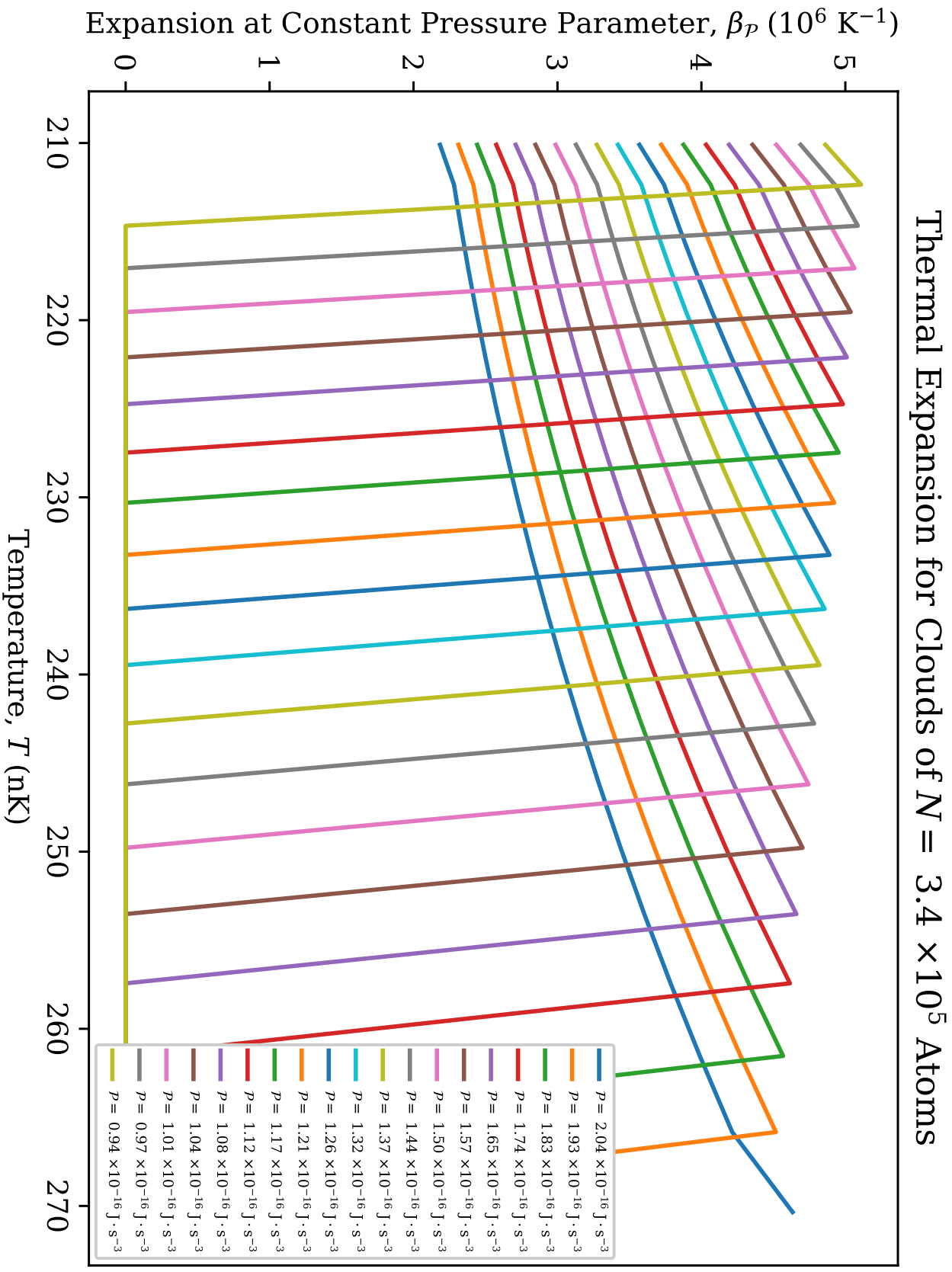

Figure 93 – Plots of the thermal expansion at constant pressure parameter $\beta_{\mathcal{P}}$ for clouds of $N = 3.4 \times 10^5$ atoms.
Source: By the author.

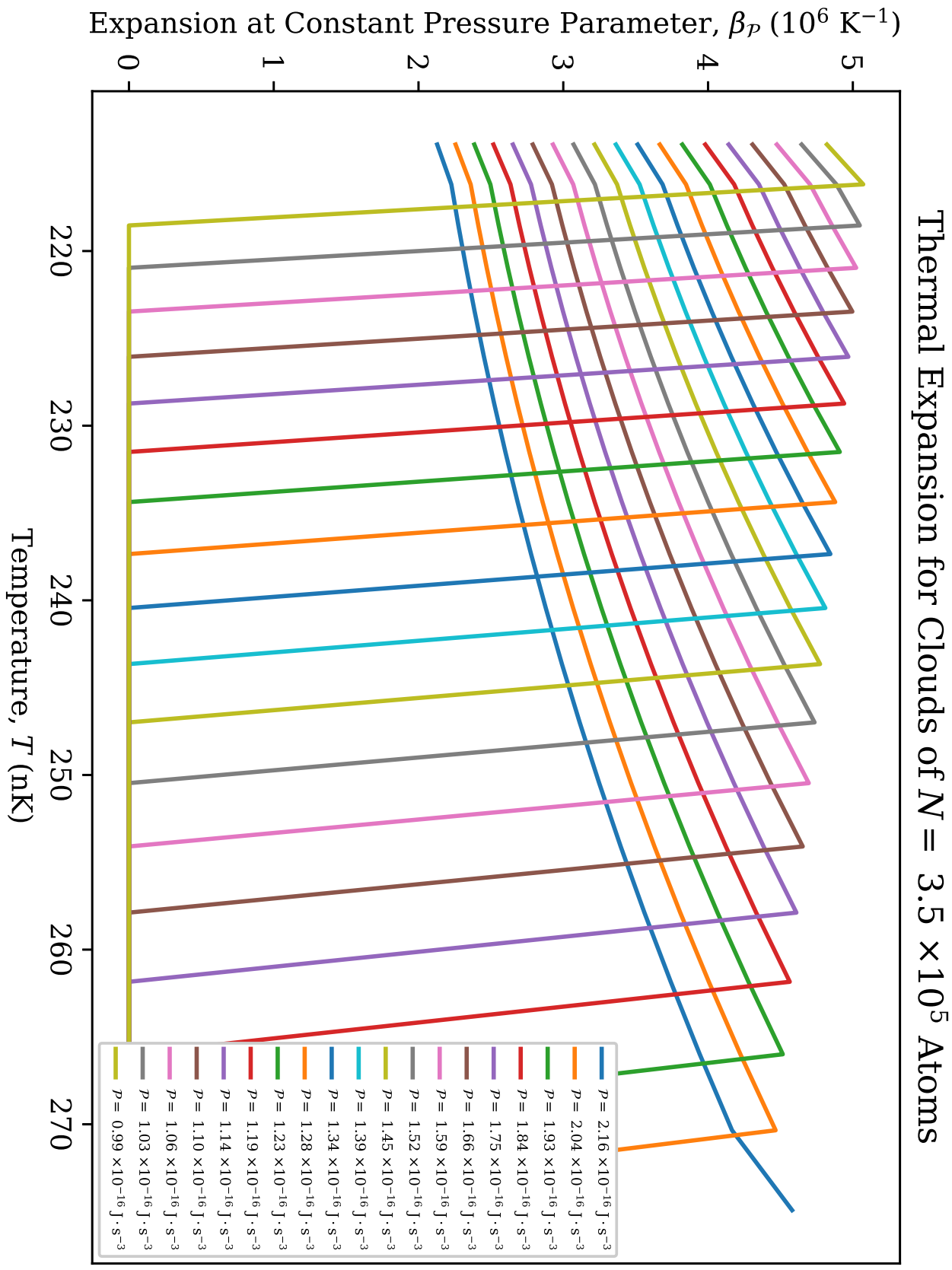

Figure 94 – Plots of the thermal expansion at constant pressure parameter $\beta_{\mathcal{P}}$ for clouds of $N = 3.5 \times 10^5$ atoms.
Source: By the author.

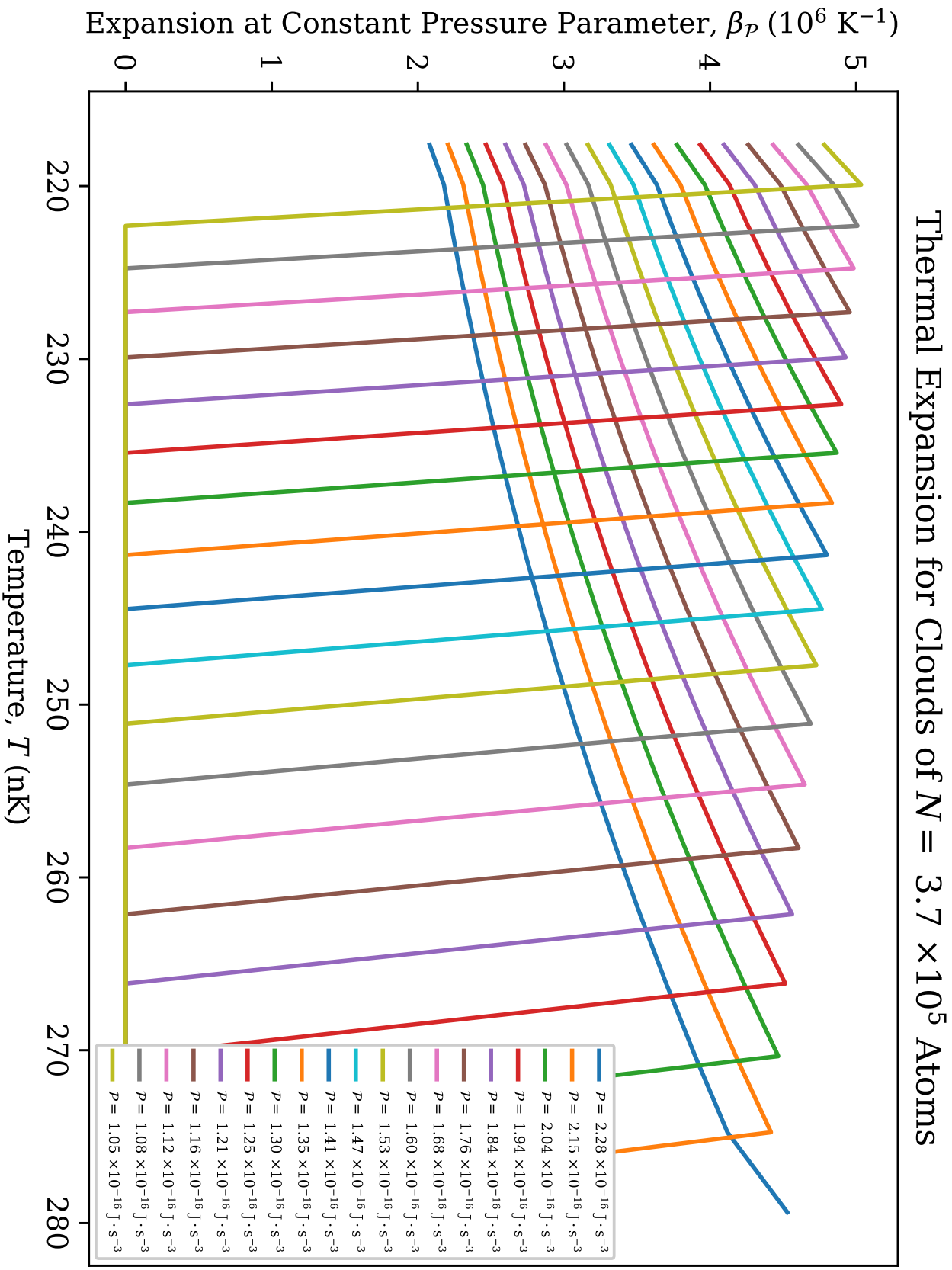

Figure 95 – Plots of the thermal expansion at constant pressure parameter $\beta_{\mathcal{P}}$ for clouds of $N = 3.7 \times 10^5$ atoms.
Source: By the author.

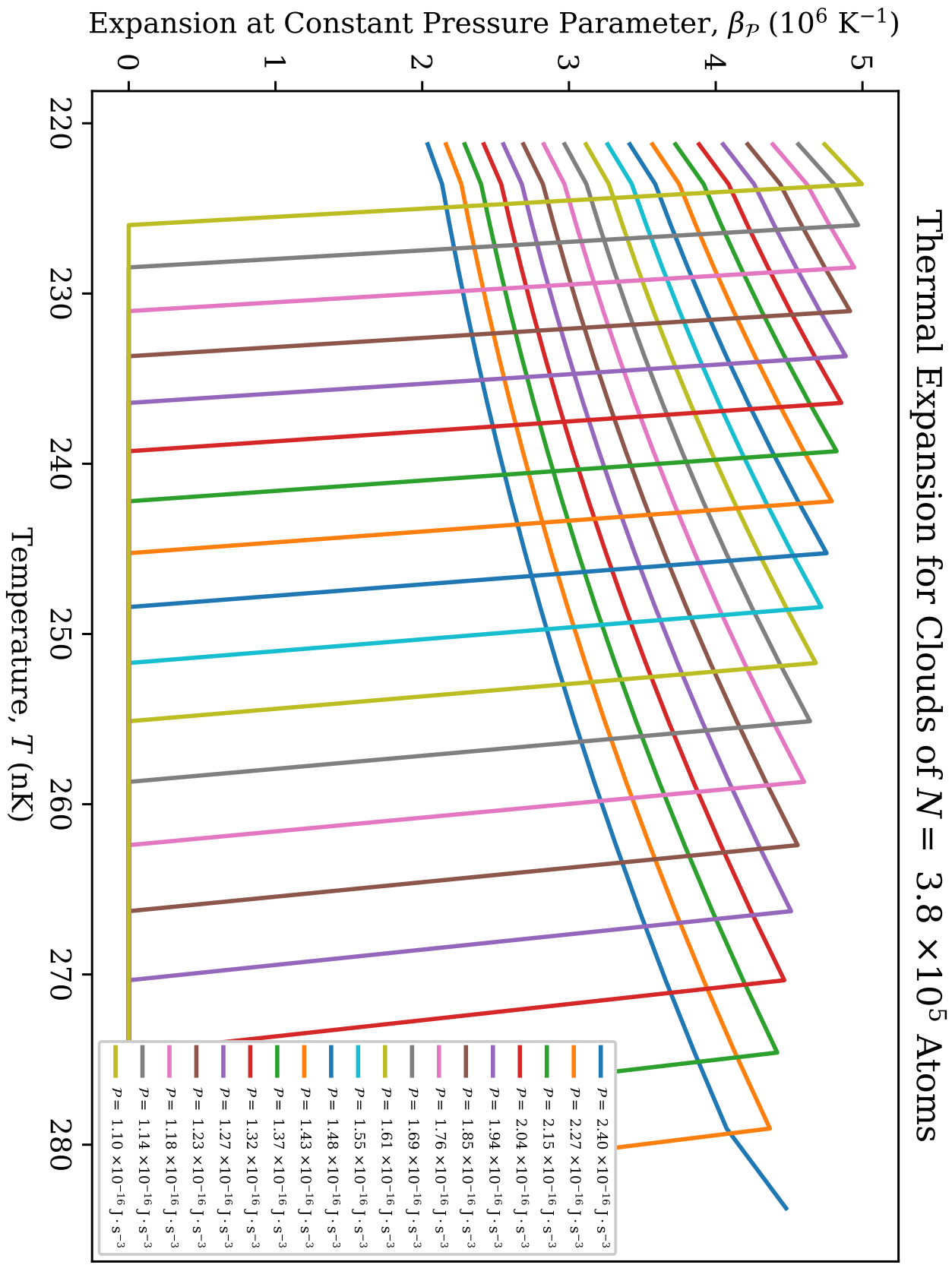

Figure 96 – Plots of the thermal expansion at constant pressure parameter $\beta_\mathcal{P}$ for clouds of $N = 3.8 \times 10^5$ atoms.
Source: By the author.

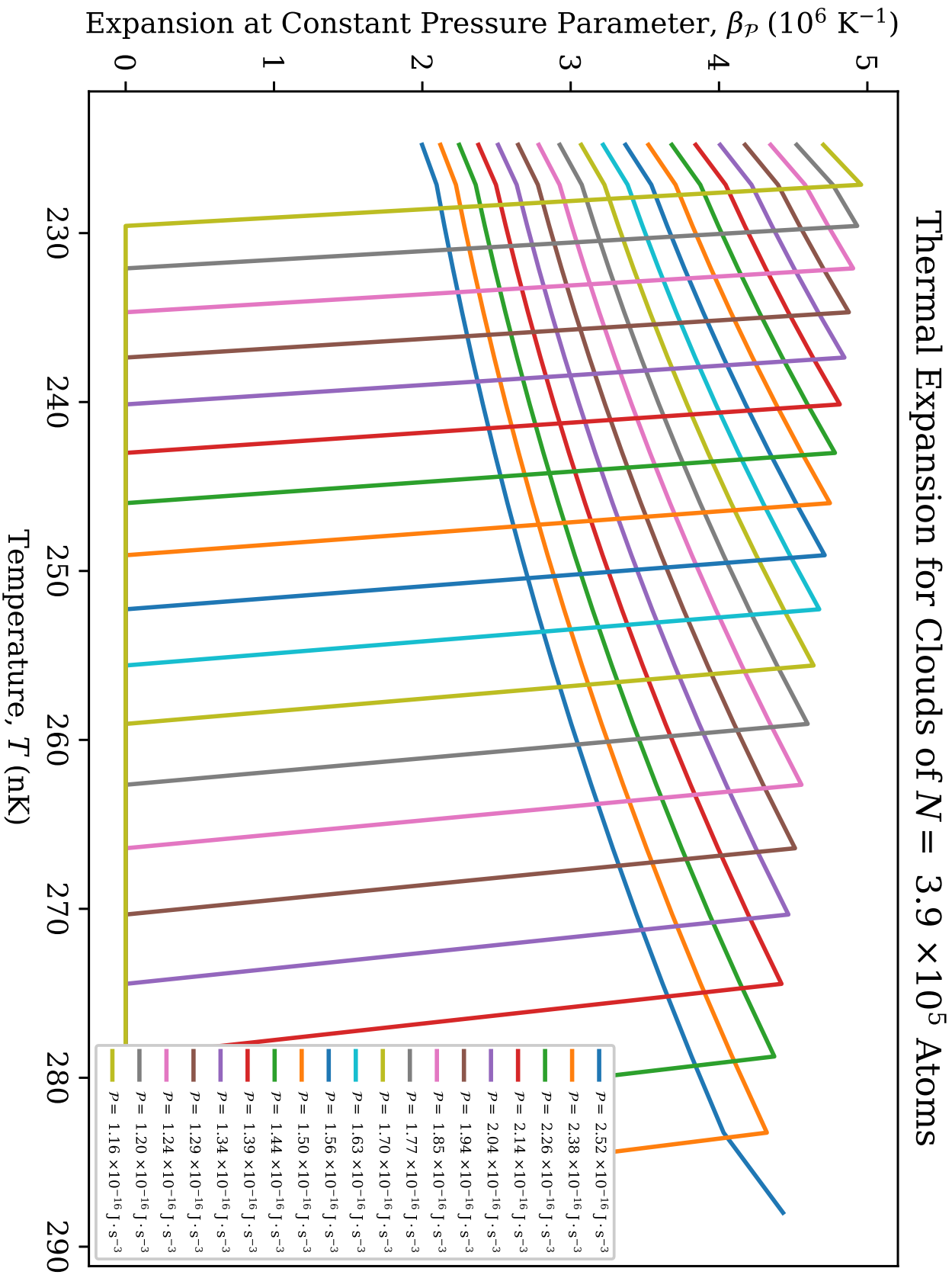

Figure 97 – Plots of the thermal expansion at constant pressure parameter $\beta_{\mathcal{P}}$ for clouds of $N = 3.9 \times 10^5$ atoms.
Source: By the author.

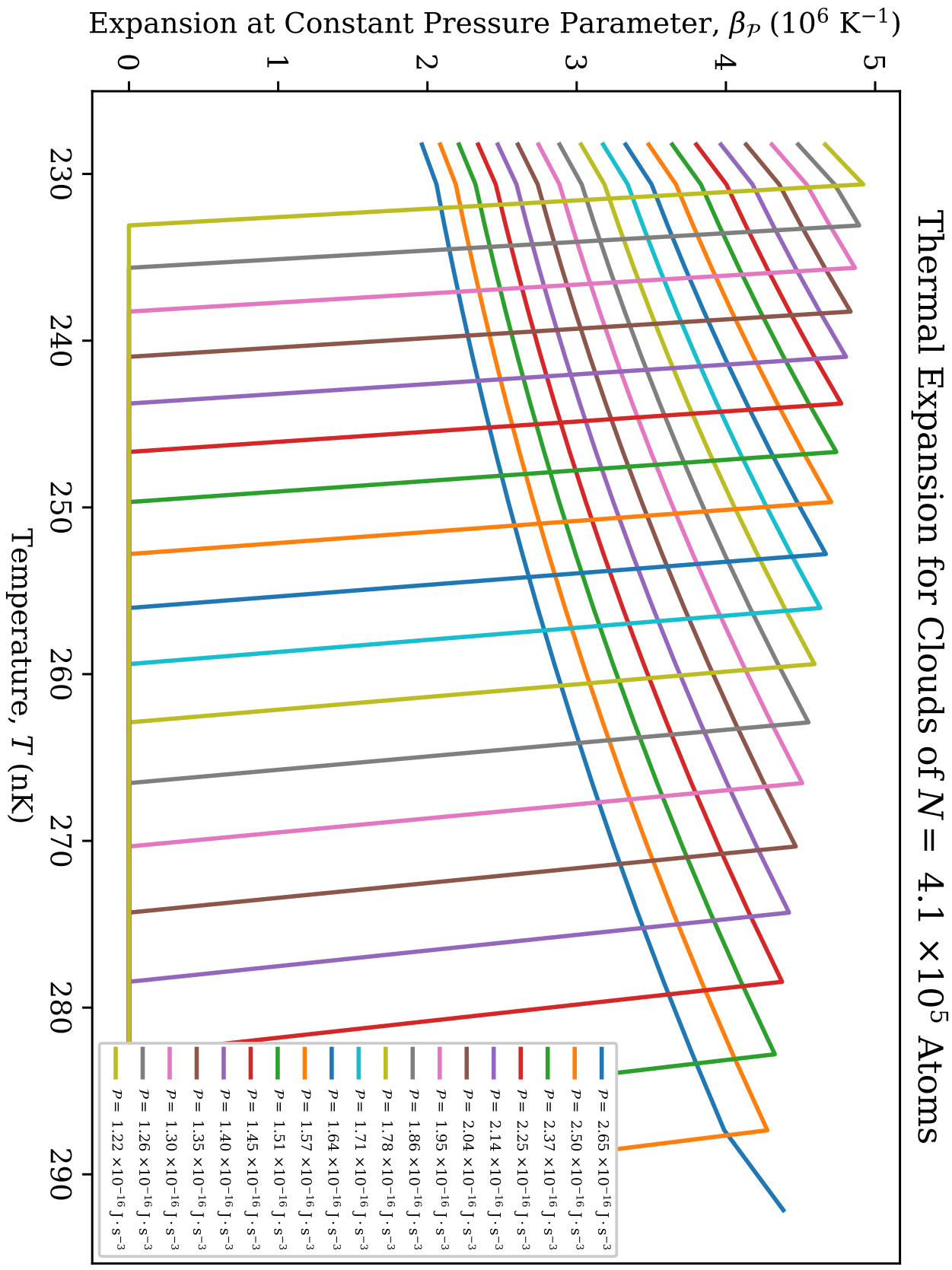

Figure 98 – Plots of the thermal expansion at constant pressure parameter $\beta_\mathcal{P}$ for clouds of $N = 4.1 \times 10^5$ atoms.
Source: By the author.

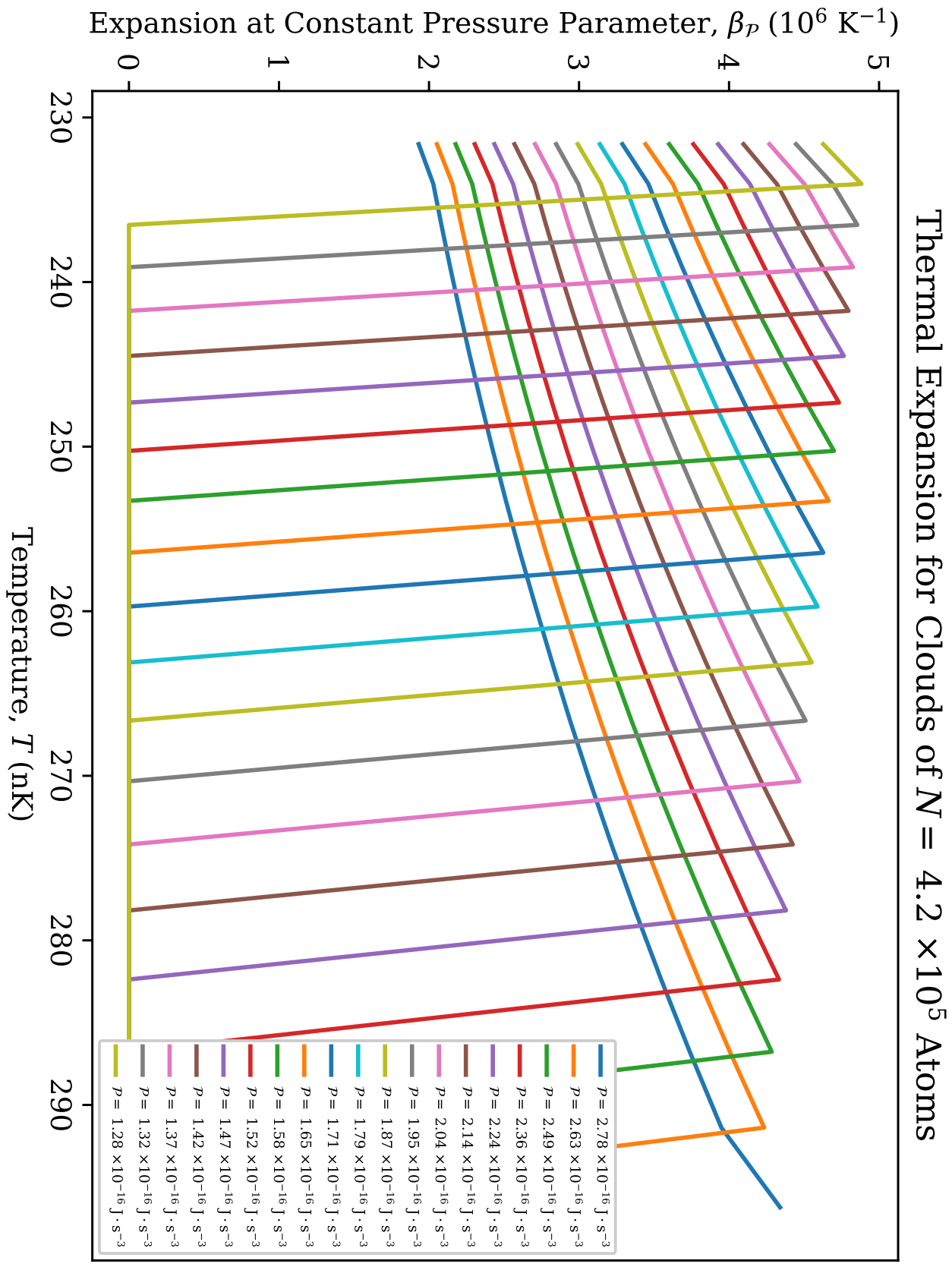

Figure 99 – Plots of the thermal expansion at constant pressure parameter $\beta_{\mathcal{P}}$ for clouds of $N = 4.2 \times 10^5$ atoms.
Source: By the author.

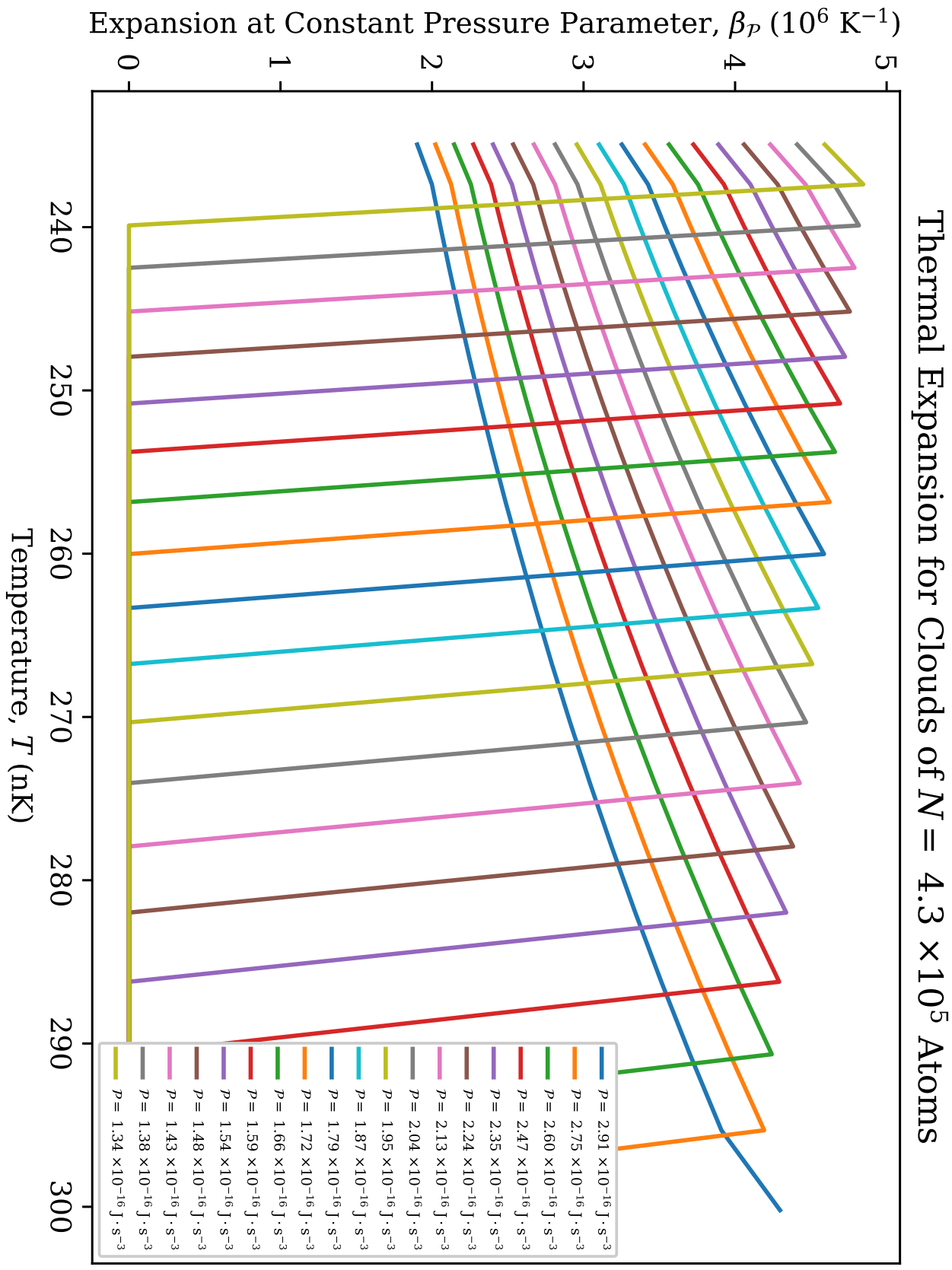

Figure 100 – Plots of the thermal expansion at constant pressure parameter $\beta_\mathcal{P}$ for clouds of $N = 4.3 \times 10^5$ atoms.
Source: By the author.

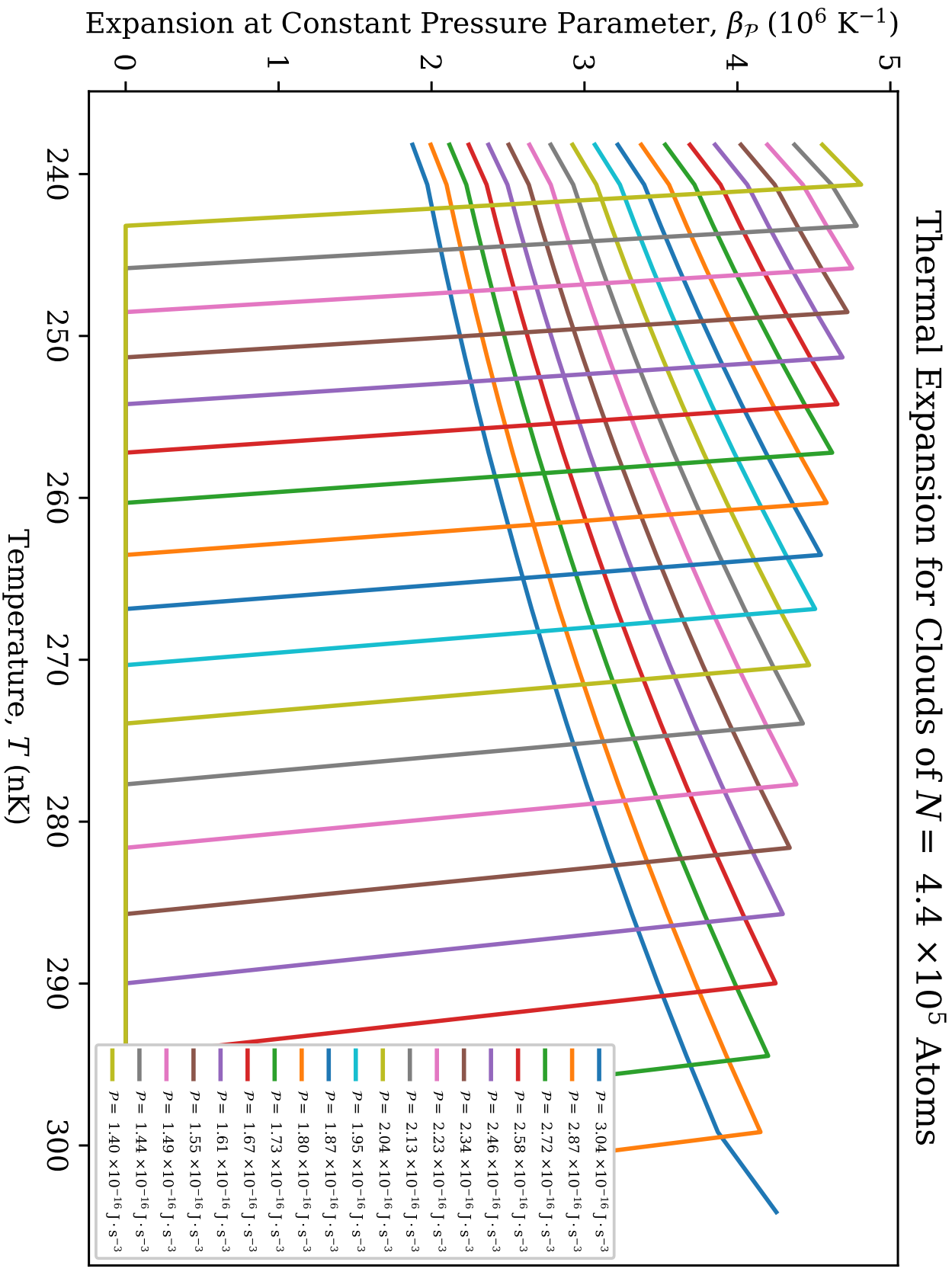

Figure 101 – Plots of the thermal expansion at constant pressure parameter $\beta_\mathcal{P}$ for clouds of $N = 4.4 \times 10^5$ atoms.
Source: By the author.

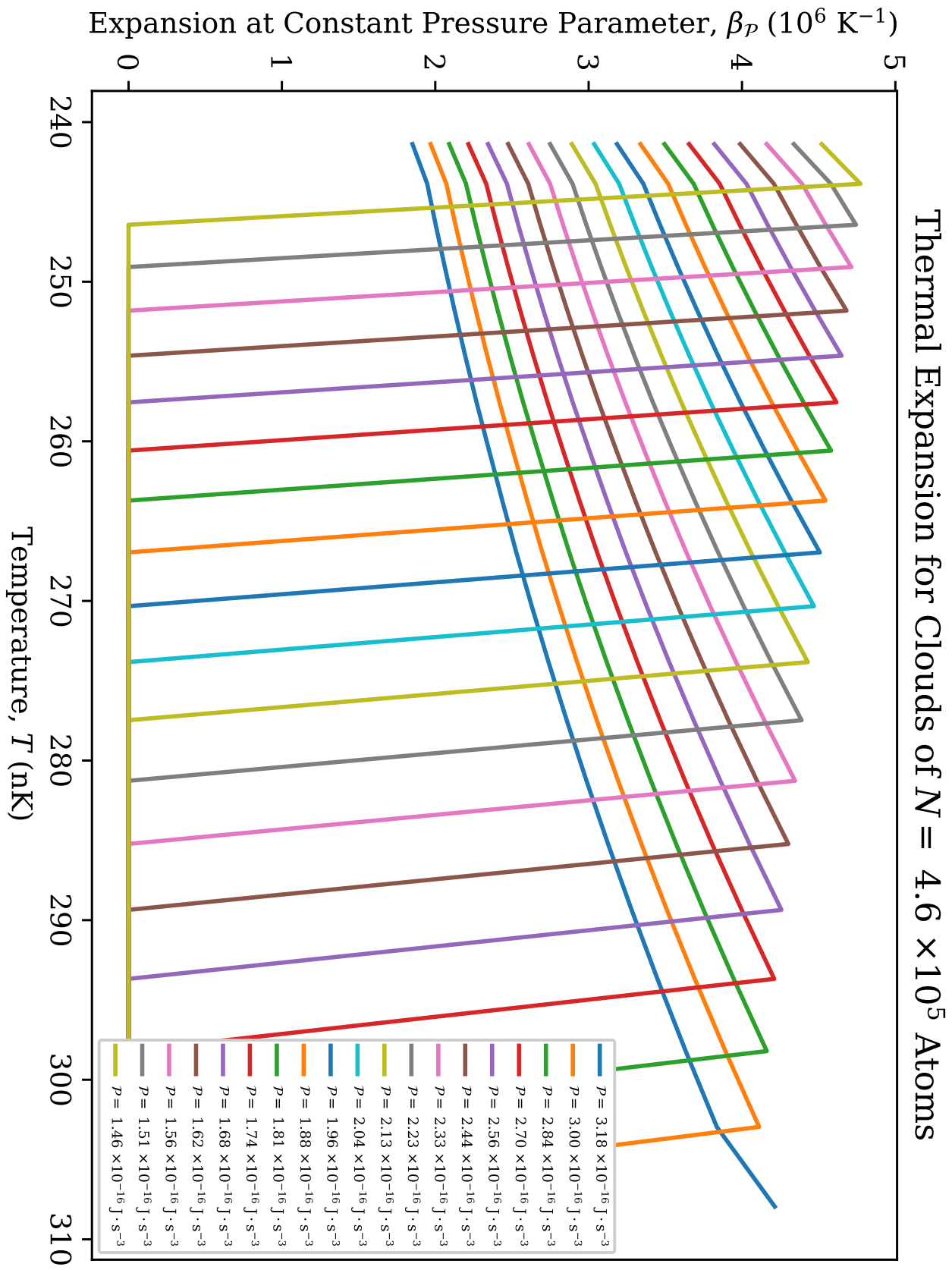

Figure 102 – Plots of the thermal expansion at constant pressure parameter $\beta_{\mathcal{P}}$ for clouds of $N = 4.6 \times 10^5$ atoms.
Source: By the author.

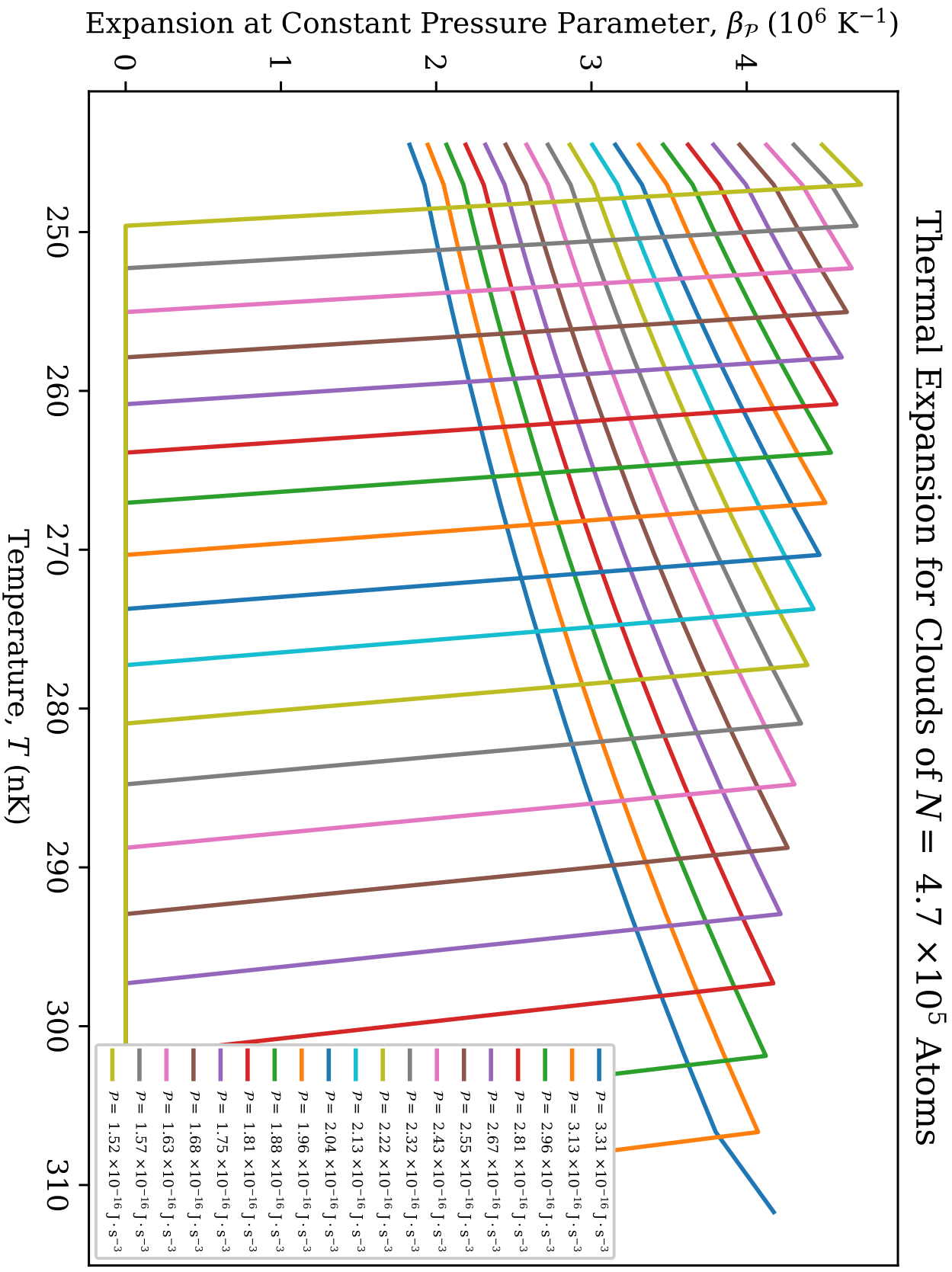

Figure 103 – Plots of the thermal expansion at constant pressure parameter $\beta_\mathcal{P}$ for clouds of $N = 4.7 \times 10^5$ atoms.
Source: By the author.

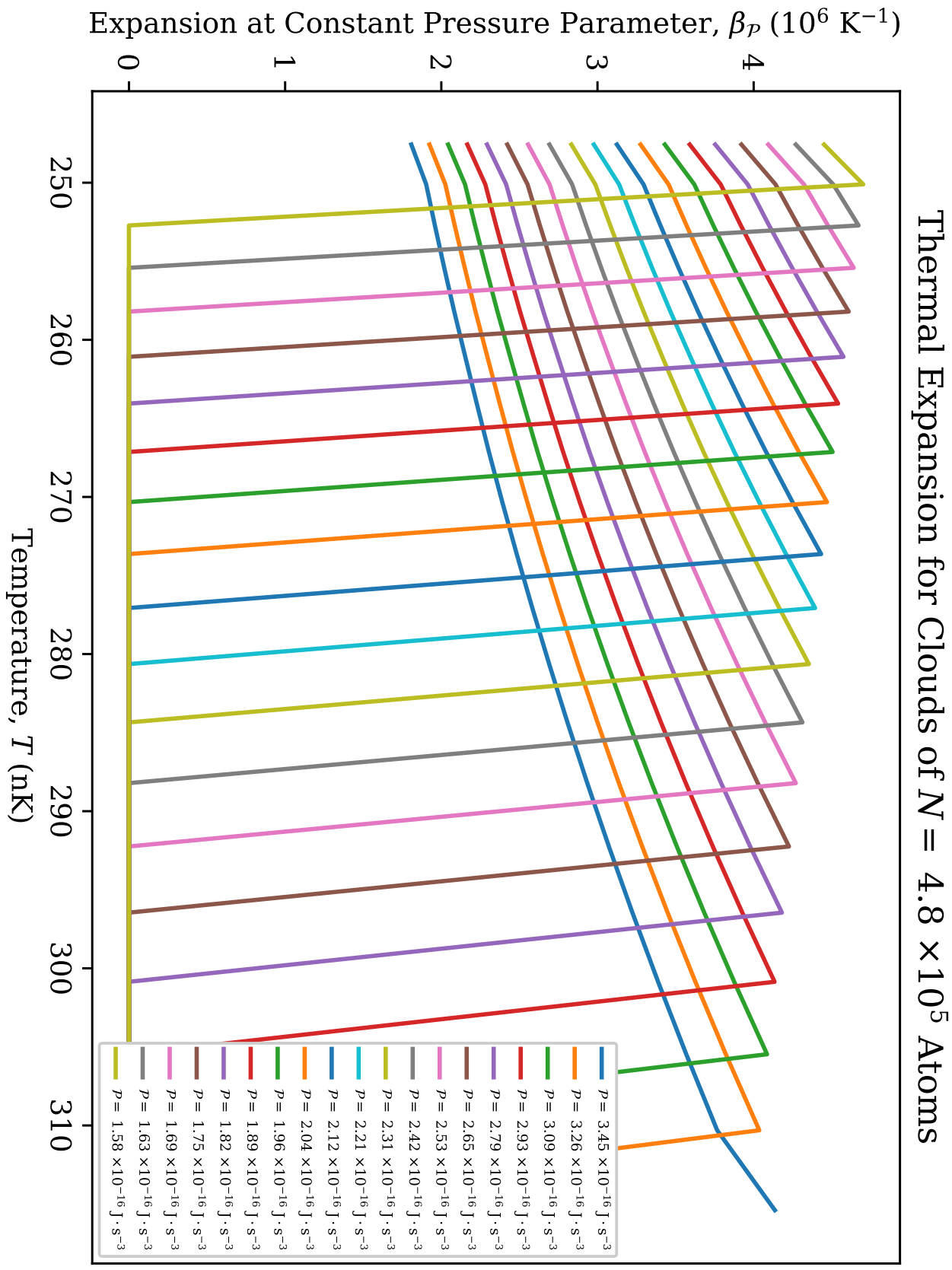

Figure 104 – Plots of the thermal expansion at constant pressure parameter $\beta_\mathcal{P}$ for clouds of $N = 4.8 \times 10^5$ atoms.
Source: By the author.

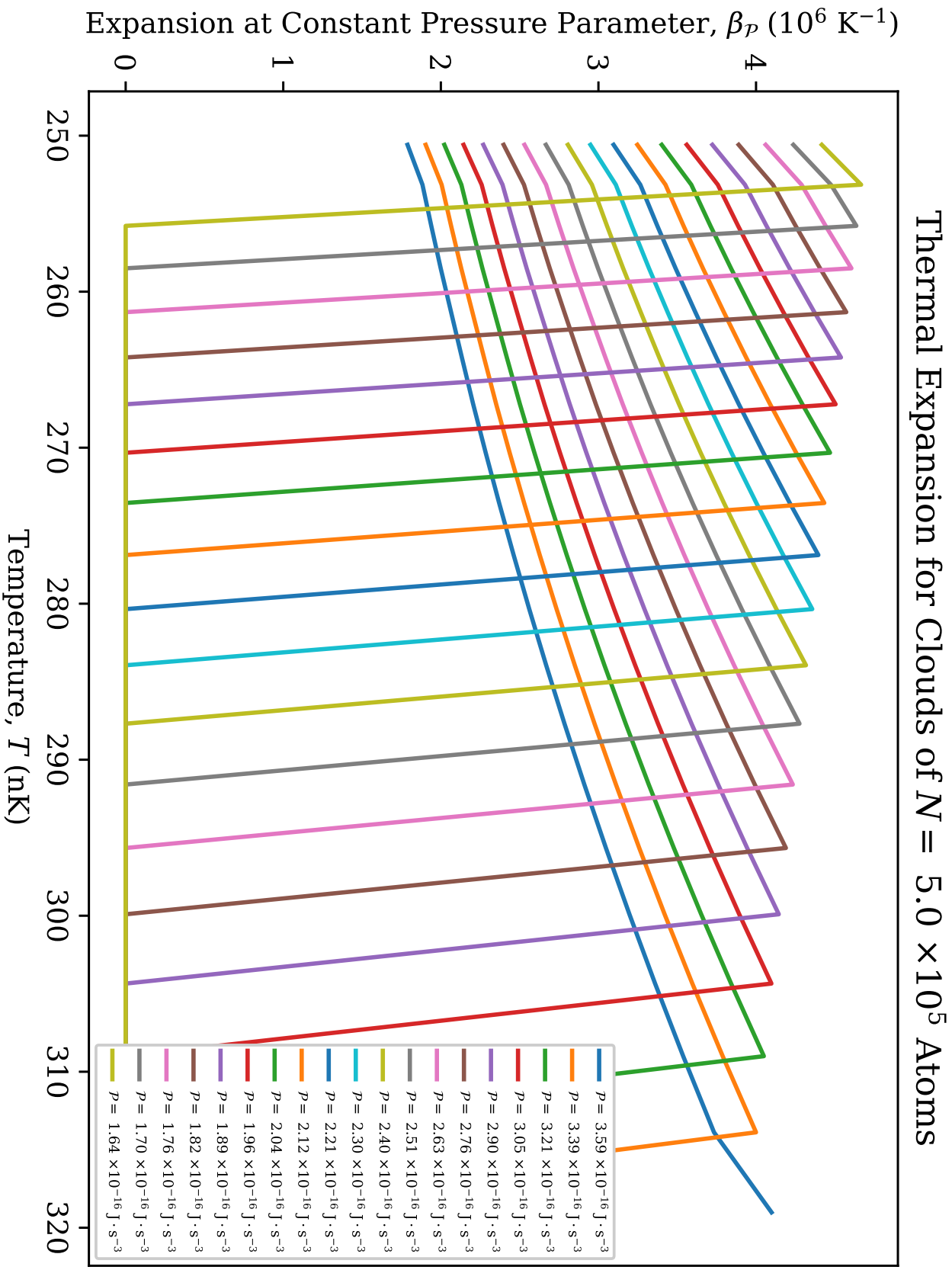

Figure 105 – Plots of the thermal expansion at constant pressure parameter $\beta_\mathcal{P}$ for clouds of $N = 5.0 \times 10^5$ atoms.
Source: By the author.

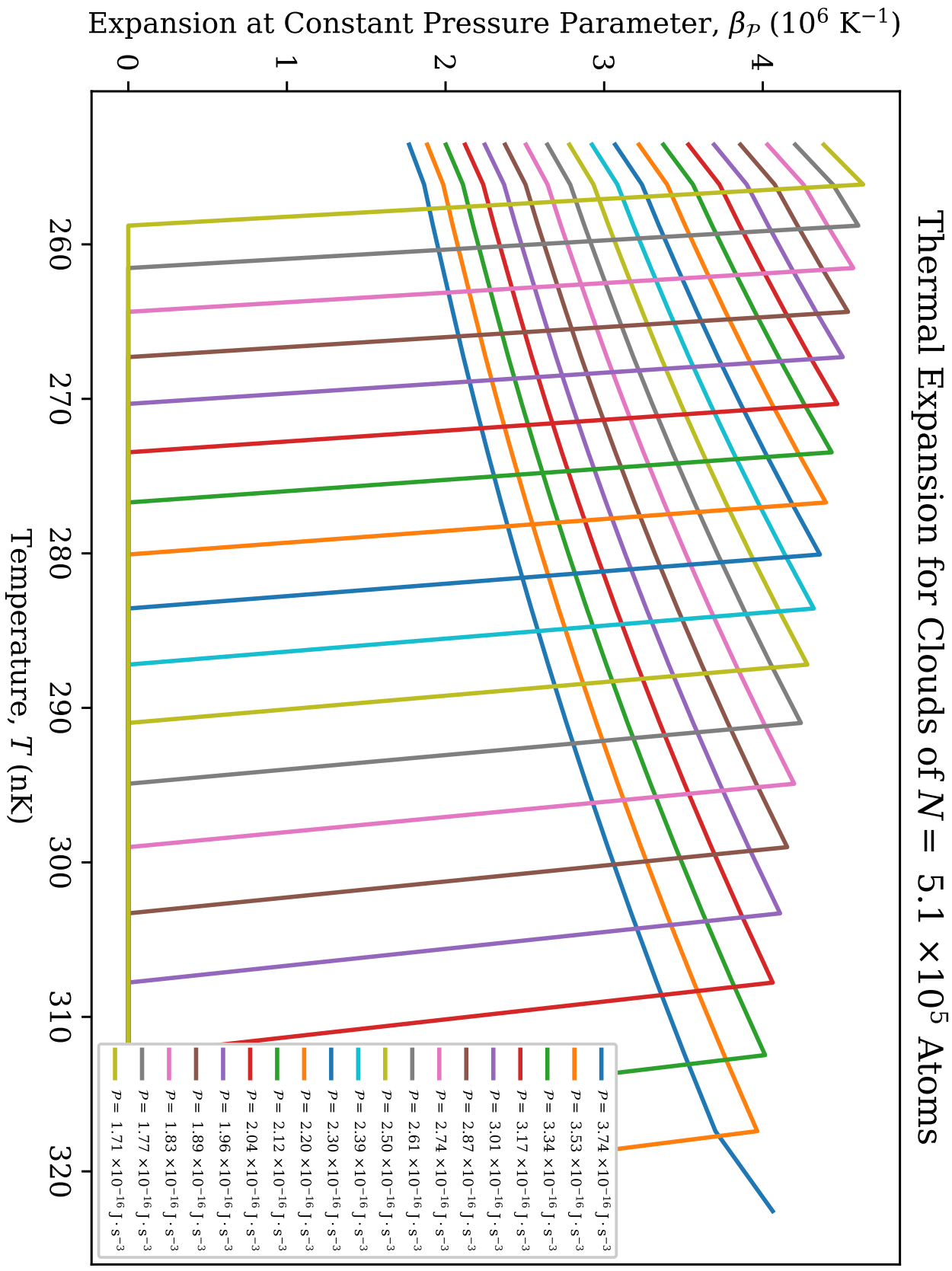

Figure 106 – Plots of the thermal expansion at constant pressure parameter $\beta_\mathcal{P}$ for clouds of $N = 5.1 \times 10^5$ atoms.
Source: By the author.

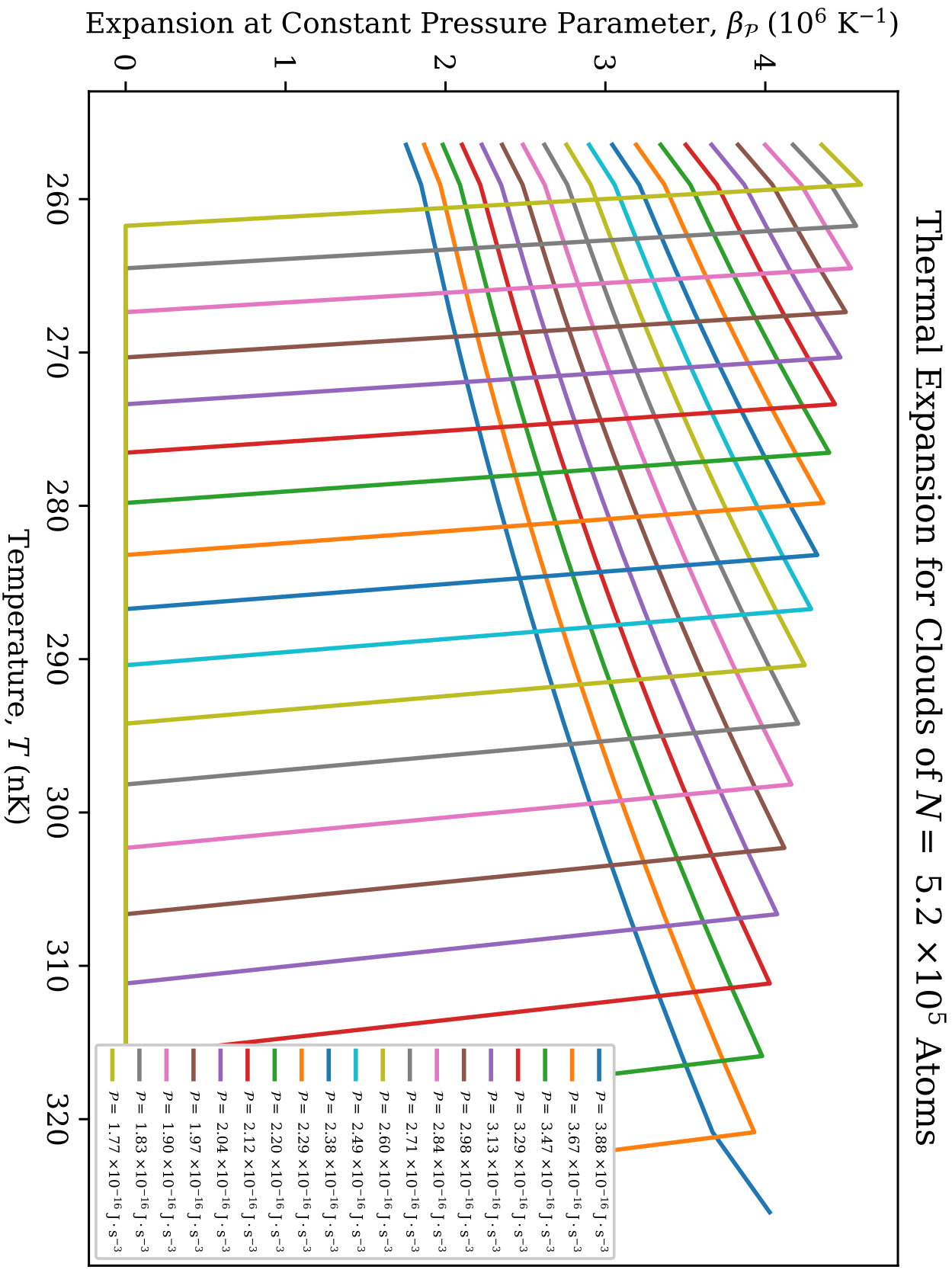

Figure 107 – Plots of the thermal expansion at constant pressure parameter $\beta_\mathcal{P}$ for clouds of $N = 5.2 \times 10^5$ atoms.
Source: By the author.

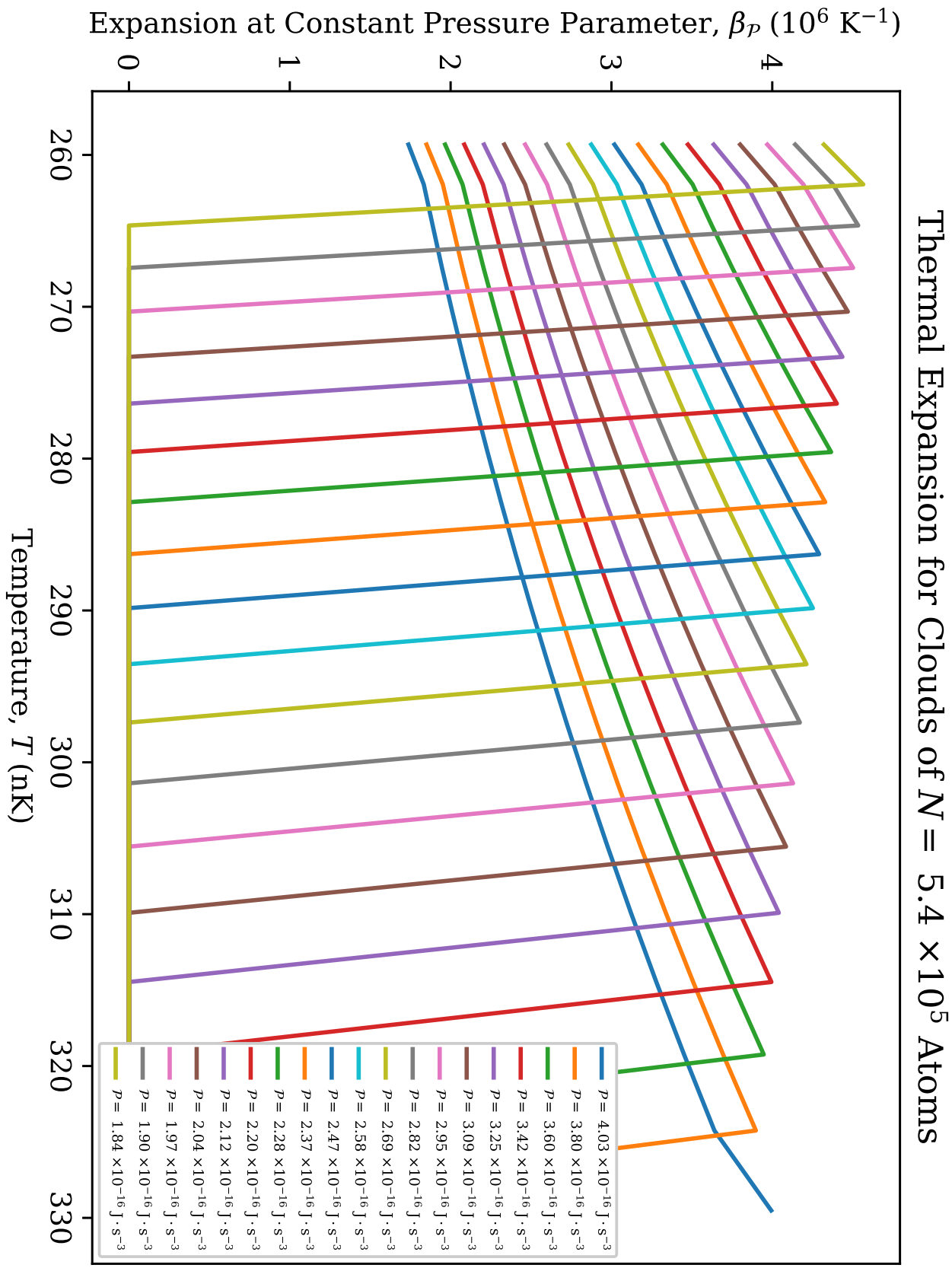

Figure 108 – Plots of the thermal expansion at constant pressure parameter $\beta_{\mathcal{P}}$ for clouds of $N = 5.4 \times 10^5$ atoms.
Source: By the author.

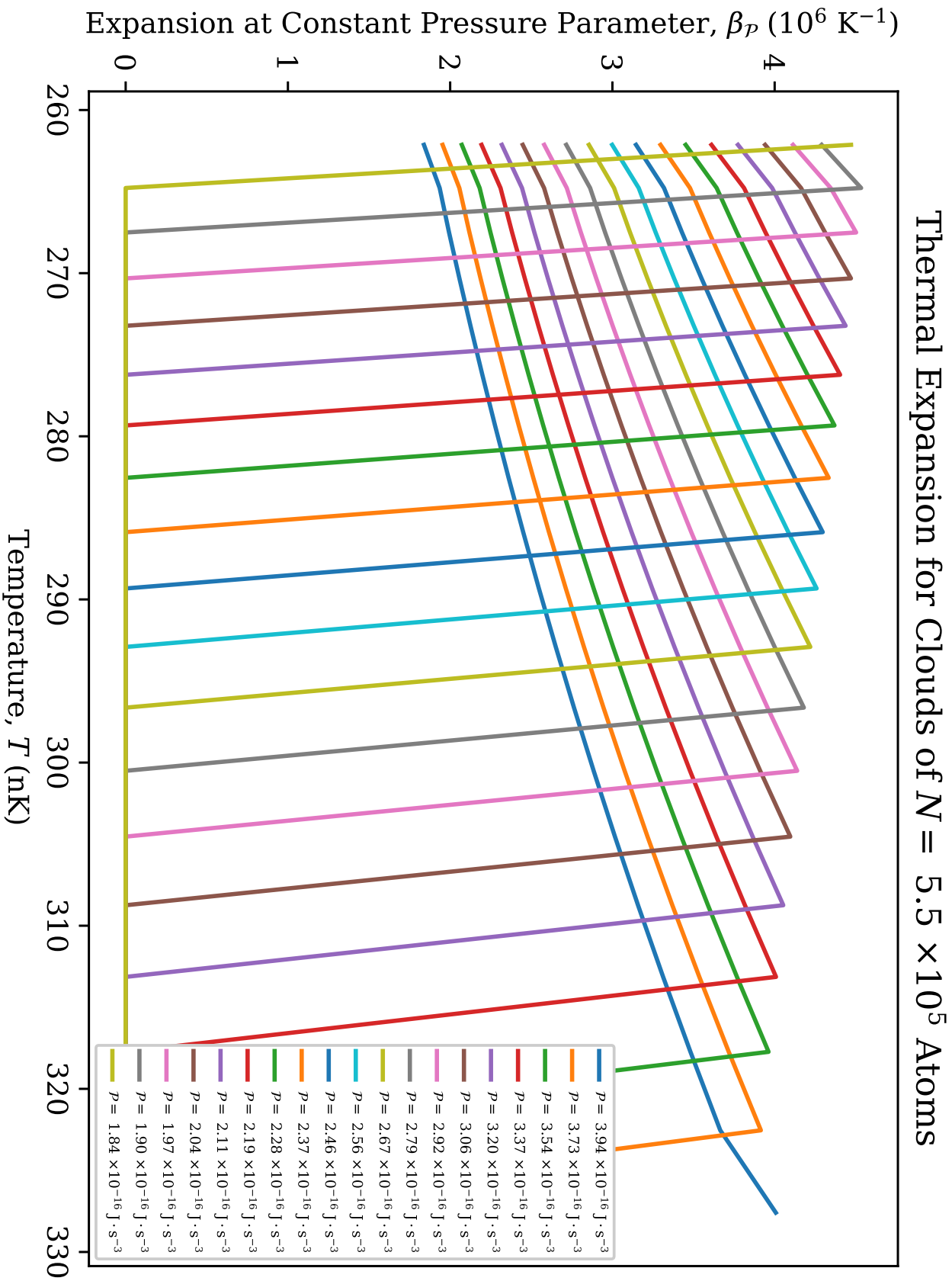

Figure 109 – Plots of the thermal expansion at constant pressure parameter $\beta_{\mathcal{P}}$ for clouds of $N = 5.5 \times 10^5$ atoms.
Source: By the author.